PolyPublie
Polytechnique Montréal

POLYTECHNIQUE MONTRÉAL
UNIVERSITÉ D'INGÉNIERIE

Titre: Title:	Improved Conditioning to Hard, Soft and Dynamic Data In Multiple-Point Geostatistical Simulation
Auteur: Author:	Hassan Rezaee
Date:	2017
Type:	Mémoire ou thèse / Dissertation or Thesis
Référence: Citation:	Rezaee, H. (2017). Improved Conditioning to Hard, Soft and Dynamic Data In Multiple-Point Geostatistical Simulation [Thèse de doctorat, École Polytechnique de Montréal]. PolyPublie. https://publications.polymtl.ca/2633/

Document en libre accès dans PolyPublie
Open Access document in PolyPublie

URL de PolyPublie: PolyPublie URL:	https://publications.polymtl.ca/2633/
Directeurs de recherche: Advisors:	Denis Marcotte
Programme: Program:	Génie minéral

Ce fichier a été téléchargé à partir de PolyPublie, le dépôt institutionnel de Polytechnique Montréal
This file has been downloaded from PolyPublie, the institutional repository of Polytechnique Montréal

https://publications.polymtl.ca

UNIVERSITÉ DE MONTRÉAL

IMPROVED CONDITIONING TO HARD, SOFT AND DYNAMIC DATA IN MULTIPLE-POINT GEOSTATISTICAL SIMULATION

HASSAN REZAEE
DÉPARTEMENT DES GÉNIES CIVIL, GÉOLOGIQUE ET DES MINES
ÉCOLE POLYTECHNIQUE DE MONTRÉAL

THÈSE PRÉSENTÉE EN VUE DE L'OBTENTION
DU DIPLÔME DE PHILOSOPHIÆ DOCTOR
(GÉNIE MINÉRAL)
MAI 2017

© Hassan Rezaee, 2017.

UNIVERSITÉ DE MONTRÉAL

ÉCOLE POLYTECHNIQUE DE MONTRÉAL

Cette thèse intitulée :

IMPROVED CONDITIONING TO HARD, SOFT AND DYNAMIC DATA IN MULTIPLE-POINT GEOSTATISTICAL SIMULATION

présentée par : REZAEE Hassan
en vue de l'obtention du diplôme de : Philosophiæ Doctor
a été dûment acceptée par le jury d'examen constitué de :

M. GOULET James, D.Sc., président
M. MARCOTTE Denis, Ph. D., membre et directeur de recherche
M. ORTIZ Julian, Ph. D., membre
M. HU Lin Ying, Ph. D., membre

DEDICATION

To my parents

ACKNOWLEDGMENTS

I would like to express my sincere thanks to Prof. Denis Marcotte for accepting me, funding my studies, and his constant support during four years. That was always a push to try harder for the perfection and completion of the work. It was quite frightening on the first place to come to Canada's cold from Iran ! Denis was very responsive throughout the years and extremely supportive.

I use the opportunity to thank my kind parents and siblings. I'm grateful beyond words.

This PhD was quite an adventure in its kind, by far the best PhD I have ever done ! It made possible due to the support of Denis in the first place and second all the wonderful people I came to meet during the internships.

My first internship with CGG Crawley, UK, was a great opportunity to see how industry handles problems related to geological modelling in real studies. In particular I thank Philippe Doyen, Thierry, Salman, Théophile, Rémi and the other Rémi !

The second internship with Jason CGG in The Hague, Netherlands, was a perfect entry point to field of geophysical seismic data processing and inversion, cheese tasting and Heineken ! I would like to thank Ali Moradi Tehrani, Raphael Bornard, Reza Saberi, Sarah Boudon and Mengmeng Zhang. The tests on seismic inversion gave us a better understanding in the case study of Chapter 4 on soft data conditioning.

I also would like to thank Pierre Biver, Tatiana Chugunova and Florent Piriac whose support for the third internship with TOTAL S.A. Pau, France, provided me a great opportunity for hands-on experience in reservoir geological modelling, and wine tasting ! It will always be an asset to me the internship with TOTAL.

All my friends, in Montreal, Europe and Iran that I happened to meet, work and hang out with during PhD and internships ; I appreciate their company and the time we spent together. In particular I would like to thank Yahya, Mohammad, Ali and Amir.

In the end, I would like to thank my dear friends, Jafar, Alireza, Abbas, Reza and Morteza from Zenjkadeh group at University of Tehran.

RÉSUMÉ

Dans cette dissertation, nous présentons trois méthodes visant à corriger autant de problèmes observés dans les simulations géostatistiques basées sur des statistiques multipoint (MPS). Le premier problème est le conditionnement aux données exactes (hard data) des algorithmes MPS par morceaux (patch-based). Le second problème est l'utilisation efficace de données auxiliaires (soft data) dans le MPS. Le dernier problème est la calibration des réalisations de faciès par MPS à des données dynamiques. Bien que le premier problème soit particulier au MPS par morceaux les deux autres sont communs à toutes les variantes de MPS ainsi qu'aux autres méthodes de modélisation des faciès.

Dans une simulation MPS de variables catégoriques les données exactes trouvées dans le voisinage de recherche du point à simuler souvent ne correspondent à aucun des patrons disponibles dans l'image d'entrainement (TI). La solution habituellement utilisée est alors d'ignorer les points du voisinage les plus éloignés jusqu'à ce que le patron soit retrouvé dans la TI. Nous proposons plutôt l'utilisation de TI alternatives (ATI) permettant d'enrichir la base de données des patrons. Les ATIs sont obtenues par simulation non-conditionnelle (MPS par morceaux) à partir de la TI originale (OTI). Parmi toutes les ATI générées, certaines seulement sont sélectionnées en fonction des structures observées et des statistiques présentes dans ces ATI par rapport aux statistiques et aux structures des OTI. On vérifie également que chaque ATI apporte suffisamment de patrons présents dans les données exactes observées. Les ATIs qui ne sont pas assez riches en patrons observés ou qui ne sont pas statistiquement similaires à l'OTI, ou qui ont un contenu structurel différent de l'OTI sont rejetées. Les ATIs sélectionnées et l'OTI sont ensuite transmises à la boucle principale de simulation. Le nombre et la taille des ATIs sélectionnées peuvent être aussi grands que souhaité pourvu que les temps de calcul demeurent réalistes. Nous avons testé l'approche sur plusieurs TI différentes, catégoriques et continues, en 2D et en 3D. Nos résultats montrent que l'utilisation des ATIs améliore le conditionnement aux données exactes, améliore la reproduction de la texture des TI et permet de simuler sur de grandes grilles même à partir de petites OTI.

Le conditionnement des modèles de faciès à des données auxiliaires est complexe, en raison de relations mal connues, souvent non-linéaires, liant les faciès et les données auxiliaires continues. Dans cette étude, nous proposons de calculer des champs de probabilité à partir des données auxiliaires en utilisant la régression logistique multinomiale. La méthode permet d'intégrer plusieurs variables auxiliaires correspondant par exemple à autant de méthodes géophysiques. Elles sont exploitées avec les données exactes pour estimer par régression logistique multinomiale les champs de probabilités de chaque faciès. Plus la relation entre les

données exactes et auxiliaires est forte, plus les champs de probabilité obtenus sont informatifs. Les champs de probabilité sont ensuite transférés à la boucle principale de simulation MPS. Pour chaque morceau à simuler, la sélection sur l'OTI ou les ATI se fait à l'aide d'une distance constituée de deux termes. Un premier terme mesure la reproduction des données exactes et la continuité de la texture, un second terme compare les proportions de chaque facies dans le morceau aux probabilités dans la zone à simuler. Ces deux termes sont combinés avec un poids défini par la qualité de la régression logistique. La méthode a été testée sur différents exemples synthétiques avec et sans données exactes et avec des variables auxiliaires présentant des degrés variables de corrélation avec les données exactes. Une étude de cas du champ d'hydrates de gaz de Mackenzie a été réalisée. Les teneurs dans les puits ont été utilisées comme données exactes. L'image tomographique de la teneur du gaz entre deux puits a été utilisée comme TI 2D et les données d'impédance acoustique provenant de l'inversion sismique ont servi de données auxiliaires. Des réalisations multiples obtenues avec l'approche proposée ont montré une bonne correspondance entre la carte d'espérance des réalisations (e-type) et les probabilités calculées.

Le problème de la calibration des modèles de faciès à des données dynamiques (e.g. des flux) est plus difficile que la calibration à des données statiques puisque par exemple la relation entre l'arrangement spatial des faciès et la réponse des flux peut être très complexe. La première étape de l'approche proposée consiste à obtenir des réalisations MPS conditionnelles aux données exactes et auxiliaires. Dans une seconde étape les réalisations de faciès sont converties en champs gaussiens grâce à une règle de codage et un simulateur de Gibbs, tout comme avec la méthode de simulation plurigaussienne. Dans une troisième étape, les champs gaussiens sont perturbés par déformation graduelle (GDM) afin de s'approcher des données dynamiques observées. Le GDM a été intégré à un processus évolutif s'inspirant d'algorithme génétique. Une population est formée et évolue au fil des générations qui se succèdent. Chaque génération comporte un mélange de réalisations évoluées obtenues par GDM et de réalisations directement issues du MPS, ces dernières assurant le maintien de suffisamment de diversité génétique au sein de la population. Les générations se suivent jusqu'à ce que les critères d'arrêt soient respectés. L'algorithme proposé est général et peut s'appliquer à toute méthode de simulation de faciès. Il a été testé sur plusieurs cas 2D et 3D avec différents types de données dynamiques. Dans tous les cas, la calibration aux données dynamiques a été grandement améliorée par rapport aux résultats obtenus avec les MPS non-calibrés.

Les idées proposées pour le conditionnement et la calibration des modèles MPS ont été rassemblées en un test intégré. L'exemple comprenait une TI 2D, 250 données exactes, trois variables auxiliaires, et trois puits avec des données dynamiques de production. Les données

auxiliaires ont été utilisées dans la régression logistique multinomiale pour calculer les cartes de probabilité. Plusieurs réalisations MPS ont été générées conditionnellement aux données exactes et auxiliaires et ont été utilisées pour générer des champs Gaussiens en utilisant l'échantillonnage de Gibbs. L'approche GDM-évolutionnaire a été appliquée pour la calibration des modèles aux courbes pétrole/eau. Le GDM-évolutionnaire s'est avéré efficace pour calibrer ces modèles aux données dynamiques. Les résultats montrent l'importance de bien intégrer les données auxiliaires et dynamiques dans les réalisations MPS.

Les stratégies de conditionnement des MPS présentées dans cette dissertation forment un tout cohérent et intégré permettant la production de modèles de faciès de haute qualité (texture) respectant les données exactes, auxiliaires et dynamiques obtenues de sources diverses. Ces modèles améliorés de faciès constituent un élément essentiel pour une meilleure prévision des performances des réservoirs et gisements et fournissent un outil permettant de guider les décisions stratégiques d'exploitation des ressources et d'évaluer l'incertitude associée. La dissertation se termine sur quelques suggestions pour travaux futurs.

ABSTRACT

In this dissertation, we present three methodologies to correct three problems observed in geostatistical simulations based on multiple-point statistics or MPS. The first problem is the conditioning to hard data of patch-based algorithms. The second problem is the efficient use of auxiliary data in patch-based MPS. The last is the calibration of facies realizations to dynamic data. The first problem is particular to patch-based MPS while the second and third are common between not only MPS approaches but also other facies modeling methods. In an MPS simulation of categorical variables, hard data found within the search neighbourhood of simulation point often do not match exactly any of the patterns available in TI. One common solution to this problem is to drop out farther nodes until a matching pattern is found in TI. We propose instead using Alternative TIs (ATI) to enrich the pattern database. ATIs are mainly unconditional patch-based simulations based on original TI (OTI). Among the ATIs generated, some are selected based on the structures observed and their statistical features (histogram and variogram) compared with those of OTI. Their pattern databases are examined for the frequency of matching patterns with existing hard data configurations in simulation grid. ATIs that are not rich enough (as measured by number of matches for the hard data), not statistically similar to OTI, or with different structural content from OTI are discarded. The selected ATIs and OTI then are passed onto the main simulation loop. ATIs can be considered of any size and number as long as they are not computationally prohibitive for MPS simulation. We have tested the idea over several 2D and 3D TIs for categorical and continuous variables. Our test results show that using ATIs enhances the conditioning capabilities, improves the texture reproduction, and allows simulating over large grids even using much smaller OTIs.

The conditioning of facies models to soft data is complex due to the imperfectly known non-linear relationship between categorical facies types and continuous soft data. In this study we propose calculating probability maps from soft data using multinomial logistic regression. This method allows integrating multiple soft data layers, namely different geophysical data sets. All soft data layers are exploited simultaneously in conjunction with hard data to calculate the facies probability maps. The stronger is the relationship between hard and soft data, the more informative are the output probability maps. The probability maps are then transferred to the main MPS simulation loop. At each patch under simulation, the selection of OTI or the ATIs is performed using a two-term distance function. The first term measures the reproduction of hard data and the continuity of texture, and the second term compares the proportion of each facies in the patch with the probability maps. These

components are merged using a weight determined by the quality of logistic regression. The method was tested over different synthetic examples with and without hard conditioning data and over varying degrees of correlation between hard and soft data. A case study of the Mackenzie gas hydrate field was performed. Grade data sampled on the wells were used as hard data. The tomography image of gas grade between two wells was taken as 2D TI, and the acoustic impedance data from seismic inversion as soft data. Multiple realizations using the proposed approach showed a good match between e-type map of realizations and the calculated probabilities maps.

The problem of calibration of facies models to dynamic data (e.g., flow data) is more difficult than the static soft data since the relationship between facies arrangement and the flow response can be very complex. The first step of the proposed approach consists of obtaining conditional MPS realizations to hard and soft data. In a second step the facies realizations are converted into Gaussian fields using the lithotype rule, and Gibbs Sampling method, all similar to the PluriGaussian simulation method. In a third step, the Gaussian fields are perturbed using the Gradual Deformation Method (GDM) in order to calibrate to the observed dynamic data. The GDM was modified resembling a Genetic Algorithm evolutionary process. A population of perturbed models is formed and evolves over successive generations. Each generation comprises a mixture of perturbed realizations obtained by GDM and realizations directly derived from MPS, the latter ensuring the maintenance of sufficient genetic diversity within the population. The generations evolve until a stopping criteria is met. The proposed algorithm is general and can be applied to all facies simulation methods. It was tested over several 2D and 3D cases with different types of dynamic data. In all cases, the calibration to dynamic data was largely improved compared with non-calibrated MPS realizations.

The proposed ideas for conditioning and calibration of MPS models were put together in an integrated test. The example included a 2D TI, 250 hard data, three soft data variables, and three production wells with dynamic data. The soft data layers were used in multinomial logistic regression to calculate the probability maps. Multiple MPS realizations were generated conditioned to hard and soft data and were used to generate Gaussian fields using Gibbs Sampling. The proposed evolutionary GDM was applied on the realizations for the calibration of models to water cut curves. The evolutionary GDM has proven to be effective in calibrating the facies models to dynamic data. The results show the importance of integrating the auxiliary and dynamic data into the MPS realizations.

The conditioning strategies of MPS presented in this dissertation form a coherent and integrated set of tools allowing the production of facies models of high quality (texture) respecting the hard, auxiliary and dynamic data obtained from various sources. These improved facies models are an essential element for better prediction of reservoir and deposits performance

and provide a tool to guide strategic resource decisions and assess the associated uncertainty. The dissertation ends with some suggestions for future work.

TABLE OF CONTENTS

DEDICATION iii

ACKNOWLEDGMENTS iv

RÉSUMÉ v

ABSTRACT viii

TABLE OF CONTENTS xi

LIST OF TABLES xv

LIST OF FIGURES xvi

LIST OF INITIALS AND ABBREVIATIONS xxv

CHAPTER 1 INTRODUCTION 1
1.1 Facies Modeling 1
1.2 Why Using MPS ? 2
1.3 MPS Workflow 4
1.4 Patch-based MPS 5
1.5 Potential problems with patch-based MPS 6

CHAPTER 2 PROBLEM STATEMENT AND LITERATURE REVIEW 10
2.1 Elements of the Problem 10
2.1.1 Hard Data Conditioning 10
2.1.2 Soft Data Conditioning 13
2.1.3 Dynamic Data Conditioning 23
2.2 Objectives of the Research 27
2.2.1 General objective 27
2.2.2 Specific objectives 27
2.3 Plan of the Thesis 28

CHAPTER 3 ARTICLE 1: MULTIPLE-POINT GEOSTATISTICAL SIMULATION USING ENRICHED PATTERN DATABASES 29
3.1 Abstract 29

3.2 Introduction . . . 30
3.3 Methodology . . . 31
3.3.1 Weighting system . . . 33
3.3.2 Pasting . . . 33
3.3.3 Flowchart . . . 38
3.3.4 Alternative Training Images . . . 38
3.3.5 ATI selection strategy for the categorical and the continuous cases . . . 44
3.4 Results . . . 49
3.4.1 Continuous TI . . . 50
3.4.2 Categorical TI . . . 54
3.4.3 3D simulations . . . 58
3.4.4 CPU Time . . . 61
3.5 Discussion . . . 61
3.6 Conclusion . . . 66
3.7 Acknowledgements . . . 67

CHAPTER 4 ARTICLE 2: INTEGRATION OF MULTIPLE SOFT DATA SETS IN MPS THRU MULTINOMIAL LOGISTIC REGRESSION: A CASE STUDY OF GAS HYDRATES . . . 68
4.1 Abstract . . . 68
4.2 Introduction . . . 69
4.3 Methodology . . . 71
4.3.1 Getting the probability fields . . . 71
4.3.2 Simulating using MPS . . . 72
4.3.3 Influence of the logistic regression . . . 76
4.4 Simulation Results . . . 76
4.4.1 Multiple soft data sets . . . 79
4.4.2 3D simulations . . . 82
4.4.3 Sensitivity to α . . . 82
4.5 Hard Data conditioning . . . 82
4.5.1 Regional effect of HD locations . . . 88
4.6 Real TI and Soft Data Conditioning . . . 88
4.7 Discussion . . . 98
4.8 Conclusions . . . 98
4.9 Acknowledgement . . . 98

CHAPTER 5 ARTICLE 3: CALIBRATION OF CATEGORICAL SIMULATIONS BY

EVOLUTIONARY GRADUAL DEFORMATION METHOD 100
5.1 Abstract 100
5.2 Introduction 101
5.3 Methodology 102
5.3.1 MPS method 103
5.3.2 Latent Gaussian variables 103
5.3.3 Deformation in Gaussian space 105
5.3.4 Facies noise removal 107
5.3.5 Optimization 109
5.4 Results 110
5.4.1 Proportion map example 110
5.4.2 Shortest path 2D example 112
5.4.3 Seismic section example 112
5.4.4 Shortest path 3D example 117
5.4.5 Water Cut Example, 2D Case 117
5.4.6 Water Cut Example, 3D Case 117
5.5 Discussion 122
5.6 Conclusions 126
5.7 Acknowledgement 126

CHAPTER 6 INTEGRATED MODEL 127
6.1 Introduction 127
6.2 Input data 127
6.2.1 Probability maps 129
6.2.2 Dynamic data 131
6.3 Modelling Process 133
6.3.1 TI Enrichment 133
6.3.2 Hard Data Conditioned Models 134
6.3.3 Soft Data Conditioned Models 136
6.3.4 Hard and Soft Data Conditioned Models 137
6.3.5 Global dynamic behaviour of conditioned models 139
6.3.6 Calibrated Models 140
6.4 Discussion and Conclusions 147

CHAPTER 7 DISCUSSION AND CONCLUSION 148
7.1 Discussion 148
7.2 Further developments 151

7.3 Conclusions 152

REFERENCES 154

LIST OF TABLES

Table 3.1 Distribution of patterns found in OTI and ATI 46
Table 5.1 Parameters used in the 2D and 3D water cut examples. 118

LIST OF FIGURES

Figure 1.1 The significant difference between the flow response of channels simulated with SISIM and MPS. The facies models on left column are colored with permeability values. The right column shows the travel time (in logarithmic scale) between source and sink. 3

Figure 1.2 The basic idea behind MPS simulation. 5

Figure 1.3 Patch-based vs. pixel-based MPS simulation. 6

Figure 1.4 Pixel-based vs. patch-based approaches in generating texture. Simulation using T=22 and OL=21 is a pixel-based simulation since the size of patch is reduced to only one pixel. Simulations are performed using distance-based approach based on quilting and a unilateral simulation path. 7

Figure 1.5 Patch-based MPS simulation using distance functions. It is not necessarily the pattern in TI corresponding to *minimum* distance that is selected, but instead a pool of pattern is first formed from the lowest distance values, and one pattern is picked at random and pasted to the simulation grid. The red plus sign shows the upper left corner location of the selected pattern and three white dots on the distance map indicate other three corners. 8

Figure 2.1 The recursive template splitting idea as used in CCSIM (Tahmasebi et al, 2012). The original template with overlap regions in gray and the parts to be simulated in green are highlighted in the simulation grid on left. Right column shows the process through which the original template is split recursively until the matching pattern is found in TI. 12

Figure 2.2 Top: three selected TIs, bottom-left: probability of finding a perfect matching pattern from the TI vs. data event size, bottom-right: portion of the original data event that has to be droped out until we find a matching pattern in the TI. 14

Figure 2.3 Same test as in Fig. 2.2 repeated with and without ATIs. The probability of finding a matching pattern on left columns and the portion of original data event dropped out to find a matching pattern as a function of data event size for channel TI (A), dunes TI (B) and multi-facies channel TI (C), see Fig. 2.2. 15

Figure 2.4 The TI, rotation map and the proportion maps were used to perform conditional simulations. Sample simulations are presented with different Tau values. With permission from Liu (2006). 17
Figure 2.5 A: TI, B: auxiliary variable, C: sample simulation and D: e-type map of 50 realizations. With permission from Chugunova and Hu (2008). . 18
Figure 2.6 A: TI, B: auxiliary variable, C: sample simulation. With permission from Chugunova and Hu (2008). 19
Figure 2.7 Sample conditional simulation of the method proposed with Mariethoz et al (2010). The TI (left) has been used to perform the conditional simulation (right) using the soft data on middle. With permission from Mariethoz et al (2010). 21
Figure 2.8 Sample conditional simulation of the method proposed with Mariethoz et al (2015). The TI on top has been used to perform the conditional simulation shown on bottom using the proportion maps of different facies in the middle rows. With permission from Mariethoz et al (2015). 22
Figure 3.1 Schematic illustration of a patch in (A) unilateral and (B) random simulation paths. Gray pixels are already simulated, white ones are to simulate, and black pixels represent HD. The irregular shape of B is due to random selection of previous patch centroids. 34
Figure 3.2 Enlarged window to include nearby conditioning data in the distance computations. Only the hatched area in the initial window is pasted with data from the matching pattern in the OTI or ATI. 35
Figure 3.3 Weighting sets for HD (a_1) and previously-simulated parts (a_2) and the final weighting matrix (α). In this case, the node highlighted in bold red square receives the highest weight. The illustration shows the weighting system for the L-shaped patch (for other possible patches see Fig. 3.4) 36
Figure 3.4 Patch shapes and the corresponding weighting system. Left: first row, middle: first column, and right: the rest of the image. W stands for the weight given to each band in the template. 37
Figure 3.5 Three possible stitching strategies in simulation. A: new pattern is placed without overlap, B: the overlap is overwritten by the new pattern, C: the overlap is cut through the minimum error path 39
Figure 3.6 $P1$ is the new pattern coming from either OTI or ATI, and $P2$ is the existing pattern simulated before. $P1$ and $P2$ are stitched along the series of pixels where the minimum overlap error is achieved (decoupage) 40

Figure 3.7 Quilting in a 3D parallepiped with multiple surface cuts. 41
Figure 3.8 The flowchart of the algorithm 42
Figure 3.9 Sample OTIs (left) with corresponding ATIs (right) obtained by unilateral unconditional simulation with weighting and decoupage. . . . 43
Figure 3.10 MPH computed over 4 × 4 templates; X: first eigenvector (18 % of variance), Y: second eigenvector (13%) and Z: third eigenvector (10%) from the MDS computed on the similarity matrix defined by the Jensen-Shannon divergence statistic. 45
Figure 3.11 Object features' distribution in OTI and set of ATIs. 3D channels (A) (based on Fig. 3.9-D), 2D balls (B) (Fig. 3.9-A), 3D balls (C) (Fig. 3.9-F) and continuous TI (D) (Fig. 3.9-B) 47
Figure 3.12 ATI selection based on tests on equality of histograms and variograms and test of equality of the object size distribution. The red rectangles identifies areas where the ATI produced undesired results. In the first and second rows, discontinuous channels are evident; in the third row the highlighted patterns contradicts the ones found in the OTI. In the 3D case (4th row) the failed ATI contains too many incomplete balls. These problems are not present in the corresponding selected ATIs. . 48
Figure 3.13 Simulation results for the continuous TI (T=8, OL=3), HD locations indicated by white circles. 51
Figure 3.14 Histogram (bottom figure) and variograms along X and Y axis (top left and right respectively) of 25 realizations (light gray) and of the continuous OTI (black). 52
Figure 3.15 Box plot of the χ^2 statistics between the histogram of the reference continuous TI and the histograms of 50 realizations, conditional to 100 HD, obtained with and without ATIs. 53
Figure 3.16 ATI involvement in simulation as a function of the number of (size 64 × 64) ATIs (left), or the size of a single ATI (right) for the continuous TI of Fig. 3.13. Values on X axis in right figure are the dimensions of ATI along both X and Y directions (e.g., 100×100 or 200×200). The simulations performed with T=6 and OL=2. 55
Figure 3.17 Simulation using a small TI with T=8 and OL=3 56
Figure 3.18 Simulation results for the channel image with $T = 15$, and $OL = 5$. Red circles HD belong to channels and the blue ones to non-channel facies 57

Figure 3.19 Variograms along X direction (A) and Y direction (B) for the 25 realizations (light gray) and the OTI (black), channel TI displayed in Fig. 3.9-D. 58
Figure 3.20 E-type maps of 25 realizations produced with and without ATIs, T=10, OL=3. OTI obtained from Fig. 3.18. 59
Figure 3.21 Simulation results using three-facies OTI with ATI (middle row) and without ATI (bottom row), T=17, and OL=6. 60
Figure 3.22 Simulation results using 3D ball TI with T=15, and OL=5. 62
Figure 3.23 Simulation results using continuous 3D TI with T=15, and OL=5. . . 63
Figure 3.24 CPU time. Top row, left, dashed line: 2D simulations, ATI size varies and simulation grid size is fixed at 64×64; solid line: simulation grid varies and TI size is fixed at 64×64. Top row, right, dashed line: 3D simulations, ATI size varies and simulation grid size is fixed at $50 \times 50 \times 50$; solid line: simulation grid varies and TI size is fixed at $50 \times 50 \times 50$. Bottom row: the number of ATIs varies, each ATI and simulated field of size $100 \times 100 \times 100$. For 2D simulations $T = 10$ and $OL = 4$; for 3D simulations, $T = 15$ and $OL = 5$. 64
Figure 4.1 Right: Binary HD and three soft data sets; Left: Probability field obtained by multinomial logistic regression. 73
Figure 4.2 Left: HD and soft data map; Right: probability fields for three categories. 74
Figure 4.3 The TI used to generate the reference model on top row. Left column: original soft data used as input in logistic regression; middle column: probability of facies 1 (black); right column: e-type map of facies 1 of 50 realizations based on the probability fields. Note the HD are not displayed on the figure, but they are used in all the simulations. Input parameters: weak case: α=0.12, medium case: α=0.31, strong case: α=0.68. Average patch size and overlap width are 15 and 5 respectively. $N_p = 10$. 77
Figure 4.4 Simulation results using the ball TI with different probability fields (colorscale: white-1, black-0). Average patch size and overlap width are 15 and 5 respectively. $\alpha = 0.4$, $N_P = 10$. 78
Figure 4.5 TI and two sample simulations (first row) conditioned to probability fields (second row); e-type maps of 25 realizations (third row) and variograms (bottom row). Average patch size and overlap width of 15 and 5 respectively; $\alpha = 0.45$, $N_p = 50$. 80

Figure 4.6 One conditional realization (right column) using the probability fields in the first two columns for the multifacies TI shown on top, (colorscale: white-1, black-0). The bottom row displays the e-type map per facies for 100 realizations using probability fields shown above in the fourth row. Average patch size and overlap width are 15 and 5 respectively. $\alpha = 0.4$, $N_P = 10$. 81

Figure 4.7 TI (top row), two soft data and probability fields (second row), reference model, one realization and e-type map based on 10 realizations (third row), variograms (fourth row) and L2-functions (fifth row) of the reference and the 10 realizations. Average patch size and overlap width of 35 and 12 respectively, $\alpha = 0.52$, $N_p = 100$. 83

Figure 4.8 3D ball TI and the probability field were used to perform 25 conditional simulations. One sample simulation and the e-type cubes are also displayed. Size of the TI and simulation grid are both 50*50*50. Average patch size and overlap width are 16 and 5 respectively. $\alpha = 0.60$, $N_p = 100$. 84

Figure 4.9 A: 3D channel TI, B: probability volume, C: sample simulation and D: e-type map of 25 realizations. Average patch size and overlap width are 30 and 10 respectively. $\alpha = 0.4$, $N_P = 100$. 85

Figure 4.10 Top row: TI, the probability field and one sample ATI (out of 10) used for the simulation; second to fifth rows: one sample realization (left), e-type map (middle), correlation plots (right) for $\alpha = 0.0$, 0.1, 0.4 and 0.7. Each e-type map is computed from 25 realizations (colorscale: white-1, black-0). ATIs are unconditional patch-based simulations of TI using quilting (El Ouassini et al, 2008; Faucher et al, 2013). Average patch size and overlap width are 20 and 7 respectively. $N_p = 25$. . . . 86

Figure 4.11 Correlation between e-type and probability field as a function of the α parameter. E-type map computed from 25 realizations for the TI and probability map shown in Fig. 4.10. 87

Figure 4.12 Sensitivity of the simulations to the weights given to HD (β) and soft data (α); C represents the % of HD reproduced (colorscale: white-1, black-0). C values are calculated over 10 realizations for a better estimate of HD reproduction. Size of the TI and simulation grid are 200*200 and 250*250 respectively. Average patch size and overlap width are 24 and 8 respectively. $N_p = 25$. 89

Figure 4.13 TI, one realization and e-type maps based on unconditional (middle row) and conditional (bottom row) realizations; HD as red dots; average patch size and overlap width 25 and 9 respectively. $\alpha = 0.4$, $N_p = 25$. 90
Figure 4.14 Mallik area, Mackenzie Delta, Northwest Territories, Canada; boreholes, and area covered by tomography and seismic investigations. Figure borrowed from Dubreuil-Boisclair et al (2012). 92
Figure 4.15 Correlation in 2L and 5L borehole logs of methane hydrate grade and seismic velocity. 93
Figure 4.16 Top row: Original TI obtained by thresholding Vp at 75th and 85th percentiles; bottom row: two large ATIs generated by unconditional simulation using the original small TI. A total number of 25 ATIs were used for the simulations. 94
Figure 4.17 Top left: original soft data (inverted Vp), top right and bottom row: probability field per category (colorscale: white-1, black-0); on each category probability field the points in boreholes belonging to the same category are overlaid, α=pseudo-$R^2 = 0.14$. 95
Figure 4.18 Three conditional simulations randomly selected from 100 realizations. Average patch size and overlap width are 8 and 3 respectively. $\alpha = 0.14$, $N_p = 25$. 96
Figure 4.19 Left: Probability fields for the three categories; Right: e-type maps per category based on 100 realizations. 97
Figure 5.1 Top left: TI generated with an object-based simulation method (Total, 2016); middle left: one realization with 20 ATIs; bottom left: one realization using only the TI, 250 HD indicated. Top right: HD reproduction rate for 50 different realizations with and without ATIs. Bottom right: L_2 function for the 50 realizations obtained with and without ATIs. 104
Figure 5.2 Dunes TI from Allard et al (2011) (top left); lithotype template (bottom left); two MPS unconditional realizations (second column from left) and corresponding Gaussian fields (two rightmost columns) . . . 106
Figure 5.3 GDM applied on the dunes TI. The two input realizations are the ones on second row far left column and lower right sub-figures. These are merged using different weights shown on top of each sub-figure. . . . 108
Figure 5.4 Two realizations (left), original and cleaned merged realizations. The cleaned realization is used in the forward modelling step. 109

Figure 5.5 Proportion map test case. First row: from left to right, two sample MPS simulations, reference map and the final GDM model. Second row: grey facies proportions. Last row: white facies proportions. GDM applied with parameters m=200, n = 2, k=4, g=110, m_k=20, m_b=10. 111

Figure 5.6 Proportion map test case. First row: Reference and target proportion. Second to last rows: best merged calibrated realisation obtained at different generations. GDM applied with parameters m=500, n = 2, k=4, g=50, m_k=20, m_b=10. 113

Figure 5.7 Proportion map test case. First row: Target proportion and e-type over 50 realizations. Second row: four different calibrated GDM realizations. GDM applied with parameters m=500, n = 2, k=4, g=50, m_k=20, m_b=10. 114

Figure 5.8 Travel time test case. P: producer well. Travel times between injector and producers are given for reference field, two sample MPS realizations and GDM output. Misfit shown on the rightmost sub-figure. GDM applied with parameters: m=50, n = 2, k=4, g=50, m_k=20, m_b=10. . 115

Figure 5.9 Seismic section calibration example. Elastic properties and wavelet: bottom left sub-figure, misfit of input MPS and GDM-calibrated: bottom right. GDM applied with parameters: m=500, n = 2, k=3, g=500, m_k=20, m_b=10. 116

Figure 5.10 TI selected from Maules Creek Australia (left) and reference shortest paths between injector-receivers (right). 118

Figure 5.11 Shortest path travel time 3D example. Top: sample initial MPS realization, middle: reference, bottom: one GDM-calibrated realization. The misfit of input realizations are displayed in the bottom figure as compared to the GDM final model misfit. GDM applied with parameters: m=50, n = 3, k=4, g=40, m_k=20, m_b=10. 119

Figure 5.12 Two-phase 2D water cut example. Water saturation (top left), reference (top right), one initial MPS realization (bottom left), GDM calibrated realization (bottom right). GDM applied with parameters: m=50, n = 2, k=4, g=10, m_k=10, m_b=5. 120

Figure 5.13 Water cut curves at wells P1 to P3 for two initial MPS realizations (left) and GDM-calibrated realization (lower right). Misfit values of 50 MPS realizations and GDM-calibrated realization (upper right). . . . 121

Figure 5.14 Two-phase 3D water cut example. Water saturation (top left), reference (top right), one initial MPS realization (bottom left), GDM calibrated realization (bottom right). GDM applied with parameters: m=50, $n = 2$, k=4, g=13, m_k=10, m_b=5. 123
Figure 5.15 Water cut curve at the well P1 for the best GDM model after N_g generations. 124
Figure 6.1 The TI was used to create the reference model from which the hard data on right are extracted. 128
Figure 6.2 Three layers of soft data. The areas highlighted with colored rectangles refer to the correlation between soft data values and facies coding. Red boxes highlight the areas where *F1* and higher values of soft data correlate positively, and the opposite for light blue rectangles. 128
Figure 6.3 Three soft data layers on top are merged in different ways generating probability fields of $F2$. $S1$ to $S3$ refer to soft layers 1 to 3, and $P(S1 + S2)$ means the probability calculated with soft layers 1 and 2. 130
Figure 6.4 The influence of different combination of soft data in classification results. 131
Figure 6.5 Reservoir grid extracted from the reference model used for flow simulations. The variations of TOF values on base 10 logarithmic scale. . 132
Figure 6.6 Water cut curves at production wells. One time unit on the X axis counts for 121 days totalling a 10 years time period of flow simulation. 133
Figure 6.7 The original TI and three randomly selected ATIs. 134
Figure 6.8 The sample realizations conditioned to hard data only. The e-type map for 100 realizations. 135
Figure 6.9 Box-plot of conditioning rates of 100 realizations with and without ATIs. 136
Figure 6.10 Sample simulation conditioned to soft data only. The e-type map for 100 realizations. The Pearson correlation coefficient between e-type map and input proportion map is 0.85. 137
Figure 6.11 The models conditioned to hard and soft data at the same time. The Pearson correlation coefficient between e-type map and input proportion map is 0.72. 138
Figure 6.12 Time Of Flight (TOF) and drainage patterns in reference model (A), unconditional simulation (B), hard conditioned model (C), soft conditioned model (D) and hard and soft conditioned model (E). 140
Figure 6.13 Shown on top are TI and the lithotype template (upper right), with three sample realizations on bottom over the reservoir grid with corresponding Gaussian variables. Realizations are the same as Fig. 6.11. 142

Figure 6.14 The dynamic response of set of realizations conditioned to hard data only (first row), conditioned to soft data only (second row), both and hard and soft data (third row) and GDM output (fourth row). GDM was used with parameter setting of m=400, $n = 1$, k=3, g=100, m_k=20, m_b=10. 144

Figure 6.15 The water rate curves at the producers in three GDM outputs as compared to the water rates reference model. GDM was used with parameter setting of m=400, $n = 1$, k=3, g=100, m_k=20, m_b=10. 145

Figure 6.16 TOF and drainage patterns of the reference model (top row) and three calibrated models (second to last rows). 146

LIST OF INITIALS AND ABBREVIATIONS

MPS	Multiple-Point Statistics
TI	Training Image
ATI	Alternative Training Image
OTI	Original Training Image
HD	Hard Data
T	Template size
OL	Overlap size
GDM	Gradual Deformation Method
EnKF	Ensemble Kalman Filter
τ	Tau factor
$d(P, S)$	Distance between P and S
P	Data event from TI
S	Data event from simulation grid
w	Weighting matrix in distance function
O	Objective function response
r	Deformation factor
α	Soft data weight in distance function
$*$	Convolution function
$\odot$	Hadamard product
E	Cumulative error function
χ^2	Chi-squared test
$P(k\|x)$	Probability of category k in the presence of soft data x
p_{TI}	Proportion in the patch from TI
p_{SI}	Proportion in the patch from probability map
R^2	McFadden's pseudo regression coefficient
L_c	Likelihood of the full model fitted with soft data
L_0	Likelihood for the null model having only the constant term
β	Weight given to hard data
N_p	Number of patterns in the pool of candidates
Z	Latent Gaussian variable
n	Number of latent Gaussian variables from each facies model
m	Number of MPS realizations in a given generation
k	Number of realizations which are combined simultaneously

m_k	Number of merged realizations produced for each generation
m_b	Number of best realizations
g	Number of generations
d_m	Merged model data
d_o	Observed data
mD	Milli Darcy
cP	Centi Poisse
sW	Water saturation

CHAPTER 1

INTRODUCTION

1.1 Facies Modeling

Facies modeling refers to the population of discrete property values on the geocellular grids in hydrocarbon reservoirs, mineral deposits or groundwater aquifers. The primary variables of interest such as permeability, porosity or ore grade often show different distributions in different facies. Given that petrophysical properties highly correlate with facies type, facies data are available on well logs or boreholes, and facies data are spatially correlated, it is recommended to start with a facies modeling step before continuous property modeling such as porosity and permeability (Pyrcz and Deutsch, 2014). Facies modeling techniques can be labelled as either deterministic or stochastic. Deterministic approaches like Indicator Kriging (Journel, 1983) gives one fixed value per pixel in all estimation runs. Such models are preferred when enough input facies data are available such that there is no need for generating multiple realizations of the underlying ground truth geology. On the other hand, stochastic methods like sequential indicator simulation (SISIM, Deutsch and Journel 1998) generate in different simulation runs different realizations of the random function governing reservoir or mineral deposit geology.

Stochastic methods are interesting choices since the set of multiple realizations can be used for uncertainty assessment and they do not suffer from the smoothing effect of the Kriging-based estimation techniques. Examples of stochastic methods include object-based simulations (Damsleth et al, 1992; Shmaryan and Deutsch, 1999; Deutsch and Tran, 2002), sequential indicator simulation (Deutsch and Journel, 1998), multiple-point statistics (MPS) (Guardiano and Srivastava, 1993; Strebelle, 2002), truncated Gaussian simulation (Le Loch and Galli, 1997; Galli et al, 1994) and process-based algorithms (Koltermann and Gorelick, 1992; Pyrcz et al, 2009). The spatial correlations are quantified within object distribution parameters, variograms and training images (TI) in object-based, truncated Gaussian and MPS methods respectively. The set of multiple realizations should give an *idea* of what the spatial facies distribution looks like. For example such realizations of the subsurface can be used in flow modeling in reservoir or hydrogeology to determine the range of expected variations of fluid flow behaviour of realizations (Koltermann and Gorelick, 1996).

1.2 Why Using MPS ?

The central idea in MPS is to infer the multiple point cumulative distribution functions (CDFs) from a TI rather than from a variogram.The TI can be seen as a realization of an undescribed random function in the head of the geologist. In the classic Kriging-based geostatistics, the estimation is based on a variogram that measures the spatial correlation between data samples. Such variogram is empirically obtained from the observed data. However, variogram inference, particularly along the horizontal direction, most of the time is not possible due to the wide horizontal spacing between wells or boreholes. In such cases it is inferred from other sources such as seismic data inverted for acoustic impedance elastic property (Chambers and Yarus, 2002; Francis, 2005; Deutsch and Journel, 1998). Variograms can also be borrowed from TIs depicting the expected geological structures from analogues, direct geological maps, outcrops, satellite imagery data, etc. Even if variogram is available, the output realizations often lack geological realism (see Fig. 1.1). As stated in Mariethoz and Caers (2014) "*We now need to recognize that in practice, what is often ultimately desired is not a multivariate distribution and its parameters estimates, but the realizations generated.*" referring to the fact that the realism of the output models is more important than the beauty of the mathematical model used. The limitations of variogram in capturing curvilinear continuities as in meandering channels, and conditioning problems of object-based algorithms led to the advent of MPS method with Guardiano and Srivastava (1993) and later on with a more practical version of it with Strebelle (2002).

As mentioned above, at the core of MPS is a TI deemed as an example or a realization of geology ones expect to see in the subsurface and is used to convey conceptual or observed geological heterogeneities from field to facies simulation. In this regard, a TI can come from geological sketches, satellite imagery data, extracted mine levels, or object-based simulations. Using TI rather than a variogram results in considerable improvement of geological realism of facies simulators outputs. An example is provided in Fig. 1.1 depicting meandering channels host to hydrocarbon fluids. The reference channel model is displayed on top left of the figure. The reservoir is hit with three producers ($P1$ to $P3$) and one injector well ($I1$). One conditional realization was produced using an MPS algorithm shown in the middle row, and one with a variogram-based simulation technique namely SISIM.

The channel was considered as permeable and more porous than the background shale (permeability values shown in Fig. 1.1). As can be seen in the reference model the channel between $I1$ and $P1$ is the shortest path of fluid flow as depicted with the time of travel on the right figure. The model produced with MPS connects very well $I1$ and $P1$ in that the shortest path between $I1$ and $P1$ is through the connecting channel in between. However, the SISIM flow

response is significantly different than the reference as in this model there is no preferential path between $I1$ and $P1$ and fluid has been dispersed to $P2$ and $P3$ producers as well.

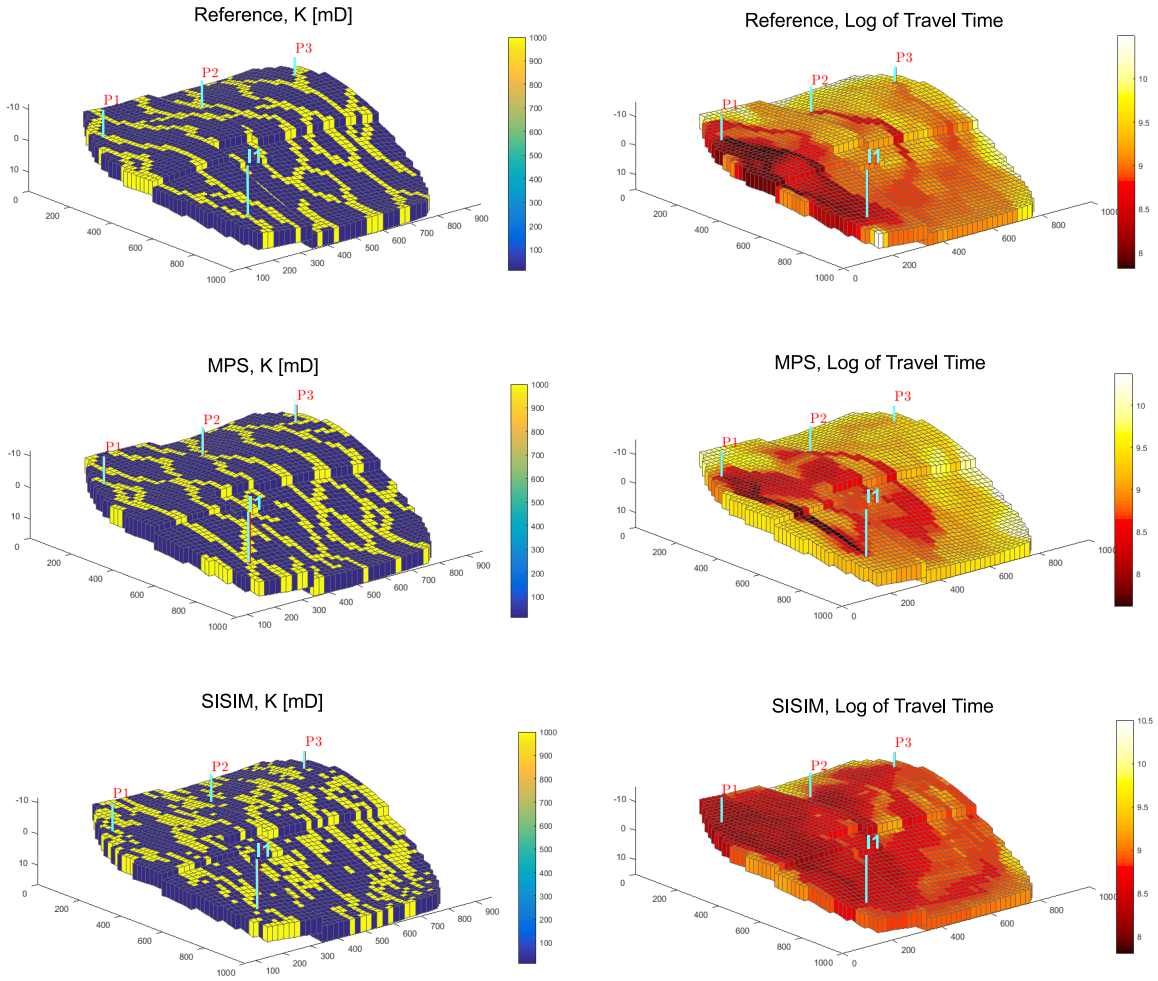

Figure 1.1 The significant difference between the flow response of channels simulated with SISIM and MPS. The facies models on left column are colored with permeability values. The right column shows the travel time (in logarithmic scale) between source and sink.

The idea of using a TI rather than a variogram is elegant and in most cases, MPS outperforms Kriging-based algorithms, however its application is still limited due to some main problems. First is the availability of a TI. TIs can come from variety of sources however one that is representative for the sub-surface heterogeneity can be cumbersome to acquire. Second is the compatibility of conditioning data with the TI. If the hard data observed on the well logs

do not match with the patterns and structures of TI, conditional facies modeling can be an extremely tedious task. In many cases an object-based simulation (Damsleth et al, 1992; Jones and Larue, 1997; Deutsch and Tran, 2002) can be an excellent choice to produce a TI. The application of object-based simulation directly for facies modeling can be limited due to the conditioning problems to dense hard data, or even soft data such as proportion or orientation maps. Facies modeling can be performed using the process models (Xie et al, 2001; Pyrcz and Deutsch, 2005; Pyrcz and Strebelle, 2006; Reza et al, 2006). Such methods are based on the physical and chemical processes that govern the geological settings of the phenomena under study. Process-based algorithms can generate facies models that are very realistic in terms of their structural contents but the computational efficiency and conditioning can be problematic (Michael et al, 2010). However, process-based models can perfectly serve as TI in MPS given that such models are stationary, are not repetitive, and structural complexity of process-based models are not challenges for this use.

1.3 MPS Workflow

Having provided a representative TI, MPS follows a sequential simulation process in which data events are extracted from the simulation grid from within the neighbourhood of the simulation point. Data events can contain hard conditioning data, soft conditioning data and/or previously simulated cells. In the next step TI or its corresponding pattern database (namely search tree) is searched using the extracted data event for the matching facies coding. Consider the TI on Fig. 1.2 left with 10×10 pixels of sand channel (black) and background shale (orange). Also consider the 2D simulation grid on right here with same size as TI. There are few conditioning data assigned on the simulation grid in advance. A search window of a specific size is defined ; here it is a circle of radius two pixels. The path through which nodes are visited for simulation can be random or unilateral (here random, for unilateral see Fig. 1.5). At each node under simulation, informed nodes are extracted from search neighbourhood of simulation point. This data event is used to search the TI for matching patterns. In some MPS algorithms such as SNESIM (Strebelle, 2002), IMPALA (Straubhaar et al, 2011) and SIMPAT (Arpat and Caers, 2007), a pattern database of all patterns present in the TI is constructed in advance so that the TI does not have to be scanned anew for each node. Or the TI can be scanned all at once using distance functions calculated with cross correlation functions as in CCSIM algorithm (Tahmasebi et al, 2012) or convolutions as in Rezaee et al (2015). The other idea is to search in the TI on random locations and match the data event from simulation with the local patterns in TI, and take the first matching pattern as in Direct Sampling method (Mariethoz et al, 2010). In either case, the simulated facies the

simulated facies cpdf (conditional probability distribution function) is read from the TI and a simulated value is drawn and pasted to the simulation point. Simulation is moved on to the next uninformed node until all nodes are visited. In some algorithms an iterative process is proposed so that the simulation points that are simulated with smaller than a threshold number of informed nodes in their neighbourhood are re-simulated (SNESIM). In patch-based algorithms the whole field is re-simulated using smaller and smaller patches (Efros and Freeman, 2001).

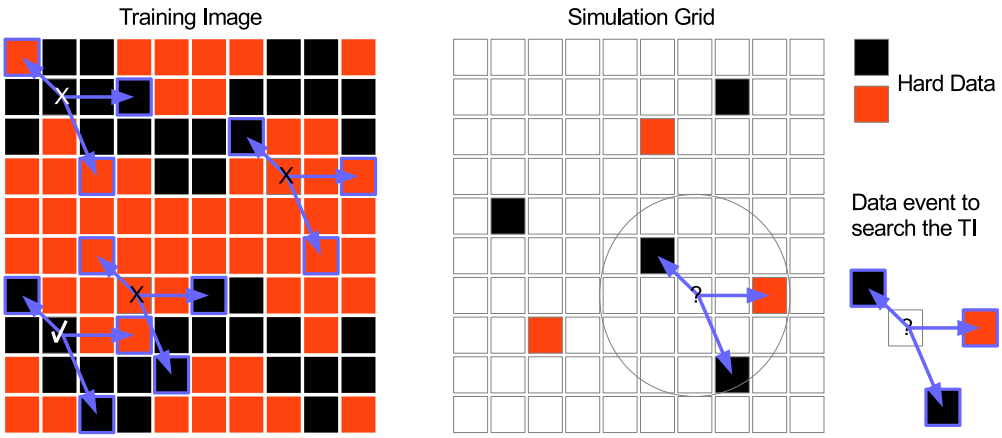

Figure 1.2 The basic idea behind MPS simulation.

Patch-based algorithms simulate better the texture of facies as observed in the TI because of simulating patches of facies values taken from TI and transferred to the simulation window. It also preserves the short-range variations of the variable in TI since they are exactly copy-pasted from the TI to the simulation field. On the other hand, in pixel-based algorithms, short-range fluctuations can be observed in the simulated field which are different from those present in the TI and are due to simulating one point at a time.

1.4 Patch-based MPS

As mentioned above MPS algorithms can be classified into pixel-based and patch-based simulations (see Fig. 1.3). The pixel-based approach simulates one node at a time while patch-based simulates a bunch of nodes similar to object-based algorithms. Patch-based algorithms follow generally a unilateral simulation path, while pixel-based can be done either with a unilateral or random path. Patch-based simulations with random path often present

artefacts and discontinuities. The patch-based unilateral algorithms bear a greater potential at reproducing better the texture of TI. Figure 1.4 shows an example where the texture of patch-based algorithm resembles more the texture of TI. With a fixed template size (T), the overlap size OL is continuously increased, i.e., smaller number of pixels simulated at once, i.e., $(T - OL)^2$. The quality of simulation decreases as the the number of points simulated simultaneously decreases. Note that $T = 5$ and $OL = 2$ in Fig. 1.3-right.

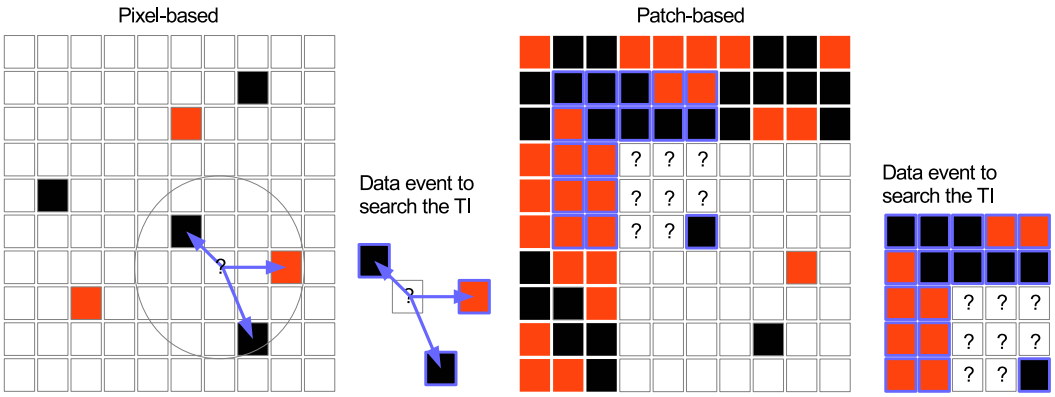

Figure 1.3 Patch-based vs. pixel-based MPS simulation.

Figure 1.5 displays few iterations of a unilateral patch-based MPS simulation based on distance functions as in Rezaee et al (2015). At the top a TI of channels and an empty simulation grid (unconditional case) are displayed. In step (1) since there are no informed nodes in the simulation grid, distance function gives the same chance for all patterns in TI to be picked, therefore one random pattern from TI is selected and pasted on the top-left corner of the simulation grid. In step (2) however, parts of the simulated patch in step (1) are used as overlap to calculate its distance with the TI. The overlap region is highlighted with red rectangles in iteration (2) and (3) as well. The most similar or one pattern in the pool of candidate patterns in the TI is selected based on the distance map (highlighted with red plus sign) and is pasted to the simulation grid. This process continues until all nodes of simulation grid are simulated.

1.5 Potential problems with patch-based MPS

One potential pitfall of patch-based MPS simulations is the verbatim copying effect observed in set of all similar simulations that lack between-realization variability. This effect can be observed particularly with small TIs. One possible solution lies in using larger multiple set of

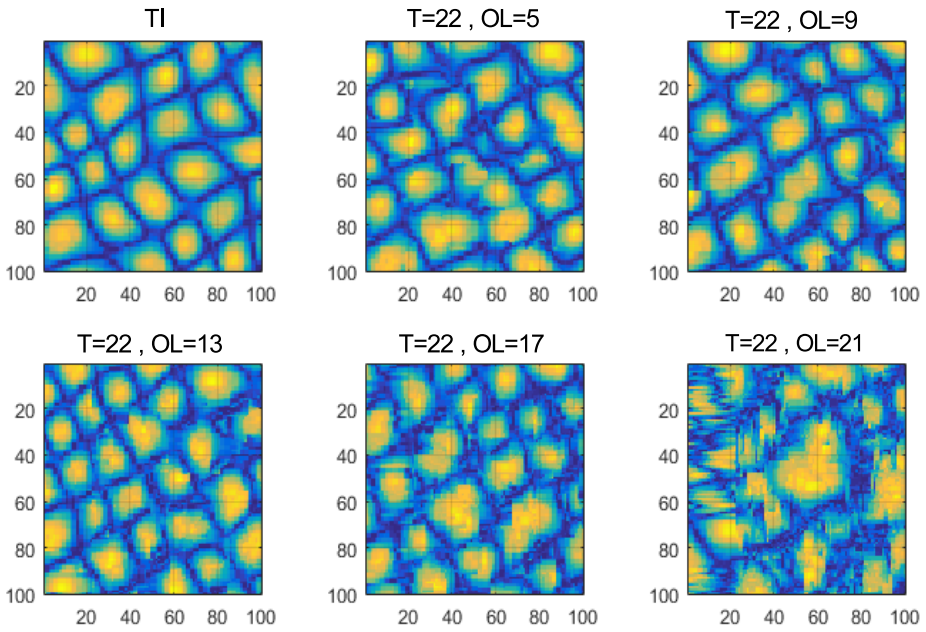

Figure 1.4 Pixel-based vs. patch-based approaches in generating texture. Simulation using T=22 and OL=21 is a pixel-based simulation since the size of patch is reduced to only one pixel. Simulations are performed using distance-based approach based on quilting and a unilateral simulation path.

TIs. The approach presented in Chapter 3 on using multiple TIs is a step forward obviating this problem of patch-based MPS.

Better reproduction of texture in patch-based MPS algorithm is associated with inherent conditioning problems. Especially in presence of dense hard data. As it will be demonstrated in the next chapter, the probability of finding matching pattern in a given TI for a data event from simulation grid drops rapidly to zero as the number of conditioning data within the patch increases. This is similar to object-based simulation where in the conditioning process to dense hard data (particularly along vertical direction) inconsistencies occur between previously simulated objects and new ones. One solution lies in enriching the TI and simply generating more patterns such that one would match the data event from simulation grid. This problem is addressed in more details with a review of the literature in Chapter 3.

Soft data conditioning is not specific to patch-based simulation but to all MPS methods and other facies modeling tools as well. The main issue here is that the physical relationship between soft data and facies types is often unknown, yet during the simulation using a MPS technique, they are taken as direct proportion maps in most cases. One has to get the

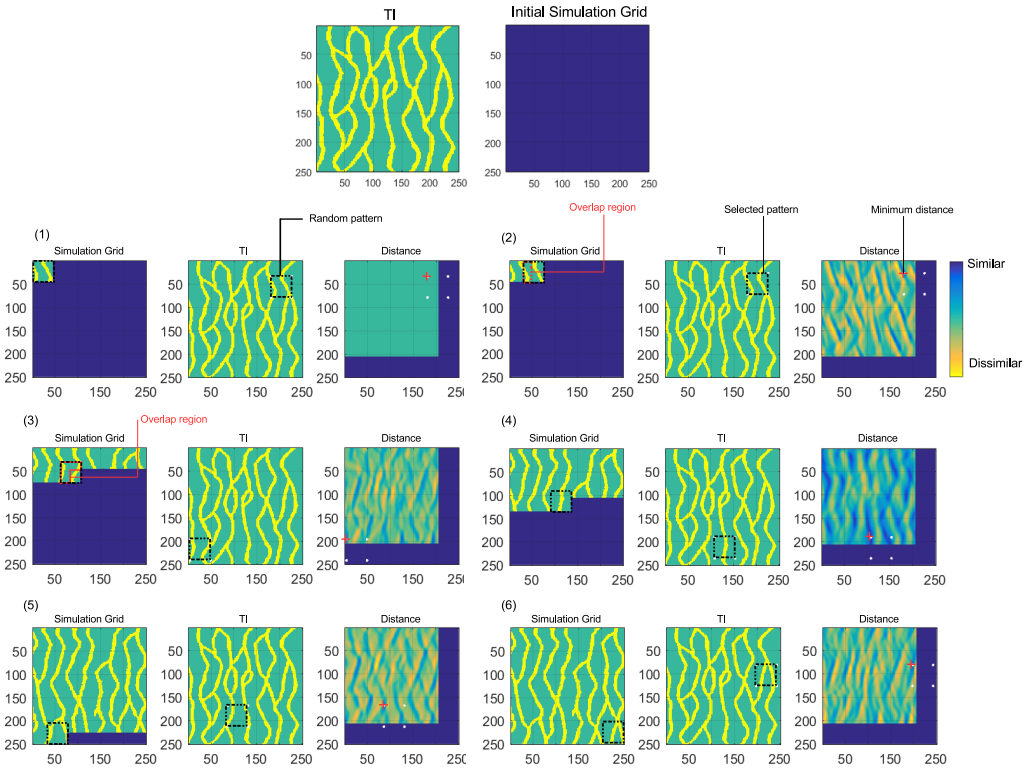

Figure 1.5 Patch-based MPS simulation using distance functions. It is not necessarily the pattern in TI corresponding to *minimum* distance that is selected, but instead a pool of pattern is first formed from the lowest distance values, and one pattern is picked at random and pasted to the simulation grid. The red plus sign shows the upper left corner location of the selected pattern and three white dots on the distance map indicate other three corners.

proportion maps from soft data sets in the first place. Soft data are often given in the form of multiple geophysical maps/cubes. With hard data labelled with facies types from well logs for example, one can perform a supervised classification between hard data and their overlaying soft data, and extend the regressed model to the rest of the simulation grid where only soft data are present. Among the techniques for supervised classification we propose using Logistic Regression model. The reason lies in the pseudo-R^2 of McFadden (McFadden, 1973) that can be used as a weighting factor given to soft data component of the similarity measure in MPS simulation, and also the simple implementation of logistic regression classification. Also, when applying logistic regression, there is fewer number of parameters that requires tuning. Chapter 4 addresses this problem with first a literature review of the available methods in this regard.

The third problem is the conditioning of MPS (or other facies simulators) facies models to dynamic data. Dynamic data are global and depend on larger areas than soft data around the conditioning data, namely wells. The direct history matching of facies is an arduous task in that the facies are defined with categorical type variables, their perturbations can deform severely the covariance model of the field. The technique we used is based on the Gradual Deformation Method, modified into an evolutionary algorithm. We propose deforming the latent Gaussian variables of the facies realizations using a Gibbs Sampling (Geman and Geman, 1984) technique as in PluriGaussian simulation (Le Loch and Galli, 1997). The perturbations are instead performed on the Gaussian fields, and their outcome is truncated using a lithotype flag defined from the TI. The new perturbed model is forward modelled whose fitness is checked with target variable. The best fitted realizations survive to the next generation of realizations. Next chapter provides more details on GDM technique and other related approaches on this problem.

CHAPTER 2

PROBLEM STATEMENT AND LITERATURE REVIEW

2.1 Elements of the Problem

Facies simulation is an important step in reservoir, mineral deposit or groundwater aquifer modeling in that further simulation of continuous properties can be improved considerably knowing what facies we are in. Among the facies modeling tools, MPS has become a popular choice since it conveys the geological information from geologist directly to the simulation grid; however as indicated in the previous chapter, it faces conditioning problems when it comes to dense hard conditioning data, multiple soft data layers, or global dynamic data. In this chapter these problems are extended to more details.

2.1.1 Hard Data Conditioning

Hard data refer to the direct observation on the wells or drill holes of facies or measurements of continuous properties such as resistivity, density, ore grade, etc. Their resolution on the vertical direction can be as fine as few centimetres in reservoir, and fractions of a meter in mining; and on the horizontal direction up to hundreds of meters to few kilometres in reservoir or tens of meters in mining. The facies model must be conditioned to the hard data. After the simulation grid is defined, before the simulation starts, hard data are relocated on the regular simulation grid. During the simulation, data events are extracted from the simulation grid and their similarity is measured with the TI. Data events from simulation grid come with previously simulated data and/or hard data. The values from the TI often do not match the entire set of existing cells in the simulation grid. Pixel-based and patch-based approaches handle the problem differently. In the former, both hard data and the overlap nodes are fixed during the simulation, i.e., one simulated value will not be overwritten with any new value until the end of simulation. Previously simulated parts are taken exactly the same as conditioning data. In patch-based simulations however, the data on overlap region can be changed during the simulation, but the hard conditioning data are fixed during the simulation. It is highly possible that the simulated value over the hard data or overlap does not perfectly match the pre-existing values. The problem is more severe for patch-based MPS similar to object simulations. The problem occurs when TI does not have enough repetitions of patterns in enough varying configurations, or when the data event is too large for the TI. A number of techniques have been proposed to the problem of hard data conditioning in

MPS. In most MPS algorithms, hard data are fixed on simulation grid before simulation starts and not changed thereafter. During the course of simulation if TI does not have any matching pattern for data event, the farthest nodes are dropped one at a time and the distance/conditional probabilities are re-calculated (Strebelle, 2002). If the reduced data event still does not have any matching pattern in TI, another node is dropped. This process continues until at least one matching pattern is found. In methods like DS (Mariethoz et al, 2010) which is based on distances rather than probabilities, output distance value is normalized between a minimum and maximum value [0-1], a threshold (e.g., 0.05) on the distance function then determines if the pattern in TI will be pasted to simulation grid or not. In case such matching pattern is not found, the best matching pattern so far stored in the pattern database is selected and pasted to the simulation grid even if the distance is well above the threshold.

In patch-based algorithms, the problem becomes harder as it is now to condition a patch of nodes simultaneously to conditioning data. In the method CCSIM (Tahmasebi et al, 2012) for example, when the matching pattern is not found, the square-shaped patch is divided into four small complementary patches, each are tested against TI for matching patterns using cross correlation functions. If for any of the smaller parts the match is not yet found, it is divided into another four smaller pieces again and this continues until the matching pattern is found in the TI which is guaranteed to find for only one pixel remained in the patch in the end of the process (see Fig. 2.2).

Window enlargement technique was proposed with Parra and Ortiz (2011) in pixel-based MPS based on a texture synthesis method borrowed from the computer graphics (Wei, 2002). During the simulation, a larger area than the usual search neighbourhood is scanned to find the nearby (but not in the simulation window) hard data, such that the algorithm foresees the forthcoming hard data, and pastes beforehand the patterns from TI that are readily compatible with the nearby hard data. The idea was adopted with Faucher et al (2013) and Rezaee et al (2015) to enhance the conditioning capabilities of patch-based simulations. However, if the TI is not rich, the chance of finding a matching pattern for an enlarged window is even slimmer.

As mentioned above, in case of non-matching data events from simulation grid and simulated values from TI, the most frequent idea is to reduce the size by dropping the farthest nodes iteratively until matches are found. The plot on Fig. 2.2, shows for three different TIs the portion of the original data event that has to be discarded until a matching pattern is found in the TI. More than 50% of the data event are discarded when the data event has only 50 pixels; more than 80% are discarded of the data when the size is 100 pixels or more. In other words 80% of the data from simulation grid are not used in the pattern matching step. One

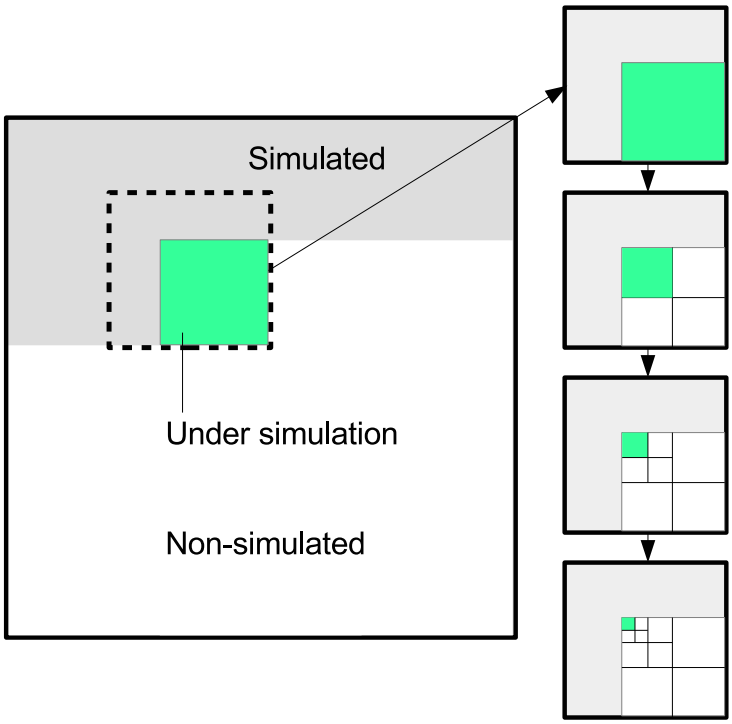

Figure 2.1 The recursive template splitting idea as used in CCSIM (Tahmasebi et al, 2012). The original template with overlap regions in gray and the parts to be simulated in green are highlighted in the simulation grid on left. Right column shows the process through which the original template is split recursively until the matching pattern is found in TI.

hundred pixels counts for a square search window of 10×10 while in practice much larger templates are required for most of the simulations. DS method scans only a portion of TI for faster computations, e.g., 50 % of the TI. The chance of finding a match within the portion of TI gets smaller than the case when the whole TI is scanned.

In all solutions presented, there is a *data reduction* mechanism, either in the form of template splitting, of farthest node drop out or in the form of similarity measure compromise as in the DS method. However, the degree of severity of the problem is high as shown in Fig. 2.2 where in the most optimistic case, only 50 % of the original data event's pixels are used to calculate the conditional probability from TI using distances or counting the number of replicates. To this problem we rather propose to enrich the TI and keep data event untouched. One solution is to take as input not only one TI but a series of TIs. Such Alternative TIs (ATIs) can be unconditional simulations using the original TI (OTI) of any size and number as long as CPU time allows. To this end the test in Fig. 2.2 was repeated once only with OTI and next with OTI+10ATIs. ATIs were unconditional simulations over the same grid size as OTI using a patch-based algorithm based on quilting (Efros and Freeman, 2001). The results are displayed in Fig. 2.3 where using 10 ATIs increases the chance of finding a matching pattern and reduces the portion of data that has to be dropped out to find a matching pattern. ATIs are more influential for the multi-facies channel TI shown in Fig. 2.3-C directly due to the increased number of facies.

In this test (Fig. 2.3) there was no control over the ATIs in terms of their pattern content and diversity, compatibility with hard data, and similarity to OTI. Such ATIs come with little effort in terms of CPU time or input parameters tuning since they are unconditional simulations using patch-based MPS where the most important parameter is to select the proper patch size. We propose to generate ATIs in large numbers but to retain only the fittest ones for the main conditional simulation.

Conditioning of patch-based MPS algorithms to dense hard data is a problem, as the TI in most of the cases is not responsive to all data events coming from simulation grid. The first objective is this dissertation seeks the solution in enriching the TI's pattern database with ATIs. The efficient way of generating and using ATIs and sample results is studied and presented in more details in Chapter 3.

2.1.2 Soft Data Conditioning

Soft data are linked in often an indirect way to the facies distribution. They are mainly obtained by geophysical prospecting and further data processing and modeling (e.g. seismic inversion). Soft data can sample different areas from the hard data, or reflect different features of the subsurface geology. They inform about the local abundance of the different

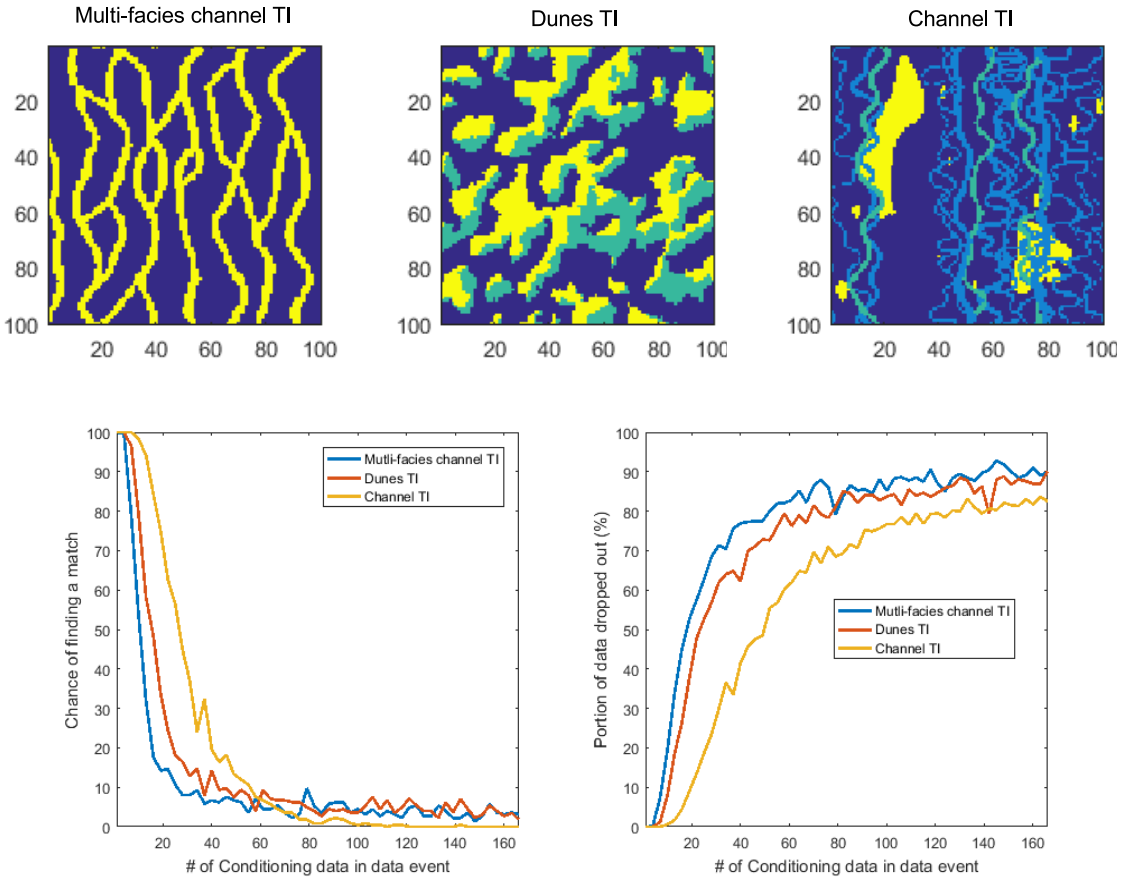

Figure 2.2 Top: three selected TIs, bottom-left: probability of finding a perfect matching pattern from the TI vs. data event size, bottom-right: portion of the original data event that has to be droped out until we find a matching pattern in the TI.

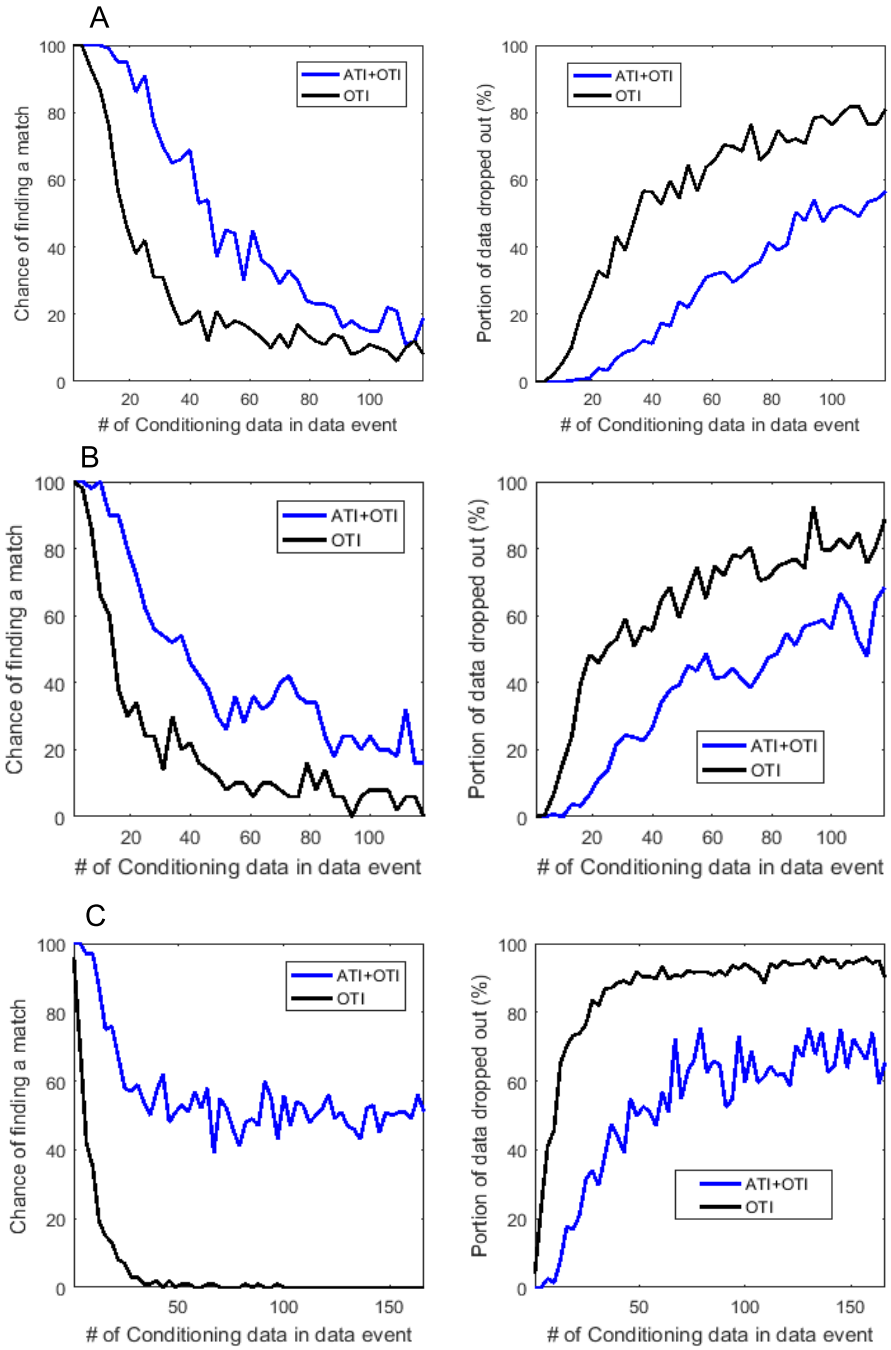

Figure 2.3 Same test as in Fig. 2.2 repeated with and without ATIs. The probability of finding a matching pattern on left columns and the portion of original data event dropped out to find a matching pattern as a function of data event size for channel TI (A), dunes TI (B) and multi-facies channel TI (C), see Fig. 2.2.

facies (at the scale of resolution of the geophysical data). Hence, they can be used to allow proportion of facies to vary in space. One method to link facies probabilities obtained from TI and MPS to facies probabilities obtained from soft data is thru the method of aggregation of probabilities. Allard et al (2012) give an excellent review of available methods. All these methods seek to simplify the computation of conditional probabilities.

Consider A as facies observation at node u under simulation, B data event around u, and C soft data within the search window. In a case of conditioning to hard data only, one needs to calculate the conditional probability of A which is solved in the form of Bayesian inference problem with $P(A|B) = \dfrac{P(A,B)}{P(A)}$ as described in Strebelle (2002). With soft data however, we have $P(A|B,C) = \dfrac{P(A,B,C)}{P(B,C)}$ that becomes more complicated to calculate the joint probability between B and C. One way to account for soft data in MPS simulation has been the use of Tau model (Journel, 2002) in a probability aggregation method (Allard et al, 2012). In the Tau model (Eq. 3.1):

$$\frac{x}{b} = \left(\frac{c}{a}\right)^{\tau} \tag{2.1}$$

with

$$a = \frac{1 - P(A)}{P(A)}, \quad b = \frac{1 - P(A|B)}{P(A|B)} \tag{2.2}$$

$$c = \frac{1 - P(A|C)}{P(A|C)}, \quad x = \frac{1 - P(A|B,C)}{P(A|B,C)} \tag{2.3}$$

where $P(A)$ would be the marginal probability of facies indicator in TI. The conditional probability $P(A|B,C)$ has become a function of $P(A)$ and two probabilities of A separately conditioned to B and C. $P(A|B)$ is the conditional probability of data event in search neighbourhood in simulation grid, and $P(A|C)$ is the soft data conditional probability. The factor Tau (τ) is an indicator of the redundancy between B and C (Krishnan et al, 2005). In practice defining the degree of redundancy between B and C is very difficult and moreover it has to be done on every single simulation node. For these reasons $\tau = 1$ is used in most practices. Figure 2.4 shows an example of the conditional simulation using the Tau model. In this figure we have as inputs a channel TI, one rotation map and the proportion map of channel facies as soft data. The simulations are repeated with $\tau = 1$, $\tau = 50$ and $\tau = -5$. As can be seen higher τ values forces more the soft proportion condition as in the case of $\tau = 50$ the e-type map does not show much uncertainty. Negative τ values reverses the effect of soft data in that the e-type map shows inverse relationship to the soft proportion map.

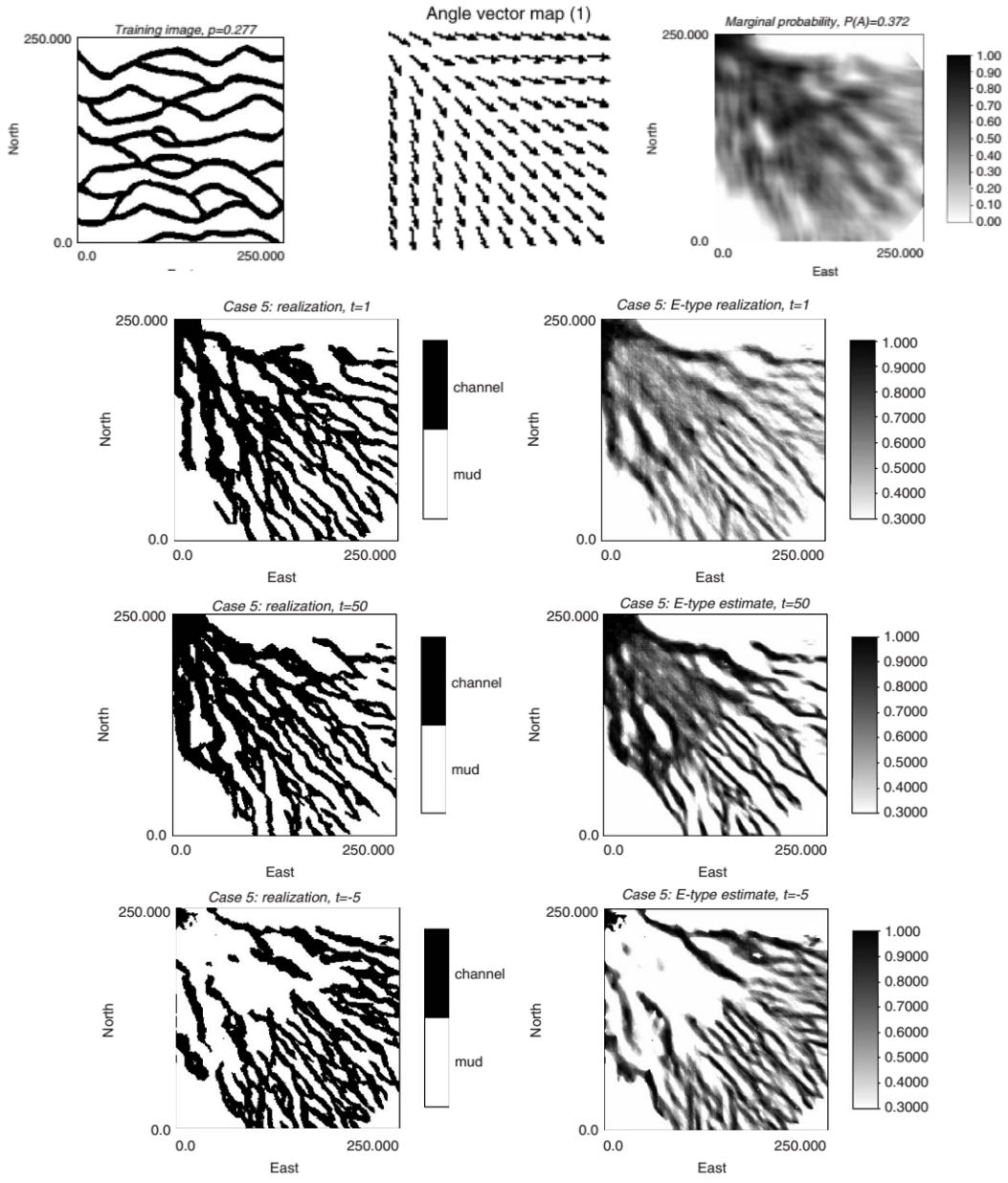

Figure 2.4 The TI, rotation map and the proportion maps were used to perform conditional simulations. Sample simulations are presented with different Tau values. With permission from Liu (2006).

Non-stationarity has been handled in the form of auxiliary variables as in Chugunova and Hu (2008) and Mariethoz et al (2010). Chugunova and Hu (2008) implement conditioning to auxiliary data in SNESIM algorithm (Strebelle, 2002) by constructing a search tree of

patterns not only of primary TI but also auxiliary variable TI. The pattern configurations to build the database or search tree for soft data are the same as for the primary TI (facies TI) search tree. In a sequential simulation, at each node data events are extracted from the neighbourhood of the simulation point; candidate patterns are identified from the principal variable TI's search tree, and among the set of candidates are selected only those that satisfy the auxiliary data condition too that comes from the auxiliary data TI on the simulation point. In this context auxiliary data could be proportion of facies within the search window, orientation of the objects, other geometrical features of facies. Figure 2.5 shows an example of the simulation conditioned to the proportion maps as auxiliary data. The reproduction of soft proportion data in the e-type map is fairly good. The patterns in the simulation (Fig. 2.5-C) is also similar to TI. Figure 2.6 shows an example of a TI of fracture network, the orientation map showing azimuths of 0 to 90 degree and the sample simulation.

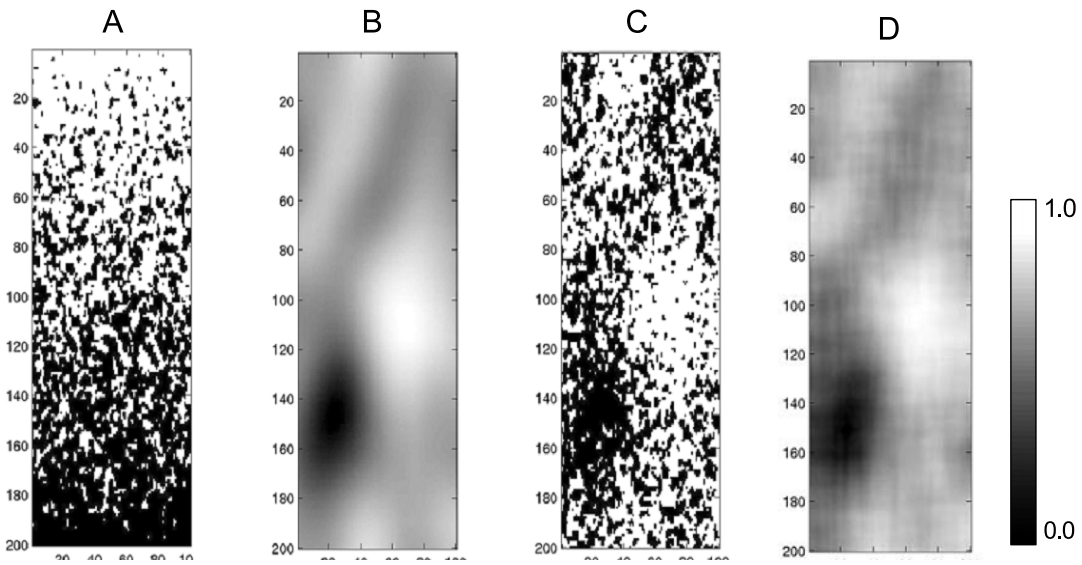

Figure 2.5 A: TI, B: auxiliary variable, C: sample simulation and D: e-type map of 50 realizations. With permission from Chugunova and Hu (2008).

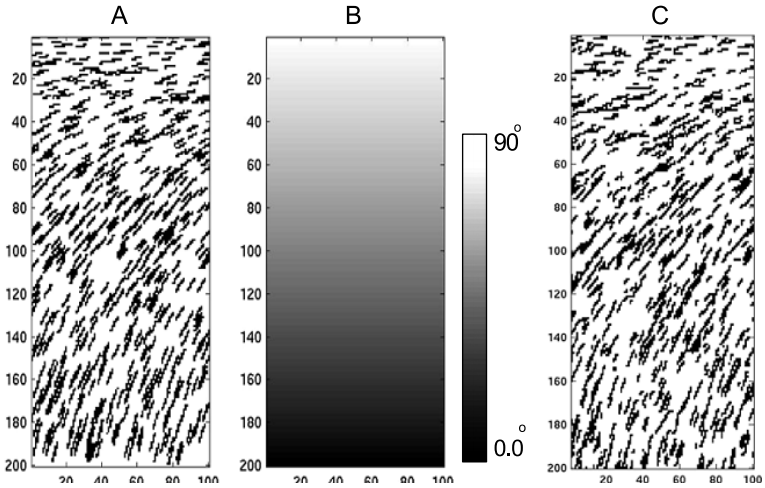

Figure 2.6 A: TI, B: auxiliary variable, C: sample simulation. With permission from Chugunova and Hu (2008).

Mariethoz et al (2010) used a two-term distance function that computes the similarity between joint data event from simulation grid and primary facies TI and soft data map. Equation 2.4 shows the distance function of DS method in the presence of m variables which is expressed as the weighted average of all distances between m variables:

$$d(P,S) = \sum_{k=1}^{m} w_k d(P_k, S_k) \quad in \quad [0,1] \tag{2.4}$$

$$\sum_{k=1}^{m} w_k = 1, \quad and \quad w_k >= 0. \tag{2.5}$$

where $d(P,S)$ is the distance operator (see Eq. 2.6), P_k and S_k are the data events of k_{th} variable in TI and simulation grid respectively. It should be mentioned that this approach simulates all m variables of m TIs simultaneously. The individual distances in Eq. 2.4 are computed using Eq. 2.6.

$$d(P,S) = \frac{\sum_{i=1}^{n} a_i \left|\left|h_i\right|\right|^{-\delta}}{\sum_{i=1}^{n} \left|\left|h_i\right|\right|^{-\delta}} \tag{2.6}$$

where $a_i = 0$ if $Z(x_i) = Z(y_i)$ and 1 otherwise, $\left|\left|h_i\right|\right|$ is the norm of the lag vector i^{th} of data event. Parameter $\delta \geq 0$ distributes weights to the pixels in the data event, where $\delta = 0$

means all pixels have the same weight. Figure 2.7 shows one sample simulation where the soft data are considered in a multi-variate context.

Mariethoz et al (2015) proposed in the frame of DS a model conditioned to the proportion data. The idea is similar to the servosystem correction process in the SNESIM algorithm (Strebelle, 2002). In this approach on-the-fly proportions are calculated within the search neighbourhood of the simulation point. The objective is to penalize the candidate patterns from TI that do not make the current proportions any closer to target proportion on the simulation node. The penalty is defined in the form of an error function (Eq. 2.7) as the root mean square different between current and target proportion.

$$E_p = \sqrt{\frac{1}{K}\sum_{k=1}^{K}\left\{(P_c^*(x,k) - P_t(x,k))^2\right\}} \tag{2.7}$$

where $P_c^*(x,k)$ is defined as the current proportion of facies k in the search neighbourhood of the simulation point. The error value is used in the DS distance function (Eq. 2.6):

$$d^* = d(P,S) + wE_p \tag{2.8}$$

where similar to Eq. 2.4 P and S are data events from TI and simulation grid whose distance is now updated with the error associated with the local proportions. In this equation w is a user-defined weight given to the local proportion condition.

Such proportion constraints can either be local or global and the search window to calculate the local proportion can be different than the one in simulation grid from which data event is extracted. The distance term on proportions however is used only in the beginning of the simulation to avoid introducing at later steps discontinuities in facies arrangements. These discontinuities introduced at later steps are, at least in part, due to the pixel-based nature of DS and cannot be avoided completely. The simulation shown in Fig. 2.8 is one sample simulation taken from (Mariethoz et al, 2015).

The methodologies available in MPS are not limited to the mentioned algorithms, more can be found in Honarkhah and Caers (2012), Faucher et al (2014) to control the global proportion of facies in the simulated field. In the more general geostatistical perspective other methods are available to condition the model to soft data including the work with Koch et al (2014), Tang et al (2013) and Caers and Hoffman (2006) in the form of an inverse problem. All the methods mentioned above including Strebelle (2002), Chugunova and Hu (2008), Mariethoz et al (2010) and Mariethoz et al (2015) allow some form of conditioning to soft data.

All the examples shown allow spatial variation of facies proportions. The main limitation for the existing methods is the requirement to have a forward model since they compare

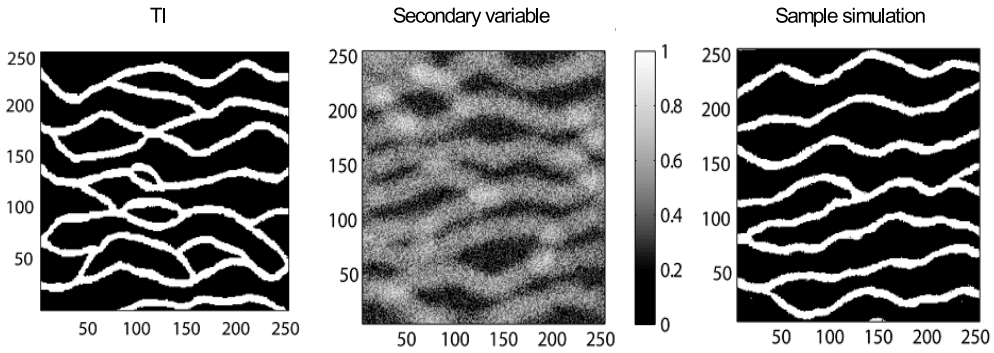

Figure 2.7 Sample conditional simulation of the method proposed with Mariethoz et al (2010). The TI (left) has been used to perform the conditional simulation (right) using the soft data on middle. With permission from Mariethoz et al (2010).

directly the soft data corresponding to the simulation (e.g., proportion) with the soft data observed (e.g., impedance volumes from seismic inversion). The second problem is that they assume soft data is perfectly known, therefore the weighting of soft data is done by trial and error, yet the correlation between facies data from wells and soft data should be quantified and be accounted for in the main conditional MPS simulation. The last problem is that with multiple soft data sets, these algorithms need as many forward models (which are probably not existent) and each forward model is typically computed from the simulation state independently of the others. We propose to use the multinomial logistic regression to merge multiple soft data layers to calculate facies probability fields. Multinomial logistic regression can also be used where one soft data layer is available and one aims at producing probability maps for multiple facies.

The probability fields calculation from a set of soft data layers and hard data with facies types is a supervised classification problem for which a variety of methods can be used. That includes the discriminant analysis (Wong et al, 1995), multinomial logistic regression (Al-Mudhafer, 2014; Dobson and Barnett, 2008; Hosmer Jr et al, 2013), neural networks (Caers and Ma, 2002; Wong et al, 1995), naive Bayes classifier (Caté et al, 2017; Porwal et al, 2006), random forests (Harris and Grunsky, 2015; Carranza and Laborte, 2015) and support vector machines (Smirnoff et al, 2008; Al-Anazi and Gates, 2012). In this dissertation the probabilities are acquired from the soft data by multinomial logistic regression, in it we attempt to come with novel solutions for the determination of the contribution of soft data in the distance computation step of MPS simulation. During the course of simulation we calculate the facies proportion within the patch, and compare that to the proportion

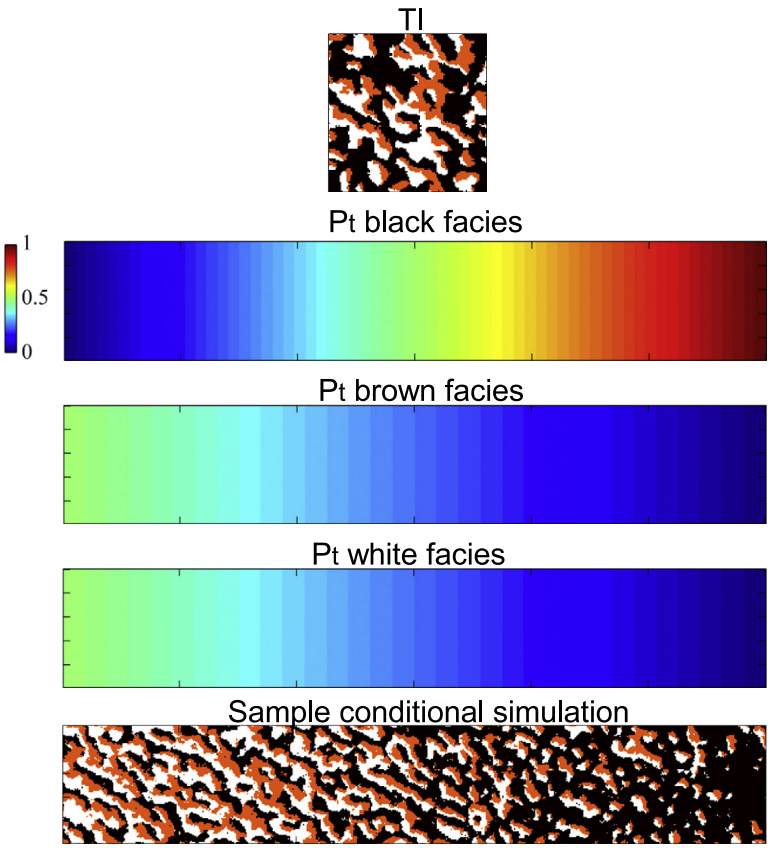

Figure 2.8 Sample conditional simulation of the method proposed with Mariethoz et al (2015). The TI on top has been used to perform the conditional simulation shown on bottom using the proportion maps of different facies in the middle rows. With permission from Mariethoz et al (2015).

maps. The weight given to soft data is from the regression coefficients of determination from multinomial logistic regression.

2.1.3 Dynamic Data Conditioning

Conditioning reservoir models to dynamic data also known as history matching is a difficult and tedious step in reservoir modeling due to the non-linear relationship between dynamic data and petrophysical properties or facies types. The output of history matching is non-unique and the uncertainty is huge in terms of different geological interpretations and petrophysical models with same dynamic output. The flow can be vastly different, it is only the output at a few points that we measure. A good review of history matching techniques can be found in Oliver and Chen (2011). History matching can be done either manually or automatically. Manual history matching is done by performing iteratively reservoir simulation for historic period and comparing results with observations and tuning the input parameters until the match is acquired (an example of such includes the work with Agarwal et al 2000). In this category of techniques the main parameters often taken into account are aquifer size, vertical permeability barriers, flow capacity, pore volume, relative permeability, and horizontal to vertical permeability anisotropy ratio.
In the otherwise automatic or evolutionary perspective, history matching has been put forward as an optimization problem (Tarantola, 2005). In such optimization problem, an objective function (Eq. 2.9) is defined as misfit between observed data and forward model of properties being perturbed. The problem is then to minimize an objective function like:

$$O = \sum_{i=1}^{P} w_i \left| d_m^i - d_o^i \right| \tag{2.9}$$

where w_i is the weight given to the i_{th} sample in the response after forward modeling d_m^i, compared to the observation data d_o^i. The input fields to perturb in history matching have been mainly the petrophysical properties such as porosity and permeability.
Examples of using evolutionary history matching are Romero and Carter (2001) with using Genetic Algorithm in reservoir modeling, Subbey et al (2004), Anterion et al (1989) and with more recent advancements Vasco and Datta-Gupta (1999) with streamline-based history matching. The other group of methods are based on perturbation operators by changing locally value of random nodes on which a decision is made on whether to keep or discard. An example implemented in Simulated Annealing framework (Deutsch, 1993; Sen et al, 1995) by *swapping* random points in the simulation grid. This method does not keep the spatial continuity of the model unless the covariance function is incorporated in the objective function. The optimization can be very tedious and long as in most cases it involves a flow simulation

as forward modeling step. The other group of methods used for dynamic data assimilation relates to the Ensemble Kalman Filter (EnKF, Evensen 2003). Unlike traditional history matching techniques, EnKF updates a group of state vectors to match the production data rather than only one model. EnKF consists of two sequential steps: first the forecast forward in time where the flow simulation is performed, and second is the update step where all the models are updated by correcting the variables describing the state of the system. The EnKF method can potentially be applied on the Gaussian fields derived from the underlying facies realizations, however the main concern is regarding the spatial correlations and the preservation of the covariance function, unless the perturbations applied to update the ensemble models guarantee this feature. Similar studies have been performed with EnKF in conjunction with the Gradual Deformation Method (Hu et al, 2013).

History matching is often performed on petrophysical properties models as inputs, a review of applications can be found in Aanonsen et al (2009). In most cases the purpose has been to generate one history matched realization. However, by the arrival of geostatistical tools enabling the generation of hundreds of realizations of petrophysical properties or geological models ones can generate a set of realizations all equally likely (Oliver and Chen, 2011).

Liu and Oliver (2005) used EnKF to history match facies models generated with Truncated Gaussian Simulation (Galli et al, 1994) by either correcting iteratively the boundaries of simulated facies or their locations. They used intersecting threshold lines in the lithotype flag to generate facies realizations from bi-Gaussian random fields. The flag was corrected each time and the dynamic response of the updated model was used to match the observation after flow simulation. It is not very clear how can this be applied to the MPS realizations of more complex geologies.

Due to the limitations of variogram-based geostatistics like truncated Gaussian simulation, Caers (2002) proposed using multiple-point statistics in history matching. The idea consists of calculating the conditional probability of transition between facies as a function of two probabilities; one that comes from a one-dimensional optimization determining the probability of transition and another conditional probability from TI. The two conditional probabilities are merged using the Tau model (Journel, 2002).

In this study we use the Gradual Deformation Method (GDM) to calibrate MPS models to dynamic data. GDM was proposed (Hu, 2000) originally for history matching by deforming gradually set of input realizations of petrophysical properties. The deformed models are generated by merging successive realizations in Gaussian space. Equation 2.10 states that each field Z_r can be expressed as the sum of the fields having the same covariance function

(Z_1 and Z_2). Equation 2.10 shows few iterations of the deformation process in GDM:

$$\begin{aligned} Z_r^1 &= Z_1\cos(r) + Z_2\sin(r), \quad i=1 \\ Z_r^2 &= Z_r^1\cos(r) + Z_3\sin(r), \quad i=2 \\ Z_r^i &= Z_r^{i-1}\cos(r) + Z_{i+1}\sin(r) \end{aligned} \tag{2.10}$$

where Z_1 and Z_2 are input Gaussian realizations of property like permeability or porosity. In the first iteration $i=1$ the first two realizations Z_1 and Z_2 are merged producing the first merged model Z_r^1. In the second iteration $i=2$, the merged model from previous iteration Z_r^1 is merged with a new realization, Z_3, and for the third the same procedure is followed until a stopping criteria is met. This equation can be implemented in an inverse modeling problem context where the forward model of the deformed model Z_r^i is compared against the observed data d_o. In this case a one-dimensional optimization needs to be solved to have the value of r.

$$r_{opt} = min\left\{O(r) = \left|d_o - G\Big(Z_r\cos(r) + Z_i\sin(r)\Big)\right|\right\} \tag{2.11}$$

where $G(Z)$ is the forward model of Z and O represents the objective function. In the presence of conditional realizations ones need to merge at least three realizations (Ying and Gomez-Hernandez, 2000) with Eq. 2.12:

$$\begin{aligned} Z_r^1 &= \alpha_1 Z_1 + \alpha_2 Z_2 + \alpha_3 Z_3, \quad i=1 \\ Z_r^2 &= \alpha_1 Z_r^1 + \alpha_2 Z_4 + \alpha_3 Z_5, \quad i=2 \\ Z_r^i &= \alpha_1 Z_r^{i-1} + \alpha_2 Z_{i+2} + \alpha_3 Z_{i+3} \end{aligned} \tag{2.12}$$

where the weights must satisfy the conditions below:

$$\begin{aligned} \alpha_1 + \alpha_2 + \alpha_3 &= 1 \\ \alpha_1^2 + \alpha_2^2 + \alpha_3^2 &= 1 \end{aligned} \tag{2.13}$$

To respect the above conditions the weights are calculated using the relations below (Hu,

2002):

$$\alpha_1 = \frac{1}{3} + \frac{2}{3}\cos(r) \tag{2.14}$$

$$\alpha_2 = \frac{1}{3} + \frac{2}{3}\sin(-\frac{\pi}{6} + r) \tag{2.15}$$

$$\alpha_3 = \frac{1}{3} + \frac{2}{3}\sin(-\frac{\pi}{6} - r) \tag{2.16}$$

Hu (2002) proposed the GDM for the deformation of correlated stochastic input models in the presence of conditioning data. As proved with Le Ravalec-Dupin and Nœtinger (2002) the covariance and other spatial statistics of the input Gaussian variables might not be preserved when the number of iterations in GDM are very large. Hu (2002) proposed a new formulation of GDM for realizations acquired from conditional simulations.

The calibration of facies models to auxiliary data namely global dynamic data has been done in few studies including Le Ravalec-Dupin and Hu (2005); Zahner et al (2016); Pirot et al (2017). The approach with Le Ravalec-Dupin and Hu (2005) applied to Boolean facies models changes iteratively by gradual deformation the size of the Boolean objects, the process continues until a match is found between target variables and the forward model of the updated Boolean model. With dense hard data this approach may face conditioning problems because of the object-based nature of the algorithm. Heidari et al (2013) applied a method combining elements of GDM and EnKF to calibrate continuous property realizations however the models are strongly correlated with a background facies model, supporting the idea of using the facies models directly in the calibration process. Zahner et al (2016) and Pirot et al (2017) proposed in an MPS framework simulating random patches in a simulated field using a TI and accepting or rejecting the updated field based on their forward response comparison with the target variable. The approach is based on MCMC algorithm which can be very long to converge. The attempts are not limited to the techniques mentioned, however there lacks a comprehensive approach that can potentially be applied to facies models of different simulators. In this dissertation a GDM method is proposed to calibrate the categorical simulations.

To apply the GDM on the facies realizations ones need to derive first the latent Gaussian variables. The method that we propose has elements of the PluriGaussian simulation where a lithotype coding flag is used to calculate using Gibbs Sampling the Gaussian fields and also to truncate the final Gaussian field into its corresponding discrete variable case. Gaussian simulations (Le Loch et al, 1994) are based on the generating two or more Gaussian fields using the standard multi-Gaussian methods, and applying a truncation rule to create categorical facies model. The truncation rule known as lithotype flag is acquired from the

geological information, maps, geologists interpretations or densely sampled hard data sets. The conditioning of PluriGaussian simulations can be challenging because the simulations are performed on the underlying Gaussian variables of facies models. One way is to force local inequality constraints using the Gibbs Sampling technique (Geman and Geman, 1984). The lack of a general algorithm that can handle the categorical simulation's calibration to dynamic data has led us to Chapter 5 in which are given the details of the proposed algorithm based on a modified version of GDM. This chapter will be associated with tests on synthetic TIs in both 2D and 3D.

2.2 Objectives of the Research

2.2.1 General objective

The general purpose of the thesis is to develop a series of new tools to enhance facies modelling of reservoirs, mineral deposits, or groundwater aquifers to better predict reservoir performance, improve ore reserve estimation and allow assessment of the related uncertainties.

2.2.2 Specific objectives

The objectives were defined based on the three problems mentioned above in the MPS conditioning.

- The first objective of the thesis is to improve hard data conditioning in patch-based MPS simulations. We aim at generating high quality facies realizations using a given TI such that both the large scale (structures) and short range (texture) variations of the TI are reproduced in simulations. The purpose is to keep the quality of simulations and performing the conditioning to dense hard data without compromising one.
- The second objective is to improve the soft-data conditioning in patch-based MPS simulations. As for the first step we work toward developing a tool that takes as input multiple soft data layers (geophysical maps), and assesses their relationship with existing hard data with facies coding, and eventually calculates the probability maps of facies. This is the scenario most likely to happen in reality. In a second step, the purpose is to condition the patch-based MPS to the output probability maps of the first step.
- The third objective is to improve the conditioning to dynamic data in patch-based MPS simulations. More specifically the plan is to outline a comprehensive method that enables us calibrate categorical simulations to global dynamic data. In this regard, we will exploit the GDM modified into an evolutionary frame.
- The fourth objective is to integrate all of the above tools in a unified MPS workflow.

2.3 Plan of the Thesis

In the four main chapters of this dissertation, 3, 4, 5 and 6, the three specific objectives for the problems of conditioning to hard, soft and dynamic data are presented respectively. In more details:

- In Chapter 3 we propose the idea of using Alternative TIs to resolve or obviate the conditioning to dense hard conditioning data. The proposed idea is tested on a variety of models resulting in better conditioning rates even with using very limiting TIs. The test results show improved conditioning rates for both categorical and continuous cases while keeping the quality of simulations on the power of patch-based algorithm. This chapter has been published in Rezaee et al (2015).
- Chapter 4 is about soft data conditioning process using a modified distance function based on probability fields obtained from a multinomial logistic regression. The proposed method is tested on several synthetic models and a real case study of Malik gas hydrates in Canada. Using logistic regression classifier proved efficient in capturing the relationship between hard and soft data. The output proportion maps were efficiently used to control the local density of facies using proposed distance function. This chapter has been published in Rezaee and Marcotte (2016).
- In Chapter 5, the proposed method for calculating Gaussian fields from facies models are presented. The approach consists of a lithotype flag and the Gibbs Sampling method as in the PluriGaussian simulations. The calibration method based on GDM is given in details. Several applications are given on large scale soft and global dynamic data. The approach is capable of calibrating facies models to dynamic or large scale soft data in tractable amount of CPU time. This chapter has been submitted to the Journal of Computational Geosciences under reference code COMG-S-17-00022. Parts of the results have been presented in the Geostats Congress 2016, Valencia, Spain.
- Chapter 6 provides an example of combining the proposed methodologies of conditioning patch-based MPS to hard, soft and dynamic data in chapters 3, 4 and 5 respectively. The test results demonstrated that properly conditioned facies models to hard and soft data, are readily calibrated to the dynamic data to some degrees. The application of the proposed GDM was shown very efficient in generating multiple calibrated realizations in a stochastic framework. This chapter is the basis for a paper under preparation.
- At the end of each chapter we discuss the results and provide the final conclusions. However an overall discussion and conclusion is presented in Chapter 7.

CHAPTER 3

ARTICLE 1: MULTIPLE-POINT GEOSTATISTICAL SIMULATION USING ENRICHED PATTERN DATABASES

Hassan Rezaee [1], **Denis Marcotte, Pejman Tahmasebi** [2], **Antoine Saucier** [3]

Stochastic Environmental Research and Risk Assessment (2015) 29 893 913

DOI 10.1007/s00477-014-0964-6

Published online: 8 October 2014
©Springer-Verlag Berlin Heidelberg 2014

3.1 Abstract

This study presents a new approach of generating a set of Alternative Training Images (ATI) to use in patch-based multiple-point simulation. The purpose of using ATI is to improve both the conditioning capabilities of the patch-based methods to hard data and the continuity of the conditionally simulated images. The ATIs are produced as a series of unconditional patch-based simulations using unilateral path with weighting and decoupage to improve continuity. A simple strategy is described to control objectively the ATI generation and keep only the few ATIs most useful to ensure hard data conditioning. Hundreds of ATIs are generated, their statistics are compared with that of the original TI and finally an ensemble of ATIs is selected in a pre-simulation step. The CPU time is kept overall at a quite reasonable level over large 2D and 3D grids by the use of fast distance computation by convolutions and FFT. Different examples are considered: categorical or continuous, with small or large training images. In 2D, the richest database obtained by adding the ATIs enables to ensure 100% hard data conditioning in all realizations for the categorical examples tested and a very strong correlation coefficient (r=0.999) in the continuous case. In 3D, the hard data

1. H. Rezaee, D. Marcotte Department of Civil, Geological and Mining Engineering, Polytechnique Montreal, C.P. 6079, Succ. Centre-ville, Montreal, QC H3C 3A7, Canada, e-mail: hassan.rezaee@polymtl.ca

2. P. Tahmasebi Department of Energy Resources Engineering, Stanford University, Stanford, USA

3. A. Saucier Department of Mathematical and Industrial Engineering, Polytechnique Montreal, Montreal, QC, Canada

reproduction rate in the simulation is increased. Different possible improvements to the method are discussed.

3.2 Introduction

Multiple-point simulation (MPS) methods based on Training Images (TI) are commonly used to model complex geological structures that two-point geostatistical methods can hardly represent adequately. Since the pioneer work of Guardiano and Srivastava (1993) the research has focused on reducing the computational load (Strebelle, 2002; Mariethoz et al, 2010; Tahmasebi et al, 2012), improving the short scale structure reproduction using patch-based approaches (Zhang et al, 2006; Arpat and Caers, 2007; El Ouassini et al, 2008; Faucher et al, 2013; Rezaee et al, 2013; Faucher et al, 2014), incorporating secondary data information (Arpat and Caers, 2007; Boucher, 2009) and improving Hard Data (HD) conditioning (Arpat and Caers, 2007; Parra and Ortiz, 2011; Faucher et al, 2013, 2014). In addition, a wealth of geological applications have been published, mostly in the petroleum sector (Strebelle et al, 2002; Caers et al, 2003; Hoffman and Caers, 2007), but also for mining applications (Osterholt and Dimitrakopoulos, 2007; Pasti et al, 2012; Rezaee et al, 2014).

Patch-based MPS methods involve a similarity or distance computation between patches in the TI and those already present in the simulated image. They were shown (Zhang et al, 2006; El Ouassini et al, 2008) to ensure superior texture reproduction compared to the single point-based approach (SNESIM) of Guardiano and Srivastava (1993) and Strebelle (2002). However, the HD reproduction remains a challenge as the probability of finding in the TI a patch with a given HD pattern quickly drops to zero as the number of HD increases. Therefore, all patch-based approaches trade the exact HD reproduction for only an approximate HD reproduction. On the contrary, SNESIM makes the HD conditioning much easier but to the detriment of texture reproduction.

The patch-based approaches perform simulations following either a unilateral or a random path. The random path offers more flexibility to allow simulating first areas with many HD, hence incorporating sooner in the simulated image the long range influence of the HD. However, the unilateral path (El Ouassini et al, 2008; Kjonsberg and Kolbjornsen, 2008; Parra and Ortiz, 2011; Tahmasebi et al, 2012; Faucher et al, 2013) is known to ensure a better continuity between patches than the random path. Different modifications to the unilateral approach were proposed to help foresee the HD influence early in the simulation (Kjonsberg and Kolbjornsen, 2008; Parra and Ortiz, 2011; Faucher et al, 2013; Tahmasebi et al, 2014).

Emery and Lantuéjoul (2014) show that a TI does not hold the definition of a random field

model unless it is an infinite realization of the underlying random field. They show that a TI needs to be quite large to include a sufficient number of replicates of a given template. Hence, increasing the TI size is desirable. One more practical approach is to use instead many independent realizations as Alternative Training Images (ATIs).
One should recognize that the Original Training Image (OTI) is only one particular representation of the texture and structure of the domain under study. This representation is subject to uncertainty on both the location of structures and the texture description. Therefore, one idea to improve the conditioning capabilities of patch-based approach is to enrich the database by generating new patterns similar to those found in the OTI. Faucher et al (2014) used for isotropic images 90^o rotations and reflexions of the OTI to enrich the pattern database. To go a step further, a good method is the patch-based unconditional unilateral simulation which can provide as many ATIs, of any specified size, as desired. The continuity and quality of each ATI can further be enhanced by applying decoupage (improperly termed quilting by Efros and Freeman, 2001) and commonly used in texture synthesis. The generated ATIs enrich the database of patterns and hence can improve HD conditioning and continuity in the simulated images. Alternative approaches to generate ATIs can also be considered such as chaos mosaic (Guo et al, 2000), tree-structured vector quantization (Wei and Levoy, 2000), and texture synthesis based on wavelet decomposition, (Portilla and Simoncelli, 2000). In the methodology section the unilateral path method with weighting and decoupage is outlined. The strategy used to select ATIs is described and the comparison of ATIs to OTIs is done based on meaningful statistics. Different OTIs, both discrete and continuous, are used to assess the merits and weaknesses of the new approach, especially regarding the HD reproduction and the continuity of the simulated fields.

3.3 Methodology

The proposed method follows a patch-based unilateral approach for both the unconditional and conditional cases. The shape of the patch used in the unilateral case is illustrated in Fig. 3.1-A. The square patch of size T presents an overlapping area (gray pixels) of width OL. The choice of these free parameters depends of the TI. For comparison Fig. 3.1-B shows a possible irregular patch obtained through random path. The black cells refer to the HD and the gray ones represent the previously-simulated nodes. The term 'conditioning data' refers to both HD and previously simulated parts, although a much higher weight is assigned to HD in the distance computation used to find a matching pattern in the OTI or the ATIs.

The distance function used here is a weighted squared euclidean distance. It is expressed as:

$$d^2(S,P) \;=\; \sum_{i=1}^{N} \alpha_i (S_i - P_i)^2 \tag{3.1}$$

where $\alpha_i > 0$ for all i, the index i identifies a point in the pattern, N is the number of pixels in the pattern, S is a pattern in the simulated image, and P is a pattern in the OTI or an ATI.

As observed by Tahmasebi et al (2012), the individual terms appearing in the distance computation can be efficiently computed as a convolution product [4]:

$$\sum_{i=1}^{N} \alpha_i P_i^2 \;=\; \breve{\alpha} * (P \odot P) \tag{3.2}$$

$$\sum_{i=1}^{N} \alpha_i S_i P_i \;=\; (\breve{\alpha} \odot \breve{S}) * P \tag{3.3}$$

where $\odot$ represents the Hadamard product (element by element), $*$ is the convolution product. The matrix α is of size $N_1 \times N_2$, the size of the simulation windows; α contains N non-zero entries, the weights of the known pixels in the current simulation window. The other $N_1 \times N_2 - N$ entries in α are zeros; the matrix $\breve{\alpha}(i,j) = \alpha(N_1 + 1 - i, N_2 + 1 - j)$ represents the α matrix after flipping on both rows and columns; S is the matrix with the pattern found in the current simulation window. The convolutions can be computed in the spectral domain by FFT as used in Duhamel and Vetterli (1990), Marcotte (1996) and Tahmasebi et al (2014) which allows fast computation particularly for large templates. As an example with Matlab, the 4.25 million distances between a pattern of size 15×15 and a large TI of size 2048×2048 are computed in 0.4 second on a low-cost laptop equipped with I3 processor. Recomputing the distances eludes the need to save the patterns of the TI in a long list or in a series of trees, one tree for each different ensemble of points defining a pattern. This simplifies considerably the programming and saves the huge memory space required by the set of search trees or the time to scan the list.

The distances between the patterns defined by the known pixels in the simulation window (already simulated or HD) and each pattern in the OTI and ATIs are computed by convolution. Then, the best pattern selected from either OTI or ATI is the pattern minimizing this distance. The void space (the white part in Fig. 3.1-A) is filled with the corresponding nodes from the TI. Note that in the process, HD present in the void space are also overwritten by values found in the TI. This enables us to evaluate the capacity of the algorithm to reproduce

4. In the published paper, second row equation reads as $\sum_{i=1}^{N} \alpha_i S_i T_i$ which is corrected into $\sum_{i=1}^{N} \alpha_i S_i P_i$

HD.

To help propagate the influence of HD at longer distances, similarly to Parra and Ortiz (2011), Faucher et al (2013) and Tahmasebi et al (2014), the simulation window is expanded to involve nearby HD in the distance computation. As illustrated in Fig. 3.2 the pattern used to compute the distances is formed by the union of the L-shaped simulated pixels in the regular window and the HD found in the enlarged window.

3.3.1 Weighting system

In the distance computation, larger weights (a_1) are given to the HD so as to favor the reproduction of the local HD (Zhang et al, 2006; Mariethoz et al, 2010; Rezaee et al, 2013; Faucher et al, 2013). As in El Ouassini et al (2008) and Faucher et al (2013), weights (a_2) are taken larger close to the area to simulate (see Fig. 3.4) to favor continuity of the pasted area with the already simulated part. A few test trials indicate that weights inversely proportional to the square of the distance to the border provide good results. The final weights (α) are obtained as $\alpha = a_1 + a_2$ (see Fig. 3.3).

3.3.2 Pasting

After the best matching pattern is found, the corresponding patch is pasted to the simulated image. In El Ouassini et al (2008) and Faucher et al (2013) only the hatched area in Fig. 3.2 is pasted because the weights favor continuity with the already simulated pixels. However, a possibly better strategy was proposed by Efros and Freeman (2001). They suggested to cut in the overlapping area along a path ensuring, for pixels along the cut, least difference between the TI and the simulated image (Fig. 3.5). This approach is therefore a compromise between pasting only the hatched area (Fig. 3.5-A) and pasting the entire patch (Fig. 3.5-B). The shortest path between a pixel on the entry boundary and a pixel on the exit boundary of the overlapping area (horizontal, vertical or L-shaped) defines the cut.

A simple example is provided for a vertical overlapping area in 2D cases. Let P_1 and P_2 be two patches with overlap areas OL_1 and OL_2 (see Fig. 3.6). The pixel-based error surface is computed as $e = (OL_1 - OL_2) \odot (OL_1 - OL_2)$. The cumulative error function E is formed by moving, in the overlap region, from top row ($i = 1$) to bottom row ($i = N$):

$$\begin{aligned}
E_{1,j} &= e_{1,j},\ j \in \{1, 2, ..., w\} \\
E_{i,1} &= e_{i,1} + min(E_{i-1,1}, E_{i-1,2}),\ i \in \{2, 3, ..., N\} \\
E_{i,w} &= e_{i,w} + min(E_{i-1,w-1}, E_{i-1,w}),\ i \in \{2, 3, ..., N\} \\
E_{i,j} &= e_{i,j} + min(E_{i-1,j-1}, E_{i-1,j}, E_{i-1,j+1}),\ i \in \{2, 3, ..., N\}, j \in \{2, 3, ..., w-1\}
\end{aligned} \tag{3.4}$$

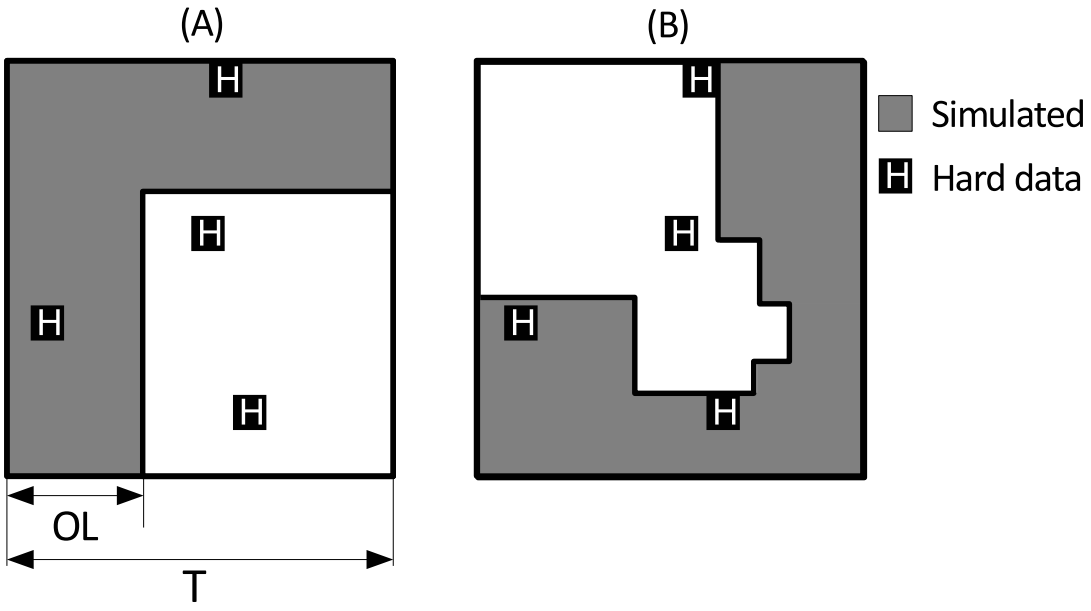

Figure 3.1 Schematic illustration of a patch in (A) unilateral and (B) random simulation paths. Gray pixels are already simulated, white ones are to simulate, and black pixels represent HD. The irregular shape of B is due to random selection of previous patch centroids.

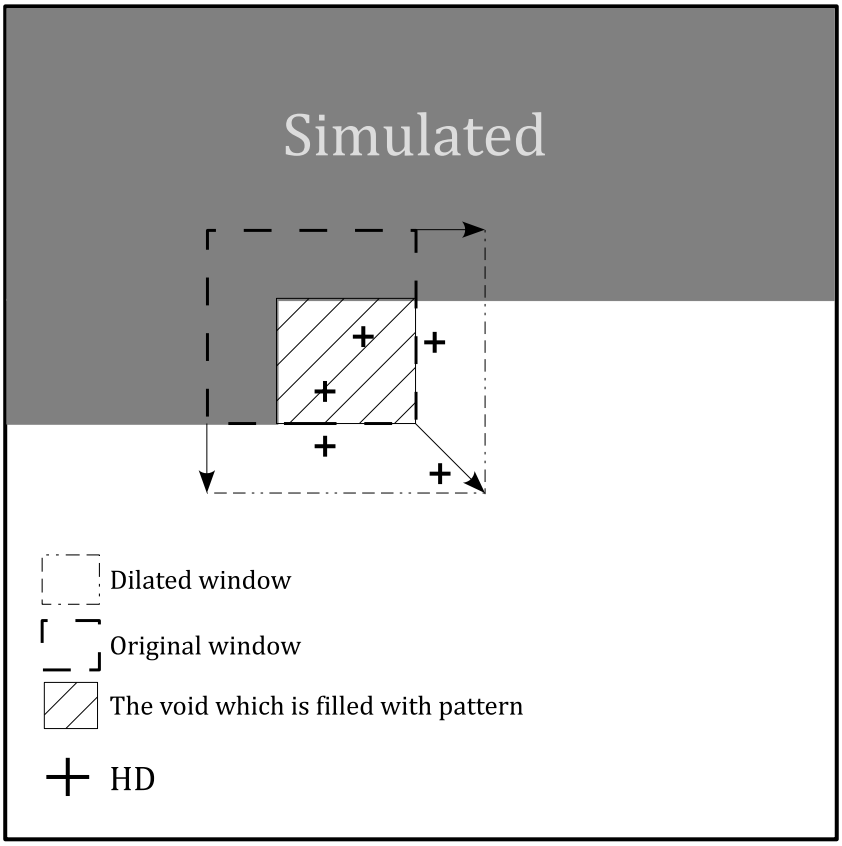

Figure 3.2 Enlarged window to include nearby conditioning data in the distance computations. Only the hatched area in the initial window is pasted with data from the matching pattern in the OTI or ATI.

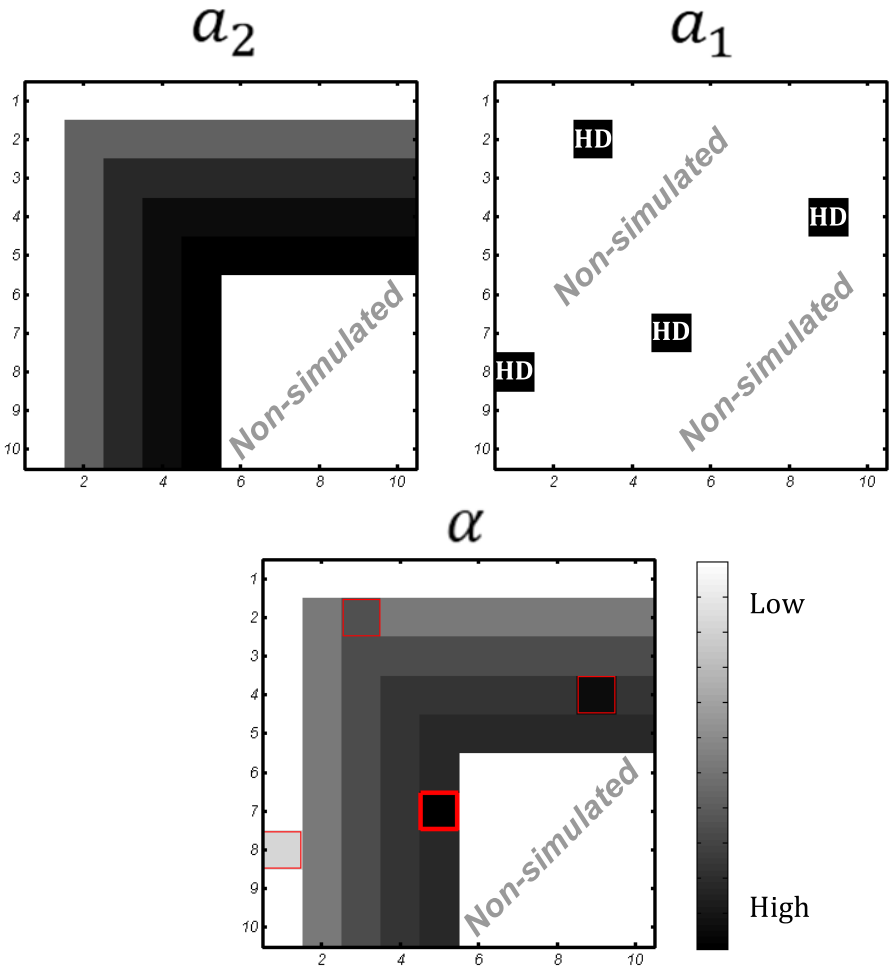

Figure 3.3 Weighting sets for HD (a_1) and previously-simulated parts (a_2) and the final weighting matrix (α). In this case, the node highlighted in bold red square receives the highest weight. The illustration shows the weighting system for the L-shaped patch (for other possible patches see Fig. 3.4)

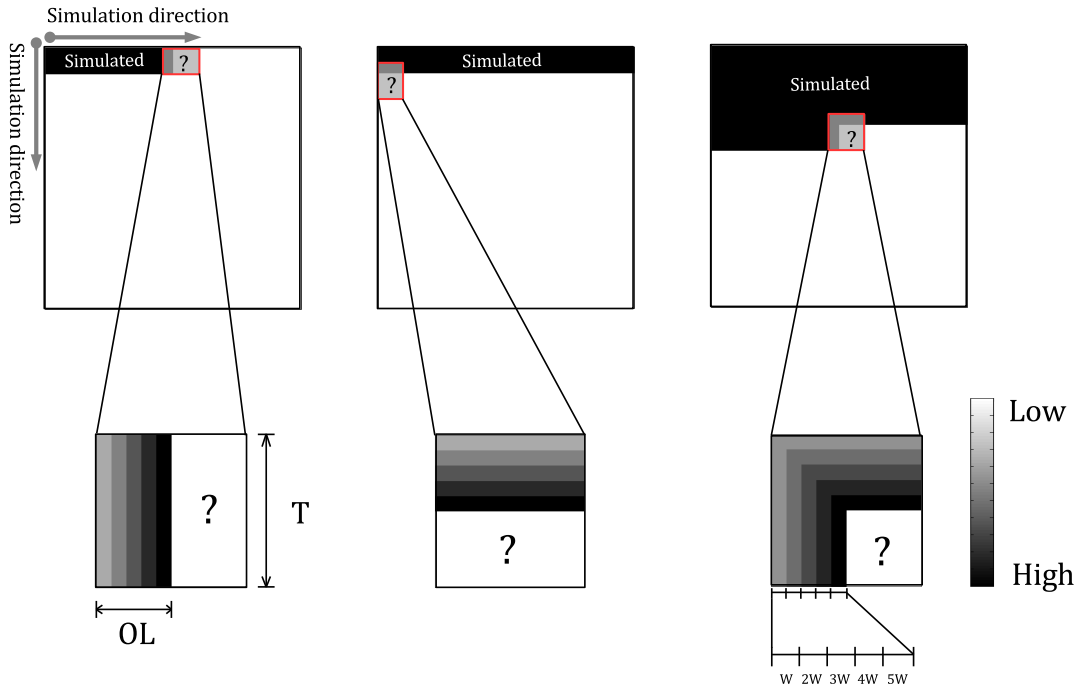

Figure 3.4 Patch shapes and the corresponding weighting system. Left: first row, middle: first column, and right: the rest of the image. W stands for the weight given to each band in the template.

where N is the number of rows and w is the width of the overlapping area. The path of the cut is identified by the pixel with minimum value in the last row of E. This pixel connects backward to the neighbor pixel (as implicitly defined by Equation 3.4) with minimum E value. The process is repeated until the first row is reached. Figure 3.6 illustrates the steps of the computations and the results obtained. The same principle can be adapted for a L-shaped overlapping area.

Pasting in 3D

In 3D however the scenario is more complicated as the shortest path problem does not define a cutting surface between the external faces of the cuboid but rather a cutting line. We used the approach of Mahmud et al (2014) to adapt the decoupage to the 3D case. Interested readers are referred to the original contribution. Figure 3.7 illustrates the idea of decoupage for a 3D unilateral path.

3.3.3 Flowchart

The flowchart of the algorithm is shown in Fig. 3.8. The size of the patch depends on the TI being used. For a TI with large scale pattern and objects, one may increase the patch size T so that the pattern shape/wavelength is better captured.
First, the OTI is searched for the best matching pattern. The corresponding minimum distance value is saved in $dist1$. If $dist1$ meets the minimum distance threshold, the corresponding pattern from OTI is pasted to the simulation grid, otherwise the entire set of ATIs are searched. The best matching pattern from ATIs has minimum distance $dist2$. If $dist2 < dist1$ the pattern from the ATI is pasted, otherwise the pattern from the OTI is pasted.

3.3.4 Alternative Training Images

The ATI concept refers to any image (or cuboid in 3D) that bears patterns similar to the patterns found in the OTI. As mentioned in the introduction, the OTI representation is subject to large uncertainty, therefore justifying to consider variations represented by the ATIs. In this study the ATIs are generated via unconditional unilateral simulations using the OTI. The general idea is to replace the stochastic model described by the OTI by a larger and richer stochastic model represented by the set of OTI+ATIs. Various methods to generate ATIs can be considered although here we used only unilateral patch-based unconditional simulations with weighting and decoupage. For simplicity, the size of ATIs is mostly chosen

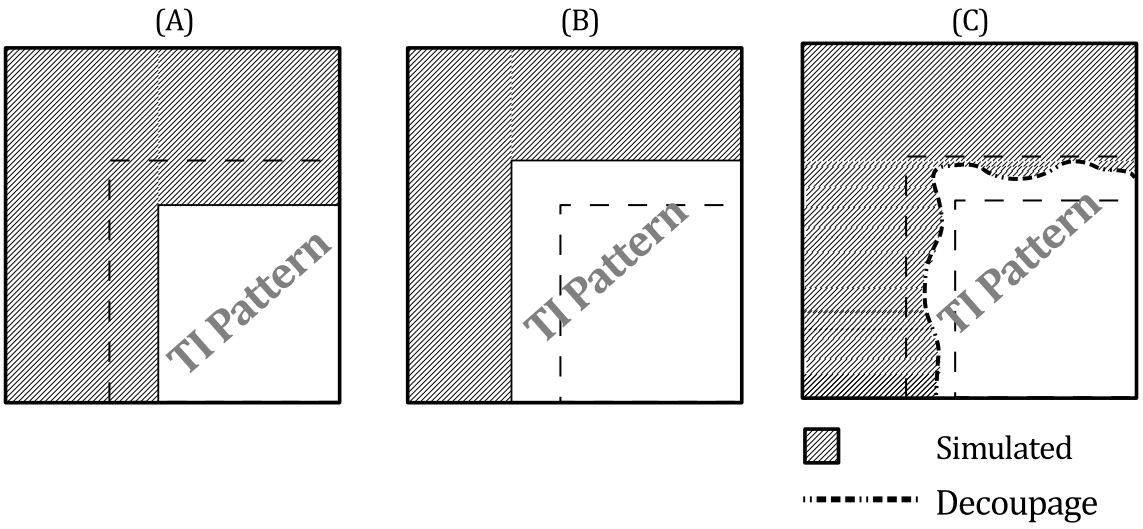

Figure 3.5 Three possible stitching strategies in simulation. A: new pattern is placed without overlap, B: the overlap is overwritten by the new pattern, C: the overlap is cut through the minimum error path

equal to the OTI size, although the ATIs can be simulated of any desired size. [5]

Unconditional simulations

Unconditional multiple-point simulations, especially those obtained by unilateral patchwork with weights (El Ouassini et al, 2008; Faucher et al, 2013) and decoupage (Efros and Freeman, 2001), can produce ATIs that bear similar structural features and patterns to those found in the OTI. A set of six OTIs is used (see Fig. 3.9-A to F) among which are the ball TI in 2D with varying radii (Fig. 3.9-A), the continuous connected low-value areas encircling disconnected high-value areas (Fig. 3.9-B [6]), the binary and 3-facies TI of channels with complex curvilinear structures (Fig. 3.9-C and D), a 3D TI of balls and a continuous Gaussian field 3D TI with Gaussian variogram (Fig. 3.9-E and F). Each OTI is shown on the left accompanied by one ATI obtained by unilateral unconditional simulations with weighting and decoupage on the right.

5. Correction made to a typo in the published paper.
6. Corrected sub-figure B from the published paper.

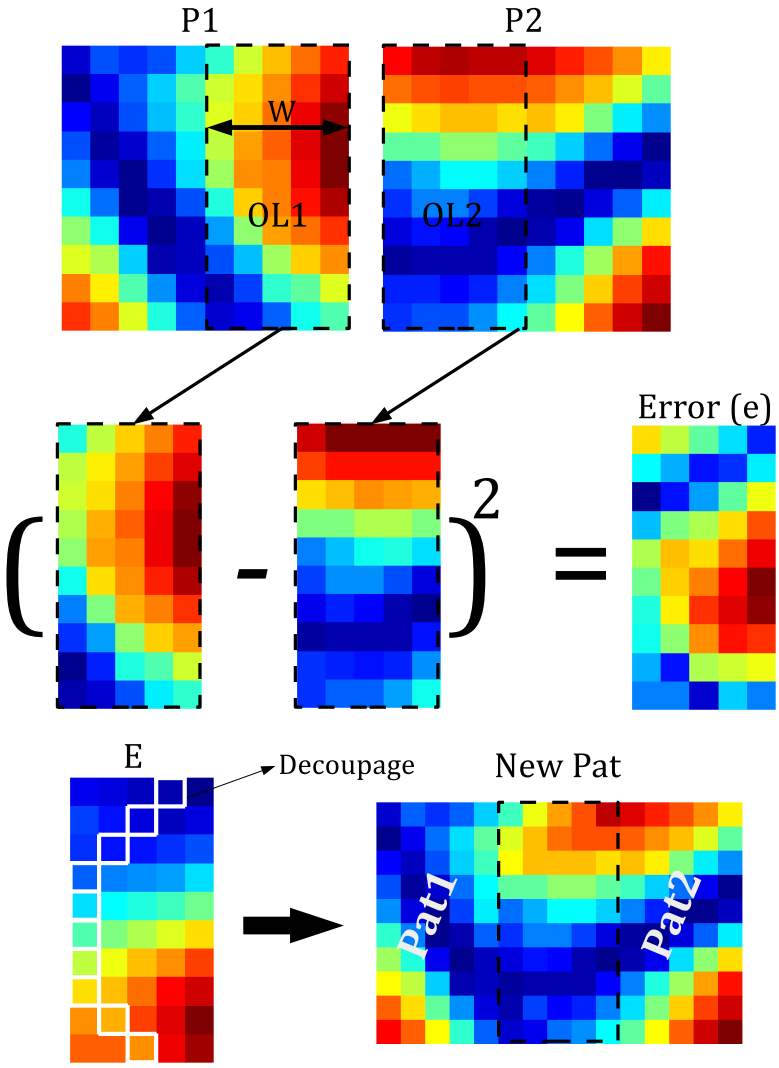

Figure 3.6 $P1$ is the new pattern coming from either OTI or ATI, and $P2$ is the existing pattern simulated before. $P1$ and $P2$ are stitched along the series of pixels where the minimum overlap error is achieved (decoupage)

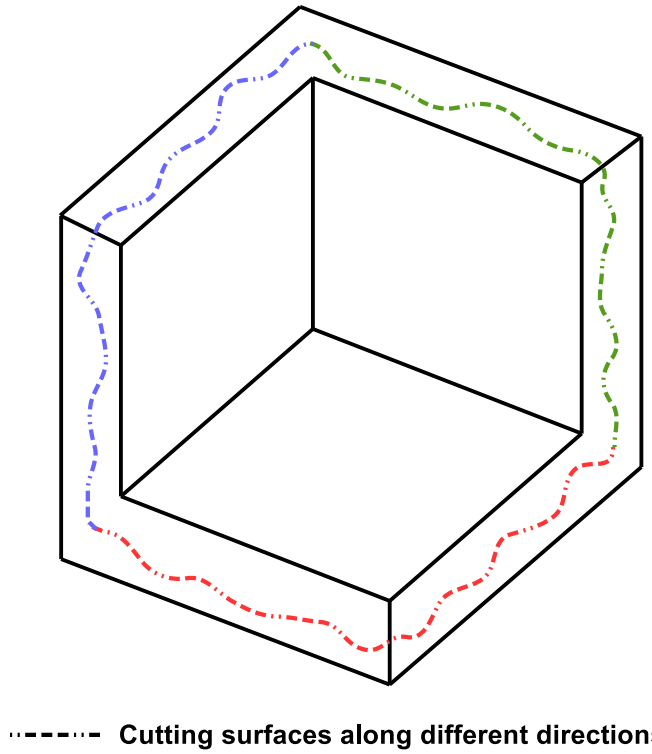

Figure 3.7 Quilting in a 3D parallepiped with multiple surface cuts.

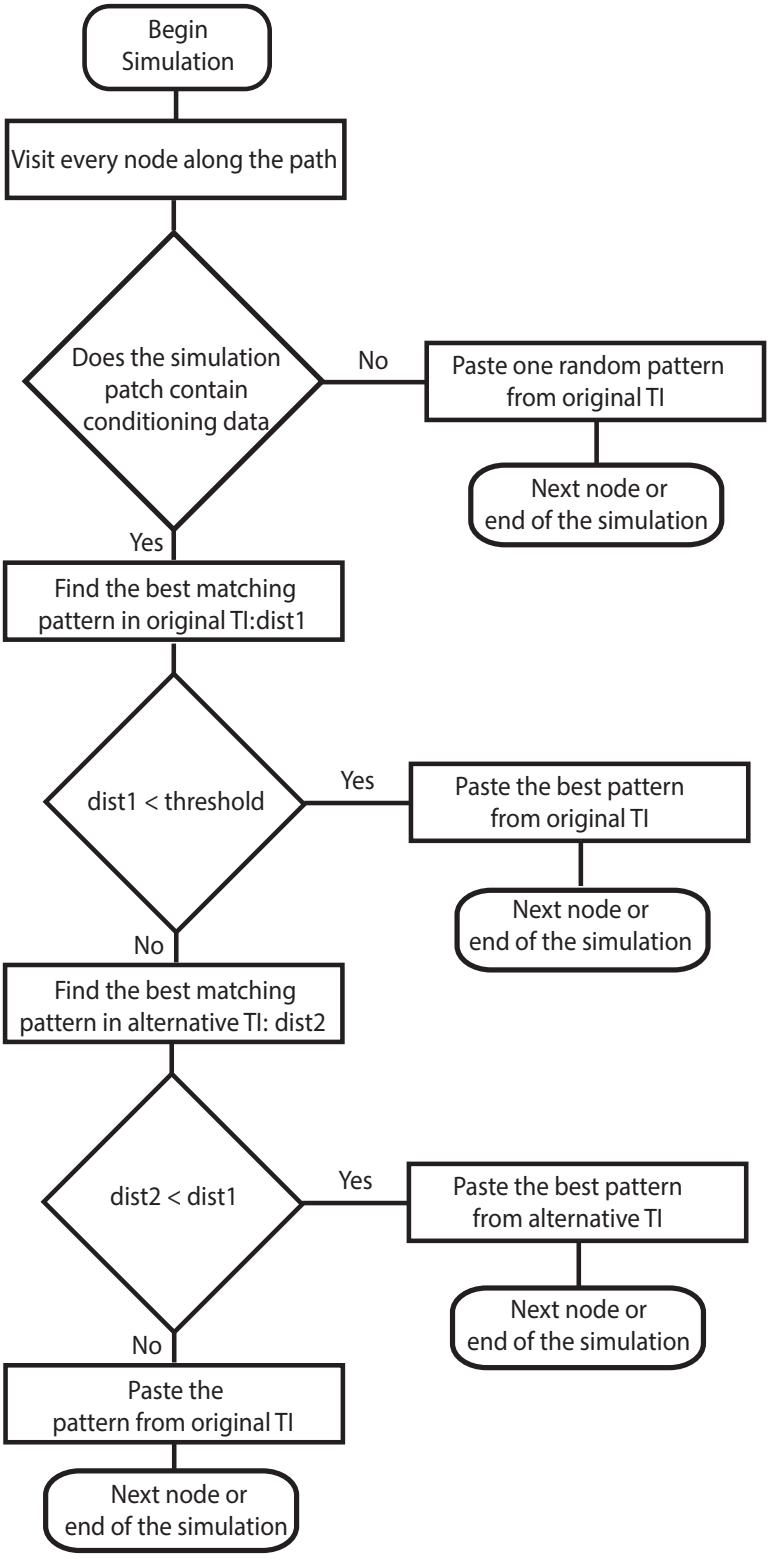

Figure 3.8 The flowchart of the algorithm

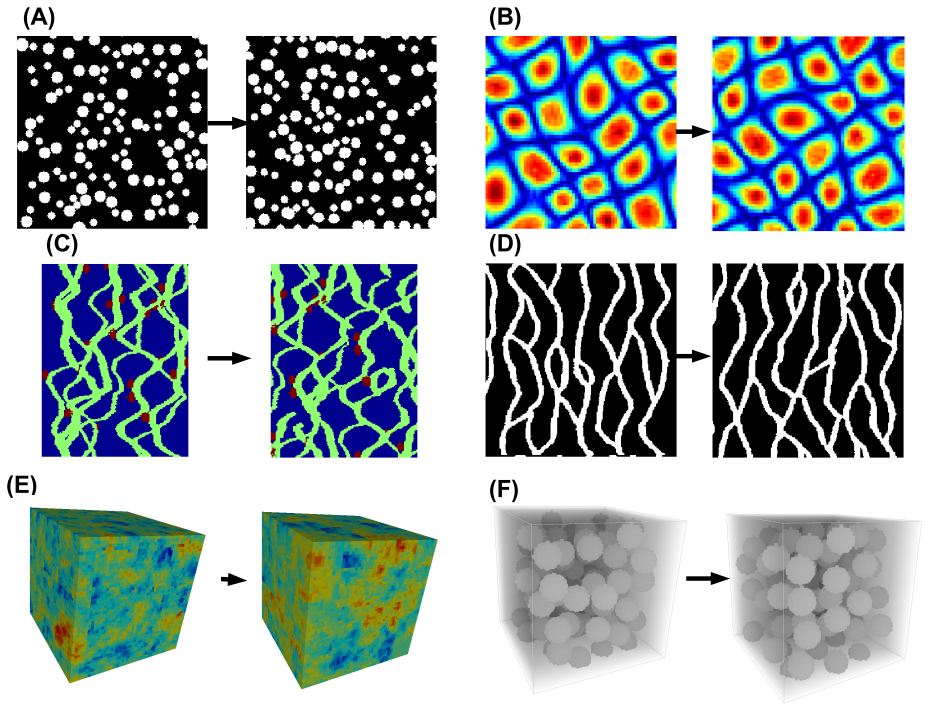

Figure 3.9 Sample OTIs (left) with corresponding ATIs (right) obtained by unilateral unconditional simulation with weighting and decoupage.

Enriched pattern database with ATIs

The role of ATIs is to enrich the pattern database so as to favor better HD reproduction and better continuity in the simulated images. Table 3.1 gives for an OTI and a single ATI the proportions of common and specific patterns as a function of the size of the square window for three different TIs. As window size increases, the number of possible patterns explode initially and then tends to stabilize as the number of large windows in the TI is limited. The proportion of specific patterns in the ATI increases steadily. Hence, ATIs are expected to be particularly useful when large templates are used in the simulation. Indeed, using more ATIs will allow more patterns to be found.

The new patterns generated by unconditional simulation are expected to be texturally similar to the patterns found in the OTI. One approach to assess this property is to compute the distances between the ATI and the OTI and plot the points on the first eigenvectors extracted by multidimensional scaling analysis (MDS) (Borg and Groenen, 1997). MDS has been used in a geostatistical context before as in Honarkhah and Caers (2010) and Deutsch and Deutsch (2014). Many possible distances can be used. Tan et al (2013) proposed to compute the multiple-point histograms (MPH) (Deutsch and Gringarten, 2000; Lange et al, 2012) of each image and then to calculate the Jensen-Shannon divergence (Cover and Thomas, 1991; Endres and Schindelin, 2003) between the resulting histograms as a distance measure for the MDS. Figure 3.10 shows the OTI and ATIs projections on the first three eigenvectors for the channel OTI shown in Fig. 3.9. The MPH is computed over 4×4 templates and over three multi-resolution. The 25 ATIs, obtained by unconditional unilateral simulation with decoupage, are well scattered around the OTI, supporting (but not proving) the similarity of textures between the OTI and the ATIs. The ATIs appear as unbiased variations around the OTI.

3.3.5 ATI selection strategy for the categorical and the continuous cases

The ATI selection process is twofold. The first step consists in discarding ATI showing statistical and geometrical characteristics significantly different from the OTI. Allard et al (2011) and Toftaker and Tjelmeland (2013) proposed a variety of statistical measures to compare realizations with the TI. We select histogram and variogram comparisons and comparison of distributions of size of objects in the OTI and the ATI. The OTI-ATI histograms are compared based on the χ^2 statistic. Similarly, the variograms are compared via Bonferroni corrected t-tests statistic (Simes, 1986) of equality on the variogram for each lag. Indeed, the correlation between variogram lag values may affect the significance level of the test statistic, but this is not a problem as the goal is to select the best ATIs among the set of proposed

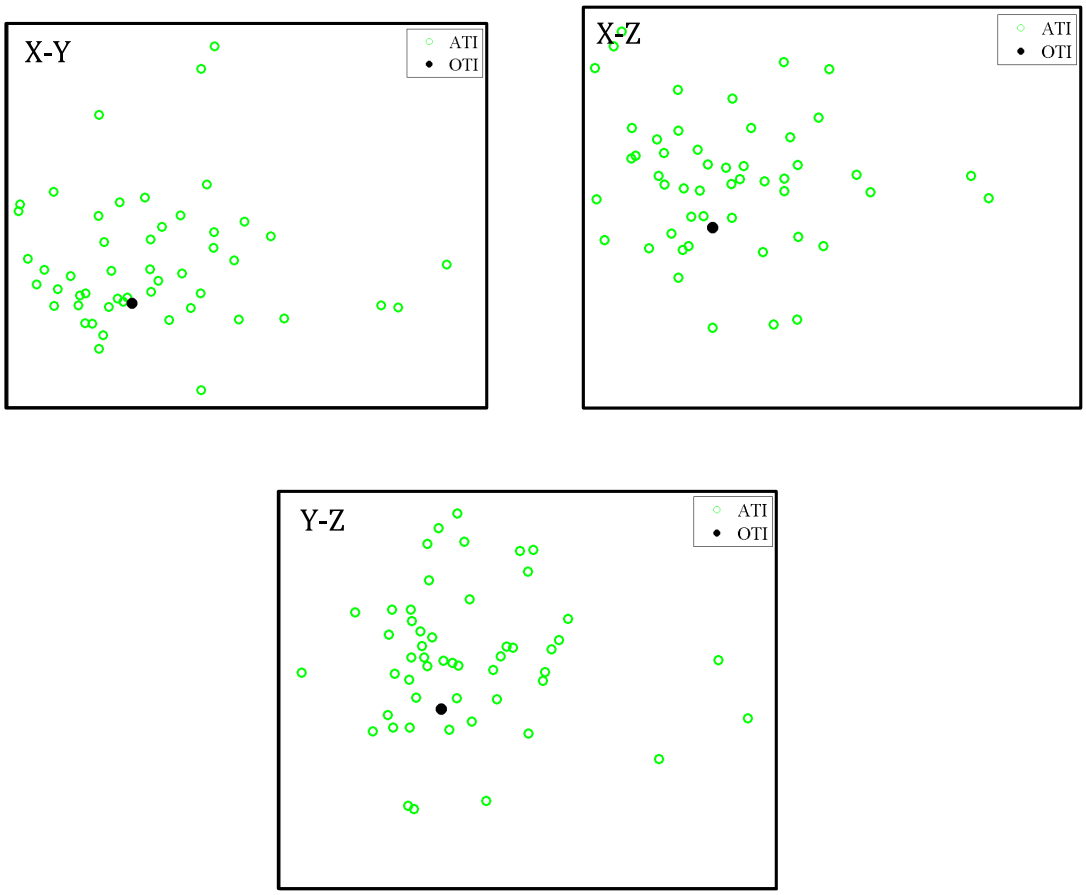

Figure 3.10 MPH computed over 4 × 4 templates; X: first eigenvector (18 % of variance), Y: second eigenvector (13%) and Z: third eigenvector (10%) from the MDS computed on the similarity matrix defined by the Jensen-Shannon divergence statistic.

Table 3.1 Distribution of patterns found in OTI and ATI for three different images and five window sizes; total number of different patterns found in both OTI or ATI and proportion of these numbers present in OTI and ATI, in OTI alone and in ATI alone.

Training Image	Template	# patterns	Common %	OTI only %	ATI only %
Channel (100 × 100)	3 × 3	120	87.5	7.5	5.0
	6 × 6	3943	44.0	31.5	24.5
	9 × 9	11214	22.7	39.0	38.3
	12 × 12	14430	9.2	45.4	45.4
	15 × 15	14111	4.8	47.6	47.6
Ball (150 × 150)	3 × 3	110	85.5	10.0	4.5
	6 × 6	1383	45.3	25.3	29.4
	9 × 9	4016	36.0	31.3	32.7
	12 × 12	7719	28.5	34.9	36.6
	15 × 15	11620	21.5	38.2	40.2
Three facies (100 × 100)	3 × 3	363	82.9	13.2	3.9
	6 × 6	4255	62.7	23.3	14.0
	9 × 9	8479	44.7	30.3	24.9
	12 × 12	10398	35.8	32.7	31.6
	15 × 15	11143	29.2	34.9	35.8

ATIs. Finally, the size distribution of objects in OTI and ATI are compared again with the χ^2 statistic. Only ATIs passing the tests on histogram, variogram and size distribution are retained. In the second step, one verifies that the new ATI brings enough patterns with HD data. Having successfully passed the two steps, the new ATI is added to the pattern database.

The geometrical features to test for ATI selection is the size of connected objects. For the channel OTI, the distributions of area of the channels are similar in the ATIs and the OTI for 8 of the 10 displayed distribution (Fig. 3.11-A). For ball TI, the radius (or equivalently the area, or the volume) distribution of individual balls was not different from the OTI for 21 of the 25 tested ATIs (Fig. 3.11-B and C). The continuous TI displayed in Fig. 3.9-B is also tested on the area distribution of the objects obtained after thresholding at the median (Fig. 3.11-D). All χ^2 tests were done at $\alpha = 5\%$ significance level, using equal frequency bins at every fifth percentile.

Figure 3.12 displays four different OTIs and one representative ATI that passed the selection test and another one that failed it. Clearly, the procedure is able to detect small discrepancies between the OTI and the (failed) ATIs. Moreover, the accepted ATIs show visually a strong similarity with the corresponding OTI. Globally more than 70 % of the ATIs passed the selection test.

From the set of potential ATIs passing the tests, only the most useful ATIs are kept to

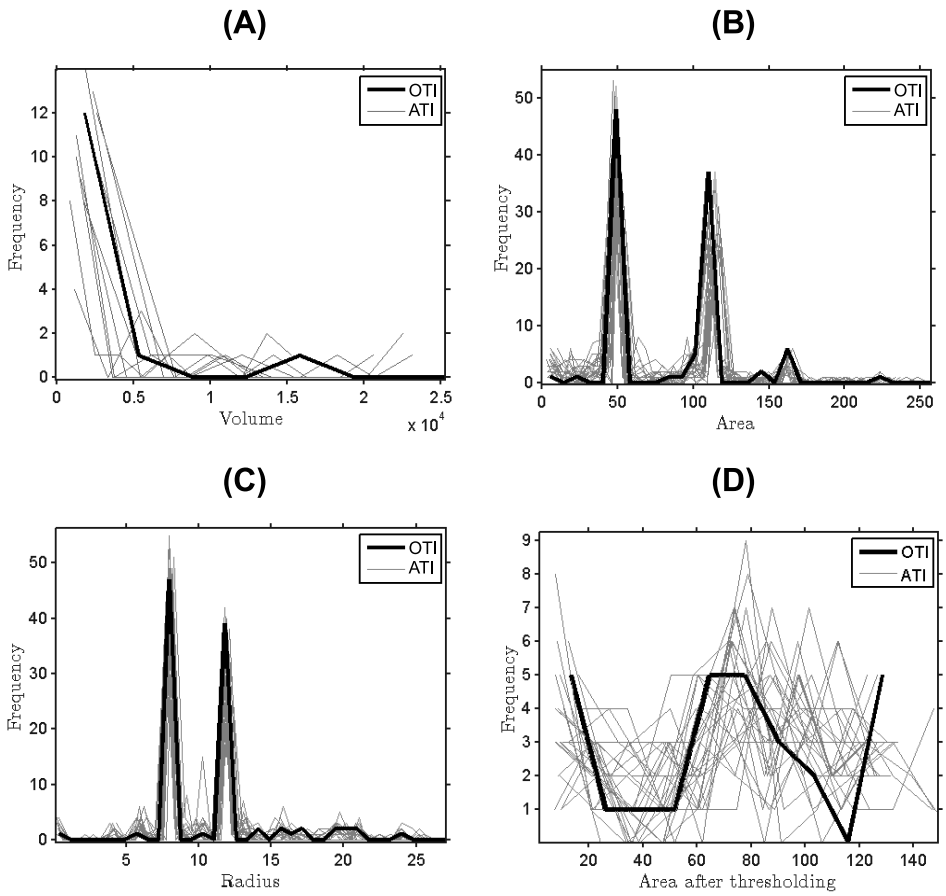

Figure 3.11 Object features' distribution in OTI and set of ATIs. 3D channels (A) (based on Fig. 3.9-D), 2D balls (B) (Fig. 3.9-A), 3D balls (C) (Fig. 3.9-F) and continuous TI (D) (Fig. 3.9-B)

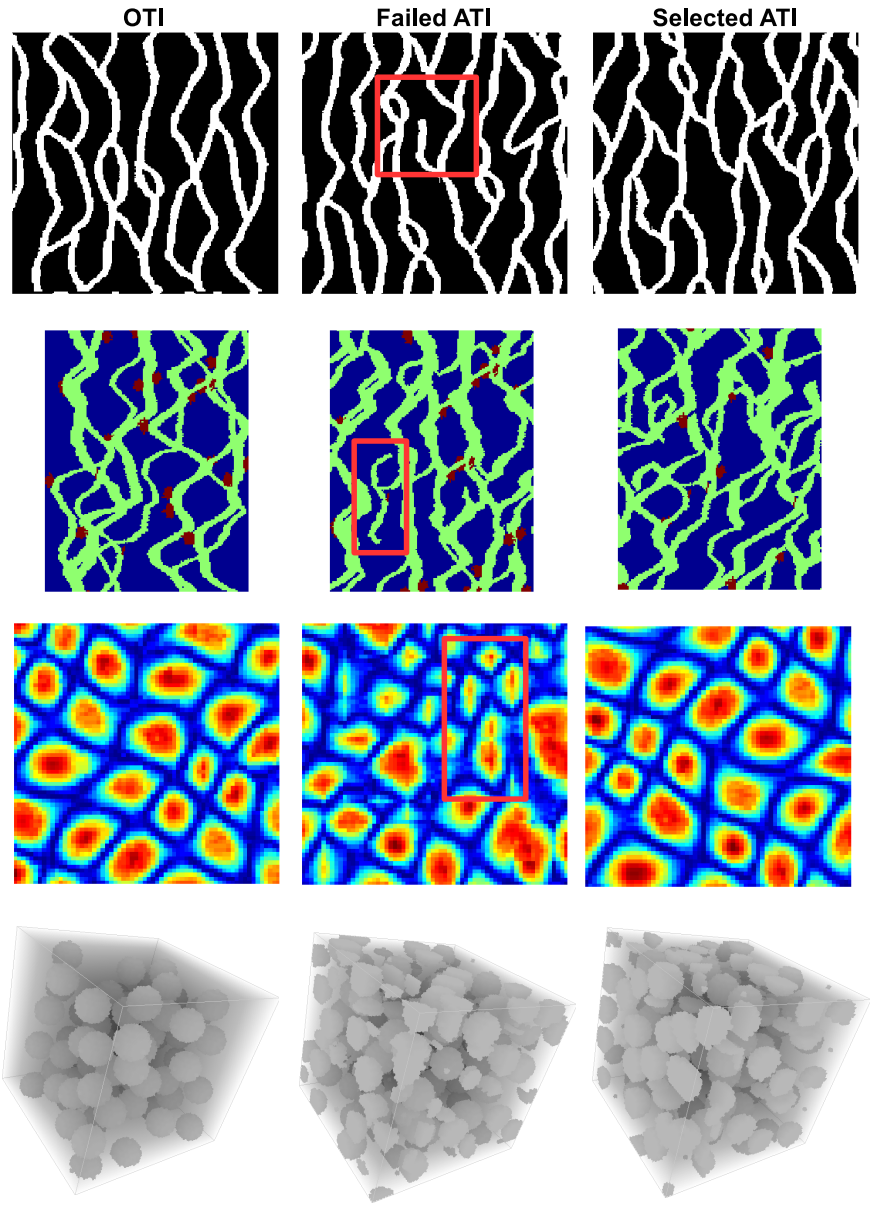

Figure 3.12 ATI selection based on tests on equality of histograms and variograms and test of equality of the object size distribution. The red rectangles identifies areas where the ATI produced undesired results. In the first and second rows, discontinuous channels are evident; in the third row the highlighted patterns contradicts the ones found in the OTI. In the 3D case (4th row) the failed ATI contains too many incomplete balls. These problems are not present in the corresponding selected ATIs.

keep the computations tractable. The strategy adopted is simply to increase the database sequentially by acceptance/rejection of a candidate ATI. The candidate ATI is kept when it includes at least n HD patterns in the current database. Additionally, when a series of consecutive candidate ATIs have been rejected, the minimum number of matching patterns n in each ATI is decreased. The pre-simulation step ends when a sufficient number of replicates of the HD pattern are found in the whole database or when a maximum total number of ATI candidates has been examined. At the end, the presence in the database of at least one replicate for each HD pattern ensures perfect HD reproduction. For the continuous case, as perfect HD reproduction is not possible, a match is obtained when the HD pattern is reproduced within a small distance threshold. Failure to obtain a matching pattern for many HD configuration might be an indication that the OTI is incompatible with the studied field or simply that more ATIs should be examined before proceeding to the conditional simulation step.
The main steps involved in the pre-simulation phase are therefore:

- Define a stopping criteria as either the total number of ATIs considered, or the maximum number of ATIs retained in the database or the database contains enough replicates of each HD pattern
- Repeat until the stopping criteria is met
  - Generate a new ATI
  - Identify all the HD patterns present in the ATI
  - Check for the equality of the histogram, variogram and the distribution of a representative (or a few representative) geometric feature. Here, we select the size of connected objects. If one of the tests is failed, reject the ATI
  - Include the ATI in the database when it contains $> n$ HD patterns, reject the ATI otherwise. After a series of consecutive reject, decrease n
  - Update the number of replicates of each HD pattern in the database

---

3.4 Results

In this section, 2D and 3D categorical and continuous images are considered. The 2D categorical images include the common channel image similar to Strebelle (2002), and a ball image as in El Ouassini et al (2008) and Faucher et al (2013, 2014). The ball image is particularly helpful to help detect any possible artifact of the simulation method. A three

categories image with channels is also used. The 2D continuous image presents [7] well connected low grade areas surrounding isolated high grade patches. In 3D, the categorical image is again the ball image and the continuous one is a Gaussian field with isotropic Gaussian variogram of practical range 21 pixels. In each case, one unconditional unilateral realization with weighting and decoupage is retained as the reference image from which are extracted the HD used in the conditional simulations. The free parameters are the size of the window (T) and the size of the overlapping area (OL), as described in Fig. 3.4. The value of T is chosen for each case after quick visual inspection of a few ATIs produced. After choosing T, we usually set $OL \approx T/3$.

3.4.1 Continuous TI

A continuous TI consisting of textures of disconnected high values and connected low values is used (see Fig. 3.13). A set of 60 ATIs are obtained by unconditional unilateral simulation with weighting and decoupage. A match is declared when the distance between the HD pattern and a pattern in the ATI is less than 0.001 (the range of the variable being [0-1]). In the final database, at least 50 matching patterns are found for each HD pattern.
Figure 3.13 shows one sample realization obtained with OTI+ATIs ($r = 0.999$) and one realization obtained using only the OTI ($r = 0.98$). In addition to a better conditioning to HD, the simulation with ATIs appears more continuous and more similar to the OTI than the simulation without the ATIs. The first- and second order statistics are evaluated and compared to the same statistics for the OTI. Figure 3.14 shows a fair reproduction of OTI's histogram and variogram in the 25 realizations produced with ATIs.
In addition to improving HD reproduction, the simulation with ATIs also improves the reproduction of the histogram of the reference image with the HD. Fig. 3.15 shows the χ^2 statistics distribution for 50 conditional realizations (using 100 HD), obtained with and without ATIs. Clearly, the statistics are significantly lower with the ATIs. A similar result was obtained also by comparison to the OTI distribution (not shown).

Frequency of use of the ATIs

For the continuous case (Fig. 3.13), the involvement of ATIs in the simulation is measured as the percentage of pasted patterns coming from an ATI (Fig. 3.16). When the ATI size is the same as the OTI (64×64), the involvement percentage increases as a function of the number of ATIs used and reaches eventually 100% (with 51 ATIs involved). On the other hand, using a single large ATI (448×448) enables also to reach 100%. These two combinations present

7. Correction made to a typo in the published paper.

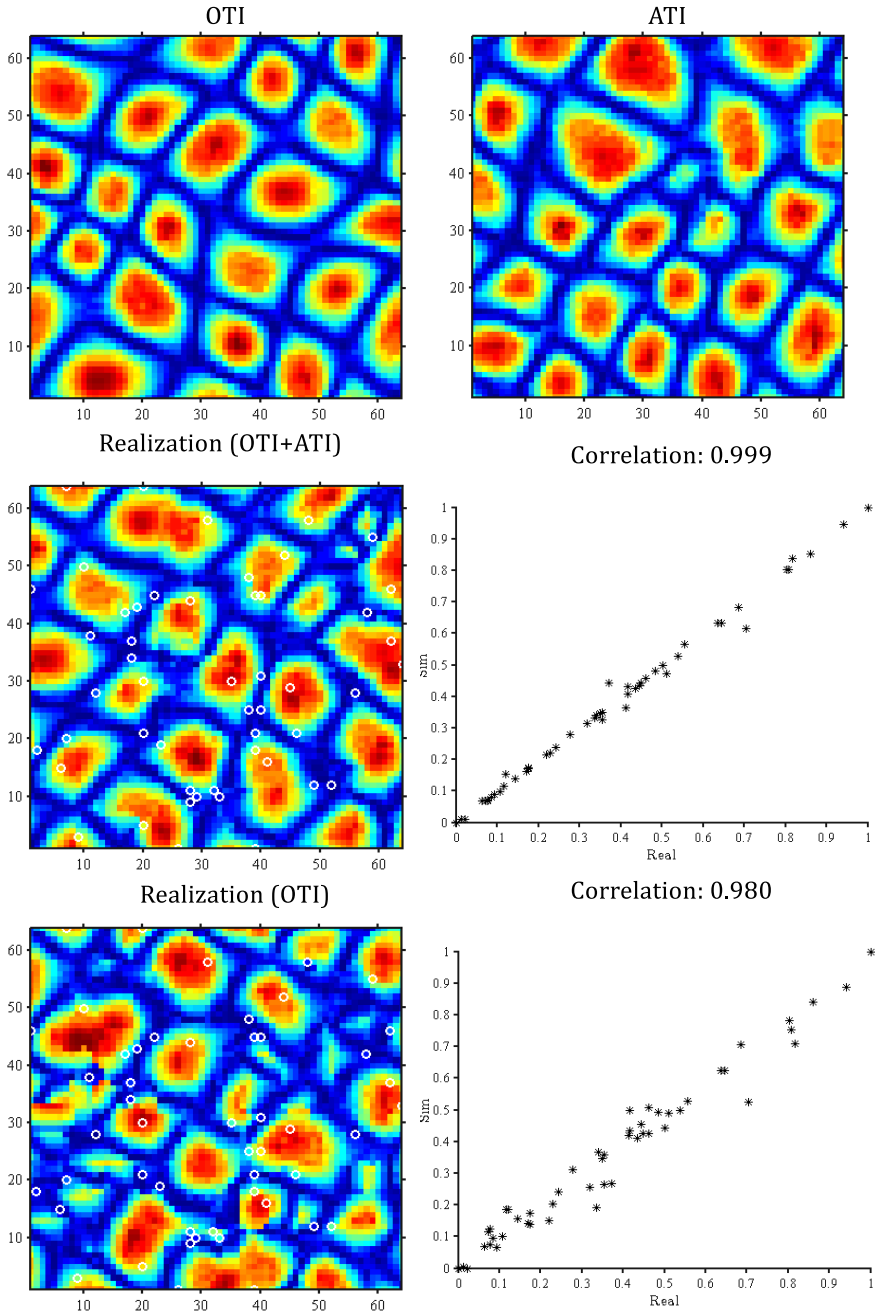

Figure 3.13 Simulation results for the continuous TI (T=8, OL=3), HD locations indicated by white circles.

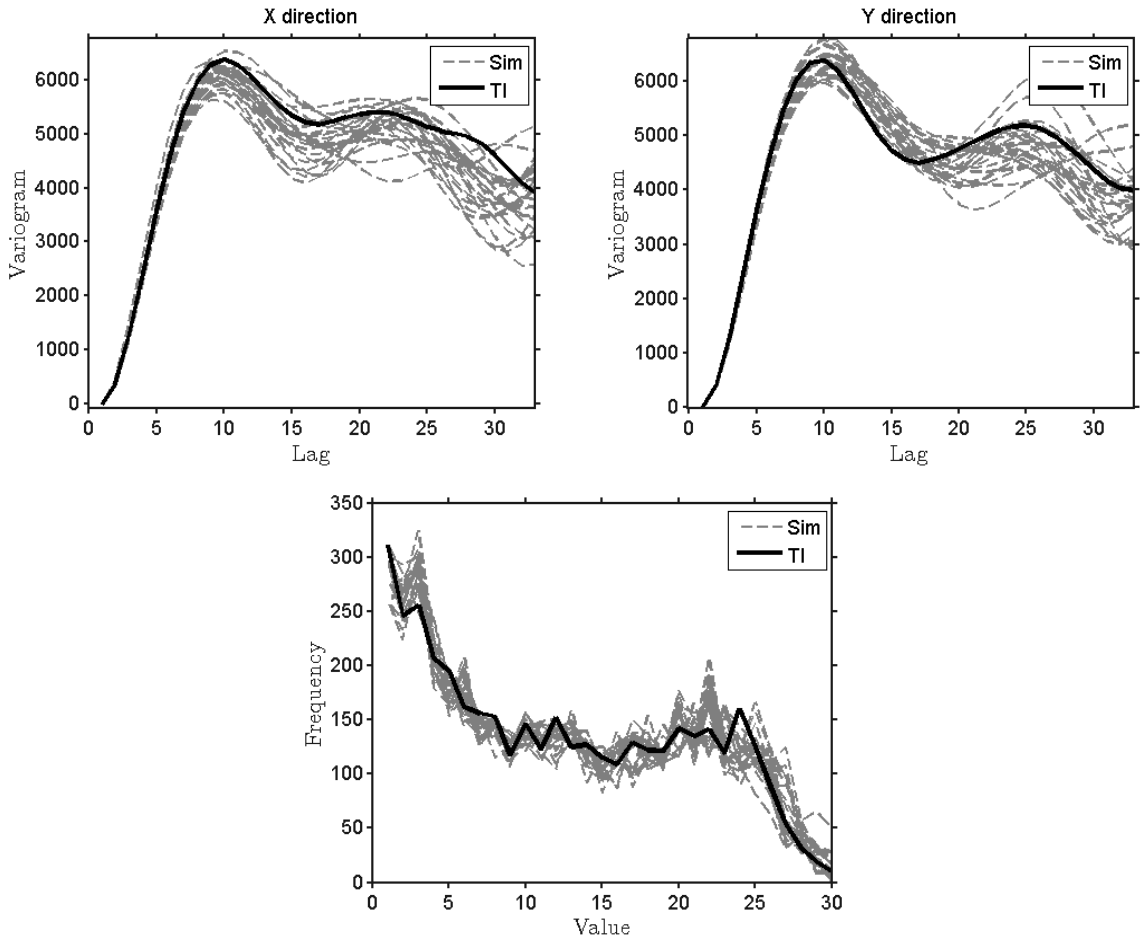

Figure 3.14 Histogram (bottom figure) and variograms along X and Y axis (top left and right respectively) of 25 realizations (light gray) and of the continuous OTI (black).

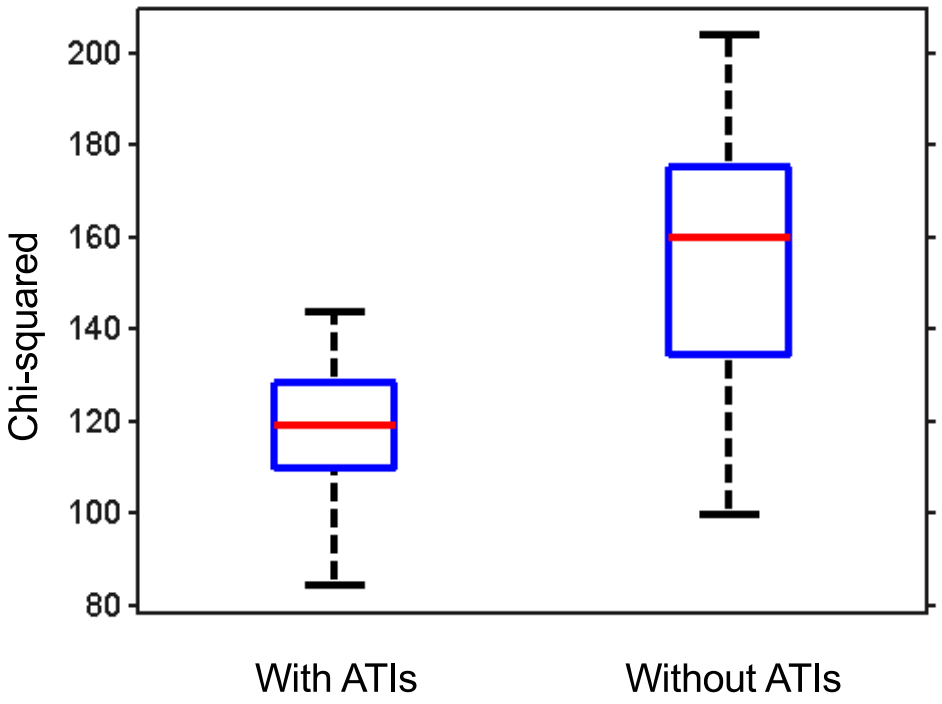

Figure 3.15 Box plot of the χ^2 statistics between the histogram of the reference continuous TI and the histograms of 50 realizations, conditional to 100 HD, obtained with and without ATIs.

similar total areas and hence similar number of available patterns.

Simulation using a very small TI

In many geological modeling problems, the available TI may not contain enough patterns to allow adequate HD reproduction. Figure 3.17 shows a small (26×26) OTI and its associated large ATI (600×600). With the ATI, the HD are well reproduced with a correlation coefficient of 0.995. Moreover, the simulated patterns propose a visually realistic generalization of the OTI. By comparison the simulation using only OTI shows a correlation coefficient of 0.945 with the HD. Moreover, some simulated patterns are quite different from those existing in the OTI.

3.4.2 Categorical TI

Two categories

The OTI is the classical channel image proposed by Strebelle (2002). A series of 73 unconditional realizations are retained in the database providing a minimum of 500 replicates for each HD pattern. Figure 3.18 shows the OTI, one of the unconditional ATIs and one conditional realization with 100 conditioning data. All the conditioning data are honored in both the simulation with and without ATIs. However, the simulation using only the OTI presents significantly more interrupted channels. Figure 3.19 shows that the X- and Y- variograms of the 15 realizations with ATIs are fairly close to the ones of the OTI.

Clustered HD

Clustered HD are problematic when only the OTI is used. The probability to retrieve a given dense pattern of HD data within an OTI is almost zero even when the OTI is deemed representative of the underlying phenomenon. With ATIs, the probability is increased as a function of number, size and variety of the ATIs considered. The likelihood of finding a significantly better match in the set OTI+ATIs is increased substantially.
Using the channel TI shown in Fig. 3.10-D, 25 realizations are produced with and without the ATIs. The ATIs database include 26 unconditional realizations of size 100×100. The e-type maps are shown in Fig. 3.20. Two areas identified as A and B are highlighted. Perfect HD reproduction entails that each channel HD (in red) should appear over a white pixel and each non-channel HD (in blue) should appear over a black pixel. The simulation with ATIs (A1 and B1) shows perfect HD reproduction. On the contrary, the simulation without ATI (A2 and B2) shows a channel HD over a dark gray pixel in A2 and two channel HD and one non-channel HD over gray pixels in B2.

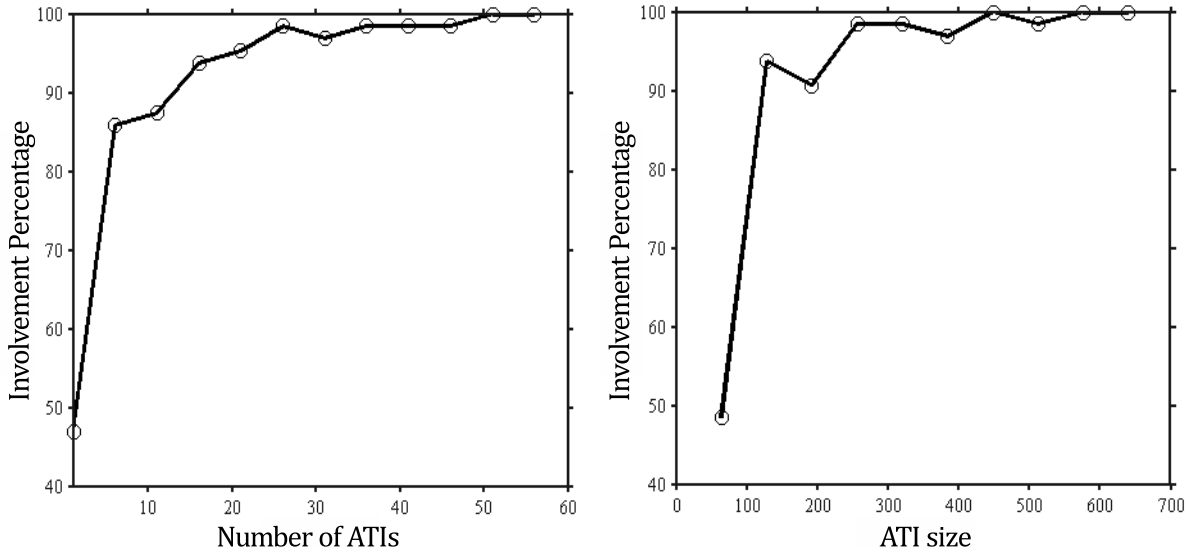

Figure 3.16 ATI involvement in simulation as a function of the number of (size 64 × 64) ATIs (left), or the size of a single ATI (right) for the continuous TI of Fig. 3.13. Values on X axis in right figure are the dimensions of ATI along both X and Y directions (e.g., 100 × 100 or 200 × 200). The simulations performed with T=6 and OL=2.

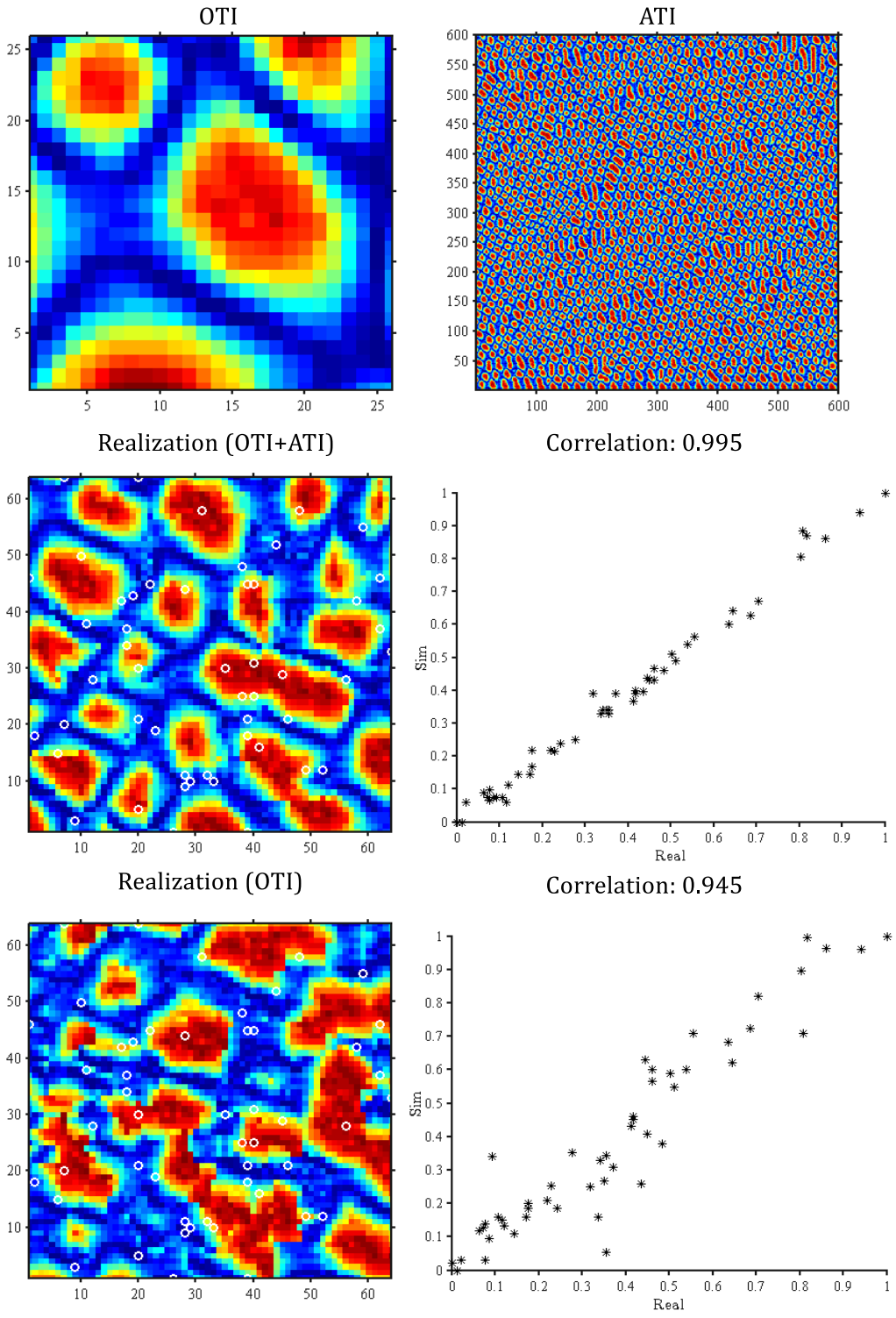

Figure 3.17 Simulation using a small TI with T=8 and OL=3

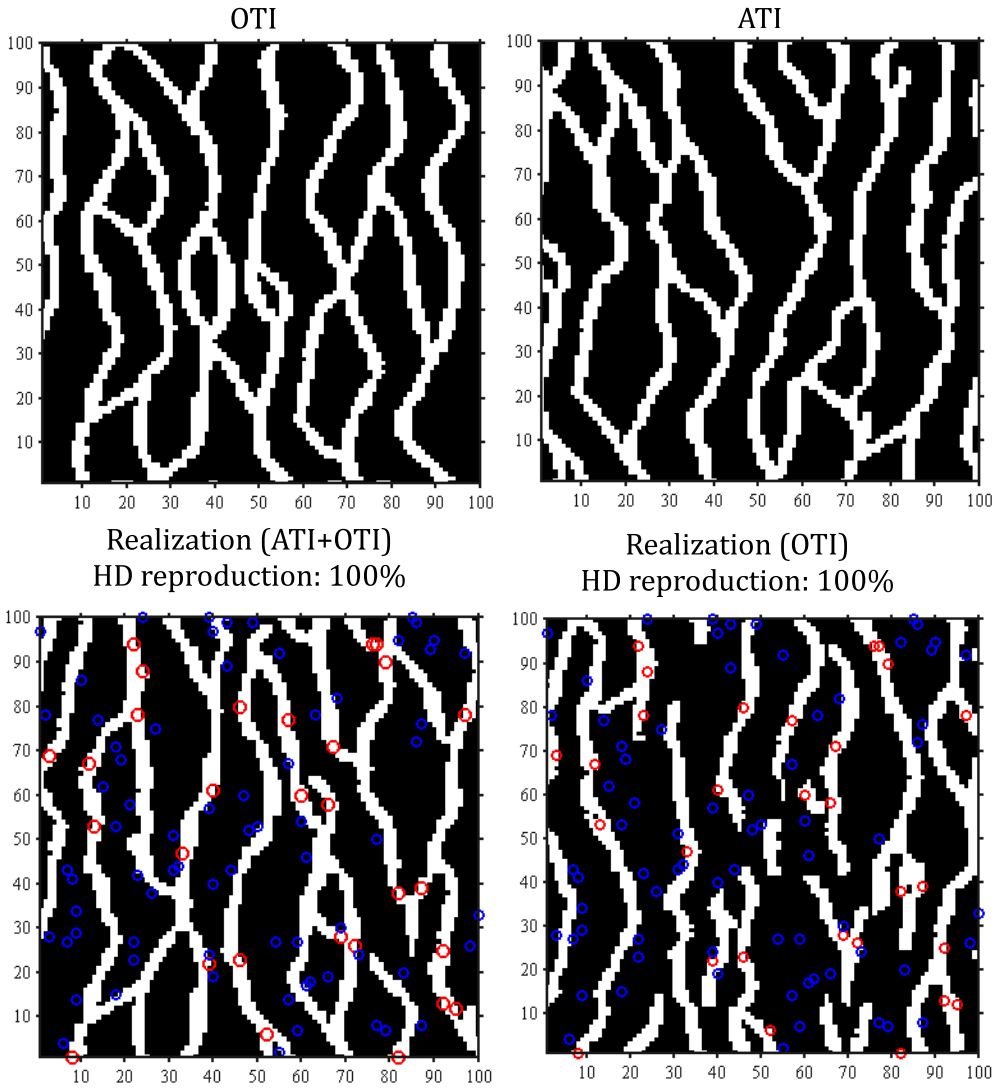

Figure 3.18 Simulation results for the channel image with $T = 15$, and $OL = 5$. Red circles HD belong to channels and the blue ones to non-channel facies

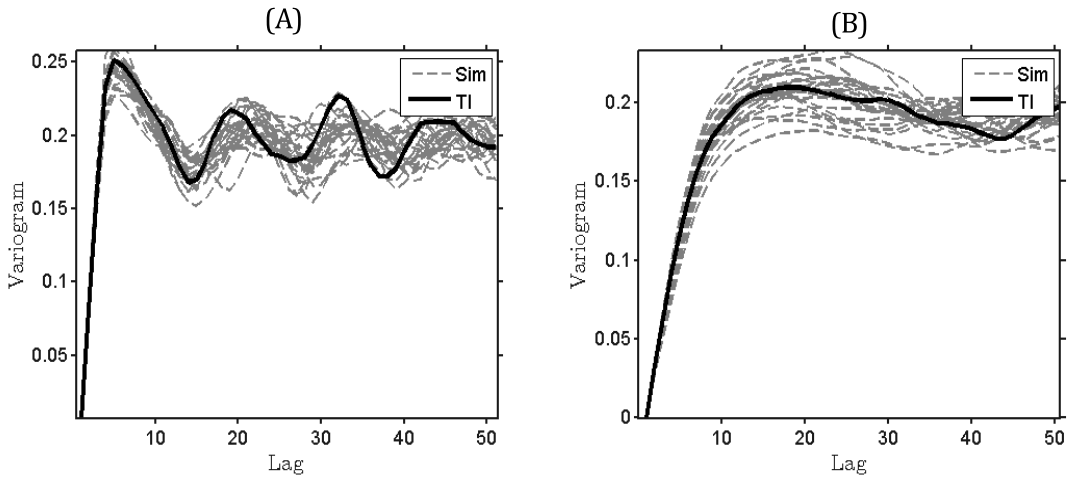

Figure 3.19 Variograms along X direction (A) and Y direction (B) for the 25 realizations (light gray) and the OTI (black), channel TI displayed in Fig. 3.9-D.

Three categories

Figure 3.21 shows a three-facies OTI (also shown in Fig. 3.9-C). Conditional simulations are performed using 125 HD taken from the reference image. The ATI used is a single large image of size 700×700 obtained by unconditional unilateral simulation with weighting and decoupage. Two sample realizations with and without the ATI are displayed on Fig. 3.21. Although both sets of realizations possess a few disconnected channels not present in the OTI, the texture and the main features of the OTI seem better reproduced when using the ATI. The average HD reproduction reaches 100% with the OTI+ATI compared to 98% with the sole OTI.

3.4.3 3D simulations

The 3D TIs shown in Fig. 3.9-E and F are used. The HD are sampled along vertical lines resembling the drill hole or well data in mining and petroleum real cases. A set of 11 and 10 ATIs are generated for the ball and the continuous TIs respectively. The set of OTI+ATIs provides [8] at least 50 matches for each HD configuration in the simulation grid. One sample simulation with ATIs and one without ATIs are shown in Fig. 3.22 and Fig. 3.23. For the

8. Corrected typo from the published paper.

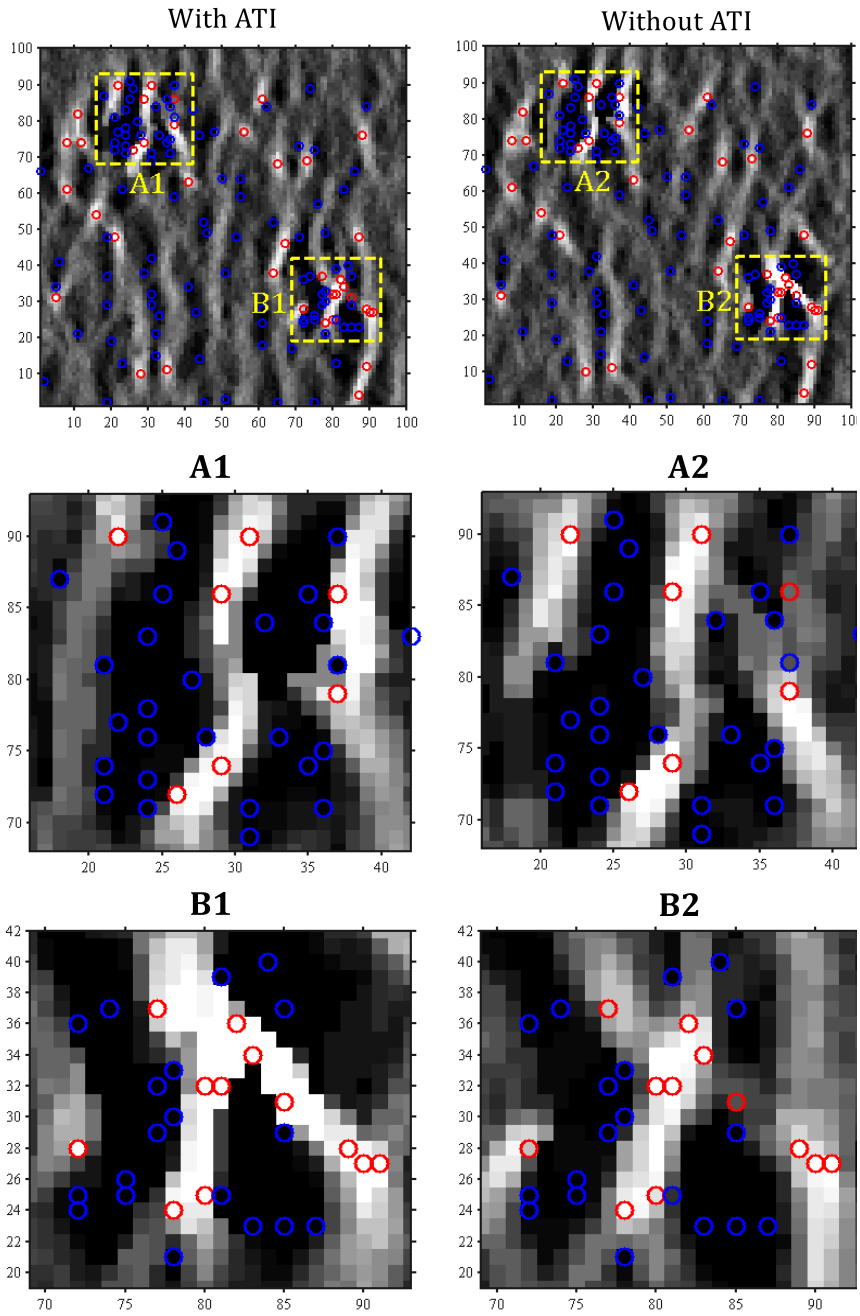

Figure 3.20 E-type maps of 25 realizations produced with and without ATIs, T=10, OL=3. OTI obtained from Fig. 3.18.

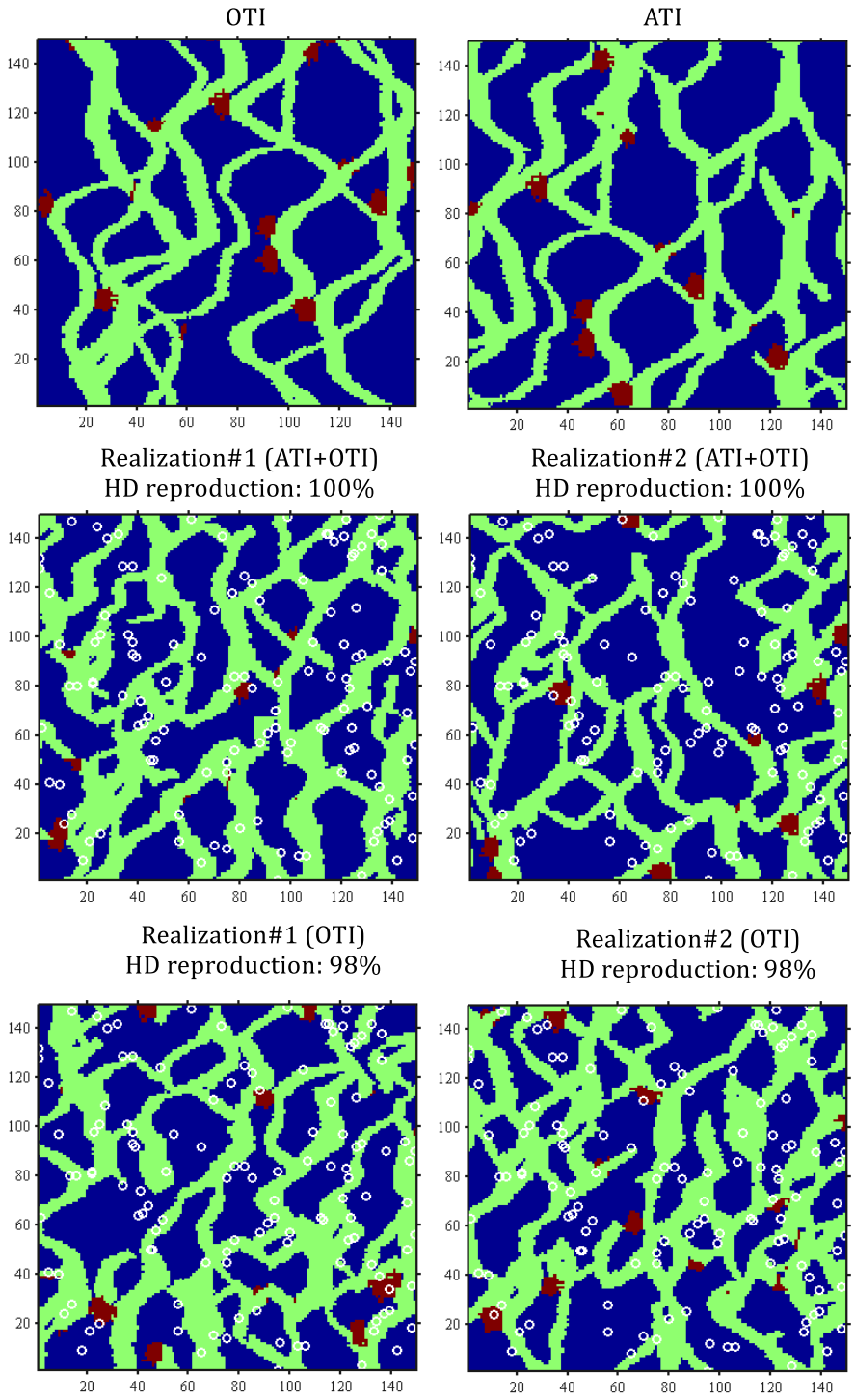

Figure 3.21 Simulation results using three-facies OTI with ATI (middle row) and without ATI (bottom row), T=17, and OL=6.

ball TI, the HD reproduction increases from 0.97 to 0.99, whereas for the continuous TI, the correlation grows from 0.95 to 0.98. More important, close examination of the simulated parallepiped shows the balls in the top figure are better formed with the ATIs than without. Also the continuity of the patterns in the continuous case appears slightly improved with the ATIs.

3.4.4 CPU Time

Computation time is one important factor in MPS simulation influencing the practicality of the MPS approach for 3D domains. The dashed line in Figure 3.24 (top row) shows the CPU time as a function of the TI size for a simulation grid 64×64 in 2D and $50 \times 50 \times 50$ in 3D. The solid line shows the CPU time as a function of the number of pixels in the simulation grid for a TI of size 64×64 in 2D and $50 \times 50 \times 50$ in 3D. In both cases, the times reported are for a single realization and the simulation is done using only the OTI. As expected, the CPU time increases linearly with the number of pixels in the simulation grid and in the TI. The bottom figure shows a linear growth with the number of ATIs used in the 3D case. The size of ATI and simulation grid in bottom figure are both $100 \times 100 \times 100$. Hence, the computing time for one million voxels with 10 ATIs is approximately 10 minutes per realization, which is deemed realistic for applications. Based on a few 3D tests, usually a set of < 10 ATIs suffices to obtain 50 matching patterns for each HD configuration. For many realizations, it is possible to parallelize the code such as to generate all realizations simultaneously.

3.5 Discussion

The proposed approach based on ATIs enables, in the examples presented, to ensure perfect HD reproduction in the categorical case and arbitrary close HD reproduction in the continuous case. The better HD reproduction is accompanied with visually better continuity in the simulated images compared to the conditionally simulated images obtained using only the OTI (see Figs 3.13, 3.17, 3.18, and 3.21). Moreover, the conditional images obtained with ATIs present textures and structures visually more similar to the OTI than the ones obtained using only the OTI. The statistics of the first two orders (histogram and variogram) of the OTI are well reproduced by the conditional simulations obtained with the ATIs (see Fig. 3.14). The approach was proven applicable even in the difficult case where only a small OTI is available (Fig. 3.17). The approach was also successful in the case with numerous clustered HD, a situation where classical patch-based approaches usually fail to reproduce HD (Fig. 3.20).

No effort was devoted to control the local mean histogram following the approach proposed

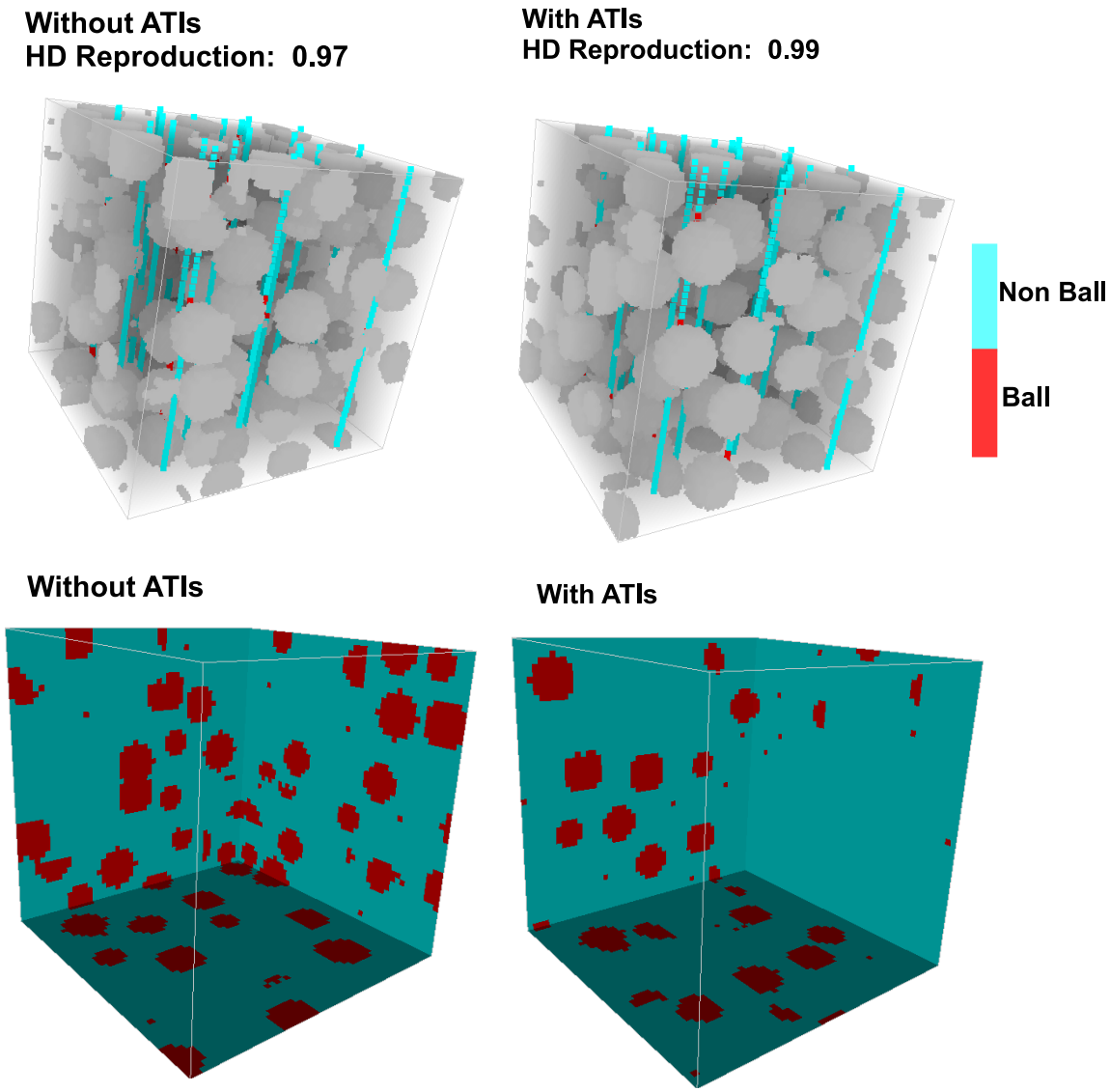

Figure 3.22 Simulation results using 3D ball TI with T=15, and OL=5.

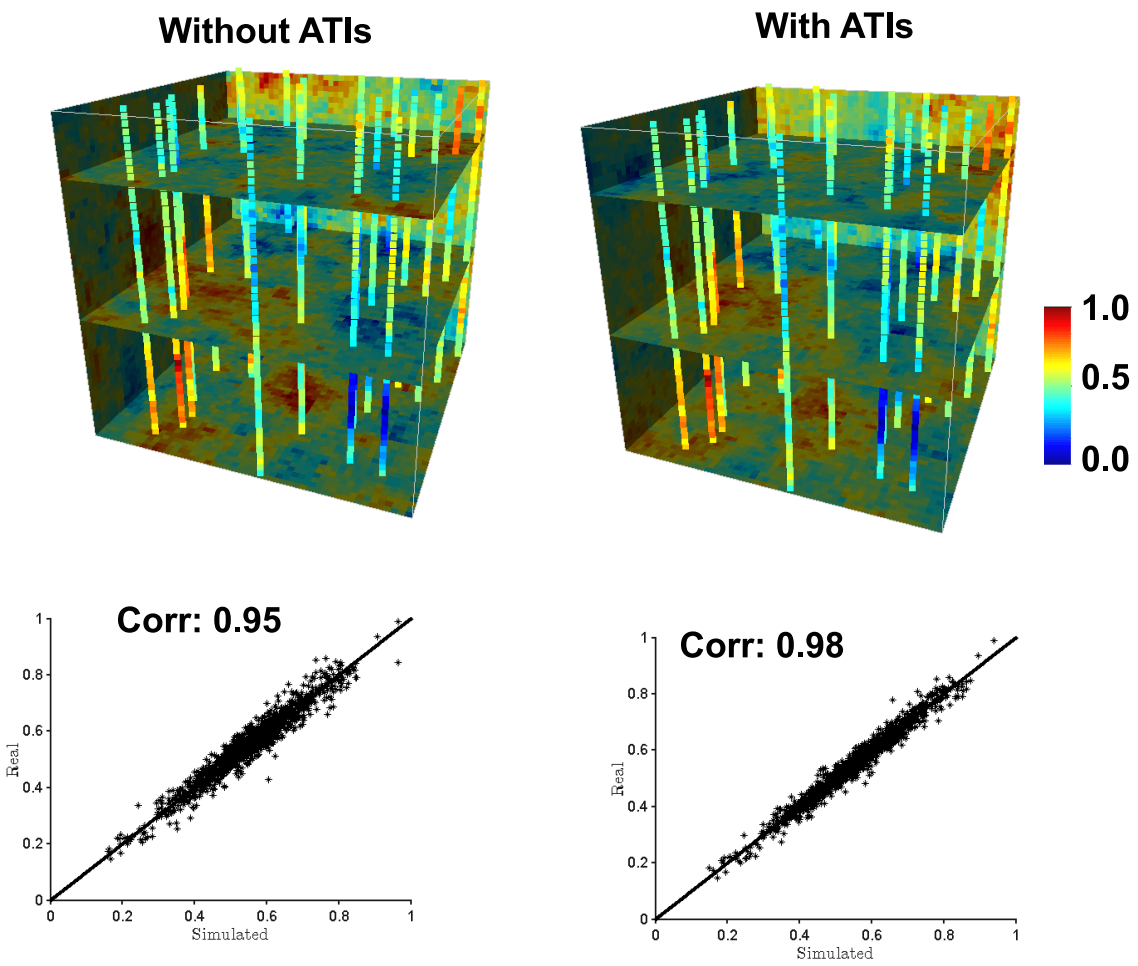

Figure 3.23 Simulation results using continuous 3D TI with T=15, and OL=5.

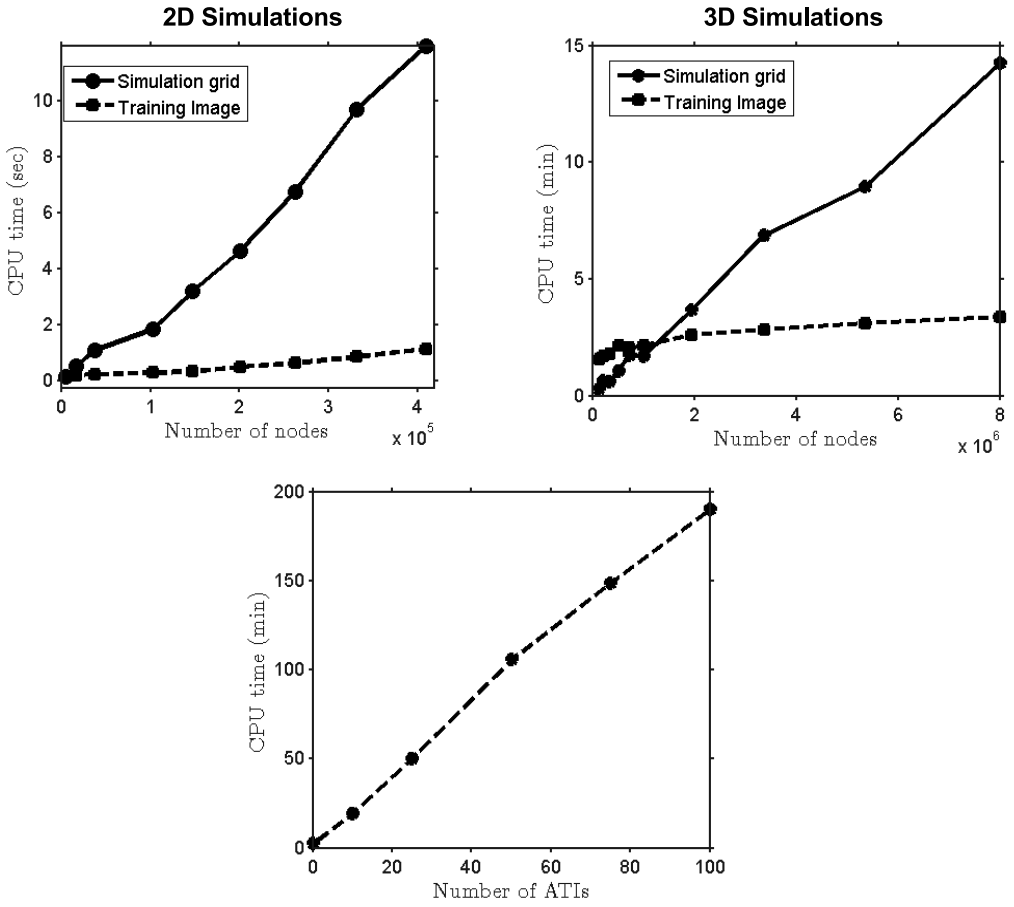

Figure 3.24 CPU time. Top row, left, dashed line: 2D simulations, ATI size varies and simulation grid size is fixed at 64×64; solid line: simulation grid varies and TI size is fixed at 64×64. Top row, right, dashed line: 3D simulations, ATI size varies and simulation grid size is fixed at $50 \times 50 \times 50$; solid line: simulation grid varies and TI size is fixed at $50 \times 50 \times 50$. Bottom row: the number of ATIs varies, each ATI and simulated field of size $100 \times 100 \times 100$. For 2D simulations $T = 10$ and $OL = 4$; for 3D simulations, $T = 15$ and $OL = 5$.

by Faucher et al (2013) and Faucher et al (2014). In the unconditional case, it is interesting to allow ATIs statistics to fluctuate around the OTI, hence control of the local-mean histogram was not deemed desirable. In the conditional case, the large number of HD data helps to fix the statistics without recourse to further control. However, with less HD, the control of the local mean histogram might be considered. Moreover, we note that the approach proposed by Faucher et al (2013) could be used to impose purposely a local mean histogram different from the available OTI. This will allow to generate ATIs with different densities of objects, but still with similar textures to the OTI. This approach was not tested here.

A twofold strategy was described to accept/reject ATIs sequentially based on a χ^2 test on the OTI histogram reproduction, a Bonferroni t-test on the OTI variogram equality and a test on the OTI object size distribution. Only the ATIs passing all the tests were then checked for their contribution to the pattern database. The ATIs showing at least n HD patterns were kept, the others were discarded. The series of tests applied in the first step were rejecting ATIs showing visible differences with the OTI (see Fig. 3.12). The acceptance/rejection can be done efficiently due to the fast distance computation with convolutions. In addition, a stopping criteria is proposed to determine when to cease considering new ATIs. This initiates the conditional simulation phase using the database composed of the OTI and all the accepted ATIs. The method of selection of ATIs is greedy and sequential. As a consequence, it does not result as the best possible set of p among n ATIs. More evolved selection algorithms could possibly be used to select a globally better susbet of ATIs, but the time required to do this optimization has to be considered and may not be worth the effort. This is subject of future research.

The proposed method is not free of artifacts. Although less numerous than with only the OTI, some interrupted channels were still present in some realizations of the channel example (Fig. 3.18). The artifacts can be diminished further by considering larger simulation windows (T and OL) or a larger set, or a more diverse set of ATIs.

Indeed, some directional effects linked to the use of a unilateral path can be expected (see El Ouassini et al, 2008 and Faucher et al, 2013). However, this inconvenient is counterbalanced by the better continuity between patches compared to the random path. Moreover, decoupage can be applied easily in the unilateral case whereas its extension to the general random case (where patch centroid can be located at any pixel) is not obvious. However, a random path over a regular subset of square overlapping patches has been proposed by Faucher et al (2014) where decoupage can also be applied easily. In some cases this approach did not produce realizations with the same continuity and the same similarity to the OTI as the unilateral path, so we did not considered it further.

As for all multipoint methods, the OTI must show features that are not totally incompatible

with the observed HD. For the categorical case, one possible useful extension to our approach is to complement the ATI database by images obtained by methods ensuring exact conditioning (e.g. by truncated Gaussian or plurigaussian methods Armstrong et al, 2011), sequential indicator simulation (SIS), Bayesian Maximum Entropy (BME) or Markovian-type categorical prediction (MCP) (Allard et al, 2011). These additional ATIs should be considered as an emergency set to be used only when a given HD pattern is unavailable in the set of ATIs produced by the methods described in this paper. The same idea can be extended to the continuous case by using Gaussian simulated images as an emergency extra ATI database.
The CPU time for 2D simulations has not been a problem since the main simulation benefits from the fast calculation of distance using convolutions. It is clear that the computing time increases linearly with the size of the simulated field (measured in number of pixels), and the size and number of ATIs. Figure 3.24 indicates that a simulated field of one million nodes with 10 ATIs, each ATI being also of size one million nodes, can be obtained on a laptop (with I7 processor) in 10 minutes, which remains a realistic time. This computing time excludes the pre-processing time to construct the ATI database. The latter depends of the number of trial ATIs and thus of the number of HD and the compatibility between the HD and the OTI. The pre-processing step is done only once no matter the number of realizations. Moreover, the use of an emergency subset of ATIs obtained by a method ensuring exact conditioning would enable to limit the number of tested ATIs to a reasonable value.
The proposed approach of simulations with ATIs was tested over a real mining case with a TI representing 3D dyke structure (the TI is described in Rezaee et al, 2014). As expected, the simulation results were improved with ATIs both in terms of the continuity of dykes and of the conditioning to available borehole data. The results are not shown as it would increase the length of the paper without adding much to the conclusions of the article. Moreover, they would divert readers' attention from the main scope of the paper which is above all methodological.

3.6 Conclusion

The proposed simulation approach preserves the qualities of patch-based approaches but improves significantly on the HD reproduction, the main strength of the point based approach SNESIM. Hence, in the categorical case, conditional categorical images honoring perfectly all the HD can be obtained, even when numerous clustered HD are present or when only a small OTI is available. In the continuous case, arbitrarily small differences with the HD values can be achieved. The conditional simulation examples presented show similar continuity, texture, structure, histogram and variograms, to those found in the OTI. The results obtained with

OTI+ATIs are consistently better than those obtained using only the OTI. An objective strategy to generate and select ATIs was proposed and tested.

3.7 Acknowledgements

This research was financed by the NSERC grant of D. Marcotte. Comments from two anonymous reviewers were helpful to improve the manuscript.

CHAPTER 4

ARTICLE 2: INTEGRATION OF MULTIPLE SOFT DATA SETS IN MPS THRU MULTINOMIAL LOGISTIC REGRESSION: A CASE STUDY OF GAS HYDRATES

Hassan Rezaee [1], **Denis Marcotte.**

Stochastic Environmental Research and Risk Assessment

DOI 10.1007/s00477-016-1277-8

Published online: 07 June 2016
©Springer-Verlag Berlin Heidelberg 2016

4.1 Abstract

A new approach is described to allow conditioning to both hard data (HD) and soft data for a patch- and distance-based Multiple-Point Geostatistical simulation. The multinomial logistic regression is used to quantify the link between HD and soft data. The soft data is converted by the logistic regression classifier into as many probability fields as there are categories. The local category proportions are used and compared to the average category probabilities within the patch. The conditioning to HD is obtained using alternative training images and by imposing large relative weights to HD. The conditioning to soft data is obtained by measuring the probability-proportion patch distance. Both 2D and 3D cases are considered. Synthetic cases show that a stationary TI can generate non-stationary realizations reproducing the HD, keeping the texture indicated by the TI and following the trends identified in probability maps obtained from soft data. A real case study, the Mallik methane-hydrate field, shows perfect reproduction of HD while keeping a good reproduction of the TI texture and probability trends.

1. H. Rezaee, D. Marcotte Department of Civil, Geological and Mining Engineering, Polytechnique Montreal, C.P. 6079, Succ. Centre-ville, Montreal, QC H3C 3A7, Canada, e-mail: hassan.rezaee@polymtl.ca

4.2 Introduction

Soft data, also called secondary data, are typically low resolution data sets useful to (*i*) deal with non-stationarity and (*ii*) improve estimation of the primary variable (Lee, 2005). As an example, in reservoir characterization the primary variable is typically the geological facies observed in boreholes and the soft data correspond to elastic properties, P-impedance, S-impedance or ratio of compressional to shear wave velocities (V_p/V_s) obtained from inverted seismic amplitude data (Xu et al, 1992; Almeida et al, 1993).

In traditional variogram-based geostatistics (Goovaerts, 1997) non-stationarity is coped in two main ways: first, by adding a secondary variable into the kriging engine (e.g. as an external trend or as an additional variable in cokriging) and second by considering the variogram itself as non-stationary (e.g. by using variograms with spatially varying anisotropies and parameters) (Higdon et al, 1999; Paciorek and Schervish, 2006; Stein, 1999; Liang and Marcotte, 2016; Rivest and Marcotte, 2012; Shamsipour et al, 2013). In Multiple-Point Statistics (MPS) simulation method (Guardiano and Srivastava, 1993; Strebelle, 2002) the random function is modeled via a Training Image (TI) assumed stationary, a disadvantage (de Vries et al, 2009) in real applications where the facies proportions and arrangements often vary spatially. One possible solution mentioned by Arpat and Caers (2007) is to decompose the variable into a trend and a residual where the trend comes from the soft data. A second solution is to consider one rich and large TI bearing repetitions of not only the textures/structures/patterns but also of the trends. Non-stationarity has been handled with auxiliary variables as in Chugunova and Hu (2008) or in a multivariate framework as in Mariethoz et al (2010). Moreover, Mariethoz et al (2015) use probability maps to account for non-stationarity in the pixel based Direct Sampling (DS) approach.

MPS methods can be classified as pixel-based or patch-based according to the number of nodes that are simulated in each step. Among the pixel-based methods SNESIM (Strebelle, 2002) and IMPALA (Straubhaar et al, 2011) draws the simulated value from the conditional probabilities extracted from the TI whereas Direct Sampling (DS) (Mariethoz et al, 2010) draws among the patterns showing a distance less than a predefined threshold. The patch-based approach can be applied following a unilateral path as in (Pickard, 1980; Daly, 2005; El Ouassini et al, 2008; Faucher et al, 2013, 2014) or following a random path as in SIMPAT (Arpat and Caers, 2007) or Bunch DS (Rezaee et al, 2013).

Mariethoz et al (2010) used a two-terms distance function that computes the distance between the joint data event on the primary and soft data. However, this forces the simulation to correlate to the soft data even when the soft data is not informative. Moreover, the TIs for the primary and the secondary variables are both needed and these must be related,

implying that some form of forward model is available to produce the soft data TI from the primary variable TI. Alternatively, the set of primary and soft data TIs might be available from a different area showing a similar geological context. Mariethoz et al (2015) proposed in the frame of DS to compute a composite distance formed of two terms: a distance based on the primary data event and a distance between proportions in the patterns and the local probabilities of facies. The distance term on proportions however is used only in the beginning of the simulation to avoid introducing at later steps discontinuities in facies arrangements. These discontinuities introduced at later steps are, at least in part, due to the pixel-based nature of DS and cannot be avoided completely.

Computation of category or facies probabilities from a series of soft data sets can be achieved using a variety of methods, including discriminant analysis (Wong et al, 1995), multinomial logistic regression (Al-Mudhafer, 2014), neural networks (Caers and Ma, 2002; Wong et al, 1995) and Bayes classification. Among these methods, multinomial logistic regression appears simpler than neural networks and Bayes classification and more general than discriminant analysis. A transverse study based on 72 articles has shown globally equivalent performances of neural networks compared to logistic regression (Dreiseitl and Ohno-Machado, 2002). Also, many studies report better performance of logistic regression compared to discriminant analysis when the multiGaussian hypothesis is not respected (e.g. Pohar et al (2004); Press and Wilson (1978)).

In this study we use patch-based MPS simulations with a unilateral sweeping (El Ouassini et al, 2008; Faucher et al, 2013; Rezaee et al, 2015). This choice is motivated by the superior pattern and texture reproduction capabilities of patch-based approaches. As in Mariethoz et al (2015), we use a two terms distance function. The first term is the usual mismatch distance which records the number of facies mismatch between the TI and the already simulated points and HD within the simulation window. The second term measures the difference of facies proportions between the whole patch to paste from the TI and the average probabilities of facies within the simulation window. The probabilities are obtained from the soft data by multinomial logistic regression (Dobson and Barnett, 2008; Hosmer Jr et al, 2013) of the HD with the soft data. The average conditional probabilities within the simulation window give the expected proportions of each facies. Note that in our approach, the local continuity is ensured due to the use of patches with unilateral sweeping. Moreover, the probabilities are obtained after calibration of soft data to the primary variable known at HD points. In absence of correlation, the local proportions estimate will be invariant throughout the whole simulated field and simply coincide with the global proportions found for all the HD. On the contrary, in case of strong correlation, the local probabilities will vary spatially with the soft data. We stress that many (p) different soft data sets can be used simultaneously as

they are all merged thru multinomial logistic regression in probability estimates for the k facies to simulate. Moreover, as in Chugunova and Hu (2008) and Mariethoz et al (2010) our approach can be applied without any HD provided either a forward model is available to compute pseudo-soft data from the primary variable TI or linked primary-soft data TIs are directly available from an analogous geological context.

4.3 Methodology

Our methodology comprises two main steps. The first step is a pre-simulation step allowing to get by multinomial logistic regression the probability fields for each category. The second step is the patch-based MPS using a composite distance. The first distance term measures the match between TI with previously simulated parts and/or HD and the second term measures the distance between proportion of each category in the patch and the average local probabilities obtained by multinomial logistic regression. These two distance terms are weighted automatically using the McFadden pseudo-R^2 (McFadden, 1973) so as to give more weights to the probability fields when the multinomial logistic regression reveals a strong link between categories and soft data.

4.3.1 Getting the probability fields

The first step involves the regression of HD to soft data to calculate the probability fields per category. The multinomial logistic regression model (Dobson and Barnett, 2008) is used to calculate the probability fields. Different variants can be used: nominal, ordinal or hierarchical. In this paper, the ordinal option is taken as it corresponds to a simpler model where all logistic regressions are imposed to be parallel, thus minimizing the number of coefficients in the model. Taking the last (K) category as the reference category, the category probabilities in this variant are given by:

$$\begin{aligned} P(1|\mathbf{x}) &= \frac{\exp[b_1 + \mathbf{b}'\mathbf{x}]}{1 + \exp[b_1 + \mathbf{b}'\mathbf{x}]} \\ P(k|\mathbf{x}) = \frac{\exp[b_k + \mathbf{b}'\mathbf{x}]}{1 + \exp[b_k + \mathbf{b}'\mathbf{x}]} &- \sum_{j=1}^{k-1} P(j|\mathbf{x}) \text{ for } k = 2...K-1 \\ P(K|\mathbf{x}) &= 1 - \sum_{k=1}^{K-1} P(k|\mathbf{x}) \end{aligned} \tag{4.1}$$

where $\mathbf{b}$ is the vector of common regression slope coefficients, b_k is the constant for category k and $\mathbf{x}$ is the vector of soft data at a given location. Whatever the number of soft data sets, the logistic regression results in a set of k different probability fields summing to one as

in Fig. 4.1 and Fig. 4.2. We stress that the probability fields obtained are by construction calibrated to HD.
The number of HD required to do the multinomial logistic regression is likely to depend of the particular data at hand and of the strength of the link between categories and soft data. When there is an insufficient number of HD to do the multinomial logistic regression, one needs an approximate or exact forward model to apply to the TI in order to get pseudo soft data for the logistic regression. Geological examples where such forward models are available are numerous: block averages, seismic amplitudes given the impedance field, pressures for a given conductivity field and stress applied, gravity field corresponding to facies with different densities, etc. Alternatively, one can borrow linked primary-soft data TIs from an analogous geological context.

4.3.2 Simulating using MPS

Our method is patch-based (Arpat and Caers, 2007; El Ouassini et al, 2008; Rezaee et al, 2015; Faucher et al, 2013, 2014) and uses distance functions and a unilateral path. Borrowed from texture synthesis field we also use the quilting (Efros and Freeman, 2001) idea to improve continuity when pasting a patch in the simulated image. Using a patch and overlap area with specified sizes, the simulation loop repeats over all patch locations along a unilateral path. Half of the realizations are obtained by following an horizontal path, half following a vertical path, as suggested by Tahmasebi et al (2014). The size of patch are also varied between an upper and lower limit ($\pm$ one pixel of the nominal patch size along each direction). The data event at each patch location includes both previously simulated and secondary data including soft and/or HD. Unlike the method used in Chugunova and Hu (2008) or SIMPAT (Arpat and Caers, 2007) that builds a search tree as in SNESIM, here the whole TI is scanned for the matching pattern at every iteration of the simulation. The computations are very efficiently performed either in the spatial domain for small patches or in the spectral domain for larger patches or in 3D (Tahmasebi et al, 2012; Marcotte, 1996). Hereafter, simulation window refers to the patch under simulation. It includes the overlap area with previously simulated patches and the area to simulate with HD eventually. To better capture the continuity, the patch size is usually selected larger when large scale structures are present in the TI (El Ouassini et al, 2008; Faucher et al, 2013).
The total distance D_T is constituted of two parts (Eq. 4.2). The first part, D_A, is computed as the facies mismatch between the candidate patch from TI and the HD and previously simulated points found within the current simulation window. The second part, D_S, is the distance between facies proportions for each candidate patch from TI and the average probabilities within the simulation window obtained from the soft data thru multinomial

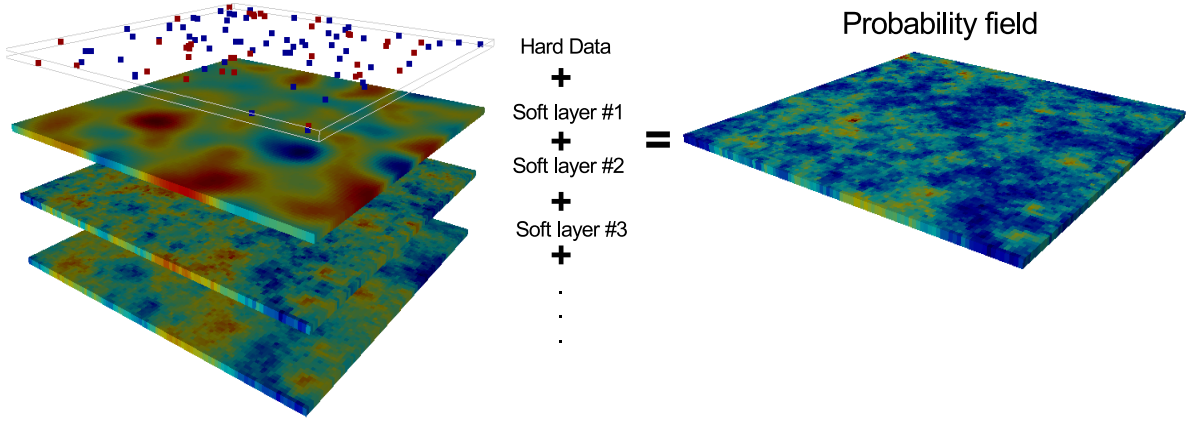

Figure 4.1 Right: Binary HD and three soft data sets; Left: Probability field obtained by multinomial logistic regression.

logistic regression.

$$D_T(x,y) = (1-\alpha)D_A(x,y) + \alpha D_S(x,y) \tag{4.2}$$

where α with $0 \leq \alpha \leq 1$ is a weighting factor to control the relative importance given to probabilities from logistic regression, and x and y are respectively the center of the window in the TI and in the simulated image. The distance D_A is computed as:

$$D_A(x,y) = 1 - \sum_{i=1}^{n} w_i I(TI(x_i - x), SI(y_i - y)) \tag{4.3}$$

where n is the number of informed pixels within the $N \times M \times L$ simulation window, w_i are weight factors (with $\sum w_i = 1$) used to favor reproduction of HD and continuity with the already simulated pixels in the overlap area (El Ouassini et al, 2008; Faucher et al, 2013), $I(\cdot,\cdot)$ takes the value 1 when the facies at point $x_i - x$ in the TI matches the facies at point $y_i - y$ in the simulated image SI. All the possible x patches within the TI are examined in turn for any given simulation window centered at y in SI. When all the weights are equal to $1/n$, D_A is simply the proportion of mismatch between facies in the simulation window and the corresponding locations in the TI.

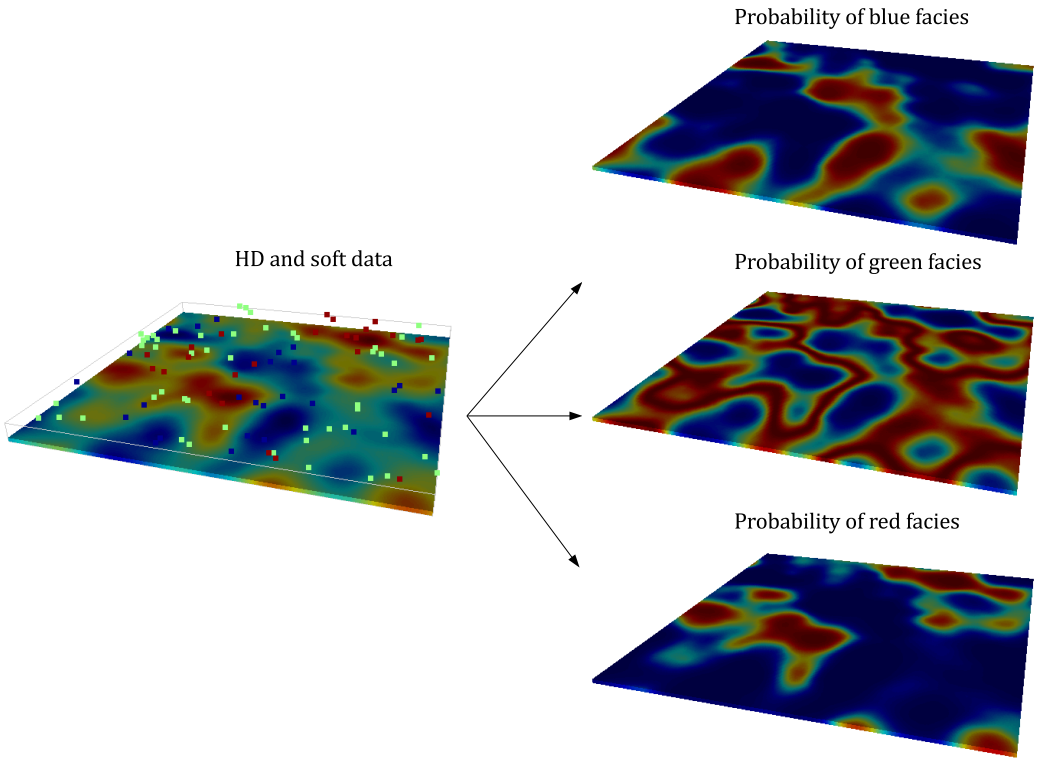

Figure 4.2 Left: HD and soft data map; Right: probability fields for three categories.

Distance D_S is defined as:

$$D_S(x,y) = \frac{1}{K}\sum_{i=1}^{K} |(p_{TI}(x;i) - p_{SI}(y;i))| \tag{4.4}$$

where K is the number of facies, $p_{TI}(x,i)$ is the proportion of facies i found within the patch centered at x in the TI and $p_{SI}(y;i)$ is the average probability for facies i computed from the multinomial logistic predictions at each pixel of the $N \times M \times L$ simulation window centered at y in SI. A similar distance was used in Mariethoz et al (2015), except that it was based on a L2 norm instead of a L1 norm. Note that both D_A and D_S are within the [0-1] interval. After computing the distances for all the patches in the TI, we choose randomly the patch to paste among the N_p patches with the smallest distances. In this study, the parameter N_p is selected in the interval [5-100], larger values being used when HD are present.

Which α?

The α weight controls the relative importance given to the probabilities computed from soft data by logistic regression. It seems logical to choose a larger weight when the link with the primary variable is strong. One frequently used statistic to measure the quality of the fit in logistic regression is the McFadden's pseudo R^2 (McFadden, 1973) which plays a similar role to the coefficient of determination R^2 in linear regression. McFadden's R^2 is computed as follows:

$$R^2 = 1 - \frac{log(L_c)}{log(L_0)} \tag{4.5}$$

where L_c is the likelihood of the full model fitted with the predictors (here the soft data), and L_0 is the likelihood for the null model having only the constant term. A high value of pseudo-R^2 indicates that the categories can be well predicted by the soft data. As $L_0 \leq L_c \leq 1$, the pseudo R^2 lies in the [0-1] interval. The likelihoods are computed as:

$$L_c = \prod_{i=1}^{n} P(HD_i|\mathbf{s}) \tag{4.6}$$

$$L_0 = \prod_{i=1}^{n} p(HD_i) = \prod_{k=1}^{K} p_k^{n_k} \tag{4.7}$$

where n_k is the number of HD in category k, $n = \sum_{k=1}^{K} n_k$ is the total number of HD used in the multinomial logistic regression, $P(HD_i|\mathbf{s})$ is the probability to observe category HD_i given the soft data $\mathbf{s}$ at the same point, and $p(HD_i)$ is the proportion, in the HD set, of category observed at HD_i.

4.3.3 Influence of the logistic regression

Logistic regression seeks to identify and quantify the link between soft data and the HD. In absence of any link, the probability fields are simply equal to the proportion of each facies in the HD. The stronger the link, the more contrasted are the probability fields. Figure 4.3 shows an example of three states of weak ($\alpha = 0.12$), medium ($\alpha = 0.31$) and strong ($\alpha = 0.68$) correlation between HD and soft data. Fifty realizations conditioned to the soft and HD were obtained. The soft data identified as Soft1 in the top row is a random Gaussian field simulated independently from the HD. In the simulations we have used 5 Alternative TIs (ATIs) as in Rezaee et al (2015) to a better reproduction of of HD and patterns. Soft2 is a smoothed model obtained from the reference image displayed on the top row. The size of the moving average window controls the correlation between the output smoothed image and the HD taken from the reference model. The size of the window is 23, 13 and 6 for weak, medium and strong correlations respectively. Soft1 and Soft2 are both used in the logistic regression to calculate the probability fields shown in the middle column. The p-values (Fisher et al, 1960) for [Soft1, Soft2] data sets are [0.98, 2.6e-5], [0.81, 1.9e-9] and [0.86, 0.02] for cases with weak, medium and strong correlation, respectively. As expected, logistic regression found non-significant Soft1 coefficients whereas Soft2 coefficients are significant for the three cases considered. The e-type maps of each facies were compared to their corresponding probability fields, the correlations for [black, gray, white] facies are [0.43, 0.33, 0.22], [0.68, 0.51, 0.47] and [0.72, 0.63, 0.62] for cases with weak, medium and strong correlation, respectively. The correlations between e-type and probability fields slightly increase with stronger HD-soft data correlation as measured by the pseudo-R^2 (or α).

4.4 Simulation Results

As a simple example, the ball TI is used (Fig. 4.4). The reason to choose such a simple unrealistic TI is that it allows easy visual inspection of any potential problem with the algorithm. Figure 4.4 shows four sample simulations using different probability fields. In all cases, most of the balls are well formed and their density follows the general trends of the probability fields.

For a less trivial case, the TI with dune structures is used (See Fig. 4.5). A number of 25 realizations are generated conditional only to the probability fields. The e-type maps are [2] calculated per facies and compared to the corresponding probability field. For all facies, the e-type maps correlate [3] well with the probability fields and the main structures of the TI

2. Corrected typo from the published paper.
3. Corrected typo from the published paper.

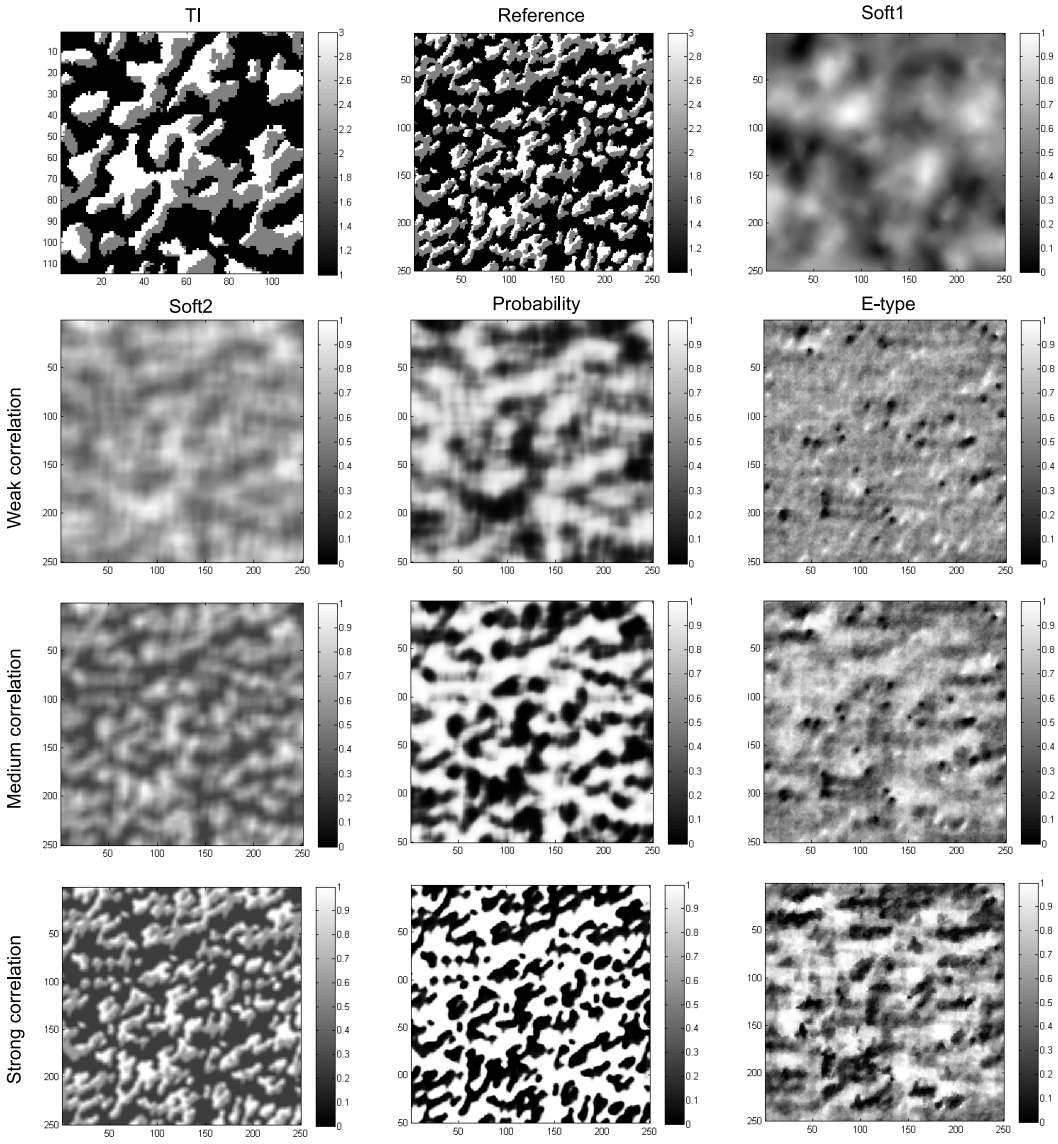

Figure 4.3 The TI used to generate the reference model on top row. Left column: original soft data used as input in logistic regression; middle column: probability of facies 1 (black); right column: e-type map of facies 1 of 50 realizations based on the probability fields. Note the HD are not displayed on the figure, but they are used in all the simulations. Input parameters: weak case: α=0.12, medium case: α=0.31, strong case: α=0.68. Average patch size and overlap width are 15 and 5 respectively. $N_p = 10$.

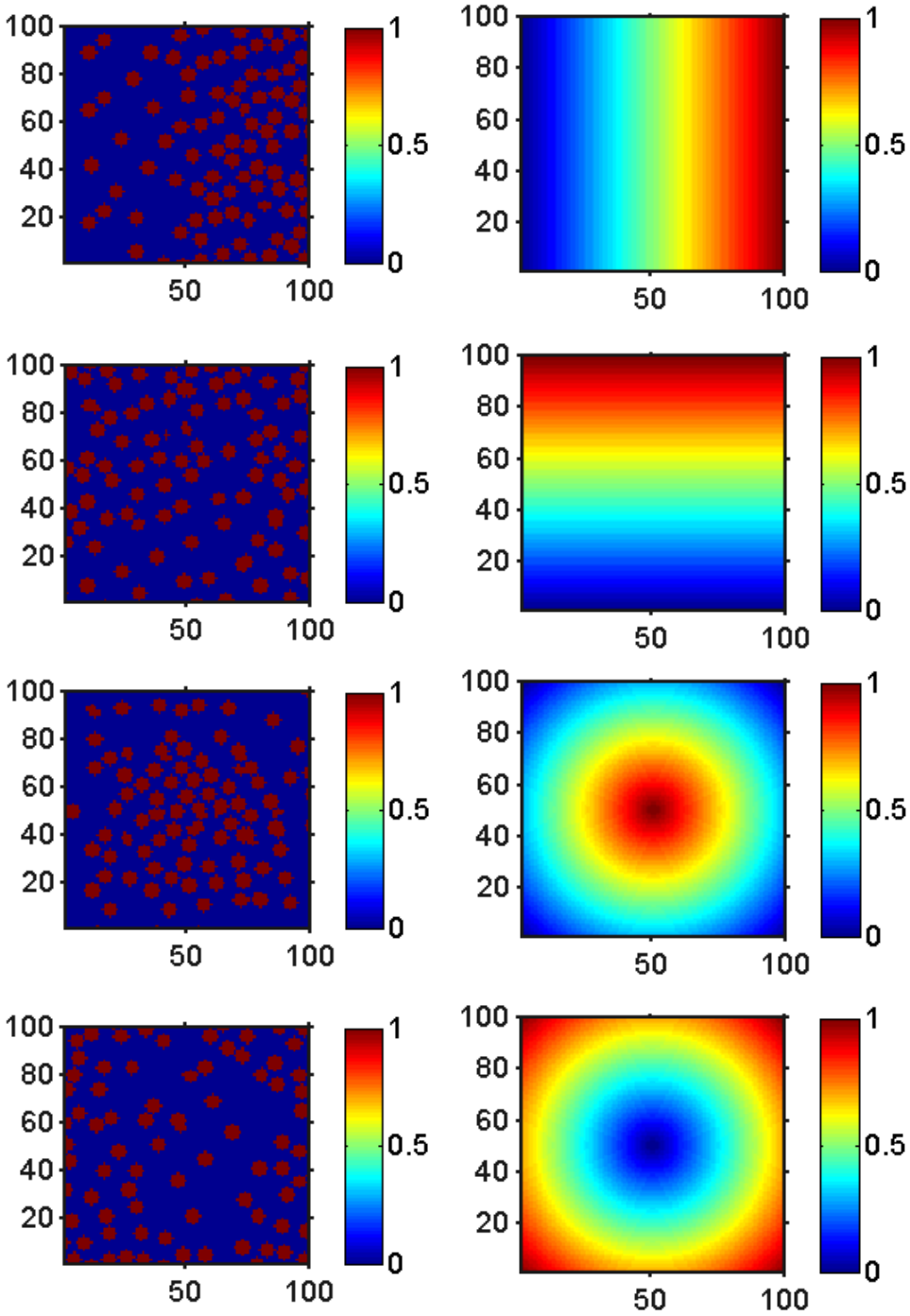

Figure 4.4 Simulation results using the ball TI with different probability fields (colorscale: white-1, black-0). Average patch size and overlap width are 15 and 5 respectively. $\alpha = 0.4$, $N_P = 10$.

are well retrieved. The correlation coefficients between facies dependent e-type map and the corresponding probability field are 0.76, 0, 0.71 for facies black, gray and white respectively. The e-type maps show a rugged texture possibly caused by the small number of realizations and the unilateral patch approach used. However, other e-type maps with similar number of realizations (see Figs 4.7, 4.10, 4.13, and 4.19) do not show this texture, so an interaction with the type of TI to simulate is also suspected. The realization indicator variograms (along Y axis) show a good match with the variogram of the TI used to perform the simulations (Fig. 4.5).

Figure 4.6 shows a multi-facies TI with two types of balls identified by different colors. The probability of occurrence of each facies is shown. Figure 4.6 shows the simulation results for three sets of probability fields. For the last case (bottom row in Fig. 4.6), 100 realizations are produced. The e-type map corresponding to each category is provided (bottom row in Fig. 4.6). The strong correlation of each e-type maps to its corresponding probability field is obvious.

4.4.1 Multiple soft data sets

For this test, we use an example directly inspired from Mariethoz and Caers (2014) (their figure II.6.2), see Fig. 4.7. An initial Gaussian simulation with an exponential variogram model with practical range 100 is used to create two soft data sets and the reference category field. The first soft data is obtained by taking the absolute values of the Gaussian field. The second soft data set is obtained by taking the average over windows of size 17 x 17 and applying a spatial shift of (10,10) to the averages. The categorical variable is obtained by computing the average of the first soft data over a window of size 21 x 21 and then applying a threshold to obtain 47% of category 1. The TI for the simulation is obtained similarly as for the category variable but starting from an independent realization of the Gaussian field. Forty HD are extracted from the reference category map and the corresponding soft data are used for calibration. The logistic regression provided a strong pseudo-R^2 of 0.52. The calculated p-values (Fisher et al, 1960) for Soft1 and Soft2 are 0.0077 and 0.0062 respectively, implying both soft data sets are complementary and contribute significantly to the classification.

The simulation combining the 40 HD, the TI and the probabilities computed from the two soft data sets shows a good reproduction of the reference field. Directional variograms are compared with the reference model variogram in Fig. 4.7. Moreover, the directional L2-functions (Lu and Torquato, 1992) are shown for the realizations and the reference model. The L2 function is a measure of connectivity that depends on multipoint statistics. It gives the probability of having a string of n pixels entirely within the white category (of course it can also be computed on the reverse image). Variograms and L2-functions of the realizations

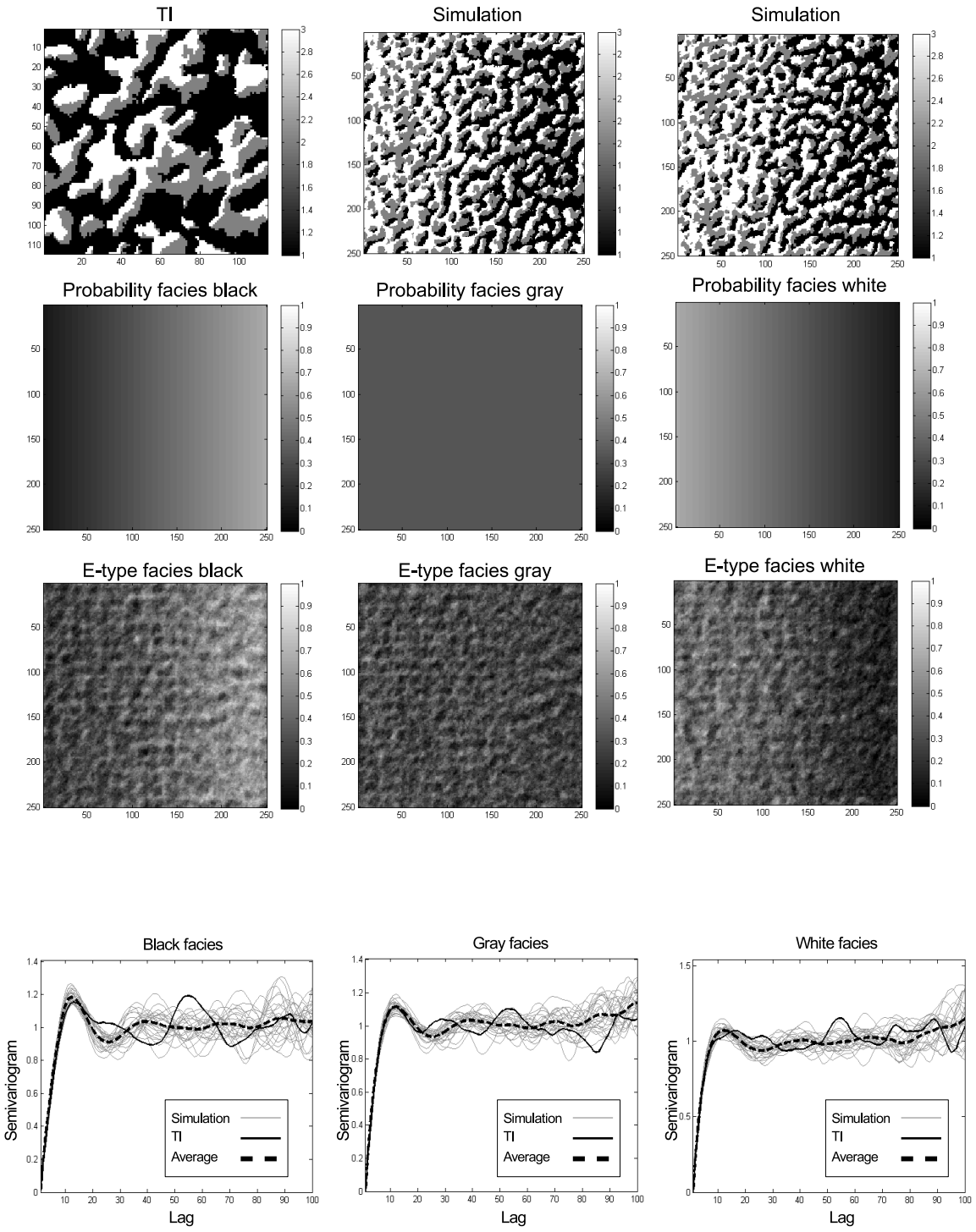

Figure 4.5 TI and two sample simulations (first row) conditioned to probability fields (second row); e-type maps of 25 realizations (third row) and variograms (bottom row). Average patch size and overlap width of 15 and 5 respectively; $\alpha = 0.45$, $N_p = 50$.

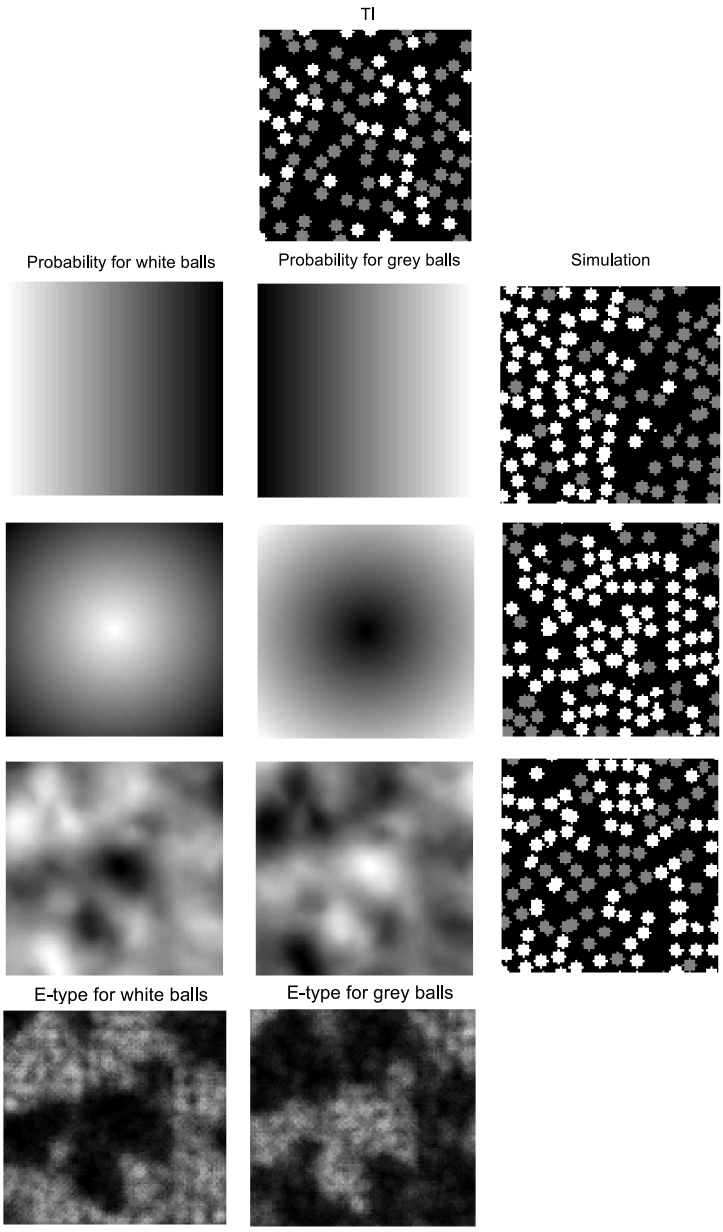

Figure 4.6 One conditional realization (right column) using the probability fields in the first two columns for the multifacies TI shown on top, (colorscale: white-1, black-0). The bottom row displays the e-type map per facies for 100 realizations using probability fields shown above in the fourth row. Average patch size and overlap width are 15 and 5 respectively. $\alpha = 0.4$, $N_P = 10$.

reproduce well the same functions for the reference model in the X-direction. In the Y-direction, the reproduction is good up to approximately $h = 15$ for the variogram and $n = 30$ for the L2-function. This is deemed sufficient considering the small size of the image and the fact that only 40 HD were used for conditioning.

4.4.2 3D simulations

The 3D quilting of Mahmud et al (2014) also implemented in Rezaee et al (2015) is used here. Moreover, the distances are computed using the FFT-based convolution functions. We have considered 3D cases with ball and channel TIs. Figure 4.8 shows the results for ball TI with sample simulation and the e-type map of 25 realizations. A number of 5 ATIs are used for this simulations to add variability between realizations. Fig. 4.9 shows the classic channel TI, probability field, sample simulation and the e-type map of 25 realizations with an imposed $\alpha = 0.60$. In all cases the simulations and their corresponding e-type map borrow their structure from TI and the trends from the probability field. The correlation coefficient between probability field and the e-type map is 0.67.

4.4.3 Sensitivity to α

The probability field contribution in the total distance is controlled by the α weight in Eq. 4.2. This weight is taken equal to McFadden pseudo-R^2. The stronger the α weight the higher the expected correlation between e-type and the probability fields. On the other hand, the stronger the α, the more difficult it is to preserve the TI textures. Figure 4.10 shows the effect of α on the realization, e-type map and correlation between soft and e-type maps. A number of 10 Alternative TIs (Rezaee et al, 2015) are exploited for the matching patterns in each simulation. The reproduction of TI texture is good even for a high α value of 0.7. Note that when $\alpha = 0$, the e-type map is uncorrelated to the soft data and it fluctuates randomly around the mean proportion (0.4).
Figure 4.11 shows the non-linear relationship between α and e-type-probability field correlation computed on 25 realizations. After a fast increase, the correlation reaches more or less a plateau for $\alpha = 0.6$ in this example.

4.5 Hard Data conditioning

Hard data can be reproduced in the simulation by assigning high weights (β expressed as a multiple of the weight given to simulated pixels) to the HD pixels. This idea was used by Zhang et al (2006); Mariethoz et al (2010); Faucher et al (2013); Rezaee et al (2013); Faucher et al (2014). Figure 4.12 displays the HD reproduction rate and sample realizations

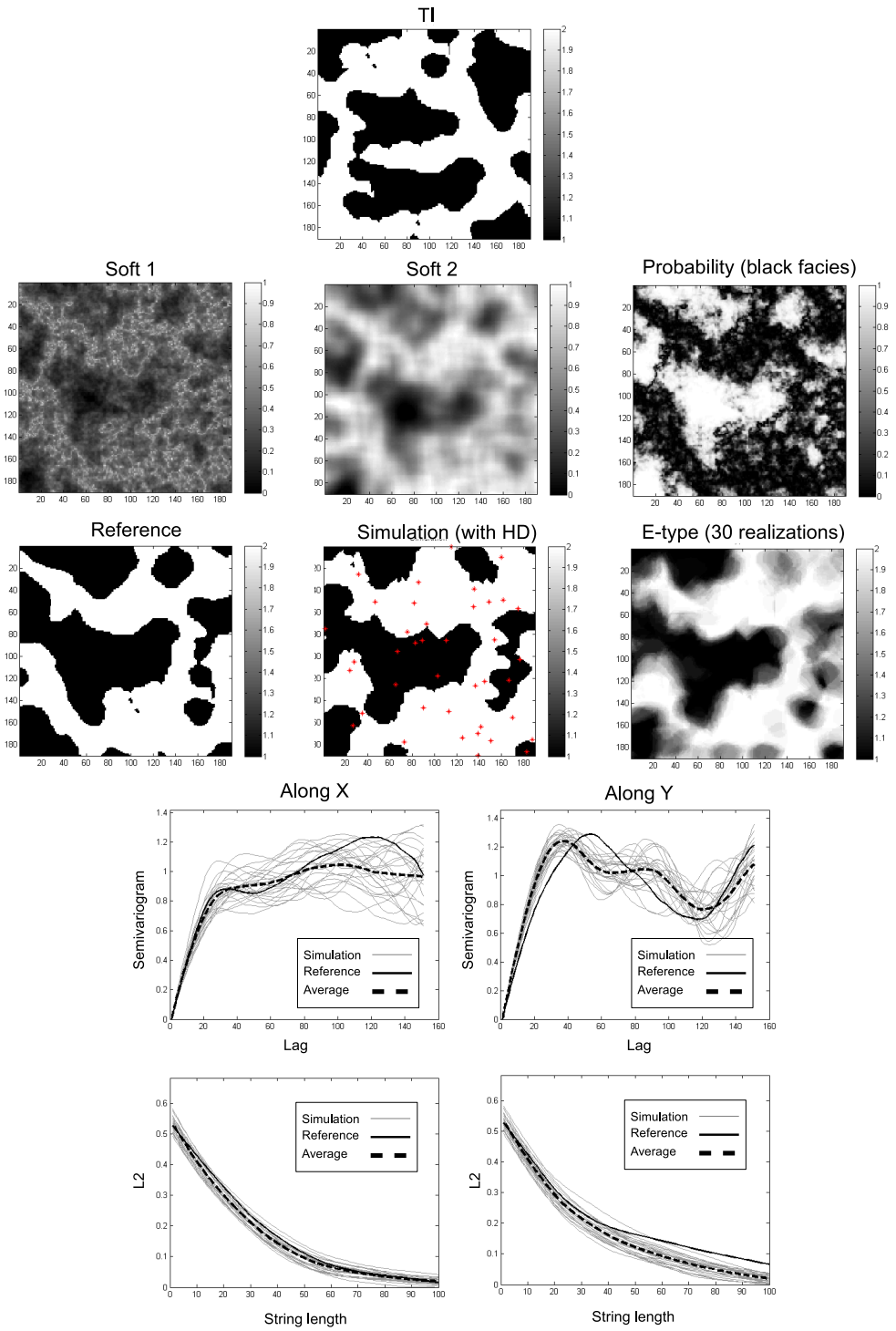

Figure 4.7 TI (top row), two soft data and probability fields (second row), reference model, one realization and e-type map based on 10 realizations (third row), variograms (fourth row) and L2-functions (fifth row) of the reference and the 10 realizations. Average patch size and overlap width of 35 and 12 respectively, $\alpha = 0.52$, $N_p = 100$.

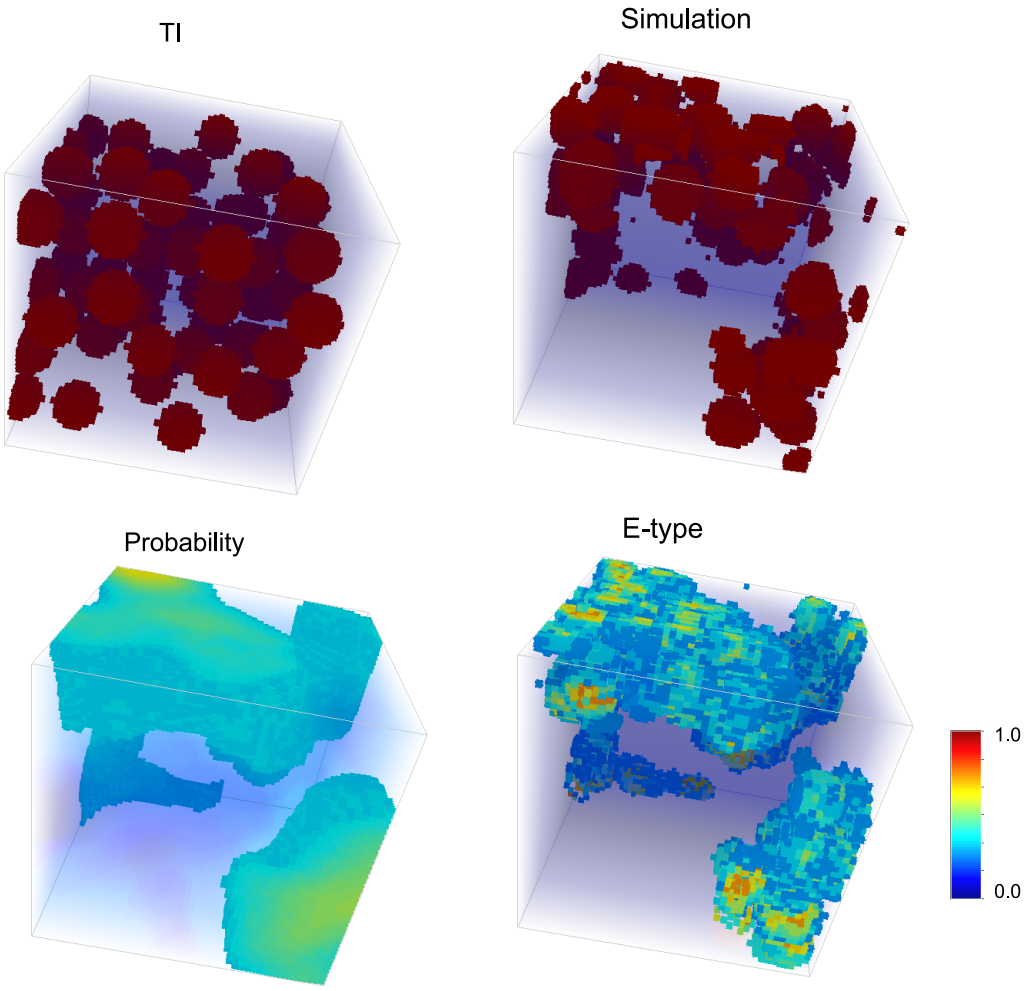

Figure 4.8 3D ball TI and the probability field were used to perform 25 conditional simulations. One sample simulation and the e-type cubes are also displayed. Size of the TI and simulation grid are both 50*50*50. Average patch size and overlap width are 16 and 5 respectively. $\alpha = 0.60$, $N_p = 100$.

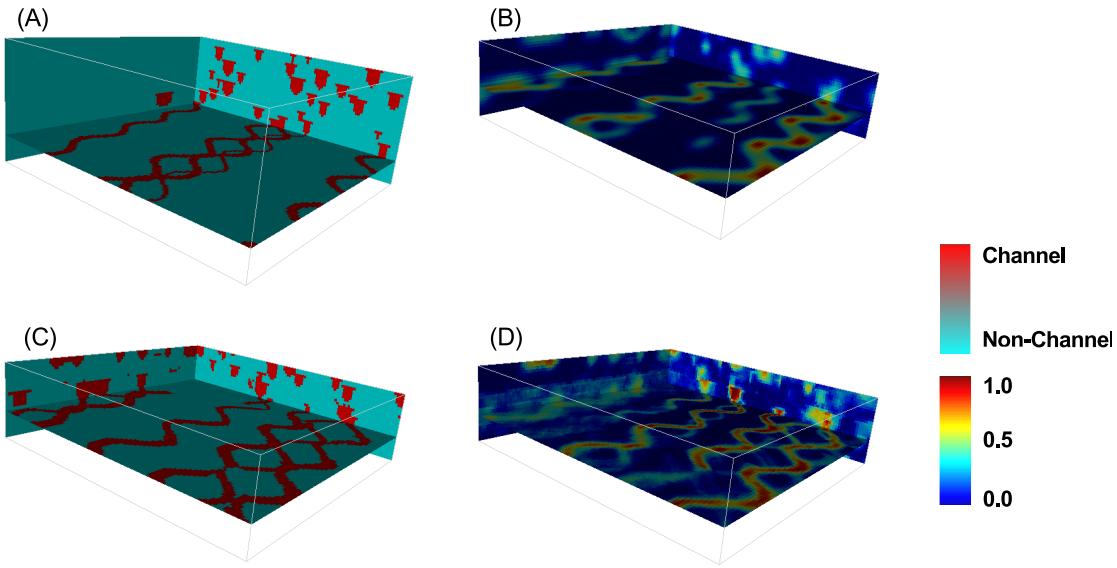

Figure 4.9 A: 3D channel TI, B: probability volume, C: sample simulation and D: e-type map of 25 realizations. Average patch size and overlap width are 30 and 10 respectively. $\alpha = 0.4$, $N_P = 100$.

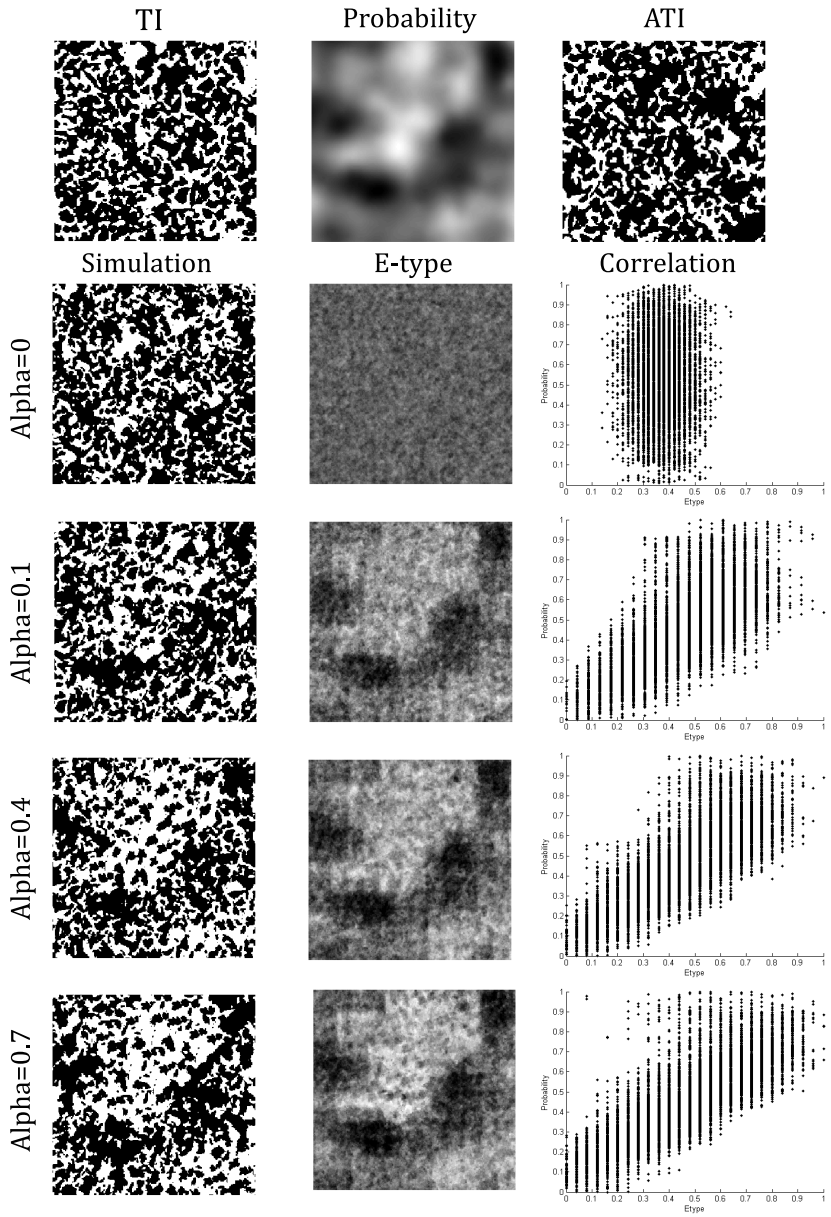

Figure 4.10 Top row: TI, the probability field and one sample ATI (out of 10) used for the simulation; second to fifth rows: one sample realization (left), e-type map (middle), correlation plots (right) for $\alpha = 0.0$, 0.1, 0.4 and 0.7. Each e-type map is computed from 25 realizations (colorscale: white-1, black-0). ATIs are unconditional patch-based simulations of TI using quilting (El Ouassini et al, 2008; Faucher et al, 2013). Average patch size and overlap width are 20 and 7 respectively. $N_p = 25$.

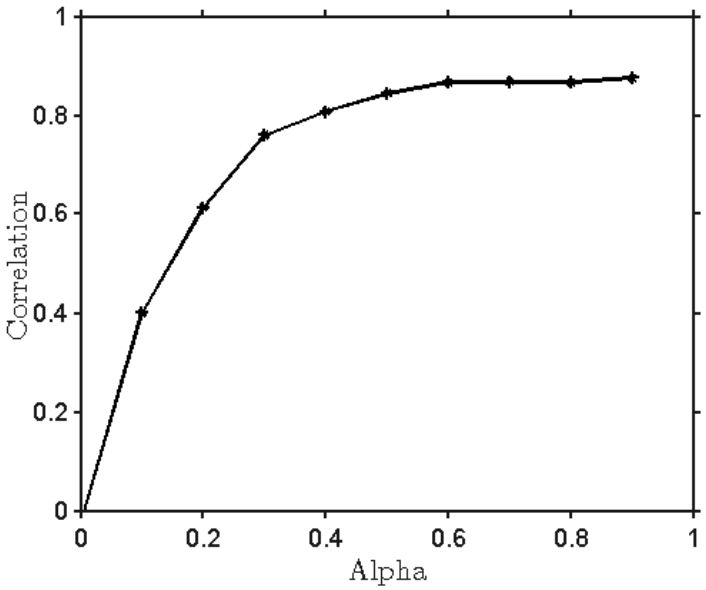

Figure 4.11 Correlation between e-type and probability field as a function of the α parameter. E-type map computed from 25 realizations for the TI and probability map shown in Fig. 4.10.

for various weights given to probability fields and HD. The simulations (second to fourth row) are performed using the ball TI, soft data and HD shown on top row.
As expected, when $\alpha = 0.1$ the simulation does not follow closely the trends from the probability fields (except indirectly thanks to the HD contributions). For increasing α, the relationship between simulation and soft data increases. As the HD weight (β) increases, the HD reproduction rate increases. Through visual checks it is clear that the best quality of balls happens with $\alpha = 0.1,\ \beta = 1$, i.e., when the distance function is mostly a function of the overlap area and the HD. The regularity of balls decreases slightly from left to right and from top to bottom as the contribution of hard and soft data increases. Nevertheless, the simulation on bottom-right ($\alpha = 0.7,\ \beta = 100$) reproduces all the HD, follows apparently the probability field and shows many well formed balls, despite some obvious defaults.

4.5.1 Regional effect of HD locations

The lack of an analytical expression for the expected posterior mean and variance of an ensemble of MPS simulations as opposed to variogram-based geostatistics makes more difficult to verify the (undesirable) regional effect of the conditioning to hard data. As proposed in Mariethoz and Caers (2014) a workaround is to generate several realizations according to two scenarios: first in unconditional simulation mode using a given TI (here the channel TI), and second using the same TI to generate several unconditional simulations which then serve as reference models to provide different sets of values at fixed HD locations. Each HD set is then used with the original TI to perform a conditional simulation. The e-type of the realizations obtained with the second scenario should not show any regional effect around the hard data locations similarly to the unconditional realizations. A series of 100 unconditional and conditional simulations are generated using the channel TI. The e-type maps in Fig. 4.13 display no evidence of regional effect around the hard data.

4.6 Real TI and Soft Data Conditioning

The idea of soft data conditioning is tested on a real case study. The Mallik methane hydrate field on the Canadian Northwest Territories is drilled and studied for a better understanding of the methane hydrate zones (Bellefleur et al, 2006; Dubreuil-Boisclair et al, 2012). The study area shown in Fig. 4.14 displays the location of four boreholes and the line indicating the cross-section on which the cross well acoustic tomography is performed in depth. The primary variable is methane hydrate grade whose values are known along the boreholes 2L and 5L. Figure 4.15 shows the grade and normalized seismic velocity logs for boreholes 2L and 5L. The rank correlations are 0.74 and 0.88 for 2L and 5L respectively. Thus, we assume

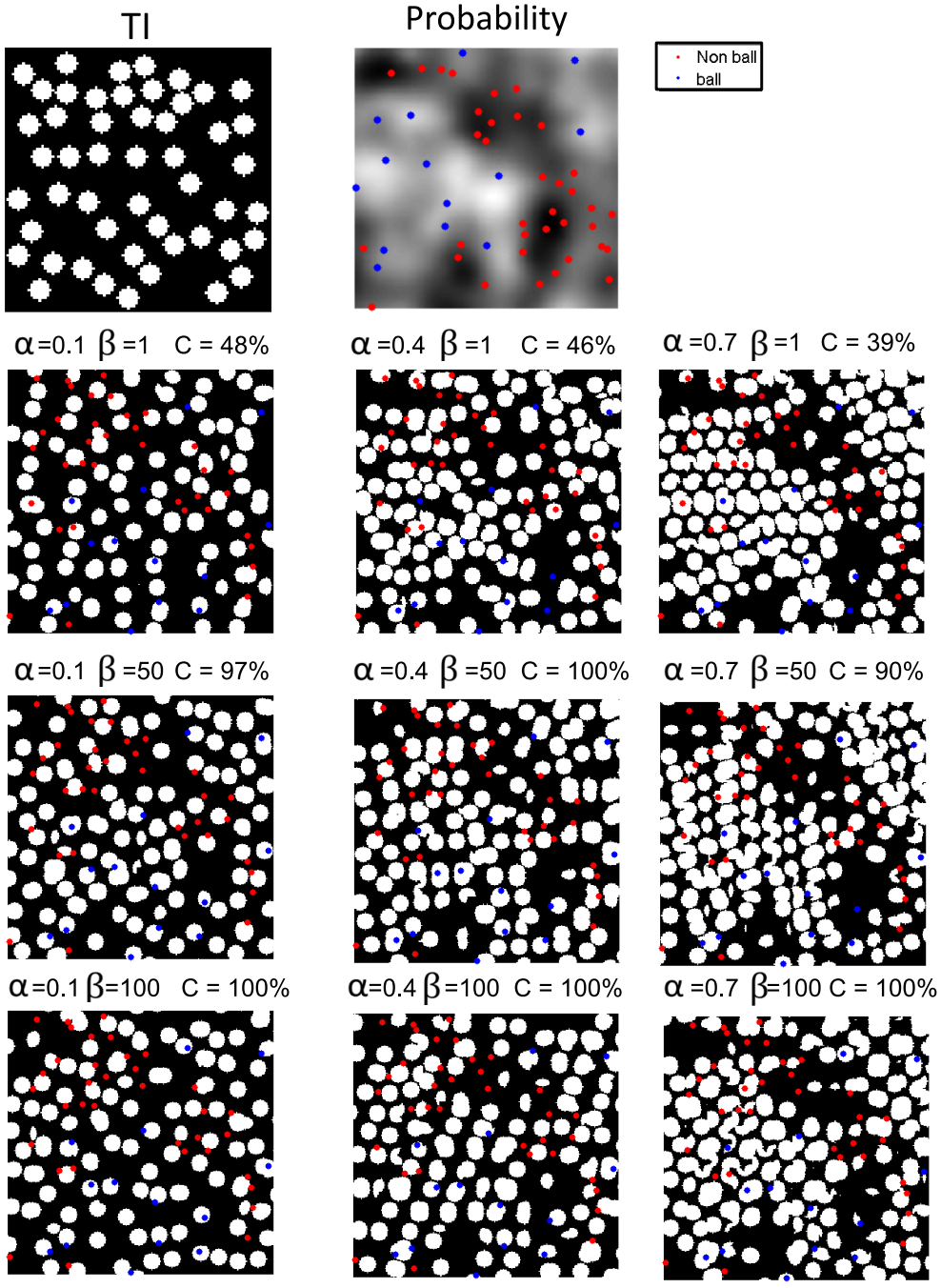

Figure 4.12 Sensitivity of the simulations to the weights given to HD (β) and soft data (α); C represents the % of HD reproduced (colorscale: white-1, black-0). C values are calculated over 10 realizations for a better estimate of HD reproduction. Size of the TI and simulation grid are 200*200 and 250*250 respectively. Average patch size and overlap width are 24 and 8 respectively. $N_p = 25$.

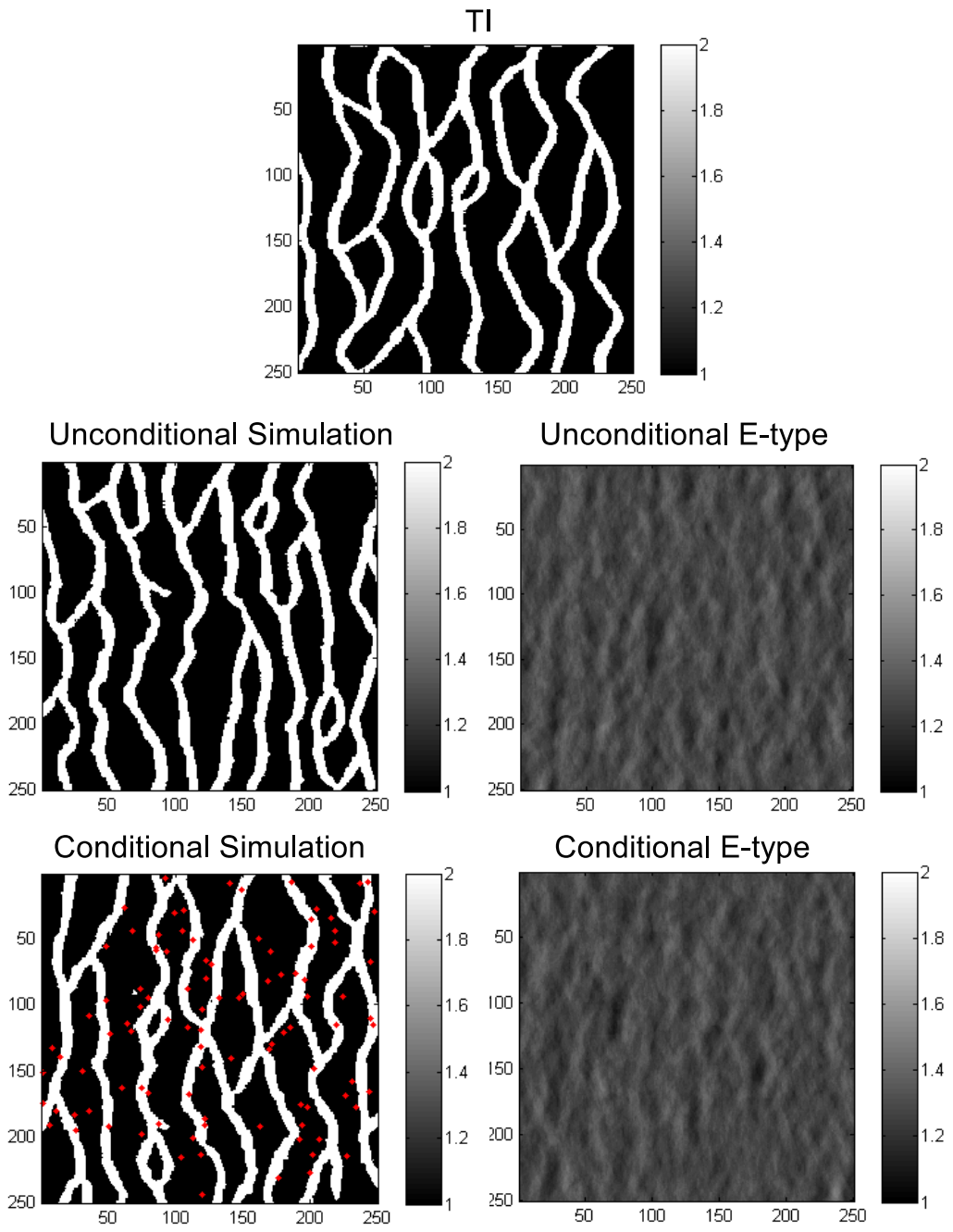

Figure 4.13 TI, one realization and e-type maps based on unconditional (middle row) and conditional (bottom row) realizations; HD as red dots; average patch size and overlap width 25 and 9 respectively. $\alpha = 0.4$, $N_p = 25$.

the tomography image is an acceptable representation of the grade variations on the plane. The tomography image and the grade data are truncated into three classes using 75th and 85th percentiles. The truncated tomography is used as a TI and the truncated grades provide HD. Figure 4.16 illustrates the inputs to the MPS simulation.

Over the whole area a seismic acquisition was carried out. It was 3D inverted into seismic compressional velocities, V_p, used as soft data. The soft data corresponds to a much lower resolution than the 2D TI (cross-hole tomography) but it covers the whole 3D field and therefore could inform on the location of methane hydrates.

An ordinal logistic regression model was fit between categories on the wells and the V_p values from inversion (soft data) at well sampling locations. Due to the large number of HD (n=4844), the logistic regression was highly significant (p-value=3.1e-5) despite a rather weak pseudo-R^2 of 0.14. The model was used to compute the probability fields for each category. The probability fields shown in Fig. 4.17 were extracted from the soft data cube on the 2D plane passing by boreholes 2L and 5L. The probability fields appear globally related to the borehole observations (despite the low pseudo-R^2) as most of borehole points of a given category fall within its highest probability zones (Fig. 4.17).

The simulations were done conditionally to both borehole data as hard constraints and probability fields. Due to the high weight ($\beta = 1000$) chosen for the HD in the distance computation and the use of Alternative TIs (Rezaee et al, 2015), all the HD were reproduced in all 100 realizations. We used 25 ATIs to obtain a perfect reproduction of HD without affecting too much the continuity of the realizations. In the set of all ATIs there were provided at least 50 matching patterns to each of the HD configurations on borehole. Figure 4.18 shows three sample simulations obtained. The category-dependent e-type maps are also calculated for 100 realizations (Fig. 4.19). Globally, a good match is obtained between the probability fields and the corresponding e-type maps as shown by e-type probability field correlation coefficients of 0.61, 0.55 and 0.72 for respectively the high, medium and low categories.

For the Mallik case study, it was possible to simultaneously reproduce the TI texture, the HD observed in two boreholes and the global trends described by V_p inversion from a regional seismic survey. This allows simulation over any 2D vertical plane where the TI is deemed representative of the texture. For 3D simulation, the same approach can be followed provided a 3D TI is readily available or simulated from the 2D TI. Admittedly, the generalization of 2D TI to 3D remains a challenge and an active area of research.

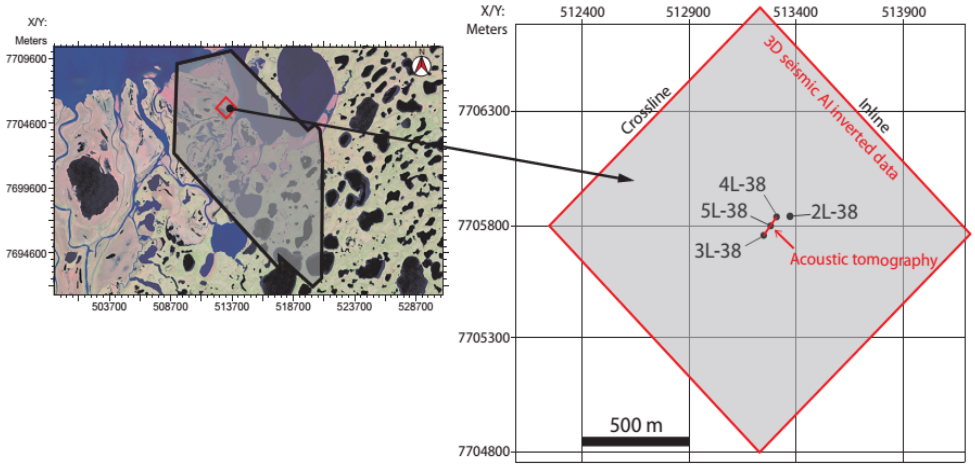

Figure 4.14 Mallik area, Mackenzie Delta, Northwest Territories, Canada; boreholes, and area covered by tomography and seismic investigations. Figure borrowed from Dubreuil-Boisclair et al (2012).

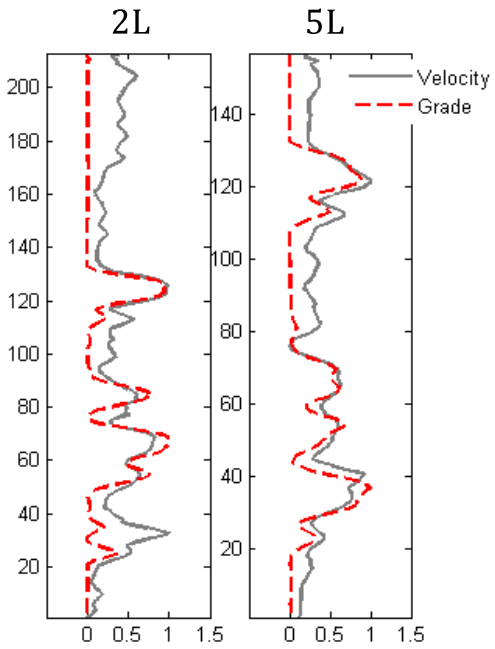

Figure 4.15 Correlation in 2L and 5L borehole logs of methane hydrate grade and seismic velocity.

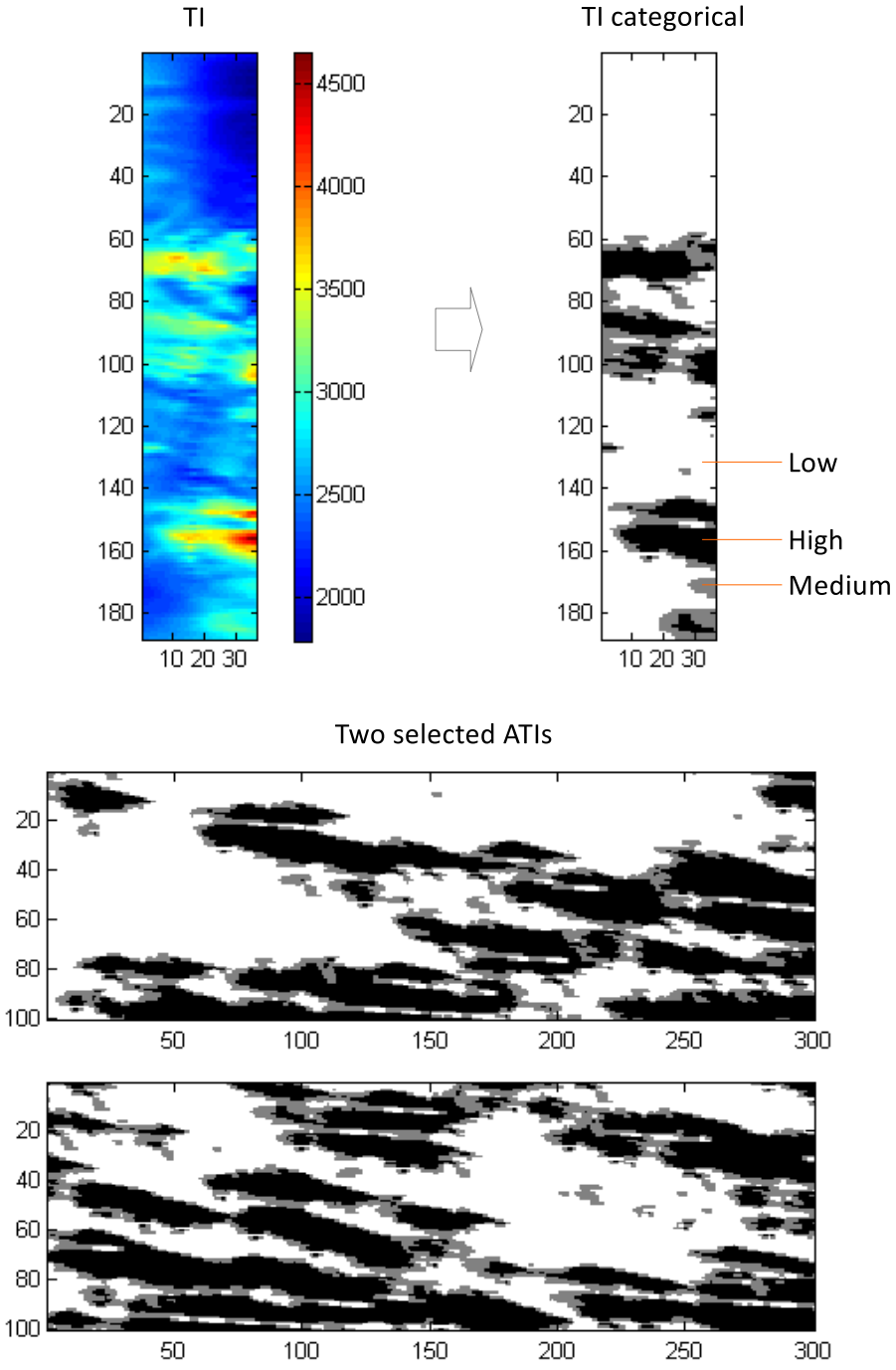

Figure 4.16 Top row: Original TI obtained by thresholding Vp at 75th and 85th percentiles; bottom row: two large ATIs generated by unconditional simulation using the original small TI. A total number of 25 ATIs were used for the simulations.

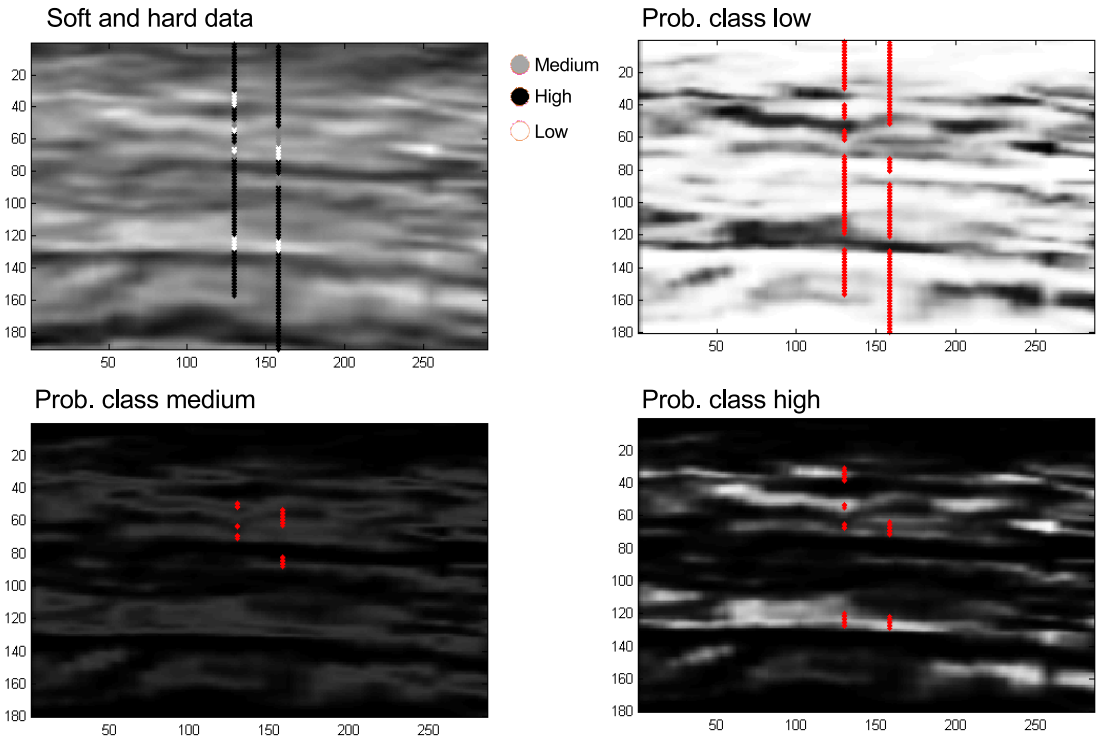

Figure 4.17 Top left: original soft data (inverted Vp), top right and bottom row: probability field per category (colorscale: white-1, black-0); on each category probability field the points in boreholes belonging to the same category are overlaid, α=pseudo-$R^2 = 0.14$.

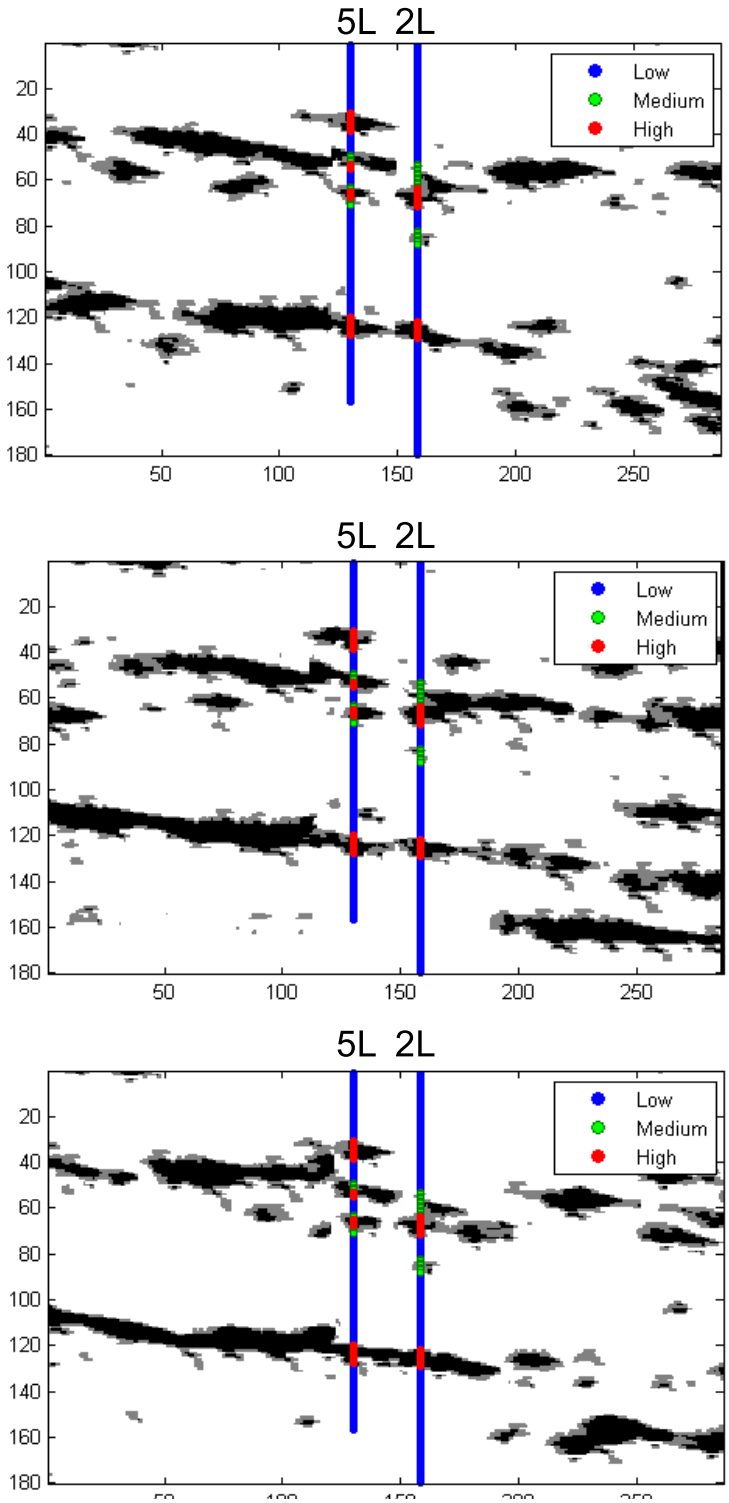

Figure 4.18 Three conditional simulations randomly selected from 100 realizations. Average patch size and overlap width are 8 and 3 respectively. $\alpha = 0.14$, $N_p = 25$.

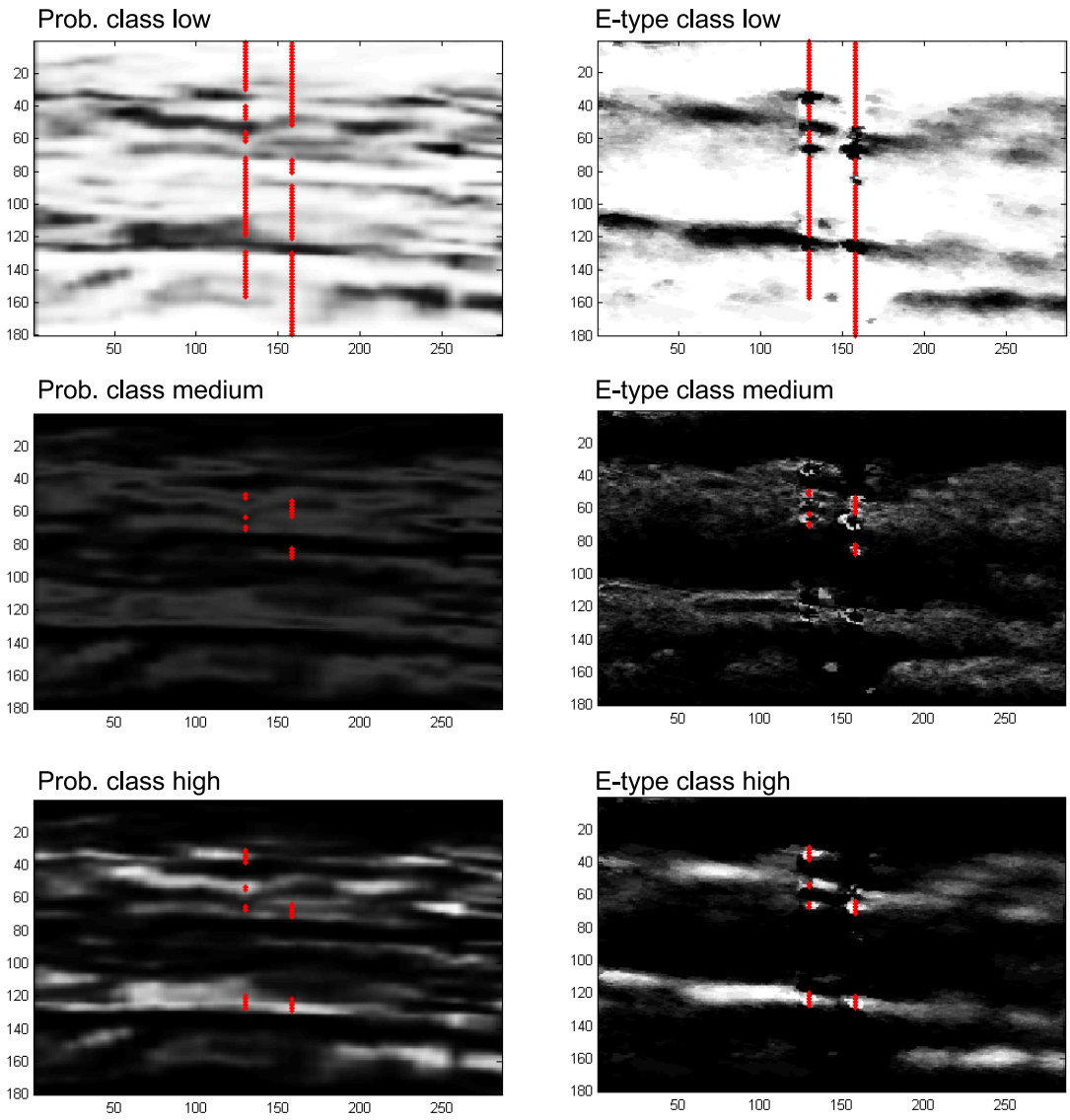

Figure 4.19 Left: Probability fields for the three categories; Right: e-type maps per category based on 100 realizations.

4.7 Discussion

The multinomial logistic regression approach used here to construct the k probability fields from p soft data has appealing aspects. First for $p > k$ it allows to merge any number of soft data in a fixed number of probability fields. For $p < k$, it relates the soft data to the different categories and could suggest to regroup some categories not well linked to the soft data. Moreover, the modeling step allows to verify the strength of the link between the soft data and HD. When the link is negligible, logistic regression returns constant probability fields equal to the category proportions found in the available HD used in the regression. The ensuing realizations will not show any particular relation to the soft data, as it should, when the α weight is small. When the link between soft data and HD is strong, the trends in the category probabilities computed from the soft data will be reproduced. The use of multinomial logistic regression allows to choose automatically the α weight equal to the McFadden's pseudo-R^2. Note that other classifiers than multinomial logistic regression, like discriminant analysis, neural networks or Bayes classifiers, could have been used in the same way. However, the α weight would have to be assessed differently with these methods.
Although all the examples presented used HD to calibrate the soft data at HD locations, the method can also be used without HD when an exact or approximate forward model is available. In that case, pseudo soft-data can be computed from the TI and used for calibration. Alternatively, the method can be used when related TIs for the categories and the soft data can be obtained from an analogous area.

4.8 Conclusions

This study showed that soft data can be useful to control the density of different simulated categories or objects in a patch-based MPS simulation. The examples presented indicate that HD points are reproduced, the TI texture is globally well represented, thanks to the use of patches and quilting, and the proportion of facies is linked to the soft data. One original contribution was to merge possibly many soft data sets into k probability fields, one per category, after calibration to known HD by a multinomial logistic regression. Hence, the soft data influence the simulation after the link with the categories has been demonstrated and quantified rather than on an ad hoc basis.

4.9 Acknowledgement

Authors would like to express their thanks to C. Dubreuil-Boisclair and E. Gloaguen for providing the data set for real case on Mallik gas hydrate field. Research was partly financed

by NSERC (RGPIN-2015-06653). Numerous comments from three anonymous reviewers were helpful in improving significantly the manuscript.

CHAPTER 5

ARTICLE 3: CALIBRATION OF CATEGORICAL SIMULATIONS BY EVOLUTIONARY GRADUAL DEFORMATION METHOD

Hassan Rezaee [1], **Denis Marcotte.**

Computational Geosciences (submitted)

5.1 Abstract

Methods to simulate facies (or categorical) fields are numerous. However, calibration of simulated facies fields to large scale or dynamic data still remains an important challenge due to the discrete nature of the fields, the non-linearity of the response with respect to the facies fields and the non-derivability of the objective function used in calibration. A new Gradual Deformation Method (GDM) is presented and tested for the calibration of facies realizations. The method starts by defining a lithological coding rule, similarly as in pluriGaussian simulation. Then, latent Gaussian fields corresponding to facies realizations are created by Gibbs sampling. The Gaussian fields corresponding to a number of facies realizations are merged. Application of the coding template to the merged Gaussian fields procure offspring facies realizations. Weights used in the merging are chosen to improve calibration. The evolutionary process evolves iteratively from generation to generation. A new generation is composed of a subset of fittest merged realizations obtained from different sets of parents randomly selected in the previous generation. The new generation is completed by a series of fresh uncalibrated facies realizations to maintain diversity and to allow escaping local minima. At the end of the evolutionary process, only the fittest realization of the last generation is kept to provide one calibrated realization. The whole process is repeated anew to get another calibrated realization. The method is applied to a variety of test cases using facies fields generated by multipoint patch-based simulation (MPS). Various target variables are considered throughout the different test cases: proportion maps, section of seismic amplitudes, inlet to outlet travel time along the shortest path and water-cut curves obtained with a flow simulator. Both conditional/unconditional MPS simulations and 2D/3D

1. H. Rezaee, D. Marcotte Department of Civil, Geological and Mining Engineering, Polytechnique Montreal, C.P. 6079, Succ. Centre-ville, Montreal, QC H3C 3A7, Canada, e-mail: hassan.rezaee@polymtl.ca

problems are considered. In all studied test cases the new GDM approach has provided excellent calibration to the target variables in a reasonable computing time. The method is general as it can be used in conjunction with any facies simulator.

5.2 Introduction

In many Earth sciences applications, static auxiliary data, such as geophysical data, or dynamic auxiliary data, like production history and pumping or tracer tests, are available. These auxiliary data represent valuable information that must be incorporated in the geological models. It is now generally acknowledged (Hearn et al, 1984; Dickinson, 1953) that the most important factor controlling the variations of static or dynamic auxiliary data is usually the geological structure or facies arrangement in the field under study. To simulate the categorical variables describing the facies, methods like pluriGaussian simulation (PGS) (Armstrong et al, 2011; Mariethoz et al, 2009; Emery, 2007), Markovian type category prediction/simulation (MCP) (Allard et al, 2011) and different variants of multipoint simulation (MPS) (Guardiano and Srivastava, 1993; Efros and Freeman, 2001; Strebelle, 2002; Chugunova and Hu, 2008; El Ouassini et al, 2008; Mariethoz et al, 2010; Straubhaar et al, 2011; Tahmasebi et al, 2012; Abdollahifard and Faez, 2013; Rezaee et al, 2015; Zhang et al, 2015b,a)(among many others) were developed over the years to help generate realistic realizations of the field.

The main difficulty with PGS, MPS and MCP remains the conditioning of the realizations to various kinds of auxiliary data. A difficulty is the nonlinear relationship between the auxiliary data and the facies arrangement. Moreover, the resolution or support of the auxiliary variable is usually only known approximately and is typically much larger than the scale of facies observations. Methods like Ensemble Kalman Filtering (EnKF) (Evensen, 2003; Peters, 2011) and gradual deformation (GDM) (Hu, 2000; Le Ravalec et al, 2000) enable to improve matching the auxiliary data when the primary data is continuous. Hence, these methods can be applied with PGS (Hu, 2000) where the categorical facies variable is associated to one or more continuous Gaussian latent variables. However, for other categorical simulation methods like MPS and MCP a method for efficient calibration to auxiliary data is still needed. Among previous attempts, Hu et al (2013); Sebacher et al (2015) used EnKF to update the field of uniform independent variables associated to the random drawing occurring in point-based MPS-SNESIM (Strebelle, 2002). However, the examples shown indicated that discontinuities were created in the MPS images. Moreover, the approach cannot be applied to mehods based on distance criteria instead of random drawing like in patch-based MPS or Discrete sampling (Mariethoz et al, 2010). Heidari et al (2013) proposed a merged model of

GDM and EnKF in an attempt to history match the continuous properties such as porosity and permeability to production data. In their examples petrophysical properties are strongly correlated to the background facies model which supports the idea of using GDM (or EnKF) directly on facies model. In Le Ravalec-Dupin and Hu (2005) size of boolean objects were continuously varied by gradual deformation of Poisson distribution parameters. New objects appeared and other disappeared. The approach reduces, without eliminating, the discontinuities in the calibration objective function. Because boolean objects are modified, hard data conditioning poses a problem with this approach. Moreover, the multi-category case was not considered. A recent approach (Zahner et al, 2016; Pirot et al, 2017) was proposed where an initial categorical realization is calibrated by iteratively patching in the simulated field pieces taken randomly from the training image. Besides necessitating a very large TI, the approach is based on a MCMC chain. Hence, it is expected to be slow because it requires many calls to the forward model and the proposed perturbations can be often rejected. Moreover, the approach could present large scale facies continuity issues, especially for cases involving multiple facies with strong contraints in their arrangement.

We seek to resolve the above-mentioned limitations. We use patch-based MPS because of their superior texture reproduction when compared to point-based MPS. The calibration to auxiliary data is done by first associating to each MPS realization one or more latent Gaussian fields and then applying GDM on these Gaussian fields. The Gaussian fields are obtained from the MPS by applying Gibbs sampling to the entire MPS realization using a coding template reflecting the main relationships between facies (as in PGS). The observed facies (e.g. in boreholes) define hard data (HD) constraints. We use direct conditional GDM as described in Hu et al (2001) and Ying and Gomez-Hernandez (2000) to gradually deform sets of MPS realizations. We present however an entirely new strategy for application of GDM that borrows ideas from evolutionary optimization concepts (Holland, 1975).

In the methodological section, we briefly review the main steps involved in our approach: MPS using a patch-based approach with alternative training images (Rezaee et al, 2015), Gibbs sampling over the entire field with forcing of common Gaussian values at HD points, definition of the coding template and finally GDM based on combination of Gaussian fields following the new proposed strategy. Many case studies aiming at exploring different kind of auxiliary data are tested in the results section. We finish with some elements of discussion.

5.3 Methodology

The three main steps of the proposed approach consist in generating the facies realizations by patch-based MPS. Then we define a lithological coding template, as in PGS, to convert

the MPS facies realizations into one or several latent Gaussian fields. Finally, we gradually deform the Gaussian fields until one of the convergence criteria is met. For this last step, we introduce a new evolutionary approach aimed at avoiding being caught early in a local minimum as often observed with GDM.

5.3.1 MPS method

Facies realizations are generated thru a patch-based MPS approach which uses a set of Alternative Training Images (ATIs) obtained by unconditional MPS simulation (Rezaee et al, 2015). The set of ATIs are used to improve the reproduction of dense hard conditioning data (HD). It can also help accommodate soft conditioning data (Rezaee and Marcotte, 2016). The approach with ATIs was demonstrated to allow good continuity of the structures and perfect or nearly perfect HD reproduction. For each patch under simulation, conditioning data comprising previously-simulated parts and/or the hard data located within that patch are used to search for matching pattern in the set of TI and ATIs. The scanning process is performed efficiently by computing weighted distance functions by convolution operator. The simulation path is unilateral. To account for possible directional artifacts (El Ouassini et al, 2008) both horizontal and vertical scans are used. In the distance computation, hard data receive the highest weights. The weights of previously simulated data decreases as a function of their distance to the edges of the patch to ensure better continuity of patterns as described in El Ouassini et al (2008).
Rezaee et al (2015) illustrated the improvements in conditioning brought by patch-based MPS simulation with ATIs particularly for cases with dense HD. Figure 5.1 shows an example of an input TI and simulations with and without ATIs. The continuity of channels are measured by the linear path L_2 function (Lu and Torquato, 1992) which gives the probability for a segment of size L to be entirely contained within a specified facies along a given direction. Figure 5.1 displays simulated channels using ATIs+TI (middle left sub-figure) visually more continuous along X axis than those obtained using only the TI (bottom left sub-figure). The better continuity with ATIs is confirmed by the L_2 (bottom right sub-figure) showing higher probabilities for all segment lengths with ATIs. Moreover, the conditioning rate of realizations with ATIs to the 250 HD are improved substantially compared to realizations without ATIs.

5.3.2 Latent Gaussian variables

Categorical variables stemming from MPS are difficult to calibrate directly to dynamic data due to their discontinuous nature. Hence, the idea we use is simply to associate one or more

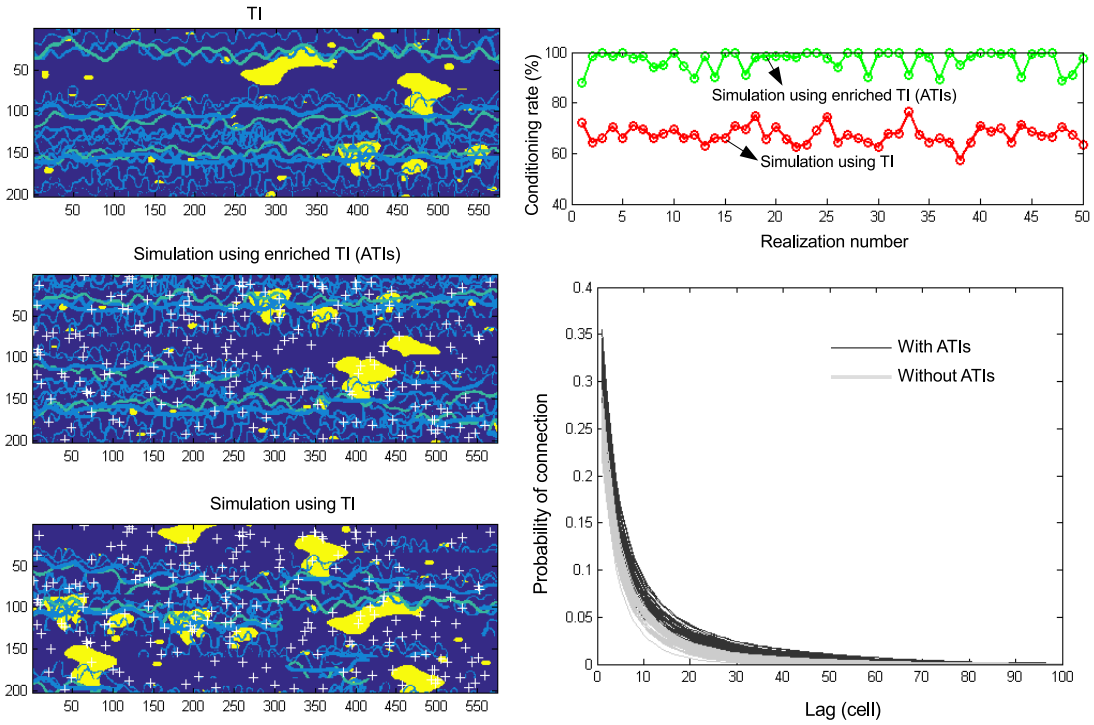

Figure 5.1 Top left: TI generated with an object-based simulation method (Total, 2016); middle left: one realization with 20 ATIs; bottom left: one realization using only the TI, 250 HD indicated. Top right: HD reproduction rate for 50 different realizations with and without ATIs. Bottom right: L_2 function for the 50 realizations obtained with and without ATIs.

latent independent Gaussian variables to each MPS realization exactly as done with PGS (Armstrong et al, 2011; Le Loch and Galli, 1997). This necessitates to determine the number of Gaussians required and the corresponding coding template defined such as to represent the main spatial relations between facies and the desired proportions of facies. The determination of the spatial structure of the Gaussians can be done by fitting the facies indicator variograms and cross-variograms or the indicator non-centered covariances and cross-covariances. We note that the choice of the Gaussians spatial structures at distances larger than a few pixels has relatively little impact in our approach as the entire MPS realization is used in the Gibbs sampling step (Geman and Geman, 1984; Freulon and de Fouquet, 1993). As the conditional distributions at each point are estimated by simple kriging, they are mostly defined by the nearest pixels.

Figure 5.2 illustrates the approach. The dunes TI is taken from the Gobi desert in northern China (Allard et al, 2011). This TI was used to generate two unconditional realizations using MPS (second column). The lithotype template (bottom left) is used. Gaussian fields obtained by Gibbs sampling are displayed (two rightmost columns) for the two realizations. The burning period of the Gibbs sampler was assessed through histogram and variogram convergence.

5.3.3 Deformation in Gaussian space

The gradual deformation of Gaussian variables has been introduced by Hu (2000) and developped further in Hu (2002); Le Ravalec-Dupin and Hu (2005). The basic idea is to combine iteratively a series of Gaussian fields such as to fit large scale or dynamic data or any response function that does not relate linearly to the main variable under study. In the unconditional case, $k \geq 2$ fields at a time can be combined as $Z_c(\mathbf{x}) = \sum_i^k a_i Z_i(\mathbf{x})$ with the weights chosen such that $\sum_i^k a_i^2 = 1$ to ensure keeping the same covariance model in the combined field as in the original fields. In the conditional case, $k \geq 3$ fields at a time can be combined as $Z_c(\mathbf{x}) = \sum_i^k a_i Z_i(\mathbf{x})$ with the weights chosen such that $\sum_i^k a_i^2 = 1$ and $\sum_i^k a_i = 1$, the latter condition being required to ensure reproduction of conditioning data.

In practice, different strategies can be used to apply GDM. The simplest strategy consists in combining at each iteration a new Gaussian realization with the current combined field. Another possible approach is to proceed hierarchically in a balanced way, by combining fields of the same level of evolution to generate combined fields having the next degree of evolution. Other variants include the possibility of applying GDM locally (Hu, 2000; Hu et al, 2001). To avoid introducing discontinuities, the local variants work on the uncorrelated random number sequence at the source of the Gaussian fields. The local variants are not well adapted to our approach as the Gaussian values over the whole field are obtained by Gibbs sampling, not

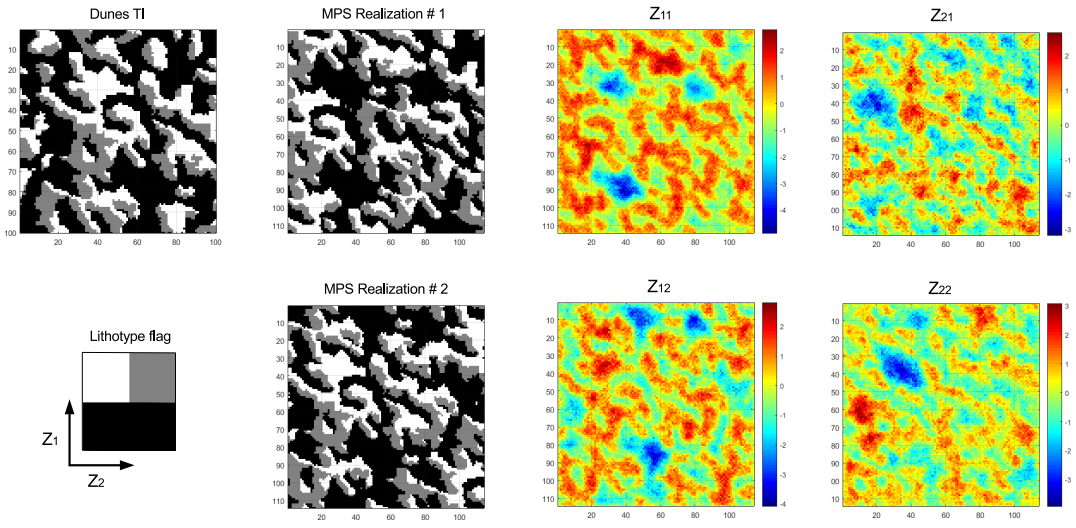

Figure 5.2 Dunes TI from Allard et al (2011) (top left); lithotype template (bottom left); two MPS unconditional realizations (second column from left) and corresponding Gaussian fields (two rightmost columns)

by direct simulation (e.g. SGS, turning bands,...). So, each Gaussian value is the result of many iterative random drawings (one per Gibbs iteration). It would be unrealistic to perturb these random drawings as the effect of any perturbation cascades over all pixels for all the following iterations.

We propose a new strategy that borrows ideas from evolutionary optimization. We call a generation a set of MPS realizations (of fixed size). Typically, a generation is formed of a mix of fresh MPS realizations and of realizations evolved thru the procedure described below. The idea is to evolve thru generations while maintaining enough variety in each generation (by adding fresh MPS realizations) to enable escaping from a local minimum.

More precisely, lets define:

– n: number of latent Gaussian variables from each facies model (e.g. $n = 2$ in Fig. 5.2);
– m: number of MPS realizations in a given generation (i.e. the fixed generation size);
– k: number of realizations which are combined simultaneously to get one merged realization;
– m_k: number of merged realizations produced for each generation;
– m_b: number of best realizations ($m_b \leq m_k$) that are retained among the m_k realizations;
– g: the number of generations considered.

Our basic algorithm to get one calibrated MPS realization is the following:

– Step 0 – Initialisation: provide m MPS realizations. Together, they form generation zero; $j = 0$;
– Step 1 – **Loop on generations**, for $j = 1 : g$;
  – Step 1a – Repeat m_k times: select randomly k realizations from population $j - 1$ and combine to form one merged realization of generation j;
  – Step 1b – Compute the forward model and the quality of each of the m_k merged realizations of generation j; the m_b best realizations are kept, the other realizations are discarded. $m - m_b$ fresh MPS realizations are added to the current generation;
– Step 2: Keep the single overall best merged realization among the merged realization of last population g.

Note that in step 1a, there are n Gaussian fields involved for each of the k selected realizations. Hence, the weights $a_{ij}, i = 1...k, j = 1...n$ have to be optimized under the constraints $\sum_{i=1}^{k} a_{ij}^2 = 1$, $\forall j = 1...n$. When facies HD are present, the constraints $\sum_{i=1}^{k} a_{ij} = 1$, $\forall j = 1...n$ also apply. Each iteration in the optimization of the weights requires the following operations to be done:

– Compute the merged Gaussians (i.e. $Z_{c,j}(\mathbf{x}) = \sum_{i=1}^{k} a_{ij} Z_{ij}(\mathbf{x})$ $\forall j = 1...n$);
– Code the facies corresponding to the merged Gaussians using the coding template;
– Compute the response function corresponding to the current facies field;
– Compute the misfit of the response function with the available auxiliary data.

Figure 5.3 illustrates the combination of $k = 2$ realizations with $n = 2$ Gaussians for different weights. For simplicity of illustration, here the same weights were applied to each Gaussian. Combined realizations represent smooth transitions between the two endpoint realizations, even in this unfavorable case where no HD were used.

5.3.4 Facies noise removal

After truncation of the Gaussians into categories some noise is usually observed on the merged image as shown in Fig. 5.4. We remove the noise by applying multi-categories version of classical morphological operators *closing* and *opening* (Serra, 1983). The *closing* favours regrouping of isolated pixels with higher facies code value, whilst *opening* favours the regrouping of isolated pixels with lower facies code value. The noise removal procedure is applied prior to computation of the forward response model to fully incorporate its effects on the response and misfit computation.

Figure 5.3 GDM applied on the dunes TI. The two input realizations are the ones on second row far left column and lower right sub-figures. These are merged using different weights shown on top of each sub-figure.

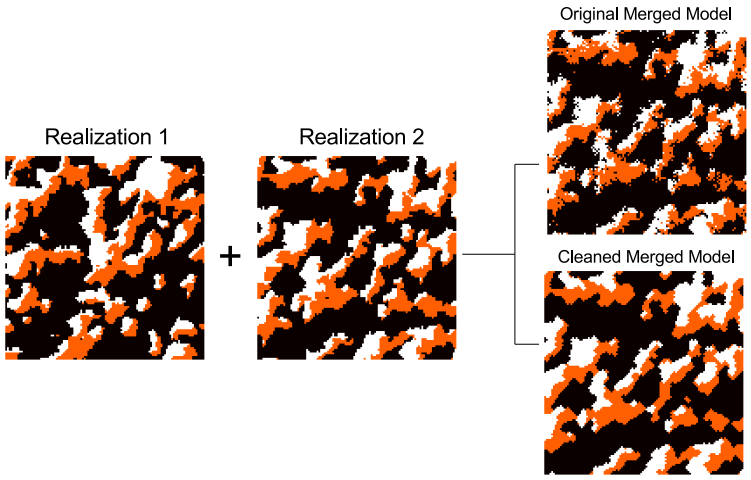

Figure 5.4 Two realizations (left), original and cleaned merged realizations. The cleaned realization is used in the forward modelling step.

5.3.5 Optimization

We used the efficient Pattern-search method implemented in Matlab (Hooke and Jeeves, 1961; Audet and Dennis Jr, 2001). The objective function in the optimization process is the sum of absolute differences between the response of the merged realization d_m and the observed data d_o:

$$O_m = \sum_{data} |(d_m - d_o)| \tag{5.1}$$

Due to the constraints on the weights used to form a merged realization, one has only $n(k-1)$ or $n(k-2)$ weights to optimize for respectively the unconditional and the conditional cases. The other weights are simply determined from the constraints and the optimized weights. Hence, in the conditional case, one has $\forall\ j = 1...n$:

$$c_{1j} = 1 - \sum_{i=1}^{k-2} a_{ij} \tag{5.2}$$

$$c_{2j} = 1 - \sum_{i=1}^{k-2} a_{ij}^2 \tag{5.3}$$

$$a_{(k-1)j} = \tfrac{1}{2}\left(c_{1j} + \sqrt{2c_{2j} - c_{1j}^2}\right) \tag{5.4}$$

$$a_{kj} = c_{1j} - a_{(k-1)j} \tag{5.5}$$

One verifies easily by direct computation that $\sum_{i=1}^{k} a_{ij}^2 = 1$ and $\sum_{i=1}^{k} a_{ij} = 1$, $\forall j = 1...n$. The computed weights $a_{(k-1)j}$ and a_{kj} are real provided $2c_{2j} - c_{1j}^2 \geq 0$ which was the case in all our tests. Otherwise, one can try a different initial solution in Pattern-search or more simply redraw from the generation pool a new set of k realizations to merge. A last alternative (because slower) would be to use a method for constrained optimization. For the particular case $k = 3$, it is possible to re-parametrize the weights with trigonometric functions such as to impose implicitly the constraints (Hu, 2002).

We emphasize that in the conditional case (i.e. with facies HD), all Gibbs sampling realizations must share the same n sets of Gaussian values at HD points in the n Gaussian fields. This is obtained by Gibbs sampling an initial MPS realization and then freezing the Gaussian values obtained at HD points for the Gibbs sampling of all the other MPS realizations. Owing to the constraint $\sum_{i=1}^{k} a_{ij} = 1,\ \forall j = 1...n$ the merged GDM realizations do recover the right facies at data points. At the end of the GDM process, a single calibrated conditional realization is obtained. So to get additional realizations, the whole process is repeated starting from a different MPS realization and different sets of Gaussian values retained at HD points.

The computation of some response functions can be CPU intensive. To diminish the computational burden, we set early stopping criteria ensuring to not iterate for only marginal improvement. This is justified as m_k merged realizations are produced at each of the g generations. Hence, calibration improvement need not be pursued too far for any single merging. Following generations will enable far better calibration than can be achieved with any single merged realization.

5.4 Results

The proposed GDM is tested over different synthetic test examples. We consider proportion maps, seismic section, shortest path problems for 2D and 3D cases and water-cut curves obtained from a flow simulator.

5.4.1 Proportion map example

Our first example comprises the gradual deformation of a set of 200 unconditional simulations using a TI of dunes (Fig. 5.2). The target variable is the local proportion of dune facies taken as the block average over local windows of size 5×5. Figure 5.5 shows two sample MPS used in the algorithm, the reference model, the output GDM model and the proportion maps. Visually, the patterns of facies proportions of the GDM realization appears quite similar to those of the reference image.

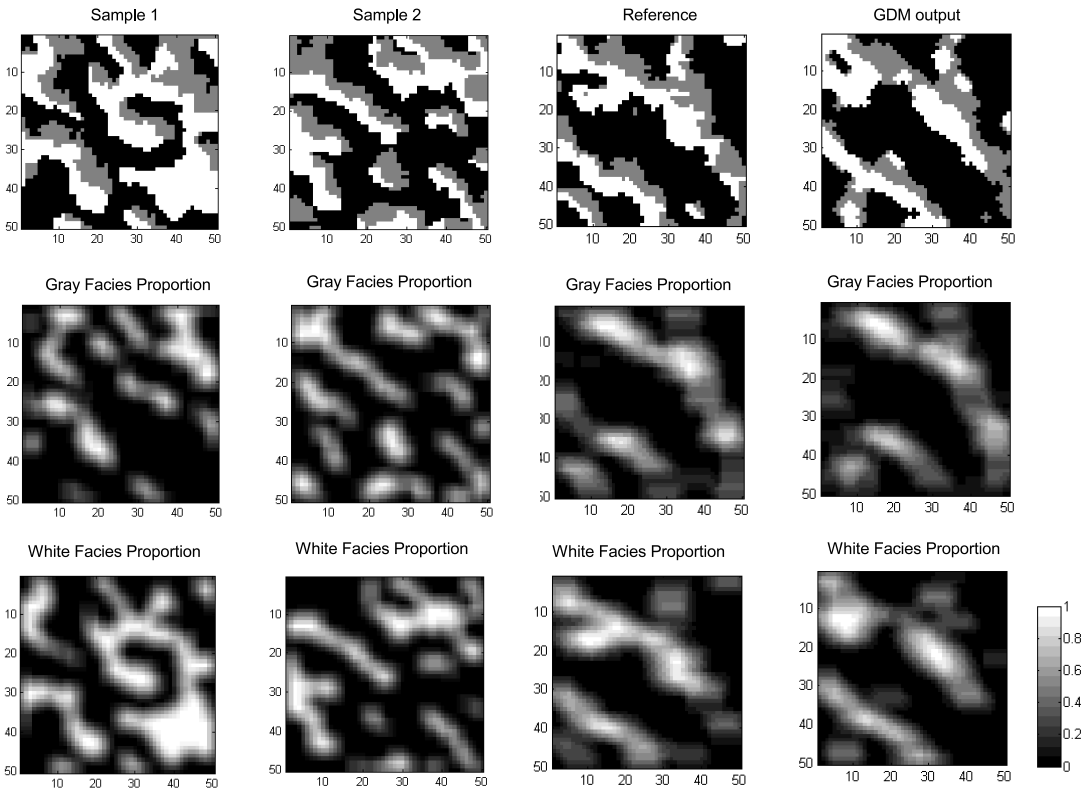

Figure 5.5 Proportion map test case. First row: from left to right, two sample MPS simulations, reference map and the final GDM model. Second row: grey facies proportions. Last row: white facies proportions. GDM applied with parameters m=200, n = 2, k=4, g=110, m_k=20, m_b=10.

Figure 5.6 illustrates the best calibrated realizations for various generations. In the first generations, important differences are observed between the best realizations. As the process evolves, the best calibrated realizations become more similar although non-negligible differences are still observable even after 50 generations.
Figure 5.7 shows different calibrated GDM realizations. The e-type map computed over 50 realizations match well the target proportions. Although common structural characteristics are observed for the different realizations, significant differences are also visible.

5.4.2 Shortest path 2D example

The harmonic average of the permeability fields along streamlines was used as a proxy for flow simulation by Caers (2003). We assume the travel time between two pixels is inversely proportional to the harmonic average of the permeability. We use the Dijkstra algorithm (Dijkstra, 1959) to find the fastest paths between inlet and outlet regions. In our example the inlet is a central injector well with four producer wells (P1 to P4) as outlets located on the corners in a quarter five-spot arrangement of injection and production wells. The proposed GDM was tested with example of the Dunes TI with three facies as shown in Fig. 5.8. Figure 5.8 shows two sample MPS realizations, the reference and GDM output. The travel times from the injector to each of the producers are given. The travel times obtained by GDM are substantially closer to the reference times than the two sample MPS realizations. Moreover, the GDM facies distribution retains visually the main arrangement observed in the reference and the initial MPS realizations. The big white-gray patch in the bottom part of the reference image is partly recovered in the GDM although this patch is absent in the initial MPS realizations shown.

5.4.3 Seismic section example

A third test case is the calibration to a known seismic section. The selected image (Fig. 5.9) shows the cross section of a series of channels over a grid of size 50×150. The channels and background are assumed to have different but constant velocities and densities. The forward model computes the synthetic seismic amplitude data corresponding to a given channel distribution in the section. Figure 5.9 shows the TI used, sample initial MPS realizations, the reference field and the calibrated GDM realization. The misfit value of the final GDM model is considerably lower than all the input MPS models as illustrated in Fig. 5.9. All the main structures of the reference model are identified and only relatively small differences with the reference are observed.

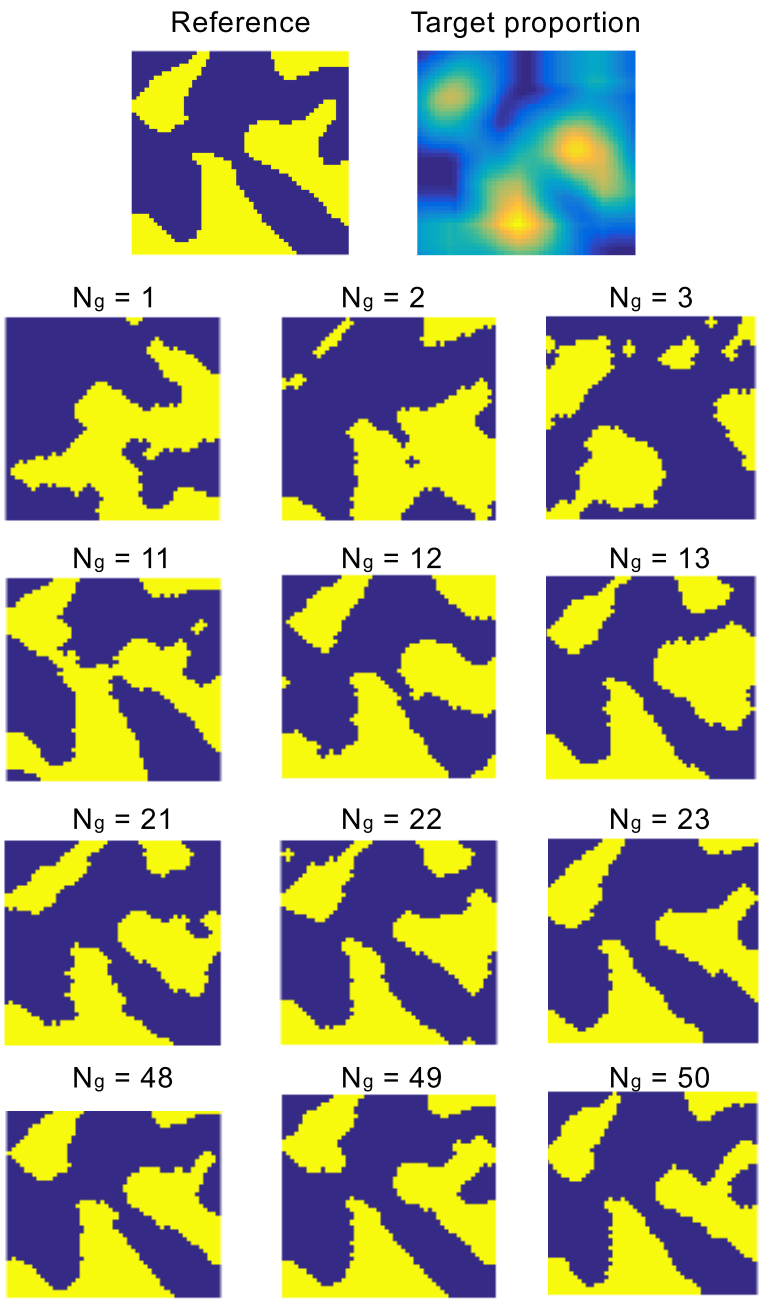

Figure 5.6 Proportion map test case. First row: Reference and target proportion. Second to last rows: best merged calibrated realisation obtained at different generations. GDM applied with parameters m=500, $n = 2$, k=4, g=50, m_k=20, m_b=10.

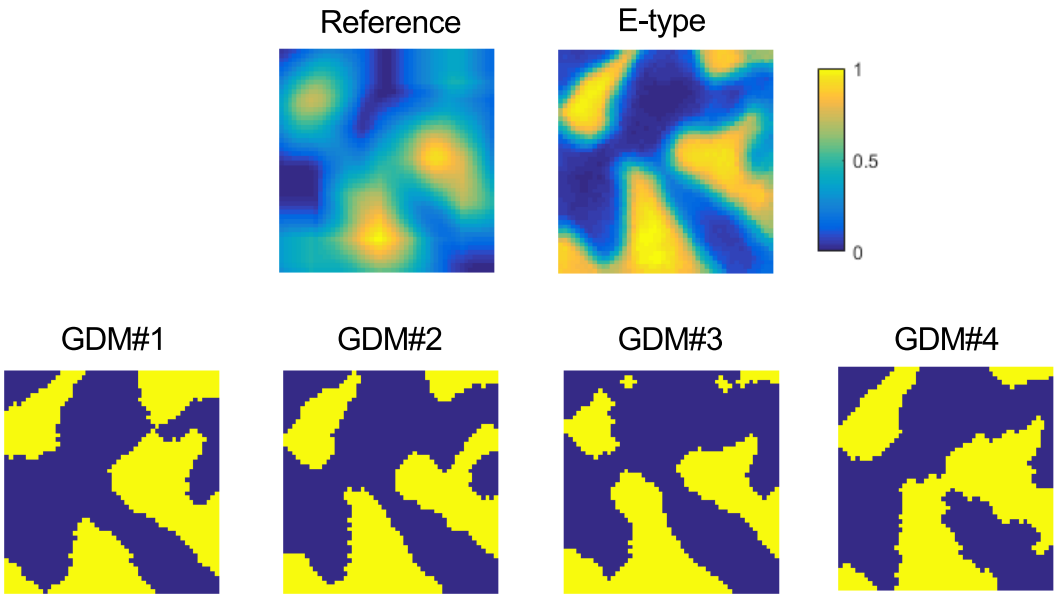

Figure 5.7 Proportion map test case. First row: Target proportion and e-type over 50 realizations. Second row: four different calibrated GDM realizations. GDM applied with parameters m=500, $n = 2$, k=4, g=50, m_k=20, m_b=10.

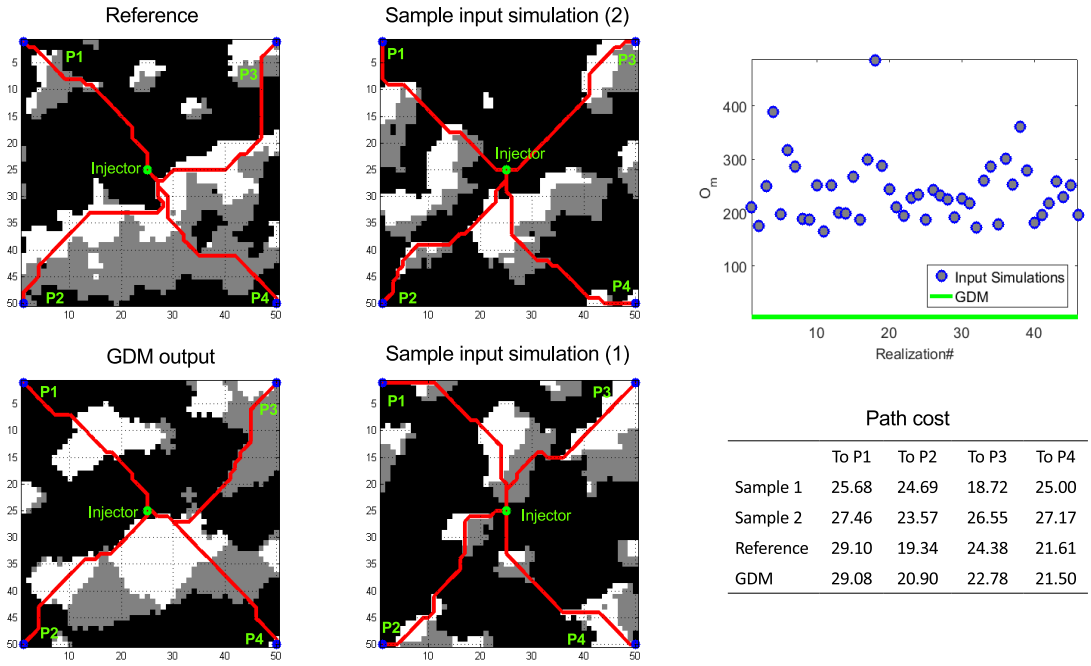

Path cost

	To P1	To P2	To P3	To P4
Sample 1	25.68	24.69	18.72	25.00
Sample 2	27.46	23.57	26.55	27.17
Reference	29.10	19.34	24.38	21.61
GDM	29.08	20.90	22.78	21.50

Figure 5.8 Travel time test case. P: producer well. Travel times between injector and producers are given for reference field, two sample MPS realizations and GDM output. Misfit shown on the rightmost sub-figure. GDM applied with parameters: m=50, n = 2, k=4, g=50, m_k=20, m_b=10.

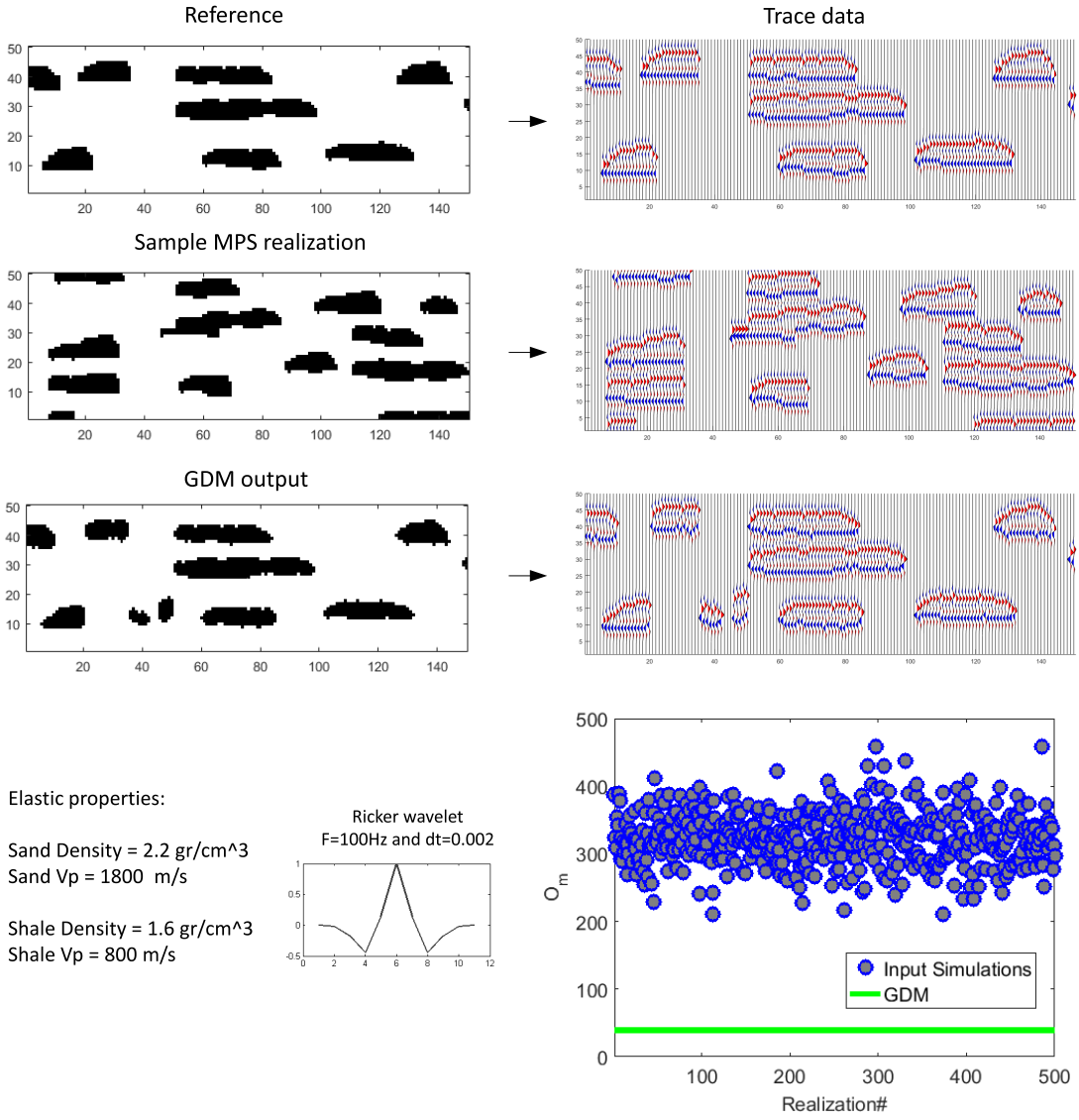

Figure 5.9 Seismic section calibration example. Elastic properties and wavelet: bottom left sub-figure, misfit of input MPS and GDM-calibrated: bottom right. GDM applied with parameters: m=500, n = 2, k=3, g=500, m_k=20, m_b=10.

5.4.4 Shortest path 3D example

The proposed GDM approach applies equally well to 3D problems. A 3D TI representing the hydrofacies in an alluvial aquifer in the Maules Creek valley, Australia [1] is used (see Fig. 5.10).
Figure 5.11 shows the paths and particle travel time for one sample initial MPS realization, the reference field and one GDM calibrated field. Although some differences exist between the GDM and the reference shortest paths, the travel time along the paths are identical.

5.4.5 Water Cut Example, 2D Case

A corner-point grid of size $50 \times 50 \times 1$ with cell dimension [1000, 1000, 5] meters was generated using the Matlab Reservoir Simulation Toolbox (MRST) (Lie, 2014; Lie et al, 2012). The facies and fluid parameters are given in Table 5.1. The fluid is injected from I1 at flowrate of 0.0021 m^3/s and is recovered at the producers (P1 to P3). The initial saturation model assumes the bottom of the reservoir is saturated with water and the top with oil. The injector pressure is constant along the whole borehole length.

The water cut curves at the three producers were calculated for 30 time periods of 121 days spanning 10 years in total. The water cut curves in the reference model were used as calibration target. Figure 5.12 shows the initial saturation model, the reference facies model, one sample simulation and the output GDM model (colored with horizontal permeability values). The MPS and the GDM respect HD at the four well locations. Water cut results at the wells are shown in Fig. 5.13. The conductive facies path between I1 and P1 makes the water cut at P1 the quickest in the reference model. This feature has been well captured in the output facies model of GDM where I1 and P1 are connected with the light blue and yellow high permeable facies. Water cut is observed later at P2 and last at P3. The three curves are well reproduced by the GDM model.

5.4.6 Water Cut Example, 3D Case

A similar 3D test case with TI from Fig. 5.10 is considered. To reduce the CPU time, only a portion the TI was used, i.e. $15 \times 15 \times 10$ cells of size [1000 - 1000 - 5] meters. The petrophysical properties of the facies and the fluid properties are presented in Table 5.1. One injector (I1) and one producer was considered (P1). The same fluid and injection rate were used as in the 2D case. Also similar to the 2D case, the bottom of the reservoir was initially water-saturated and the top oil-saturated (see sW grid Fig. 5.14). The flow simulation was

1. online available at http://trainingimages.org/training-images-library.html

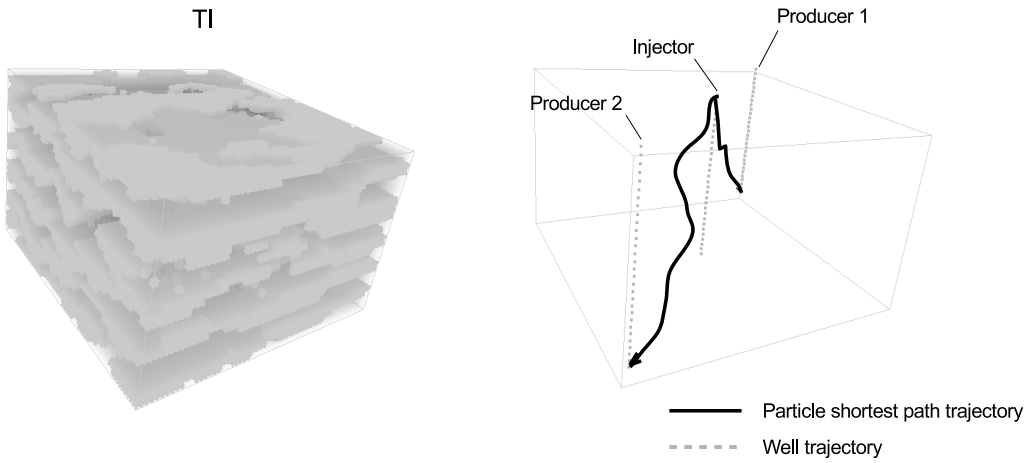

Figure 5.10 TI selected from Maules Creek Australia (left) and reference shortest paths between injector-receivers (right).

Table 5.1 Parameters used in the 2D and 3D water cut examples.

Case	Property	Value	Units
2D (Fig. 5.12)	Porosity	F1-10 ; F2-20 ; F3-35	%
	Horizontal Perm.	F1-300 ; F2:-500 ; F3-1000	mD
	Vertical Perm.	F1-30 ; F2-50 ; F3-100	mD
3D (Fig. 5.14)	Porosity	F1-10 ; F2-20	%
	Horizontal Perm.	F1-10 ; F2-500	mD
	Vertical Perm.	F1-1 ; F2-50	mD
2D and 3D	Viscosity	Water-1 ; Oil-5	cP
•	Compressibility	Water-0 ; Oil-0.001	psi^{-1}
	Density	Water-1000 ; Oil-700	kg/m^3

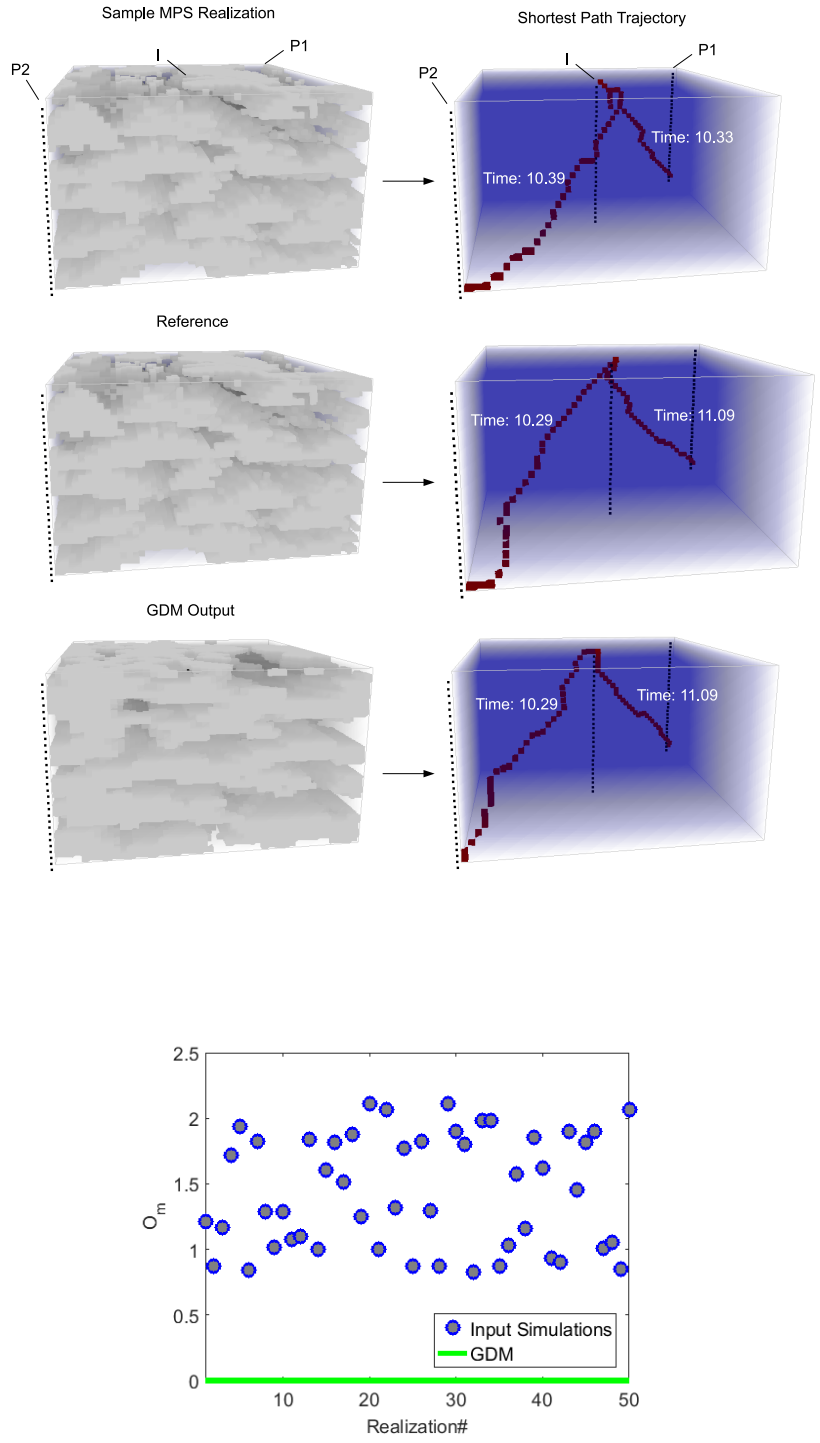

Figure 5.11 Shortest path travel time 3D example. Top: sample initial MPS realization, middle: reference, bottom: one GDM-calibrated realization. The misfit of input realizations are displayed in the bottom figure as compared to the GDM final model misfit. GDM applied with parameters: m=50, n = 3, k=4, g=40, m_k=20, m_b=10.

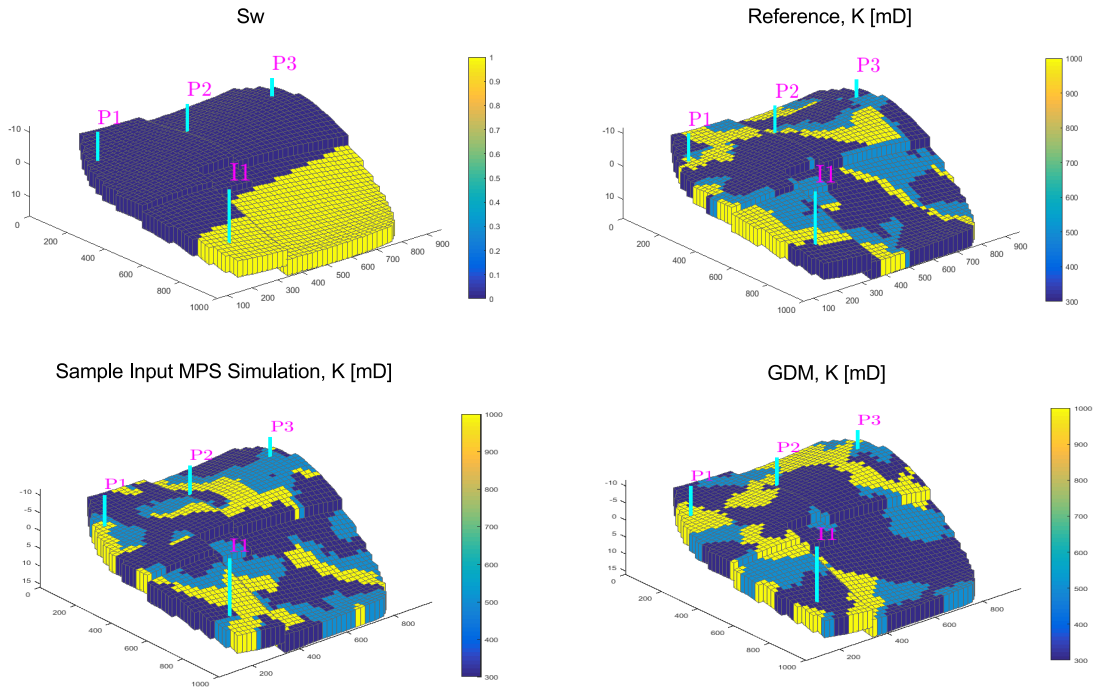

Figure 5.12 Two-phase 2D water cut example. Water saturation (top left), reference (top right), one initial MPS realization (bottom left), GDM calibrated realization (bottom right). GDM applied with parameters: m=50, n = 2, k=4, g=10, m_k=10, m_b=5.

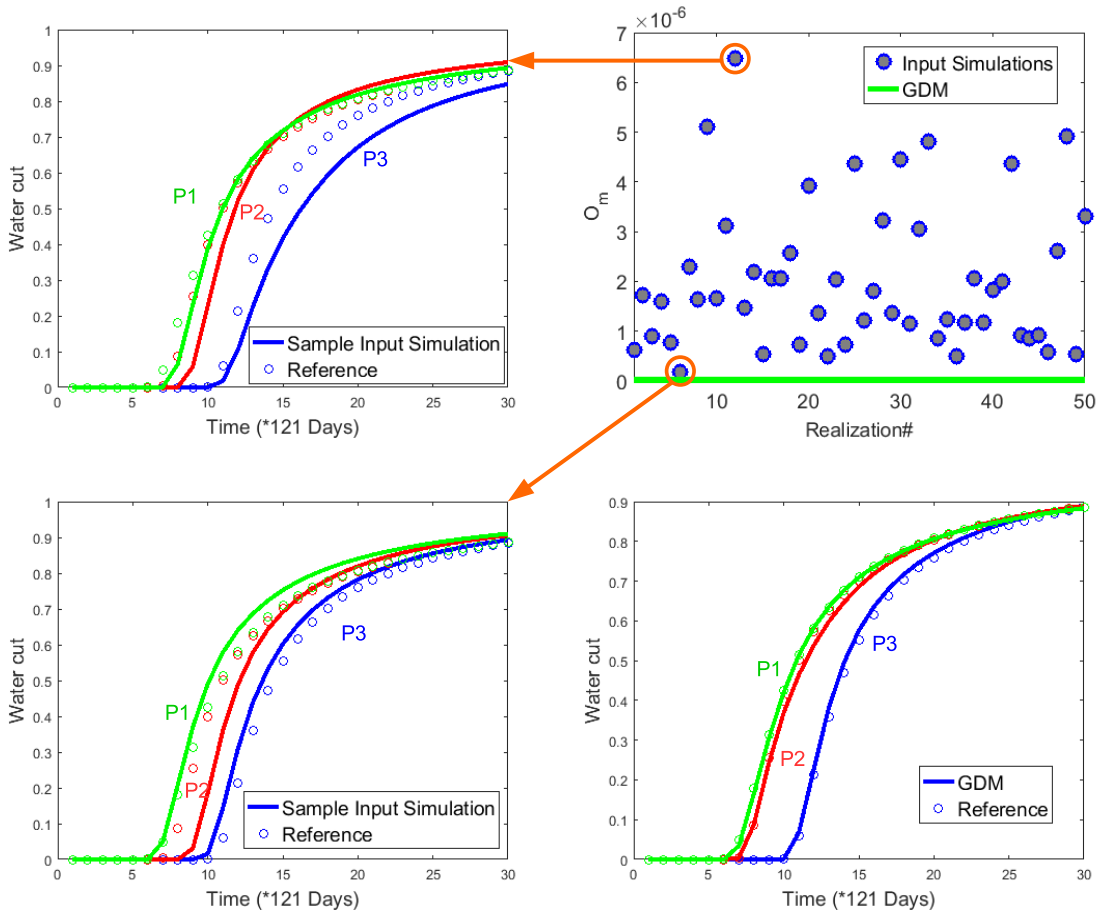

Figure 5.13 Water cut curves at wells P1 to P3 for two initial MPS realizations (left) and GDM-calibrated realization (lower right). Misfit values of 50 MPS realizations and GDM-calibrated realization (upper right).

run over a time span of 10 years sampled 15 times at every 244 days. Figure 5.14 shows the reference model, one sample simulation and the GDM output. The output water rate at the producer (P1) is plotted for the reference model and the best GDM output obtained at increasing generations in Fig. 5.15. Thirteen generations are sufficient to calibrate the target water cut curve.

5.5 Discussion

The proposed calibration method enables to calibrate multipoint realizations to dynamic or other auxiliary data. The basic idea is to associate latent Gaussian fields to the MPS facies thru a lithotype or coding template and Gibbs sampling. The number of Gaussians is kept low (from one to three). Once in the Gaussian space, the fields are gradually deformed using GDM.

Our method of application of GDM is original. It borrows ideas from evolutionary optimization methods. For the next generation, a group of m_k offspring are created by each merging k randomly selected realizations (mating parents). Only the m_b fittest offspring survive. The new generation is completed by adding $m - m_b$ fresh MPS realizations to allow enough diversity in the new generation. The process is repeated for as many generations as desired (or needed) to reach a good calibration to the auxiliary data. Note that for each of the m_k mating, the k realizations are randomly selected from a pool of m individuals. Hence, each merging can involve only evolved parents, only fresh MPS realizations or a mix of the two in various proportions. Moreover, it might occur that the best merged model from current generation is not involved in any of the mating. Moreover, it is unlikely that any of individuals in current generation (including the fittest individual) mate for a significant portion of the offspring for next generation. So, promotion of diversity and possibility to escape from local minima is intrinsically built-in our approach.

The proposed GDM approach was tested for different types of target variables: proportion maps, section of seismic amplitudes, global travel time between source and sink (proxy for flow simulation), and dynamic response in flow simulation. In all cases GDM was able to produce well calibrated realizations in a reasonable computing time. The best calibrated realization in the last generation showed significantly better fitness statistics than any of the raw MPS realizations in all the test cases.

In our approach, two particular steps are more CPU demanding. The first one is the Gibbs sampling step which has to be applied to all points for each MPS realization considered. We note however that only the correlation at short distances need to be reproduced as all large scale features are implicitly controlled by the MPS realization. Hence, the burning period

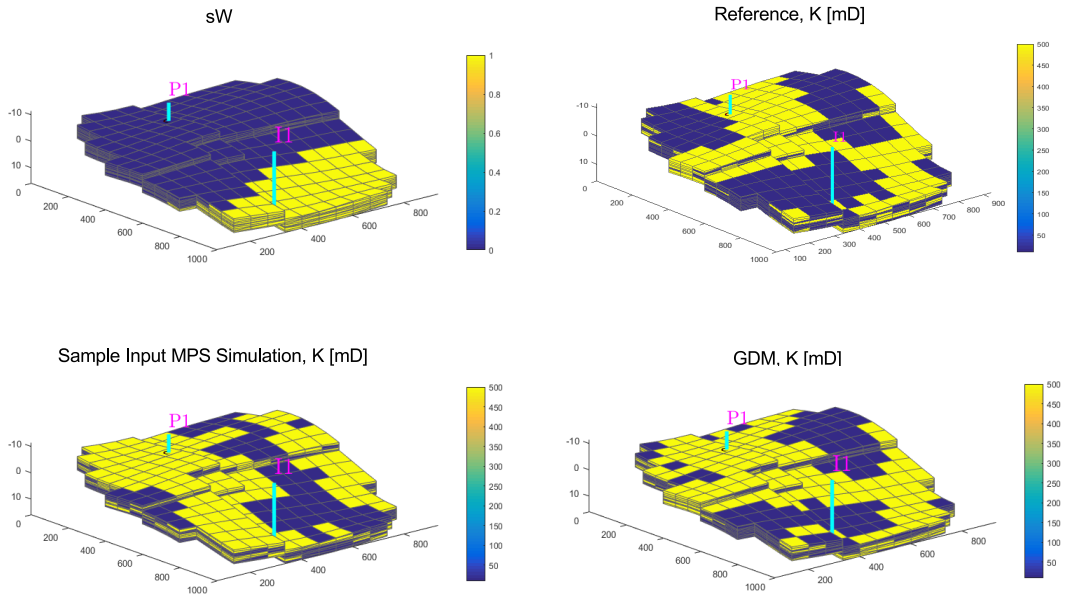

Figure 5.14 Two-phase 3D water cut example. Water saturation (top left), reference (top right), one initial MPS realization (bottom left), GDM calibrated realization (bottom right). GDM applied with parameters: m=50, n = 2, k=4, g=13, m_k=10, m_b=5.

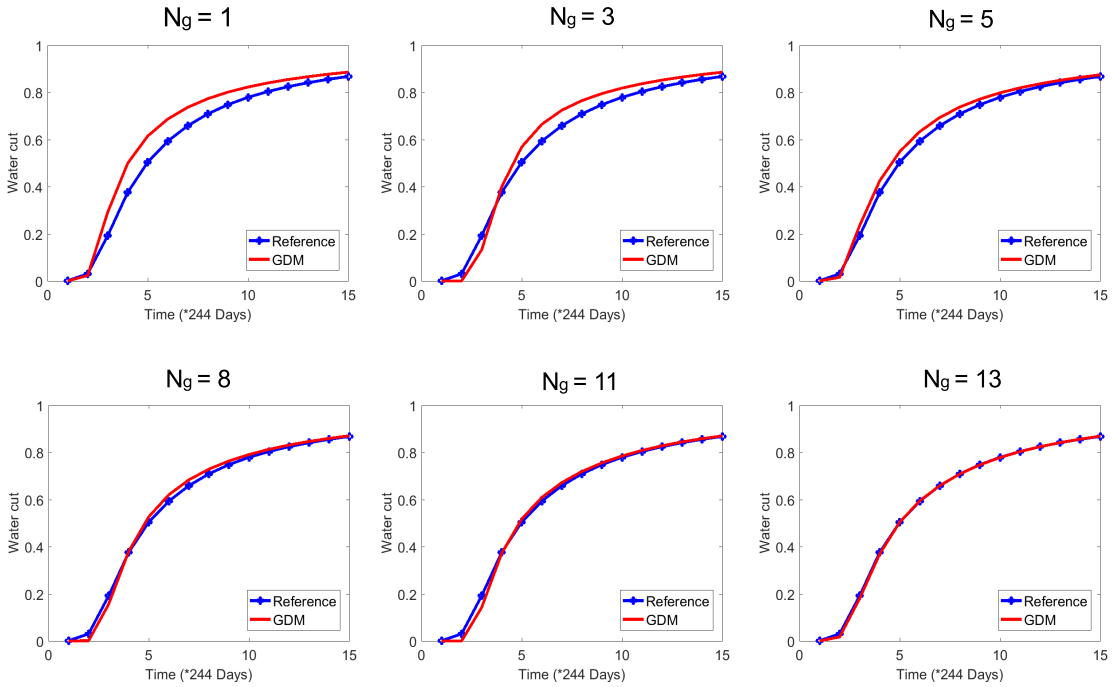

Figure 5.15 Water cut curve at the well P1 for the best GDM model after N_g generations.

and the number of iterations can be kept small without affecting the results significantly. The second demanding step can be the computation of the forward model giving the response of the model and the associated misfit value. The time required is then strongly depending on the particular response function of interest. For large fields and demanding forward model, one could have to recourse to parallel computing of the different responses. We note that our approach is easily parallelizable. For a given generation each merged offspring can be assigned to a separate computing unit. The creation of all required MPS realizations, can be distributed as well.

We emphasize that the spatial structures of the Gaussians in the Gibbs sampling step need not be modelled with any more detail than specifying the type of model to use (e.g. spherical or cubic covariance) and a correlation distance roughly compatible with the size of the facies units. The details of the structure of the resulting Gibbs sampled fields, including possible large scale features such as anisotropies and non-stationarity of the field, are jointly controlled by the initial MPS realization itself and the coding template adopted.

At the end of the last generation, we keep only the fittest individual among the offspring. The other calibrated realizations in the last generation cannot be considered independent as they most likely share common parents or ancestors. It is advisable to start anew the whole process to get independent calibrated realizations.

One difficulty with the proposed approach is the possible presence of noise in the facies image obtained after merging the Gaussian values corresponding to different MPS realizations, especially when no facies HD are present (unconditional case). The noise can be reduced by selecting a more continuous Gaussian covariance (e.g. cubic model instead of spherical), or by increasing the correlation distance. One solution that gave good results in our tests was to apply simple morphological operators. *Opening* and *closing* with a small diamond structuring element of size 3×3 was efficient at removing speckles in images. The operators were applied of course prior to computation of the forward model to ensure including their effects in the optimization and the calibration. In the conditional case, the facies HD reduced the differences between the Gaussian fields involved in the merging. This had the effect of also reducing the noise.

One requirement of our approach, common to all calibration methods, is to have an adequate forward model for computation of response and misfit objective function. Any forward model error affects negatively the performance of the calibration.

In this study the evolutionary GDM was applied to facies models obtained by MPS. The approach is however general and can be applied to facies models obtained with other categorical simulators such as MCP, object-based, process-based, or else, as long as the methods used can produce conditional realizations honouring the facies HD when present. One can

also use a mix of facies models obtained by different methods (e.g. object-based, MPS and MCP) or based on different TIs to favor more diversity and variability in the merged and final calibrated realizations.

5.6 Conclusions

A new evolutionary gradual deformation method was developed to calibrate MPS realizations to large scale soft data and global dynamic data. The method was applied on different target variables such as proportion maps, seismic amplitude section, 2D and 3D travel times along shortest paths, and water-cut curves obtained from flow simulation. Both unconditional and conditional cases were tested. The computation time of the method was tractable in all cases considered. The approach is general, it can be applied to calibrate facies models obtained by any simulation method.

5.7 Acknowledgement

Research was partly financed by NSERC (RGPIN-2015-06653). Also authors would like to express their thanks to TOTAL for providing the TI in Fig. 5.1.

CHAPTER 6

INTEGRATED MODEL

6.1 Introduction

The three ideas proposed in previous chapters on MPS conditioning to hard and soft data and their calibration to dynamic data were tested and applied on various cases separately, however in real domain all such conditioning data should be accounted for in facies modeling. This chapter presents a small example with hard, soft and dynamic data. Using a binary sand-shale TI, a reference model is created and used to generate soft, hard and dynamic data. Multiple realizations are created conditioned to both hard and soft data. Simulations are performed using ATIs and the probability fields calculated from all soft data sets. Hard data conditioning rate is 100% in all realizations, and the e-type map of the realizations resembles the input probability fields. The conditional simulations to both hard and soft data are used in GDM to generate calibrated models to water cut curves simulated over the reference model.

6.2 Input data

We start from a TI of size 200×200 with two facies *F1* and *F2* colored blue and yellow for shale and sand respectively (Fig. 6.1). *F2* comprises approximately 37% of the the reference model was generated using a conditional MPS simulation over a grid of 500×500. The simulation was conditioned to soft data with a smooth trend showing larger proportion of *F2* eastward. Figure 6.1 shows the TI on left with the reference model in the middle. The reference model was sampled over 250 locations considered as hard data (Fig. 6.1 right sub-figure). We generate three layers of soft data. Soft data are generated in the way that each reflects only some parts of the reference model. Soft data layers are displayed in Fig. 6.2. Soft data layer 2 is mainly reflecting the trend while layer 1 remotely indicates high proportion areas for *F2* in the western part, and layer 3 has higher resolution and correlates positively to *F1* (highlighted with red rectangles on Fig.6.2). Layers 2 and 3 bear subtle local correlations to the facies proportions in the reference field, but missed completely the global trend.

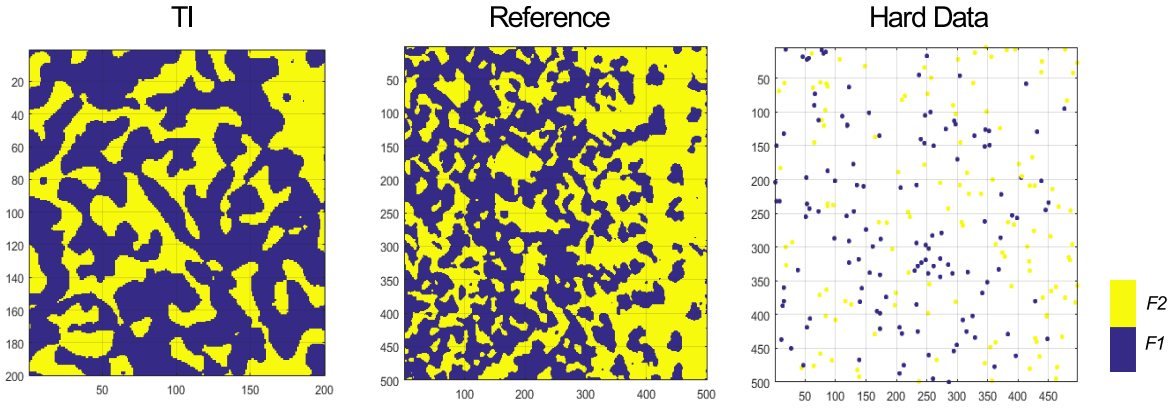

Figure 6.1 The TI was used to create the reference model from which the hard data on right are extracted.

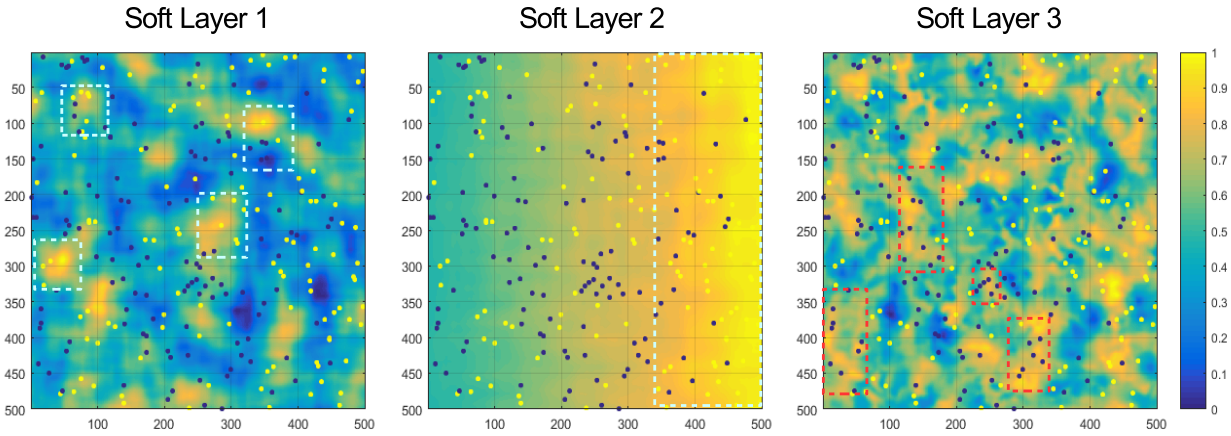

Figure 6.2 Three layers of soft data. The areas highlighted with colored rectangles refer to the correlation between soft data values and facies coding. Red boxes highlight the areas where *F1* and higher values of soft data correlate positively, and the opposite for light blue rectangles.

6.2.1 Probability maps

Next step is to integrate all soft data layers with hard data to produce facies probability maps. Multinomial logistic regression aims at exploiting all *useful* information in soft data layers to calculate the probability per facies maps. As for testing and comparison purposes, the probability fields were calculated seven times each integrating in multinomial logistic regression different layers of soft data layers as inputs. Figure 6.3 shows the input soft layers ($S1$, $S2$ and $S3$) on top, and the corresponding output probability maps of *F2* on middle and bottom rows. Probability fields based on individual soft layers as inputs (second row) capture much less details of the reference model than the combined soft layers (bottom row) illustrating better both the trend and local details captured with $S1$ and $S3$. To have a clearer understanding of the influence of each soft layer on the classification, the true positive rate is calculated for each combination too. The true positive rate of classification is in this case the portion of $F2$ classes which are correctly classified as $F2$ (Fig. 6.4). The most influential soft layer is $S2$ showing the trend. This can be verified with the map (in Fig. 6.3) without $S2$ in $P(S1 + S3)$ which largely misses the trend and to some degrees the details. Based on this figure the least effective soft layer is $S3$, and the most effective combination is $P(S1+S2+S3)$ that shows greater details as compared with other maps with not full set of soft layers. The probability for *F1* is not shown; it is simply the complement of that of *F2*. The probability maps from $P(S1 + S2 + S3)$ were used in MPS conditional simulations.

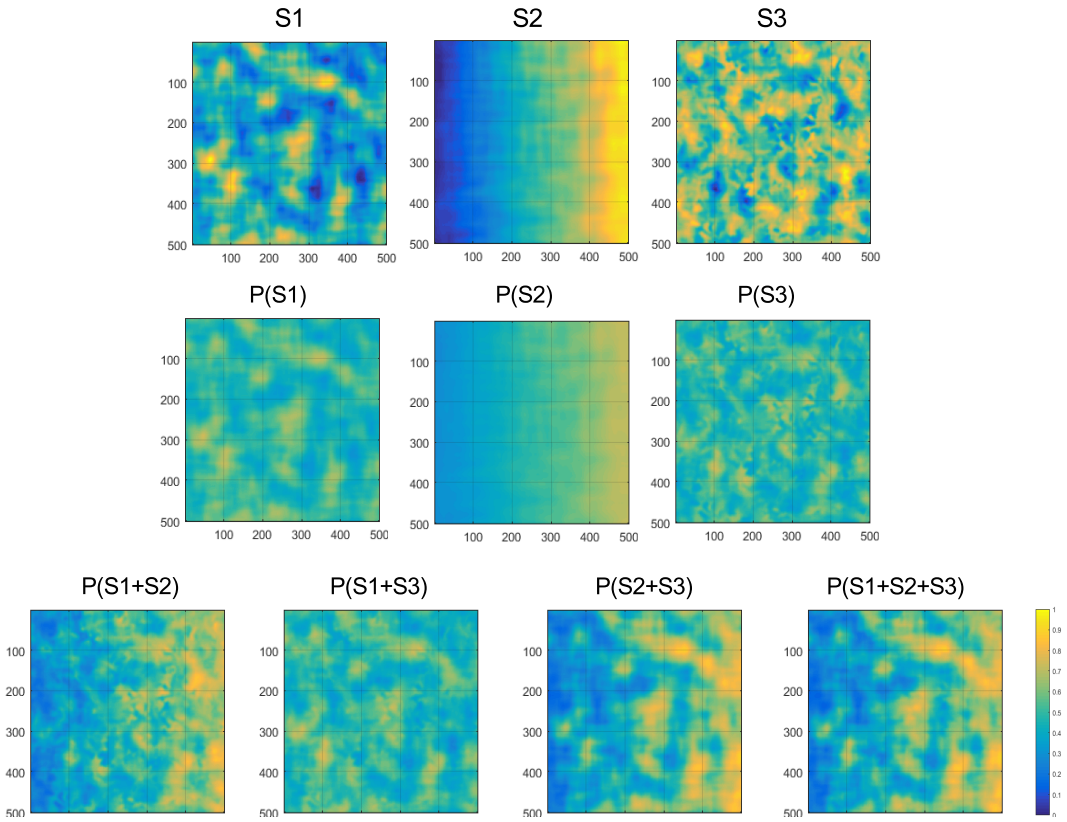

Figure 6.3 Three soft data layers on top are merged in different ways generating probability fields of $F2$. $S1$ to $S3$ refer to soft layers 1 to 3, and $P(S1 + S2)$ means the probability calculated with soft layers 1 and 2.

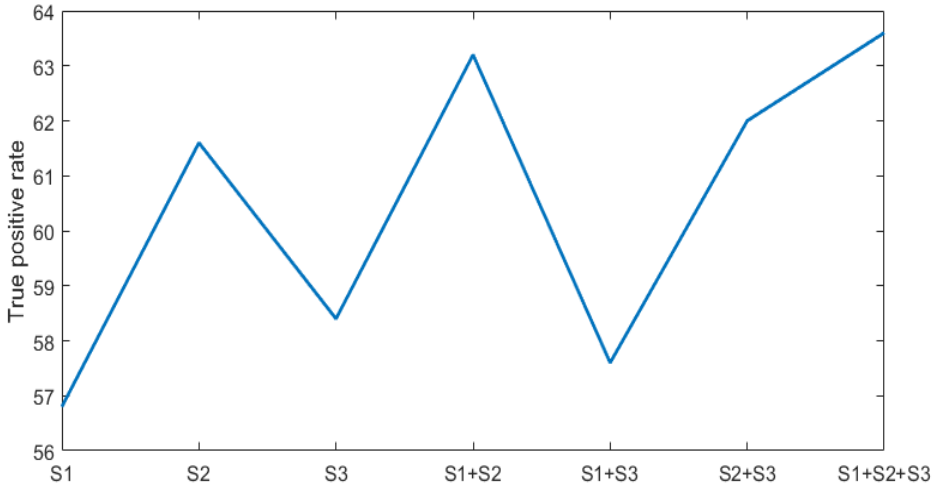

Figure 6.4 The influence of different combination of soft data in classification results.

6.2.2 Dynamic data

The reservoir grid was taken smaller (50×50) than the original grid (500×500) for the sake of faster flow simulations. Figure 6.5 shows the reference model and the reservoir grid highlighted with red dashed line rectangle. There are 4 wells inside the modelling box (corresponding to hard data locations). We consider one injection $I1$ and three production wells $P1$ to $P3$. Details on the petrophysical properties of the medium and flow features are given in Section 6.3.6. The dynamic response of the reference model within the reservoir grid in the form of water cut curves at production wells is displayed in Fig. 6.6. Due to the permeable connecting body between $I1$ and $P3$, water breakout first happens at $P3$ followed with $P2$ and $P1$ respectively. The residence time from injector to producer known as time of flight (TOF) is considered as one of the flow diagnostic defined as the amount of time it takes for a neutral particle to travel from a nearest injector to a specific point in the reservoir volume (Lie, 2014). From it one can identify the high- and low-flow (stagnant) regions in dark red and yellow respectively. An stagnant area can be identified on the lower left part of the grid. Drainage (area of influence) is defined as a region in the reservoir volume drained by each producer (Lie, 2014). It is obtained by thresholding the tracer distributions.

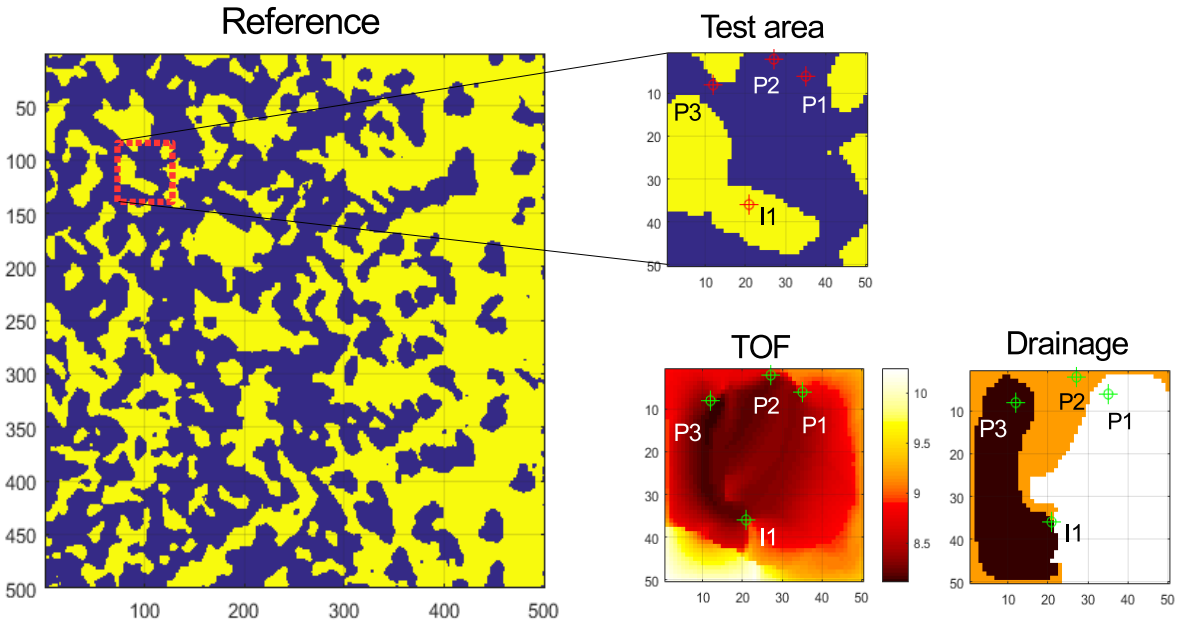

Figure 6.5 Reservoir grid extracted from the reference model used for flow simulations. The variations of TOF values on base 10 logarithmic scale.

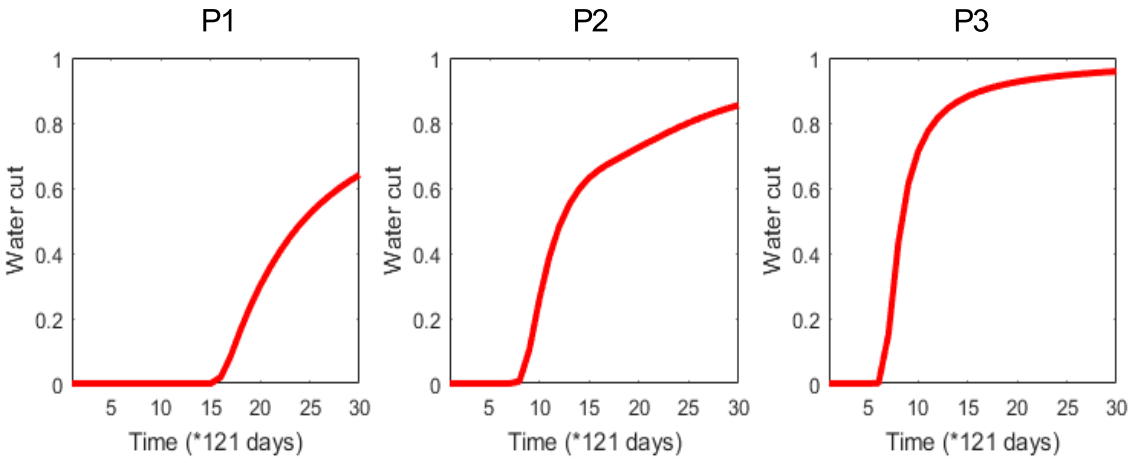

Figure 6.6 Water cut curves at production wells. One time unit on the X axis counts for 121 days totalling a 10 years time period of flow simulation.

6.3 Modelling Process

The purpose is to generate multiple realizations of facies areal distribution conditioned to hard and soft data and calibrated to dynamic water cut curves.

6.3.1 TI Enrichment

The facies modelling process starts with generating a number of ATIs from the original TI to enrich the pattern database. ATIs are simulated over the same grid size as reference model (500×500). They are selected through the process described in Section 3.3.5. Figure 6.7 shows three sample ATIs randomly selected among the 10 ATIs considered for simulations. The simulation patch size is considered 50×50. The average number of matching patterns for all hard data patches in the original TI was 20,000, however within 10 ATIs of the same size, the number reaches 210,000 increasing by a factor of 10 almost equal to the number of added ATIs.

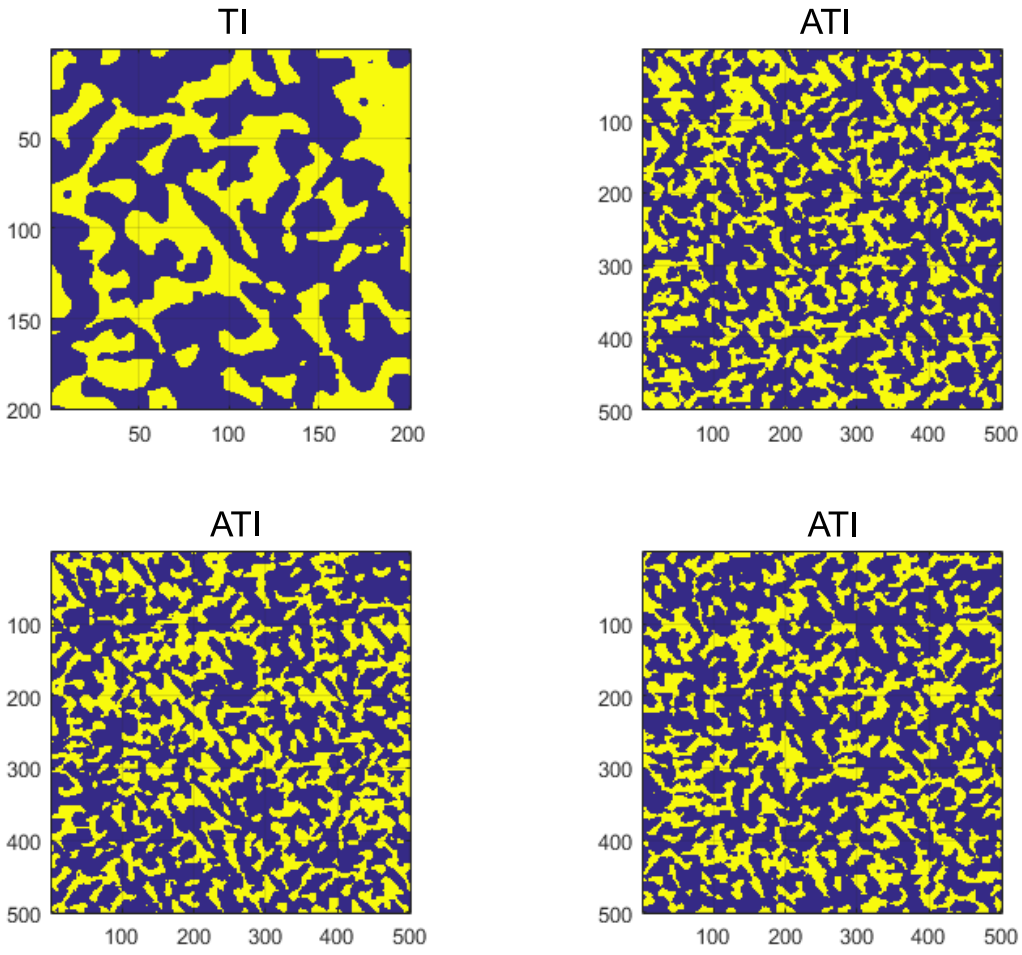

Figure 6.7 The original TI and three randomly selected ATIs.

6.3.2 Hard Data Conditioned Models

The first conditional simulations use only hard data. Figure 6.8 shows two sample simulations with hard data. The test was repeated with and without ATIs for better understanding of ATIs influence on conditioning rates. Figure 6.9 displays the box-plot of conditioning rates to hard data over 100 realizations with and without ATIs. The conditioning rate for all 100 simulations with ATIs is 100 % while the average conditioning rate for simulations without ATIs reduces to 83 %. In both cases the hard data weight was considered 50 times more than

overlap area pixels. The facies structures in simulations displayed in Fig. 6.8 are similar to TI, however as can be seen in the e-type map, hard data only are not enough to impose the E-W trend and local proportion variations. This requires to add soft conditioning data.

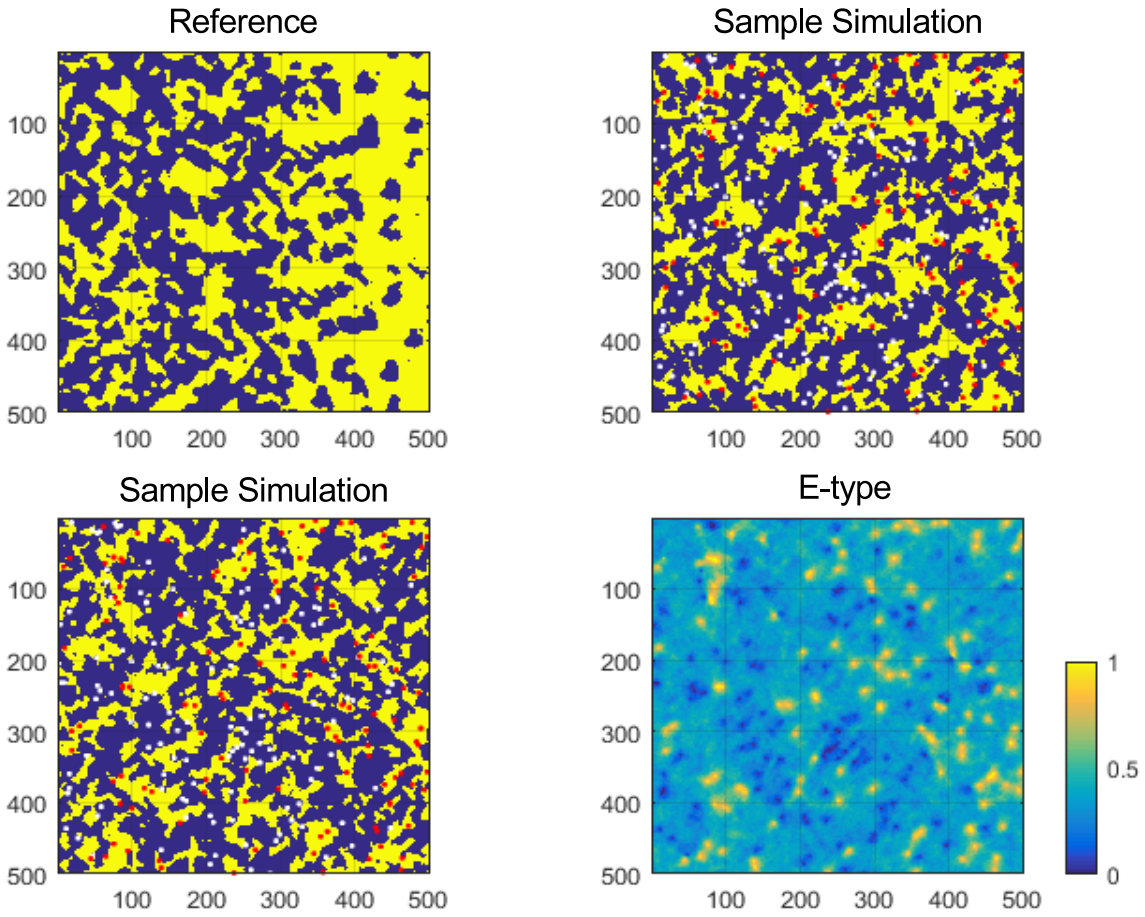

Figure 6.8 The sample realizations conditioned to hard data only. The e-type map for 100 realizations.

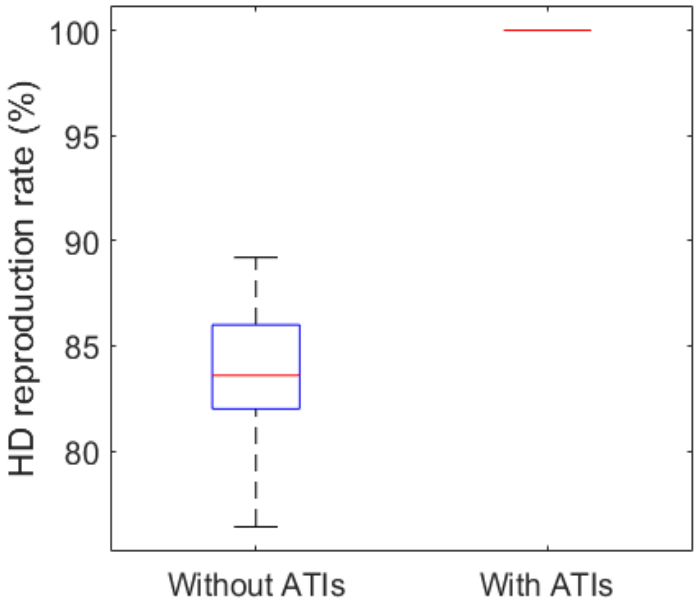

Figure 6.9 Box-plot of conditioning rates of 100 realizations with and without ATIs.

6.3.3 Soft Data Conditioned Models

Soft data conditioning is done using the approach in Chapter 4. The value of $\alpha \approx 0.65$, weight given to soft data in MPS, was determined using the McFadden test described in Section 4.3.2. A unilateral simulation with patch size randomly selected from [40-60] pixels was used. The number of candidates to select the final pattern from has been 100. For testing purposes the first simulations were performed using only soft data for a better understanding of the interaction of soft and hard data on the conditional simulations. Figure 6.10 shows sample conditional simulations and also the e-type of 100 realizations. The e-type map shows a match with input proportion map of *F2*, both the E-W trend and local high proportion areas. The Pearson correlation coefficient between e-type map and the input proportion field is 0.85. However, such models are not valid as long as they are not properly conditioned to hard data.

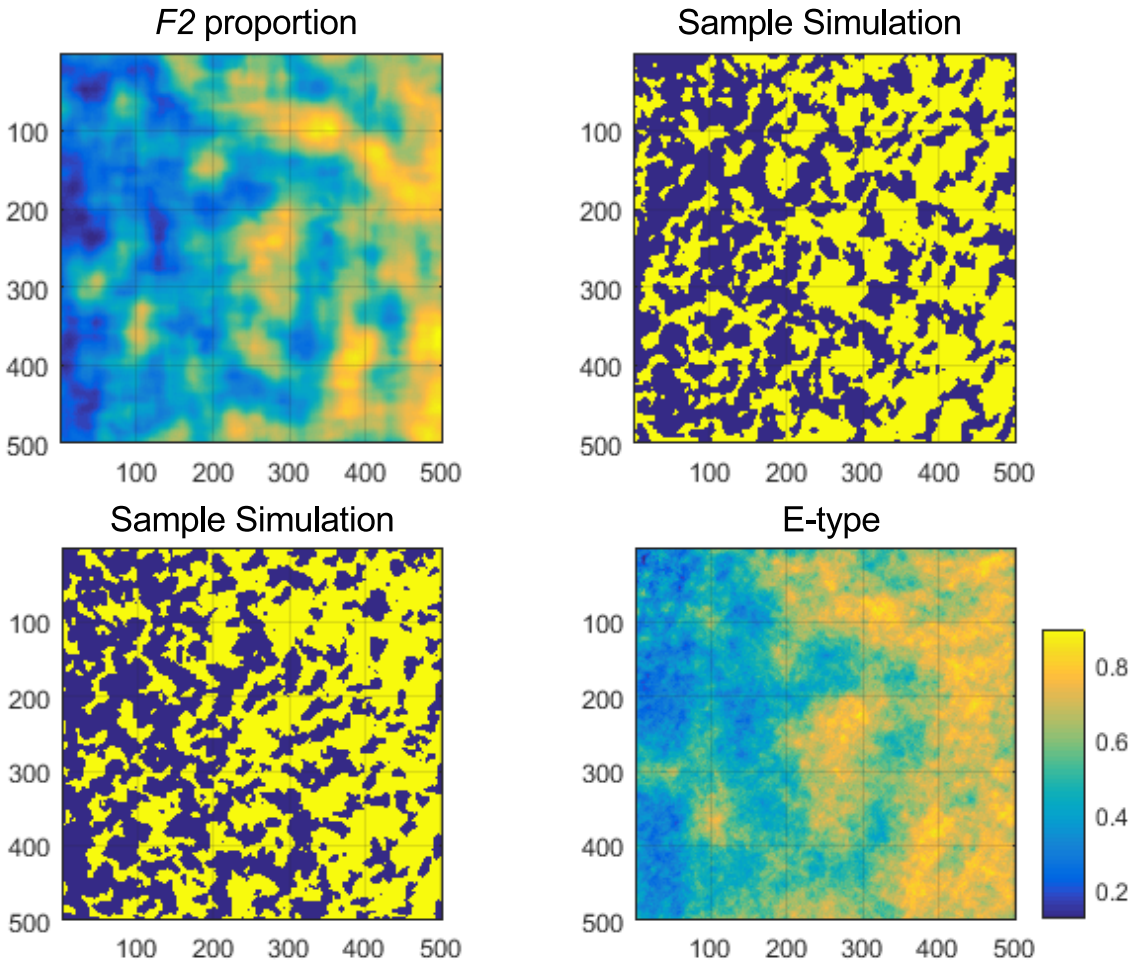

Figure 6.10 Sample simulation conditioned to soft data only. The e-type map for 100 realizations. The Pearson correlation coefficient between e-type map and input proportion map is 0.85.

6.3.4 Hard and Soft Data Conditioned Models

The simulations in this part were conditioned to both hard and soft data. This would eventually provide input realizations for dynamic data calibration using GDM. Figure 6.11 shows the simulation results. Among 400 realizations two sample simulations are displayed that show the trend while reproducing locally the hard conditioning data. Here, a higher number of realizations (400) was used to better assess the e-type map. The reproduction

of hard data has been 100% in all realizations, and the input probability fields are well reproduced by the e-type map. The Pearson correlation coefficient between e-type map and probability map is 0.72, lower than that of the soft data conditioned models (Fig. 6.10) which is due to the hard data by fixing the conditioning data sampling points. The 0.13 reduction of correlation which is deemed acceptable considering the necessity to reproduce hard data. The reproduction of hard data in soft-conditioned models by mere chance is 54%. The E-W trend has been captured with more details as compared to results in Section 6.3.2 and 6.3.3. The facies configurations on the reservoir grid from conditional simulations using both hard and soft data were used for flow simulations.

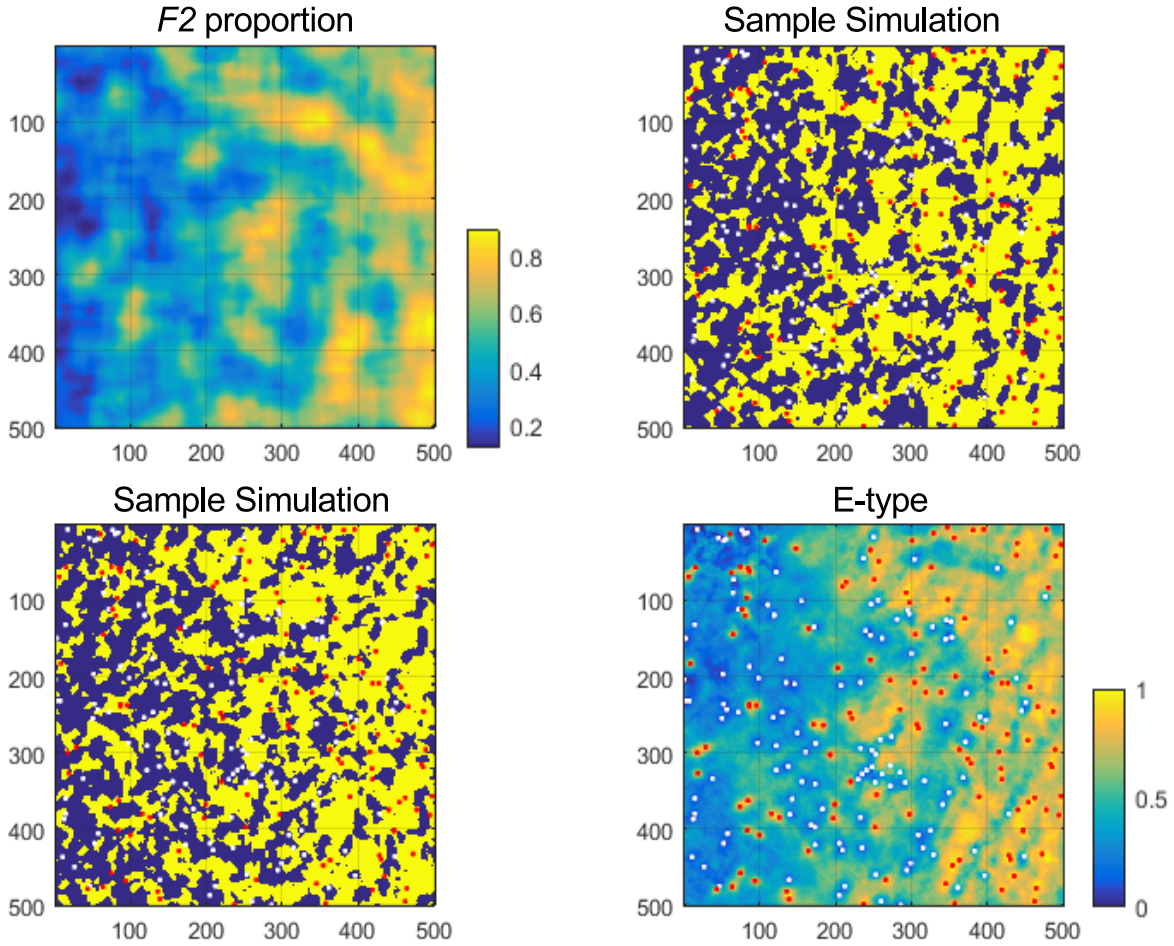

Figure 6.11 The models conditioned to hard and soft data at the same time. The Pearson correlation coefficient between e-type map and input proportion map is 0.72.

6.3.5 Global dynamic behaviour of conditioned models

To have a perspective on the global dynamic response of the simulated field, a quarter-five spot well configuration was considered with an injector placed in the middle and four producers on the corners of the grid. Flow simulations were repeated over the entire simulation grid (for faster computation time resized using a nearest neighbour approach into a smaller grid of 250×250 cells). The flow simulation was performed using the unconditional, hard conditioned, soft conditioned, and hard and soft conditioned models. The TOF and drainage maps were calculated, results shown in Fig. 6.12. The reference model TOF and drainage maps are shown on top. The flow is stronger on the east side of the grid, between central injector and two upper right and bottom right producers due to the more permeable eastern side. It can be recognized with darker colors. The unconditional and hard conditioned models displayed in sub-figures B and C do not show any preferable flow path between the injector and producers. With the addition of soft data fluid flows more to the east side (D). The models conditioned to both hard and soft data display closest flow behaviour to the reference model.

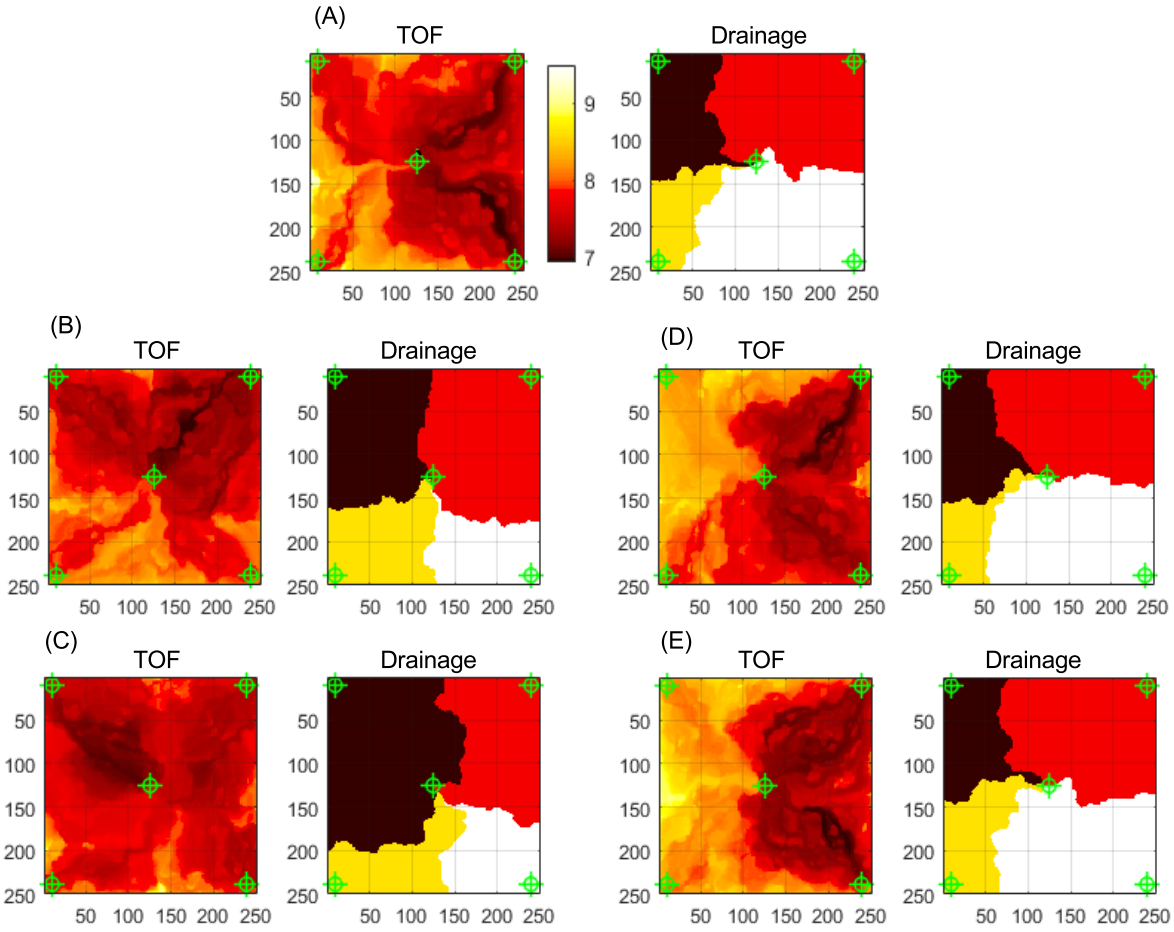

Figure 6.12 Time Of Flight (TOF) and drainage patterns in reference model (A), unconditional simulation (B), hard conditioned model (C), soft conditioned model (D) and hard and soft conditioned model (E).

6.3.6 Calibrated Models

The calibration was performed using the GDM approach described in Section 5.3. The initial reservoir was built on a 50×50 grid with cell size 1000×1000 meters using the MATLAB Reservoir Simulation Toolbox (MRST) (Lie, 2014; Lie et al, 2012). From each of the realizations conditioned to hard and soft data (Fig. 6.11) were derived one Gaussian field within the reservoir grid. Figure 6.13 shows three sample realizations and their corresponding Gaussian fields. With only one Gaussian variable, the lithotype flag consists of a single threshold en-

suring a proportion of 37% for $F2$. The petrophysical properties considered for facies were [10 - 35] and [10 - 1000] for [porosity (%) - permeability (mD)] pairs for [blue - yellow] facies respectively in the TI. A two phase [water-oil] fluid was injected from $I1$ at 0.0021 m^3/s injection rate and the production rate was measured at $P1$ to $P3$. All the flow simulations were performed using MRST (Lie, 2014; Lie et al, 2012). The two-phase oil-water model was considered with incompressible water and oil with constant compressibility of 0.0001 psi^{-1}. The [viscosity (cP)-density (kg/m^3)] pairs for [water-oil] were [1-1000] and [5-700] respectively. The initial saturation model is set to a simple scenario where the bottom of the reservoir was totally filled with water and the top with oil (see Fig. 5.12). The bottom hole pressure is fixed and it is assumed that the well is perforated thoroughly from top to bottom.

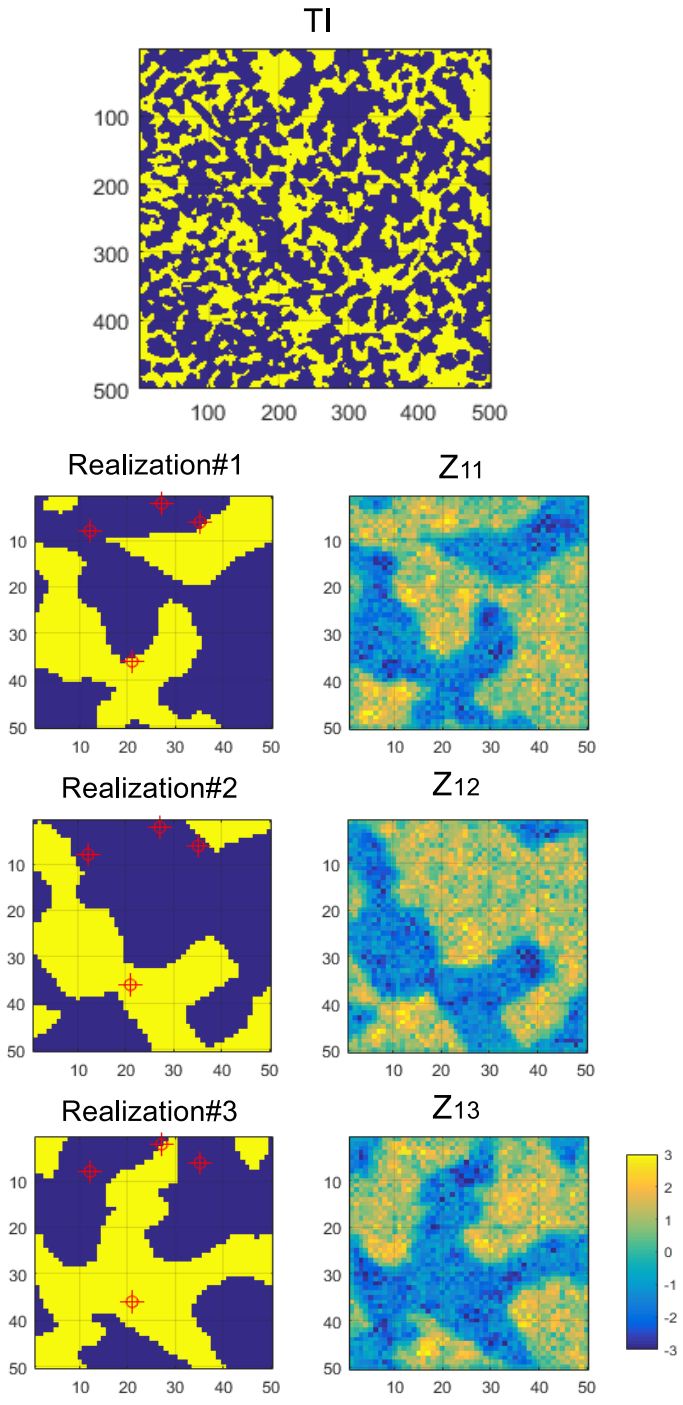

Figure 6.13 Shown on top are TI and the lithotype template (upper right), with three sample realizations on bottom over the reservoir grid with corresponding Gaussian variables. Realizations are the same as Fig. 6.11.

Flow simulation was performed using different types of input MPS realizations including unconditional simulations, hard data conditioned models (Section 6.3.2), soft data conditioned models (Section 6.3.3) and the models conditioned to both hard and soft (Section 6.3.4). From each set, 50 random realizations were selected and fed into the flow simulation. Figure 6.14 first and second rows show the water cut curves at $P1$ to $P3$ for unconditional models, and the hard data conditioned models respectively. The reference water cut (observed data at wells) are displayed with thick red line. As can be seen the water cut values are considerably different from the observed data. Third row on the same figure shows the production results using the soft data conditioned models, and as it shows the reference water cut curves for all producers lay well within those of the realizations. Since such models are not hard conditioned, still considerable variability can be seen between realizations and with the observed data. Fourth row on Fig. 6.14 displays the dynamic response of fully conditioned models to both hard and soft data. The water cut curves at all producers mimic the reference curves even without applying any GDM. And finally the results from GDM are displayed on the bottom row for 19 gradually deformed realizations.

Three realizations and their corresponding water cut curves are displayed in Fig. 6.15. The local patterns of yellow facies throughout the grid changes while the global structures are the same, namely the connecting body of yellow facies passing through $I1$ to $P3$. All GDM facies are conditioned to facies data at well locations. The TOF and drainage maps (Fig. 6.16) show close characters to the reference model.

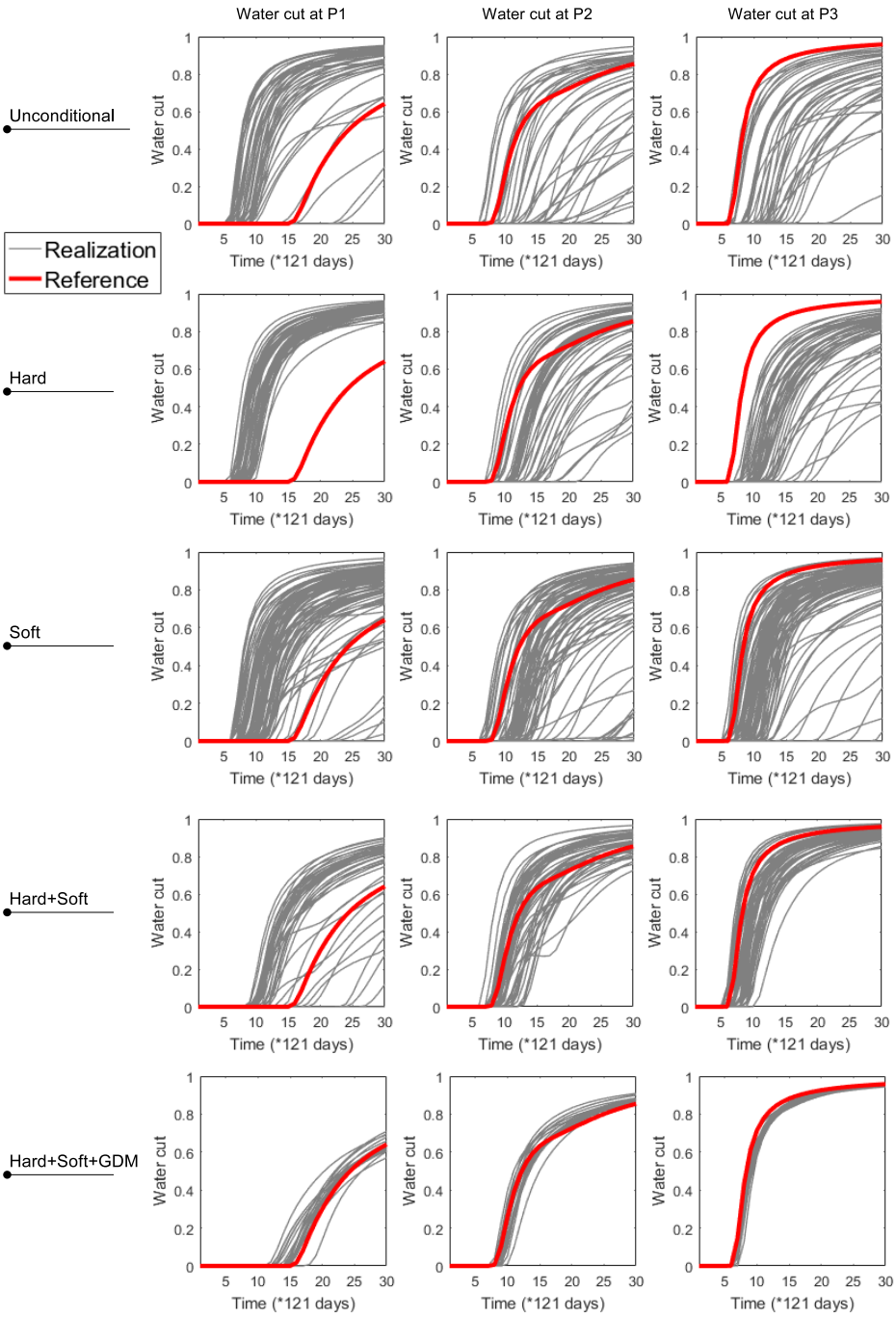

Figure 6.14 The dynamic response of set of realizations conditioned to hard data only (first row), conditioned to soft data only (second row), both and hard and soft data (third row) and GDM output (fourth row). GDM was used with parameter setting of m=400, n = 1, k=3, g=100, m_k=20, m_b=10.

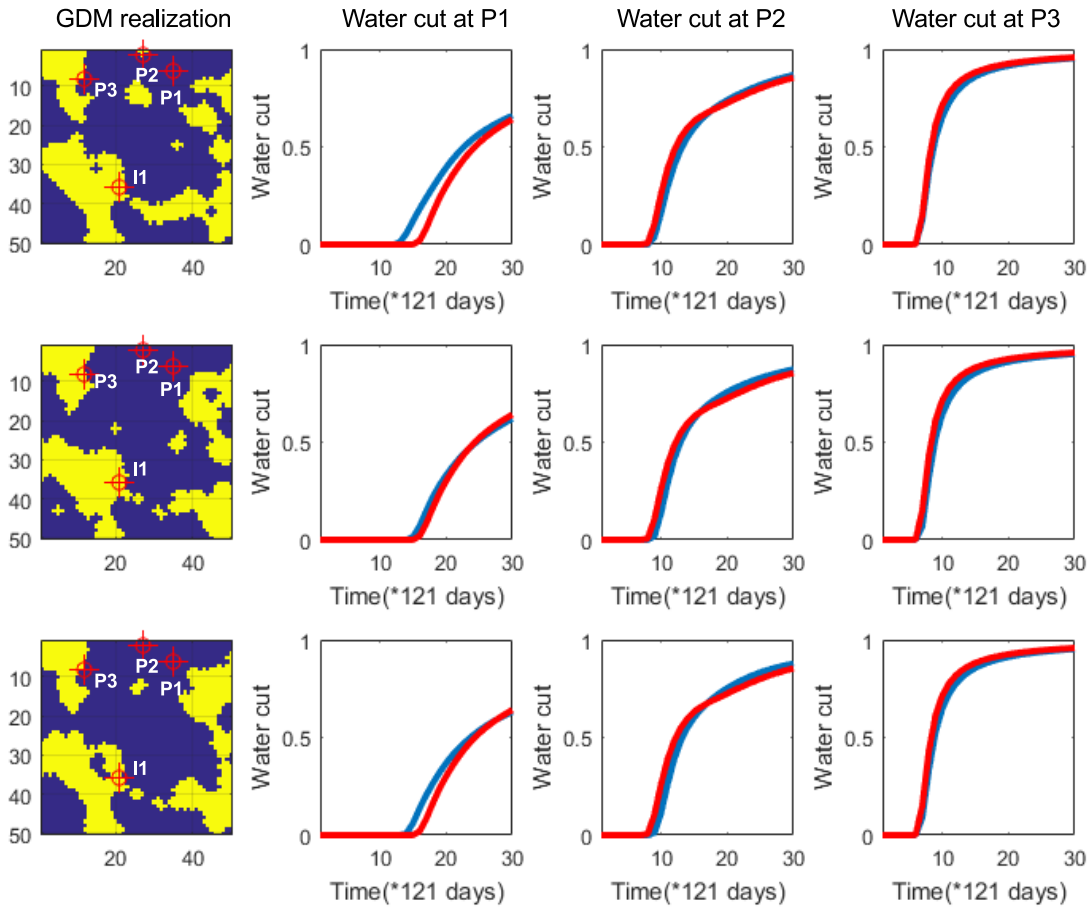

Figure 6.15 The water rate curves at the producers in three GDM outputs as compared to the water rates reference model. GDM was used with parameter setting of m=400, n = 1, k=3, g=100, m_k=20, m_b=10.

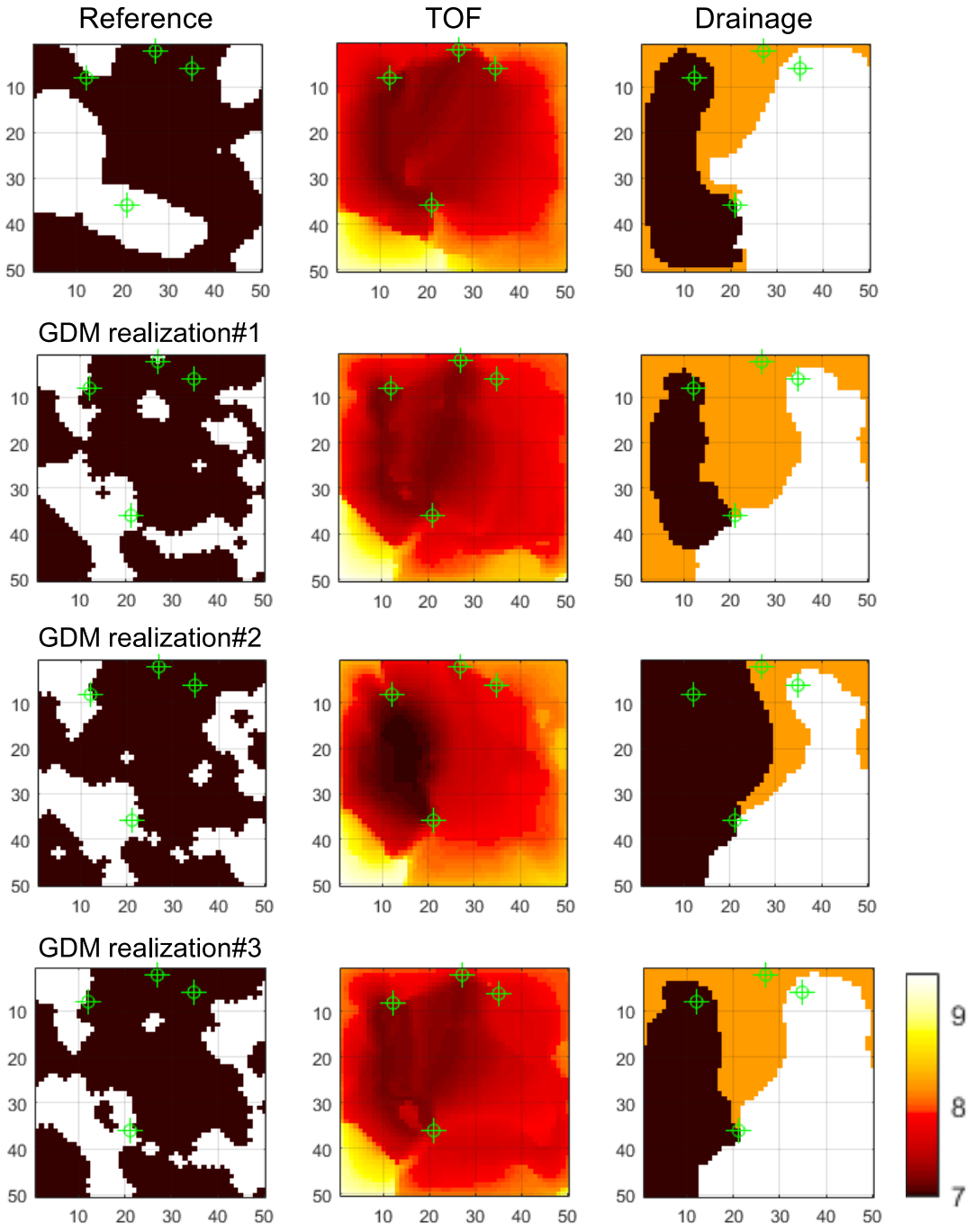

Figure 6.16 TOF and drainage patterns of the reference model (top row) and three calibrated models (second to last rows).

6.4 Discussion and Conclusions

A 2D synthetic integrated facies modeling case was presented with 250 hard data, 3 layers of soft data and 4 wells. The purpose of this chapter was to show a facies modeling example and their further calibration using the idea proposed in this dissertation.

A conditioning workflow was presented to all available soft and hard data sets before calibration with dynamic data (Fig. 6.14 and Fig. 6.11). Due to the non-linear relationship between facies and their flow behaviour, it can be extremely difficult to calibrate the facies models (Fig. 6.14).

Soft data come from a variety of sources all of which reflect the geology on different scales and in different ways. The entire set of soft data must be exploited for capturing most from the underlying reference model. The incorporation of soft data for probability field calculation by multinomial logistic regression can help significantly to recover the right facies in the simulated fields. In the worst case scenario, they have no impact.

It was observed that hard data do not influence the dynamic response of the facies model (Fig. 6.14). There are two possible reasons. First is the number of conditioning data. We used 250 data. It is expected that with more hard data, output facies models resemble more the reference model. Second is the fact that flow behaviour of the facies model depends more on the global positioning of different facies which is controlled with soft data while hard data can force only at individual pixels the facies values.

The final purpose of reservoir simulation is not to reproduce the geology but to calculate recoverable hydrocarbons and production characteristics (Alexander, 1993). However, it was shown in this study that models that are conditioned properly to hard and soft data are geologically more realistic and closer to the reference model and therefore they give more reliable results.

CHAPTER 7

DISCUSSION AND CONCLUSION

In this study we proposed a number of methodologies to enhance the patch-based MPS simulations conditioning and their further calibration. We proposed to enrich the TI pattern database rather than dropping out the nodes from the simulation grid's data event. This approach when coupled with a proper pasting strategy namely quilting/decoupage delivered excellent results both in terms of conditioning rates and texture reproduction. This method enabled to reach first thesis specific objective as described in section 2.2.2.
For the problem of soft data conditioning we started with taking as input multiple soft data sets from geophysical investigations. The multinomial logistic regression was applied to calculate the proportion maps of TI facies. We also proposed using the McFadden's R^2 as the weight given to soft data distance component in MPS simulations. The simulation results using the proposed soft data conditioning approach was very satisfactory both on synthetic and real case studies. The local density of facies was properly controlled with the proportion maps while the models were conditioned to hard data and texture was preserved as well. This method fulfills the second thesis specific objective of soft data conditioning explained in section 2.2.2.
For the calibration of MPS facies models we proposed an evolutionary GDM based on the Gaussian fields acquired from facies models using a Gibbs Sampling and lithotype flag similar to PluriGaussian simulations. The calibration technique was proved efficient in generating deformed facies models that reproduced the target global dynamic data without sacrificing on the quality of facies reproduction. The calibration problem explained in Chapter 5 and mentioned in section 2.2.2 was solved with the proposed GDM approach.
The integrated model of Chapter 6 illustrated an example including hard, soft and dynamic data. The efficiency of the proposed MPS method was illustrated in this example. This test provided an example for the fourth thesis specific objective as described in section 2.2.2, however further tests on larger grids, real domain applications can be performed.

7.1 Discussion

An important issue of MPS simulation is the requirement for training data namely the TI. Depending on the source of TI, it can have different spatial resolutions which not necessarily is the same as hard data. The resolution of TI determines that of the final conditional

simulations. Therefore the conditioning of MPS using a TI with different resolution than hard data can be a challenging task in MPS. This issue has not been investigated in this study as it is assumed in all examples that the TI has the same resolution as hard data. The problem of resolution however is shared between all MPS algorithms, and not specific to the approach proposed in this study. This topic is still an open area of research in MPS.

With new developments being made in MPS, it is natural to have a variety of input parameters for different simulation methods. For practitioners without a deep understanding of the details of each MPS method, it can be difficult to fine tune the input parameters. One advantage of patch-based algorithms lies in their fewer number of input parameters. However, it still bears few important input parameters which must be tuned. These parameters include number of candidate patterns in the pool, size of patch, overlap region width, and the weighting matrices.

Number of patterns in the pool depends on the TI being used. If the TI has enough repetitions of the geological structures, this parameter can be set to large values such as 100-500 to add variability between realizations, however in case TI is devoid of diverse patterns, high values will result in discontinuities and poor hard data reproduction; in such cases it is advised to set it to values less than 10. Values much less cause verbatim copying of the TI textures. The other approach that can be taken to avoid determining the number of patterns in the pool however is to use a distance threshold instead, such as a fixed percentile of the distance distribution e.g., the pool contains all the patterns with distances less than the 1^{st} or 5^{th} percentiles.

The patch size depends on the geometrical features of the geological structures present in the TI. Obviously patches smaller than the minimum object size in the TI cannot capture the variability of objects hence it results in generating unrealistic objects not present in the TI, usually in the form of very elongated structures since the algorithm does not *know* when to terminate the object. Very large patches on the other hand will produce exact copies of large portions of the TI in the simulation. The most important criteria in selecting an optimum patch size is the similarity (and not copying) of the simulated structures and the ones present in the TI. In practice what we suggest to do is to start with a small simulation grid for testing purposes. Few patch size values are checked (starting values based on experience patch size can be set to 0.1 to the TI size) and repeating the simulation using each patch size. These simulations are very rapid and efficient; the patch size that results in least amount of unrealistic geological structures is selected. Usually we allow slight fluctuations around the central patch size. The patch size can be determined for a given TI based on entropy measures based on the idea that a properly-selected patch size captures most randomness of the texture of a TI (Honarkhah and Caers, 2010). In this study we have relied on a trial and

error and visual inspection of the results in an iterative process to determine the patch size. Overlap region width is directly related to the patch size; usually set to $\frac{1}{3}$ of the patch size being used. The influence of overlap width appears in the continuity component of the simulations. For a channel TI for example where the continuity becomes an important feature of the simulated fields, a wider overlap is advised as it will have a more significant effect on the results. Wider overlaps enhance the continuity of channels in simulated fields, however it results in higher CPU times since too many nodes are re-simulated, therefore a trade-off state must be adopted in the end through a trial and error process. However, for small to middle size TIs this parameter's influence is negligible.

The weights given to hard data and other previously-simulated parts of the patch should also be tuned before performing the conditional simulation. In the absence of any hard data, we suggest that higher weights are associated to the data on the border of either a rectangular or L-shaped patch as to have a better continuity. In this case, weights are considered inversely proportional to the square of the distance to the border of the patch. In the conditional case however, the weights assigned to hard data is very large usually. It is often >10 times more than the previously-simulated pixels weights e.g., 100 or 1000. It does not make a difference if it is 100 or 110 for example, hence in practice there is slight effort needed for tuning the weights given to HD.

Selection of ATIs and generally how to evaluate the quality of a MPS method is a common question in all MPS algorithms. First it should be stressed that the validation can still be largely done through visual inspections. However, besides checking the histograms and directional variograms one idea is to check the frequency of patterns in TI and the simulations. In practice, the frequencies of common patterns are plotted in a logarithmic scale between TI and simulations as in Rezaee et al (2014). However this is subject to two conditions: one that the patterns extracted from TI and simulations have to be from very small patches, as there might not be enough combinations of facies within patches in an OTI as soon as the size of the patch is large, and second that the TI is well representative of the subsurface geology being modelled. In most scenarios it is not advised to seek to reproduce strictly what is present in an OTI since a given TI is only one interpretation of the geological setting. We should not even always seek to reproduce exactly the proportions of facies as the proportion in the OTI are not necessarily representative of the proportion in the real field.

In the framework presented for soft data conditioning, auxiliary TIs for soft data are neither used nor needed. Hence, there is no need to know the forward model between the main variable and the soft ones. One advantage of the proposed approach is that the soft data can only partially fill the simulation grid as often happens in real field where different geophysical investigations take place on different regions, not exactly overlapping and covering the whole

field. With a classification step before doing the conditional MPS simulation, partially filled soft data sets can be combined to compute the probability fields on the entire grid. it suffices to define different classification models using only the soft variables that are available at the estimation point.

Regarding the proposed calibration approach there are two main points worth stressing: the multi-normality of Gaussian variables used and the possibility of direct use of PluriGaussian simulations instead of MPS. For the multi-normality, the joint distributions are truncated multivariate normal by construction and the conditional distributions are truncated normal. However the marginal distributions of the values drawn from these conditional distributions do not necessarily appear as normal due to the full conditioning to all facies data in realizations and also the truncation effects. This part of the algorithm indeed deserves further investigation in future, however the results presented in this study are not subject to the exact manner Gaussians are acquired. Finally, because of the resemblance of the proposed GDM approach and the PluriGaussian simulation, it can be attractive to use directly the PluriGaussian simulation instead of MPS to get the facies realizations. However, this is not possible since the type of geological structures tackled with MPS are not reproducible in a PluriGaussian simulation. In particular PluriGaussian simulation does not allow directional constraint with independent latent Gaussian variables whereas MPS allows different kinds of constraints that might be difficult to implement with PluriGaussian simulation. Also directional ordering and other non-symmetrical facies arrangements are only possible in MPS.

7.2 Further developments

Despite the improvements developed in this thesis, some parts of the methodology deserve further research as described in the next section.

Generating ATIs in 3D can be problematic since the quilting method is not obviously extendible to 3D cases. The idea of quilting works properly in 2D and using it for ATI generation is very efficient. However, the proposed 3D cut by Mahmud et al (2014) is just an approximation among many other ways of performing the cut. The ATIs generated with quilting in 3D might have artefacts and discontinuities. Moreover, for very large simulation grids and TIs, and also large number of ATIs the CPU time for generating ATIs can be large. Possibly methods can be borrowed from computer graphics fields to this problem (Mariethoz and Lefebvre, 2014; Manke and Wünsche, 2009). Another possible way to acquire the 3D ATIs is through object-based simulations. In an unconditional simulation, object-based realization can serve perfectly for this purpose given that enough information is available to sample the objects' geometrical features from.

TIs are usually available in 2D images, sketches and maps, yet most simulations domains are defined on 3D grids. One important step is to generate 3D TIs from only 2D sources. Methods are available for this including Comunian et al (2012) that takes one TI representing the geological structures on XY and one over XZ or YZ planes depending on anisotropies. In either case often one sole TI represents the entire set of 2D slices available in the 3D grid. The application of ATIs can be very useful in diversifying and enriching the pattern database in each direction. However further research is required to develop a real practical tool for production of 3D TIs. One idea is to resort to object-based simulation for the production of TI where the object-based simulation would be calibrated by the 2D TIs or at least to characteristics extracted from the 2D TIs.

We used as classification tool the multinomial logistic regression. This method, as any classification method, requires a large training set, which might not be available. One additional difficulty is the fact that soft data typically represents the heterogeneities at much larger support than hard data which may lead to poor classification results even if the soft data is informative on a large scale. Finally, we measure the distance to the logistic regression probability fields by comparing with the facies proportions in each patch. This criterion could loose sensitivity for very large patches. Although other classifiers such as discriminant analysis, random forests, naive Bayes, support vector machines could have been used, they would have all been subjected to the same limitations mentioned. However, for each of these methods, a similar measure to Mcfadden R^2 will have to be defined so as to set automatically the weight given to soft data in the distance computation. For convenience, in all our tests, we used fields with complete soft data. However, our algorithm can easily be adapted to account for incomplete fields. It suffices to simply switch the probability field distance to 0 when no soft data are available in some parts of the simulated field.

The application of GDM on latent Gaussian variables of the facies models can potentially face problems for the channel TI (Fig. 1.5), or TIs showing similar structure. The continuity of channels is quickly lost when several realizations are merged. Potential ideas include generating dependent realizations where from one realization to another the location of channels changes only slightly avoiding disconnecting part of the channel in the output merged model. Primary tests performed for this idea (Rezaee and Marcotte, 2017) gave satisfactory results however it needs to be studied in more details.

7.3 Conclusions

The problem related to hard data conditioning was solved with enriched TI databases. It was shown that patch-based simulations using quilting and ATIs considerably improve the

quality of simulations in terms of texture reproduction and conditioning rates. The approach was proved efficient in reproducing hard data for both categorical and continuous TIs. Conditional simulations to soft data was performed using the probability maps calculated with multinomial logistic regression, and a two-term distance function based on convolution functions. The proposed idea was tested over synthetic TIs and a real TI of gas grade. The simulations reproduced the texture of TI and the local proportion enforced with probability maps. The calibration to dynamic data and large scale soft data was performed using a new version of GDM. A variety of tests were carried out including 2D and 3D shortest path travel cost between source and sink, large scale proportion maps, seismic section and water cut tests over 2D and 3D scenarios. In all cases, the calibration results were satisfactory. All the ideas proposed were tested in an integrated model of available hard, soft and dynamic data. The dynamic data assimilation was performed using the proposed GDM approach. It was concluded that soft data have much more influence on the calibration of facies models to dynamic data, while hard data control locally the flow behaviour of the model. The hard and soft data conditioned models bear similar flow signatures even without applying GDM. This thesis proposes original solutions to three long standing problems in patch-based MPS simulation: conditioning to numerous hard data, integration in a consistent way of multiple soft-data and automatic calibration of MPS realizations to dynamic data. By enabling to combine in a coherent way very different and complementary sources of information such as the TI itself, hard data, multiple soft data and dynamic data, the tools developed in this thesis constitute original contributions toward the use of patch-based MPS method to solve engineering problem found in petroleum, mining and hydrogeology domains.

REFERENCES

Aanonsen SI, Nævdal G, Oliver DS, Reynolds AC, Vallès B (2009) The ensemble Kalman filter in reservoir engineering–a review. SPE Journal 14(03):393–412

Abdollahifard MJ, Faez K (2013) Stochastic simulation of patterns using Bayesian pattern modeling. Computational Geosciences 17(1):99–116

Agarwal B, Hermansen H, Sylte J, Thomas L (2000) Reservoir characterization of ekofisk field: a giant, fractured chalk reservoir in the Norwegian North Sea–history match. SPE Reservoir Evaluation & Engineering 3(06):534–543

Al-Anazi A, Gates I (2012) Support vector regression to predict porosity and permeability: effect of sample size. Computers & Geosciences 39:64–76

Al-Mudhafer WJ (2014) Multinomial Logistic Regression for Bayesian estimation of vertical facies modeling in heterogeneous sandstone reservoirs. In: Offshore Technology Conference-Asia, Offshore Technology Conference

Alexander J (1993) A discussion on the use of analogues for reservoir geology. Geological Society, London, Special Publications 69(1):175–194

Allard D, D'Or D, Froidevaux R (2011) An efficient maximum entropy approach for categorical variable prediction. European Journal of Soil Science 62(3):381–393

Allard D, Comunian A, Renard P (2012) Probability aggregation methods in geoscience. Mathematical Geosciences 44(5):545–581

Almeida AS, Tran T, Ballin PR (1993) An integrated approach to reservoir studies using stochastic simulation techniques. In: Soares A (ed) Geostatistics Troia'92, pp 371–383

Anterion F, Eymard R, Karcher B (1989) Use of parameter gradients for reservoir history matching. In: SPE Symposium on Reservoir Simulation, Society of Petroleum Engineers

Armstrong M, Galli A, Beucher H, Loch G, Renard D, Doligez B, Eschard R, Geffroy F (2011) PluriGaussian simulations in geosciences. Springer Science & Business Media

Arpat GB, Caers J (2007) Conditional simulation with patterns. Mathematical Geology 39(2):177–203

Audet C, Dennis Jr JE (2001) Pattern search algorithms for mixed variable programming. SIAM Journal on Optimization 11(3):573–594

Bellefleur G, Riedel M, Brent T (2006) Seismic characterization and continuity analysis of gas-hydrate horizons near Mallik research wells, Mackenzie Delta, Canada. The Leading Edge 25(5):599–604

Borg I, Groenen P (1997) Modern multidimensional scaling: theory and applications. Springer, New York

Boucher A (2009) Sub-pixel mapping of coarse satellite remote sensing images with stochastic simulations from training images. Mathematical Geosciences 41(3):265–290

Caers J (2002) Geostatistical history matching under training-image based geological model constraints. In: SPE annual technical conference and exhibition, Society of Petroleum Engineers

Caers J (2003) Efficient gradual deformation using a streamline-based proxy method. Journal of Petroleum Science and Engineering 39(1):57–83

Caers J, Hoffman T (2006) The probability perturbation method: a new look at Bayesian inverse modeling. Mathematical Geology 38(1):81–100

Caers J, Ma X (2002) Modeling conditional distributions of facies from seismic using neural nets. Mathematical Geology 34(2):143–167

Caers J, Strebelle S, Payrazyan K (2003) Stochastic integration of seismic data and geologic scenarios: a west Africa submarine channel saga. The Leading Edge 22(3):192–196

Carranza EJM, Laborte AG (2015) Random forest predictive modeling of mineral prospectivity with small number of prospects and data with missing values in abra (philippines). Computers & Geosciences 74:60–70

Caté A, Perozzi L, Gloaguen E, Blouin M (2017) Machine learning as a tool for geologists. The Leading Edge DOI http://dx.doi.org/10.1190/tle36030064.1

Chambers RL, Yarus JM (2002) Quantitative use of seismic attributes for reservoir characterization. CSEG recorder 27(6):14–25

Chugunova TL, Hu LY (2008) Multiple-point simulations constrained by continuous auxiliary data. Mathematical Geosciences 40(2):133–146

Comunian A, Renard P, Straubhaar J (2012) 3D multiple-point statistics simulation using 2D training images. Computers & Geosciences 40:49–65

Cover TM, Thomas JA (1991) Elements of information theory. Wiley, New-York

Daly C (2005) Higher order models using entropy, markov random fields and sequential simulation. In: Geostatistics Banff 2004, Springer, pp 215–224

Damsleth E, Tjolsen CB, Omre H, Haldorsen HH (1992) A two-stage stochastic model applied to a North Sea reservoir. Journal of Petroleum Technology 44(04):402–486

Deutsch C, Gringarten E (2000) Accounting for multiple-point continuity in geostatistical modeling. In: 6th International Geostatistics Congress, Geostatistics Association of Southern Africa, pp 156–165

Deutsch C, Tran T (2002) FLUVSIM: a program for object-based stochastic modeling of fluvial depositional systems. Computers & Geosciences 28(4):525–535

Deutsch CV (1993) Conditioning reservoir models to well test information. In: Geostatistics Tróia 92, Springer, pp 505–518

Deutsch CV, Journel A (1998) Geostatistical software library and user's guide. Oxford University Press, New York

Deutsch J, Deutsch C (2014) A multidimensional scaling approach to enforce reproduction of transition probabilities in truncated pluriGaussian simulation. Stochastic Environmental Research and Risk Assessment 28:707–716

Dickinson G (1953) Geological aspects of abnormal reservoir pressures in Gulf coast Louisiana. AAPG Bulletin 37(2):410–432

Dijkstra EW (1959) A note on two problems in connexion with graphs. Numerische Mathematik 40(2):269–271

Dobson AJ, Barnett A (2008) An introduction to generalized linear models. CRC press

Dreiseitl S, Ohno-Machado L (2002) Logistic regression and artificial neural network classification models: a methodology review. Journal of Biomedical Informatics 35(5):352–359

Dubreuil-Boisclair C, Gloaguen E, Bellefleur G, Marcotte D (2012) Non-gaussian gas hydrate grade simulation at the Mallik site, Mackenzie Delta, Canada. Marine and Petroleum Geology 35(1):20–27

Duhamel P, Vetterli M (1990) Fast Fourier transforms: a tutorial review and a state of the art. Signal processing 19(4):259–299

Efros AA, Freeman WT (2001) Image quilting for texture synthesis and transfer. In: Proceedings of the 28th Annual Conference on Computer Graphics and Interactive Techniques, ACM, pp 341–346

El Ouassini A, Saucier A, Marcotte D, Favis BD (2008) A patchwork approach to stochastic simulation: A route towards the analysis of morphology in multiphase systems. Chaos, Solitons and Fractals 36(2):418–436

Emery X (2007) Simulation of geological domains using the pluriGaussian model: new developments and computer programs. Computers & Geosciences 33(9):1189–1201

Emery X, Lantuéjoul C (2014) Can a training image be a substitute for a random field model? Mathematical Geosciences 46:133–147

Endres DM, Schindelin JE (2003) A new metric for probability distributions. IEEE Transactions on Information Theory 49:1858–1860.

Evensen G (2003) The ensemble Kalman filter: Theoretical formulation and practical implementation. Ocean Dynamics 53(4):343–367

Faucher C, Saucier A, Marcotte D (2013) A new patchwork simulation method with control of the local-mean histogram. Stochastic Environmental Research and Risk Assessment 27(1):253–273

Faucher C, Saucier A, Marcotte D (2014) Corrective pattern-matching simulation with controlled local-mean histogram. Stochastic Environmental Research and Risk Assessment 28(8):2027–2050

Fisher SRA, Fisher RA, Genetiker S, Fisher RA, Genetician S, Fisher RA, Généticien S (1960) The design of experiments, vol 12. Oliver and Boyd Edinburgh

Francis A (2005) Limitations of deterministic and advantages of stochastic seismic inversion. Recorder 30(1):5–11

Freulon X, de Fouquet C (1993) Conditioning a Gaussian model with inequalities. In: Geostatistics Tróia92, Springer, pp 201–212

Galli A, Beucher H, Le Loch G, Doligez B (1994) The pros and cons of the truncated Gaussian method. In: Geostatistical simulations, Springer, pp 217–233

Geman S, Geman D (1984) Stochastic relaxation, Gibbs distributions, and the Bayesian restoration of images. IEEE Transactions on Pattern Analysis and Machine Intelligence (6):721–741

Goovaerts P (1997) Geostatistics for Natural Resources Evaluation. Oxford University Press

Guardiano F, Srivastava M (1993) Multivariate geostatistics: Beyond bivariate moments. In: Soares A (ed) Geostatistics Troia'92, vol 5, pp 133–144

Guo B, Shum H, Xu YQ (2000) Chaos mosaic: Fast and memory efficient texture synthesis. Microsoft Research Paper MSR-TR-2000-32

Harris J, Grunsky E (2015) Predictive lithological mapping of canada's north using random forest classification applied to geophysical and geochemical data. Computers & Geosciences 80:9–25

Hearn C, Ebanks Jr W, Tye R, Ranganathan V (1984) Geological factors influencing reservoir performance of the Hartzog Draw field, Wyoming. Journal of Petroleum Technology 36(08):1–335

Heidari L, Gervais V, Le Ravalec M, Wackernagel H (2013) History matching of petroleum reservoir models by the ensemble Kalman filter and parameterization methods. Computers & Geosciences 55:84–95

Higdon D, Swall J, Kern J (1999) Non-stationary spatial modeling. Bayesian Statistics 6(1):761–768

Hoffman B, Caers J (2007) History matching by jointly perturbing local facies proportions and their spatial distribution: application to a North Sea reservoir. Journal of Petroleum Science and Engineering 57(3):257–272

Holland JH (1975) Adaptation in natural and artificial systems: an introductory analysis with applications to biology, control, and artificial intelligence. University of Michigan Press

Honarkhah M, Caers J (2010) Stochastic simulation of patterns using distance-based pattern modeling. Mathematical Geosciences 42(5):487–517

Honarkhah M, Caers J (2012) Direct pattern-based simulation of non-stationary geostatistical models. Mathematical Geosciences 44(6):651–672

Hooke R, Jeeves TA (1961) Direct search solution of numerical and statistical problems. Journal of the ACM (JACM) 8(2):212–229

Hosmer Jr DW, Lemeshow S, Sturdivant RX (2013) Applied logistic regression, vol 398. John Wiley & Sons

Hu L, Zhao Y, Liu Y, Scheepens C, Bouchard A (2013) Updating multipoint simulations using the ensemble Kalman filter. Computers & Geosciences 51:7–15

Hu LY (2000) Gradual deformation and iterative calibration of Gaussian-related stochastic models. Mathematical Geology 32(1):87–108

Hu LY (2002) Combination of dependent realizations within the gradual deformation method. Mathematical Geology 34(8):953–963

Hu LY, Blanc G, Noetinger B (2001) Gradual deformation and iterative calibration of sequential stochastic simulations. Mathematical Geology 33(4):475–489

Jones T, Larue D (1997) Object-based modeling and deepwater depositional systems. In: IAMG, vol 97, pp 438–443

Journel A (1983) Nonparametric estimation of spatial distributions. Journal of the International Association for Mathematical Geology 15(3):445–468

Journel AG (2002) Combining knowledge from diverse sources: an alternative to traditional data independence hypotheses. Mathematical Geology 34(5):573–596

Kjonsberg H, Kolbjornsen O (2008) Markov mesh simulations with data conditioning through indicator kriging. In: Proceedings of the 8th International Geostatistics Congress, Santiago, Chile

Koch J, He X, Jensen KH, Refsgaard JC (2014) Challenges in conditioning a stochastic geological model of a heterogeneous glacial aquifer to a comprehensive soft data set. Hydrology and Earth System Sciences 18(8):2907–2923

Koltermann C, Gorelick S (1996) Heterogeneity in sedimentary deposits: a review of structure-imitating, process-imitating, and descriptive approaches. Water Resources Research 32(9):2617–2658

Koltermann CE, Gorelick SM (1992) Paleoclimatic signature in terrestrial flood deposits. Science 256(5065):1775–1782

Krishnan S, Boucher A, Journel AG (2005) Evaluating information redundancy through the Tau model. In: Geostatistics Banff 2004, Springer, pp 1037–1046

Lange K, Frydendall J, Cordua K, Hansen T, Melnikova Y, Mosegaard K (2012) A frequency matching method: solving inverse problems by use of geologically realistic prior information. Mathematical Geosciences 44(7):783–803

Le Loch G, Galli A (1997) Truncated pluriGaussian method: theoretical and practical points of view. Geostatistics Wollongong 96(1):211–222

Le Loch G, Beucher H, Galli A, Doligez B (1994) Improvement in the truncated gaussian method: combining several gaussian functions. In: ECMOR IV-4th European Conference on the Mathematics of Oil Recovery

Le Ravalec M, Noetinger B, Hu LY (2000) The FFT moving average (FFT-MA) generator: An efficient numerical method for generating and conditioning Gaussian simulations. Mathematical Geology 32(6):701–723

Le Ravalec-Dupin M, Hu LY (2005) Gradual deformation of Boolean simulations. In: Geostatistics Banff 2004, Springer, pp 939–948

Le Ravalec-Dupin M, Nœtinger B (2002) Optimization with the gradual deformation method. Mathematical Geology 34(2):125–142

Lee SJ (2005) Models of soft data in geostatistics and their application in environmental and health mapping. PhD thesis, University of North Carolina at Chapel Hill

Liang M, Marcotte D (2016) A class of non-stationary covariance functions with compact support. Stochastic Environmental Research and Risk Assessment 30(3):973–987

Lie KA (2014) An introduction to reservoir simulation using Matlab. SINTEF ICT

Lie KA, Krogstad S, Ligaarden IS, Natvig JR, Nilsen HM, Skaflestad B (2012) Open-source Matlab implementation of consistent discretisations on complex grids. Computational Geosciences 16(2):297–322

Liu N, Oliver DS (2005) Ensemble Kalman filter for automatic history matching of geologic facies. Journal of Petroleum Science and Engineering 47(3):147–161

Liu Y (2006) Using the Snesim program for multiple-point statistical simulation. Computers & Geosciences 32(10):1544–1563

Lu B, Torquato S (1992) Lineal-path function for random heterogeneous materials. Physical Review A 45(2):922

Mahmud K, Mariethoz G, Caers J, Tahmasebi P, Baker A (2014) Simulation of earth textures by conditional image quilting. Water Resources Research 50(4):3088–3107

Manke F, Wünsche B (2009) Fast spatially controllable 2D/3D texture synthesis and morphing for multiple input textures. In: GRAPP, pp 5–12

Marcotte D (1996) Fast variogram computation with FFT. Computers and Geosciences 22(10):1175–1186

Mariethoz G, Caers J (2014) Multiple-point geostatistics: stochastic modeling with training images. John Wiley & Sons

Mariethoz G, Lefebvre S (2014) Bridges between multiple-point geostatistics and texture synthesis: Review and guidelines for future research. Computers & Geosciences 66:66–80

Mariethoz G, Renard P, Cornaton F, Jaquet O (2009) Truncated pluriGaussian simulations to characterize aquifer heterogeneity. Ground Water 47(1):13–24

Mariethoz G, Renard P, Straubhaar J (2010) The Direct Sampling method to perform multiple-point geostatistical simulations. Water Resources Research 46(11)

Mariethoz G, Straubhaar J, Renard P, Chugunova T, Biver P (2015) Constraining distance-based multipoint simulations to proportions and trends. Environmental Modelling and Software 72:184–197

McFadden D (1973) Conditional logit analysis of qualitative choice behavior

Michael H, Li H, Boucher A, Sun T, Caers J, Gorelick S (2010) Combining geologic-process models and geostatistics for conditional simulation of 3-d subsurface heterogeneity. Water Resources Research 46(5)

Oliver DS, Chen Y (2011) Recent progress on reservoir history matching: a review. Computational Geosciences 15(1):185–221

Osterholt V, Dimitrakopoulos R (2007) Simulation of orebody geology with multiple-point geostatistics: Application at Yandi channel iron ore deposit. implications for resource uncertainty. In: Orebody Modelling and Strategic Mine Planning, The Australasian Institute of Mining and Metallurgy, pp 51–60

Paciorek CJ, Schervish MJ (2006) Spatial modelling using a new class of nonstationary covariance functions. Environmetrics 17(5):483–506

Parra A, Ortiz JM (2011) Adapting a texture synthesis algorithm for conditional multiple point geostatistical simulation. Stochastic Environmental Research and Risk Assessment 25(8):1101–1111

Pasti HA, Cpsta JF, Boucher A (2012) Multiple-point geostatistics for modeling lithological domains at a Brazilian iron re deposit using the single normal equations simulation algorithm. In: Abrahamsen H, Kolbjornsen (eds) Geostatistics Oslo, Springer

Peters E (2011) Performance of the ensemble Kalman filter outside of existing wells for a channelized reservoir. Computational Geosciences 15(2):345–358

Pickard DK (1980) Unilateral markov fields. Advances in Applied Probability pp 655–671

Pirot G, Linde N, Mariethoz G, Bradford J (2017) Probabilistic inversion with graph cuts: Application to the Boise hydrogeophysical research site. Water Resources Research DOI 10.1002/2016WR019347

Pohar M, Blas M, Turk S (2004) Comparison of logistic regression and linear discriminant analysis: a simulation study. Metodoloski Zvezki 1(1):143

Portilla J, Simoncelli EP (2000) A parametric texture model based on joint statistics of complex wavelet coefficients. International Journal of Computer Vision 40(1):49–70

Porwal A, Carranza EJM, Hale M (2006) Bayesian network classifiers for mineral potential mapping. Computers & Geosciences 32(1):1–16

Press SJ, Wilson S (1978) Choosing between logistic regression and discriminant analysis. Journal of the American Statistical Association 73(364):699–705

Pyrcz M, Boisvert JB, Deutsch CV (2009) ALLUVSIM: A program for event-based stochastic modeling of fluvial depositional systems. Computers & Geosciences 35(8):1671–1685

Pyrcz MJ, Deutsch CV (2005) Conditioning event-based fluvial models. In: Geostatistics Banff 2004, Springer, pp 135–144

Pyrcz MJ, Deutsch CV (2014) Geostatistical reservoir modeling. Oxford University Press

Pyrcz MJ, Strebelle S (2006) Event-based geostatistical modeling: application to deep-water systems. In: Reservoir characterization: integrating technology and business practices, Gulf Coast Section, SEPM Twenty-sixth Annual Research Conference, SEPM, pp 893–922

Reza ZA, Pranter MJ, Weimer P (2006) Moddre: A program to model deepwater-reservoir elements using geomorphic and stratigraphic constraints. Computers & geosciences 32(8):1205–1220

Rezaee H, Marcotte D (2016) Integration of multiple soft data sets in MPS thru multinomial logistic regression: a case study of gas hydrates. Stochastic Environmental Research and Risk Assessment pp 1–19

Rezaee H, Marcotte D (2017) A gradual deformation method to produce multipoint simulation compliant to dynamic data. In: Geostatistics Valencia 2016, Springer

Rezaee H, Mariethoz G, Koneshloo M, Asghari O (2013) Multiple-point geostatistical simulation using the bunch-pasting direct sampling method. Computers and Geosciences 54:293–308

Rezaee H, Asghari O, Koneshloo M, Ortiz J (2014) Multiple-point geostatistical simulation of dykes: Application at Sungun Porphyry Copper System, Iran. Stochastic Environmental Research and Risk Assessment pp 1913–1927

Rezaee H, Marcotte D, Tahmasebi P, Saucier A (2015) Multiple-point geostatistical simulation using enriched pattern databases. Stochastic Environmental Research and Risk Assessment 29(3):893–913

Rivest M, Marcotte D (2012) Kriging groundwater solute concentrations using flow coordinates and nonstationary covariance functions. Journal of Hydrology 472:238–253

Romero C, Carter J (2001) Using genetic algorithms for reservoir characterisation. Journal of Petroleum Science and Engineering 31(2):113–123

Sebacher B, Stordal AS, Hanea R (2015) Bridging multipoint statistics and truncated Gaussian fields for improved estimation of channelized reservoirs with ensemble methods. Computational Geosciences 19(2):341–369

Sen MK, Datta-Gupta A, Stoffa P, Lake L, Pope G (1995) Stochastic reservoir modeling using simulated annealing and genetic algorithm. SPE Formation Evaluation 10(01):49–56

Serra J (1983) Image Analysis and Mathematical Morphology. Academic Press, Inc. Orlando, FL, USA

Shamsipour P, Marcotte D, Chouteau M, Rivest M, Bouchedda A (2013) 3D stochastic gravity inversion using nonstationary covariances. Geophysics 78(2):G15–G24

Shmaryan L, Deutsch C (1999) Object-based modeling of fluvial/deepwater reservoirs with fast data conditioning: methodology and case studies. In: SPE annual technical conference, pp 877–886

Simes RJ (1986) An improved Bonferroni procedure for multiple tests of significance. Biometrika 73(3):751–754

Smirnoff A, Boisvert E, Paradis SJ (2008) Support vector machine for 3d modelling from sparse geological information of various origins. Computers & Geosciences 34(2):127–143

Stein ML (1999) Interpolation of spatial data: some theory for kriging. Springer Science & Business Media

Straubhaar J, Renard P, Mariethoz G, Froidevaux R, Besson O (2011) An improved parallel multiple-point algorithm using a list approach. Mathematical Geosciences 43(3):305–328

Strebelle S (2002) Conditional simulation of complex geological structures using multiple-point statistics. Mathematical Geology 34(1):1–21

Strebelle S, Payrazyan K, Caers J (2002) Modeling of a deepwater turbidite reservoir conditional to seismic data using multiple-point geostatistics. In: SPE Annual Technical Conference and Exhibition, SPE, p SPE paper 77425

Subbey S, Christie M, Sambridge M (2004) Prediction under uncertainty in reservoir modeling. Journal of Petroleum Science and Engineering 44(1):143–153

Tahmasebi P, Hezarkhani A, Sahimi M (2012) Multiple-point geostatistical modeling based on the cross-correlation functions. Computational Geosciences 16(3):779–797

Tahmasebi P, Sahimi M, Caers J (2014) MS-CCSIM: Accelerating pattern-based geostatistical simulation of categorical variables using a multi-scale search in Fourier space. Computers & Geosciences 67:75–88

Tan X, Tahmasebi P, Caers J (2013) Comparing training-image based algorithms using an analysis of distance. Mathematical Geosciences pp 1–21

Tang Y, Atkinson PM, Wardrop NA, Zhang J (2013) Multiple-point geostatistical simulation for post-processing a remotely sensed land cover classification. Spatial Statistics 5:69–84

Tarantola A (2005) Inverse problem theory and methods for model parameter estimation. SIAM

Toftaker H, Tjelmeland H (2013) Construction of binary multi-grid markov random field prior models from training images. Mathematical Geosciences 45(4):383–409

Total (2016) Personal communication

Vasco D, Datta-Gupta A (1999) Asymptotic solutions for solute transport: a formalism for tracer tomography. Water Resources Research 35(1):1–16

de Vries L, Carrera J, Falivene O, Gratacos O, Slooten L (2009) Application of multiple point geostatistics to non-stationary images. Mathematical Geosciences 41(1):29–42

Wei LY (2002) Texture synthesis by fixed neighborhood searching. Phd dissertation

Wei LY, Levoy M (2000) Fast texture synthesis using tree-structured vector quantization. In: Proceedings of the 27th annual conference on Computer graphics and interactive techniques, ACM Press/Addison-Wesley Publishing Co., pp 479–488

Wong P, Jian F, Taggart I (1995) A critical comparison of neural networks and discriminant analysis in lithofacies, porosity and permeability predictions. Journal of Petroleum Geology 18(2):191–206

Xie Y, Cullick AS, Deutsch CV, et al (2001) Surface-geometry and trend modeling for integration of stratigraphic data in reservoir models. In: SPE Western Regional Meeting, Society of Petroleum Engineers

Xu W, Tran TT, Srivastava RM, G JA (1992) Integrating seismic data in reservoir modeling; the collocated cokriging alternative. In: SPE Annual Technical Conference and Exhibition, 4-7 October, Washington, D.C., Society of Petroleum Engineers, pp 833–842

Ying Z, Gomez-Hernandez J (2000) An improved deformation algorithm for automatic history matching. Stanford Center for Reservoir Forecasting, Annual Report 13

Zahner T, Lochbühler T, Mariethoz G, Linde N (2016) Image synthesis with graph cuts: a fast model proposal mechanism in probabilistic inversion. Geophysical Journal International 204(2):1179–1190

Zhang T, Switzer, P Journel A (2006) Filter-based classification of training image patterns for spatial simulation. Mathematical Geology 38:63–80

Zhang T, Du Y, Huang T, Li X (2015a) GPU-accelerated 3D reconstruction of porous media using multiple-point statistics. Computational Geosciences 19(1):79–98

Zhang T, Du Y, Huang T, Peng Y (2015b) Reconstruction of spatial data using isometric mapping and multiple-point statistics. Computational Geosciences 19(5):1047–1062